Modeling and Simulation of Stochastic Phenomena in Carbon Nanotube-Based Single Molecule Sensors

by

Zachary Ward Ulissi

M.A.St. Cambridge University (2010)
B.E. Chemical Engineering, University of Delaware (2009)
B.S. Physics, University of Delaware (2009)

Submitted to the Department of Chemical Engineering
in partial fulfillment of the requirements for the degree of

Doctor of Philosophy in Chemical Engineering

at the

MASSACHUSETTS INSTITUTE OF TECHNOLOGY

June 2015

Signature redacted

Author .....
Department of Chemical Engineering
May 14, 2015

Signature redacted

Certified by .....
Michael S. Strano
Carbon P. Dubbs Professor
Thesis Supervisor

Signature redacted

Certified by .....
Richard D. Braatz
Edwin R. Gilliland Professor
Thesis Supervisor

Signature redacted

Accepted by .....
Richard D. Braatz
Professor of Chemical Engineering
Chairman, Committee for Graduate Students

Modeling and Simulation of Stochastic Phenomena in Carbon Nanotube-Based Single Molecule Sensors

by

Zachary Ward Ulissi

Submitted to the Department of Chemical Engineering
on May 14, 2015, in partial fulfillment of the
requirements for the degree of
Doctor of Philosophy in Chemical Engineering

Abstract

Shrinking sensors to the nanoscale introduces novel selectivity mechanisms and enables the ultimate sensitivity limit, single-molecule detection. Single-walled carbon nanotubes, with a bright fluorescence signal and no photobleaching, are a platform for implantable near-IR sensors capable of selectively detecting a range of small-molecules including the radical signalling molecule nitric oxide, the hormone estradiol, and sugars such as glucose. Selectivity is achieved by engineering an adsorbed phase of polymers, DNA, or surfactants at the nanotube/solution interface. Understanding these sensors requires a range of modeling and simulation tools and presents a unique opportunity to learn how these phases interact with small molecules. This thesis work discusses methods and limits to integrating data from many noisy stochastic sensors, show how these sensors can be used to monitor nitric oxide inside cells with unprecedented spatiotemporal resolution, and describes what is needed to engineer a selective adsorbed phase.

In addition, another method of stochastic detection is described based on the stochastic ionic pore-blocking of transport inside individual single-walled carbon nanotubes. We discuss the current state-of-the-art for making and analysing devices with a single nanometer-scale pore, which necessarily leads to stochastic transport fluctuations. We also present work on the analysis on many devices with single characterized SWCNT pores. A maximum in transport rates inside SWCNTs with diameters of approximately 1.6 nm is shown and discussed, with implications for how we model transport at this scale and the design of new SWCNT membranes.

Finally, we discuss how complex surfaces of interconnected nanoscale structures could lead to new materials with interesting mechanical properties. One example of such a structure is an interlocking sheet of graphene rings, analogous to macroscopic chainmail. Such a sheet would have interesting properties, as entropic out-of-plane fluctuations would lead to a negative Poisson's ratio, known as an auxetic material. We present simulations for what the properties of a sheet might look like. In addition, we present simulations for how these properties change as a membrane is strained and showing the conditions over which these surfaces have desirable properties. These results offer a path towards materials with tunable auxetic properties.

Thesis Supervisor: Michael S. Strano
Title: Carbon P. Dubbs Professor

Thesis Supervisor: Richard D. Braatz
Title: Edwin R. Gilliland Professor

Acknowledgments

I wish to express my gratitude for the support of both of my advisors, Michael Strano and Richard Braatz. They gave me an extraordinary amount of freedom throughout my PhD to choose my own projects and methods, and had helpful suggestions and ideas regardless of what I chose to work on. They also provided two unique viewpoints on how to conduct research, structure thoughts, write papers, and be successful as an academic. Seeking advice from each independently always yielded a complete understanding of the possibilities and allowed me to make fully informed decisions. They have also been incredibly helpful in shaping my future career choices.

The freedom in my PhD would not have been possible without the support of the Department of Energy Computational Science Graduate Fellowship. This program and the associated community of computational scientists in the national labs and academia was incredibly helpful in building my network of potential collaborators and providing a forum each summer to discuss my research with scientists from different fields who shared similar techniques and methods. I expect to continue being involved with this very special community in the future. I am also grateful for the support of the National Science Foundation Graduate Research Fellowship Program, which provided support for my Master's degree at Cambridge University. I am certain that experience and the perspective it provided helped make me a more balanced person than I was when I finished my undergraduate degree.

This thesis work benefited from a large number of collaborations within both of my research groups. Working with others to understand experimental problems and suggest modeling approaches and insight has been incredibly rewarding. I am especially impressed at the positive and supportive culture within my labs. I am indebted to the entirety of the Braatz and Strano groups, but a few that I worked particularly closely with are Jingqing Zhang, Ardemis Boghossian, Rishabh Jain, Mark Molaro, Steven Shimizu, Wonjoon Choi, Fatih Sen. Five graduate students joined MichaelâĂŹs group in my year (Sayalee, Rishabh, Darin, Lee, and myself), and they have been incredible helpful in navigating the long PhD journey.

The MIT cycling team has also been a constant source of support, encouragement, social interaction. I could not have asked for a more enthusiastic group of friends to share my time at MIT with. Research projects will inevitably have periods of slow progress or frustration,

but a quick bike ride with friends each morning always put the problems in perspective. The cycling team also introduced me to my best friend and partner of my time at MIT, Shaena Berlin.

I also have to acknowledge the support of so many mentors and programs that led to me pursuing my PhD. Growing up next to the NIH in Bethesda, I was surrounded by a number of incredible science teachers, including Carolyn Ott and Dr. Mei Wang. I was also incredibly fortunate to start working at the NIH as a high school student through the ORWH-NIH-FAES program for local students. During this time Alexander Sviridov and Amir Gandjbakhche of the NICHD were unbelievably patient in showing me how to do research. At the University of Delaware, Abraham Lenhoff and Dion Vlachos were consistently supportive and encouraged me to continue my research aspirations.

Finally, this work would not have been possible without the continuing support of my family, including my father Stephen Mark Ulissi, my mom Ellen Fulton, my brother Sebastian, and my extended family. I will always remember their simple and consistent advice: Do not strive for happiness; instead strive for excellence and you will be happy. They have supported me at every step of the way regardless of the choices (and mistakes) I have made. Such a continuous source of a support has made facing challenges and risks much easier.

Contents

List of Figures

List of Tables

Chapter 1

Introduction

1.1 Overview of Single-Walled Carbon Nanotube Physics

Bulk materials, when constrained to one or two dimensions isolated, can adopt significantly different properties due to confinement as illustrated in Figure 1-1. Individual sheets SP^2 bonded carbon, known as graphene, have extraordinary in-plane conductivity and structural rigidity for a materials of its thickness. These properties are distinct from its properties when stacked into a bulk configuration (graphite). A sheet of graphene rolled into spheres, known as buckyballs, most commonly in the form C_{60} which have electronic states due to the finite number of atoms. In between 2-dimensional and 0-dimensional confinement lie carbon nanotubes, which are sheets of graphene rolled into a cylinder.

Carbon nanotubes actually represent a family of materials since their geometric and electronic properties depend on the precise basis graphene sheet used to form the unit cylinder, known as the carbon nanotube chirality. The chirality of a nanotube is typically represented as the 2D vector (m, n) on a graphene sheet that defines this basis sheet. Single-walled carbon nanotubes (SWCNTs) are a single cylinder, while multi-walled carbon nanotubes (MWCNTs) are multiple concentric cylinders with different diamters and are typically much larger. The SWCNT chirality determines the diameter through the simple geometric relation

$$d = \frac{0.246 \text{ [nm]}}{\pi}\sqrt{m^2 + n^2 + mn.}$$

Typical diameters for SWCNT are 1-2 nm. MWCNT diameters are typically much larger.

The chirality also specifies the electronic structure: chiralities with $m = n$ are metallic,

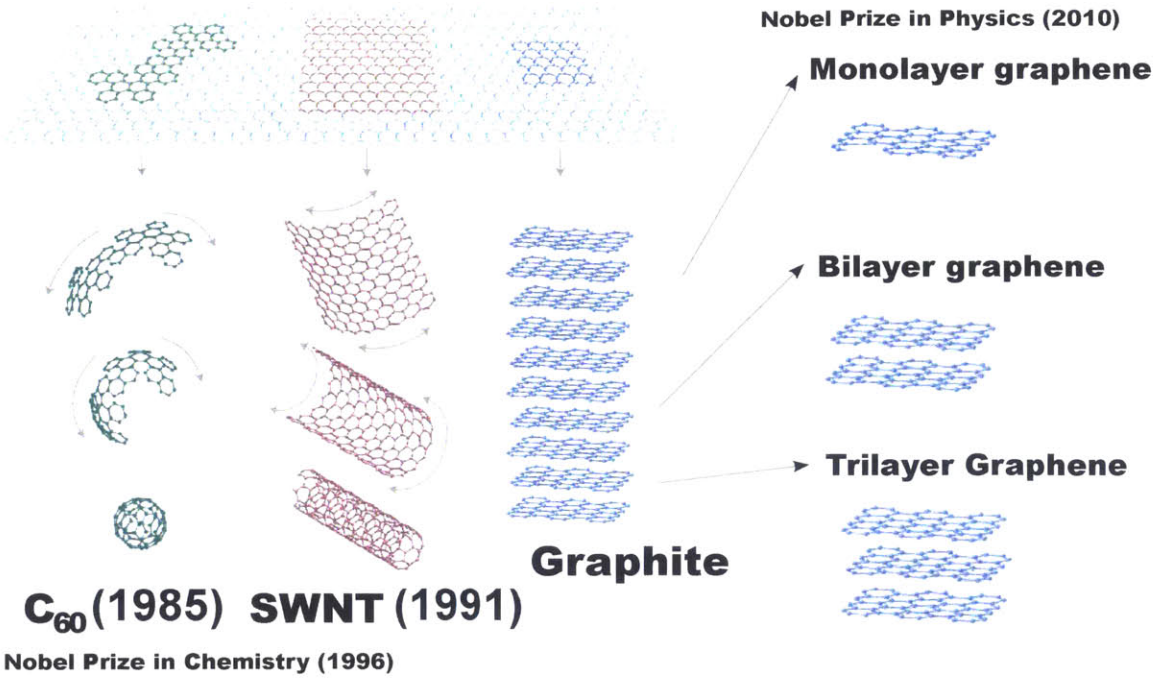

Figure 1-1: Low-dimensional carbon materials, modified from [77]. SP^2-bonded carbon can form structures with zero periodic dimensions (C_{60}, Buckyballs), one periodic dimension (carbon nanotubes), or two periodic dimensions (graphene sheets).

chiralities with $\mod(m-n,3)=0$ are semi-metals (semiconductors with a very small band gap), and other chiralities are semiconducting. The electronic structure of single-walled carbon nanotubes, shown in Figure 1-2 for a semiconducing SWCNT, has discrete Van Hove singularities forming valence and conduction bands in the material. The first and second valence and conduction bands are shown in the cartoon. Each semiconducting SWCNT chirality will have a different electronic density of states. The difference between the first valence and conduction bands, E_{11}, and the difference between the second valence and conduction bands, E_{22}, can be seen for a solution with many SWCNT chiralities in Figure 1-2. These two energy levels are important for understanding the fluorescence properties of SWCNT.

SWCNT have a very strong fluorescence signal compared to small-molecule fluorophores due to their size and mechanism for fluorescent emission which relies on the formation and recombination of localized electron/hole pairs, known as excitons, on the SWCNT. A very simplified picture of SWCNT excitonic physics, necessary to understand the SWCNT-based optical sensors discussed in this work is included here and a cartoon is included in Figure 1-3. Incident radiation near the E_{22} energy level can result in the formation of an exciton

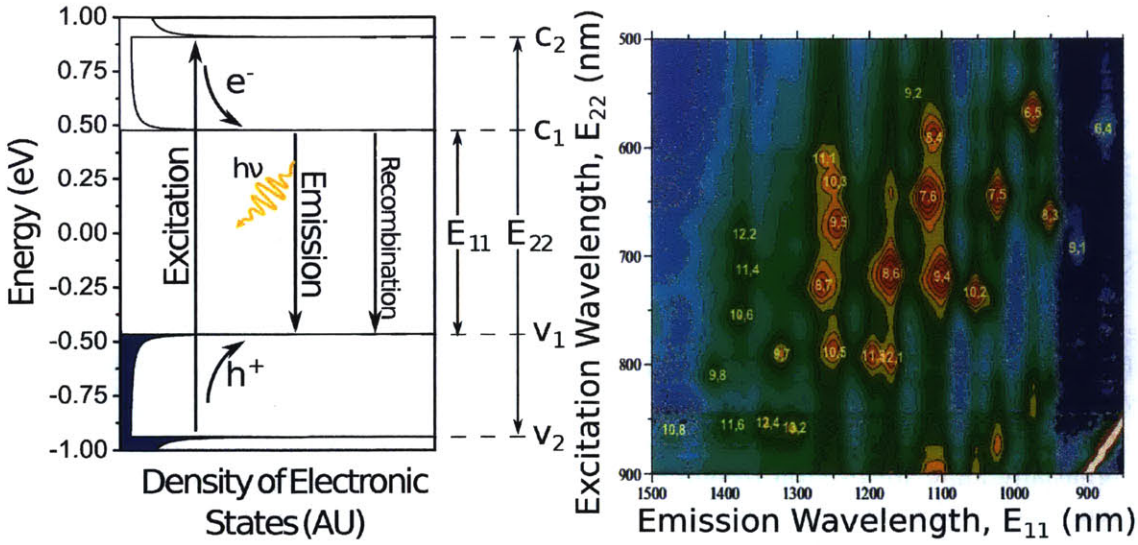

Figure 1-2: Electronic structure of Single-Walled Carbon Nanotubes. (left) Cartoon of the electronic density of states (DOS) for a semiconducting SWCNT showing the characteristic Van Hove singularities. The near-IR fluorescence used for sensors in this thesis is primarily due to the generation of excitons (electron/hole pairs) at the E_{22} transition. After relaxing to the first valence/conduction band, excitons can recombine radiatively to yield photons at the E_{11} level. (right) Map of the fluorescence emission for a solution with a collection of SWCNT at various excitation/emission combinations [12]. This is effectively a map of the E_{11} and E_{22} positions for each SWCNT species in the solution.

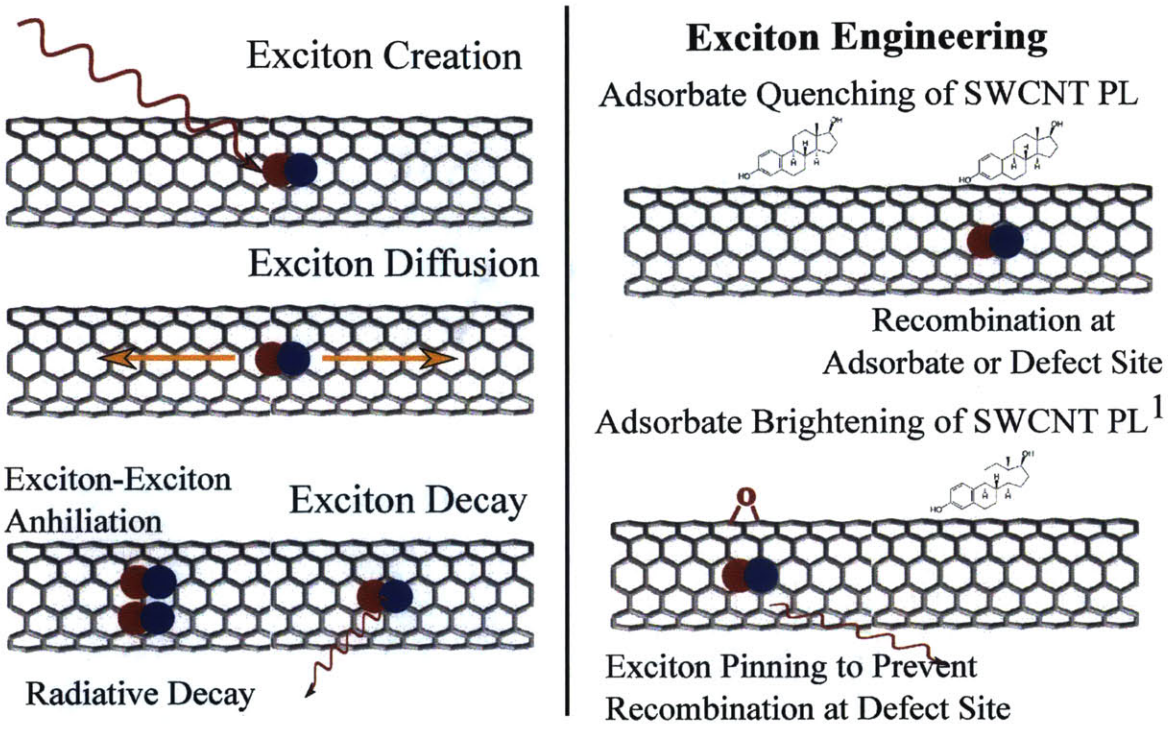

Figure 1-3: Adjusting the radiative decay of excitons through SWCNT surface modification. (left) A cartoon of a typical excitation/decay process for an exciton on a pristine SWCNT. Excitons are created with incident radiation, diffuse along the SWCNT and can undergo exciton-exciton annihilation or radiative decay (among others). (right) Some adsorbates will preferentially allow for exciton recombination. Alternatively, some defects such as singlet-oxygen functionalization trap excitons preventing them from interacting with quenching defects and allowing them to recombine with fluorescence emission.

that is localized along a SWCNT. The exciton can diffuse in a 1-dimensional fashion along the length of the SWCNT. Excitons typically relax to the first valence/conduction band, and those that do and then recombine yield light with energy near the E_{11} energy. This is the typical pathway that leads to the strong fluorescence signal in SWCNT. Excitons can also interact with the ends of the SWCNT, with other excitons, or with defects in the SWCNT electronic structure leading to recombination without radiative decay, leading to a reduction in fluorescence efficiency. Some small molecules, when adsorbed to the SWCNT surface, can increase the rate of these non-radiative exciton losses, resulting in a drop in fluorescence intensity. Conversely other defects, such as the introduction of singlet-oxygen surface functionalization, traps excitons locally, prevents them from interacting with other defects on the surface, and thus allows them to recombine radiatively more efficiently leading to an increase in fluorescence efficiency.

A key challenge in the use of nanoscale carbon devices has been the preparation of high-quality samples. Global production of bulk mixed multi-walled carbon nanotubes, sufficient for applications that use CNTs as filler to improve mechanical properties, is already well above the kiloton/year level [54]. Bulk quantities of higher-quality single-walled carbon nanotube samples are more expensive and have lower availability, but recent manufacturers have introduced products at approximately the $10/gram level [2] with production above 50 ton / year [224]. Even high-quality SWCNT used in experimental devices produce a range of nanotube chiralities, with varying electronic structure and diameter, making single-chirality devices difficult to manufacture. Advances in recent years have revolutionized the process of separating multi-chirality solutions into high-purity single-chirality samples [112, 157, 158, 243, 244, 249]. These separation processes now allow for the routine preparation of liter-scale high-purity solutions of some chiralities, making the production of experimental single-chirality devices possible.

1.2 Why Study Single-Walled Carbon Nanotube Devices?

SWCNT are exciting to study outside of their possible applications due to the diversity of physical phenomena necessary to understand many practical devices. As an example, modeling and understanding SWCNT-based optical sensors, discussed in Part I of this thesis, require a range of modeling and simulation tools to understand the many physical phenomena involved. The relevant techniques are illustrated in Figure 1-6. Modeling techniques range from atomic/electronic methods to understand the exciton behavior, to the device level where continuum or stochastic methods are used. These devices also represent a useful platform for developing these methods. For example, the ability to measure transport rates through individual SWCNTs with varying diameter will inform the development of more accurate simulation techniques for sub-continuum transport at the nanoscale.

Single-walled carbon nanotubes are just one of many possible nanoscale structures that exhibit interesting structural and electronic effects due to nanoscale confinement yet they have received a disproportionate amount of scientific and popular attention in comparison to other materials. This is due to a number of reasons:

1. Simple structure - an all-carbon material is attractive from a raw-material point of view, and the symmetry and simple structure is appealing for the development of

theoretical models and simulations.

2. Variety of electronic structure - very few materials have an electronic structure that can be tuned to various band gaps, or even to control metal/semiconducting characteristics. Separated single-chirality SWCNT samples allow for the preparation of devices with tunable characteristics without resorting to more complicated methods such as chemical doping or mechanical strain.

3. Precise diameter - SWCNT diameter is typically very uniform along the length, and the diameter is set by the chirality. Using single-chirality samples allows for the preparation of structures with a very specific internal diameter at the 1 nm scale. Preparing similar cylinders using self-assembled dendritic monomers or using lithographic techniques to make holes in bulk structures are difficult to tune and rarely scale to the 1 nm diameter range.

4. Strong fluorescence signal - the strong near-IR fluorescence signal is ideally suited to a range of biological applications where small-molecule fluorophores have not been successful. This effect can be tailored to selective detect certain molecules through the addition of adsorbed phases as illustrated in Figure 1-4 for several DNA wrappings.

5. Growing industrial production and preparation methods - there are now a number of companies producing SWCNTs for various applications. Even more importantly, there is a large body of literature on how to analyse sample purity using established spectroscopic techniques. Separating SWCNT into individual chiralities is also increasingly straightforward.

Other nanoscale with similar electronic or geometric structure, such as boron nitride nanotubes, offer only some of these benefits. New materials must first overcome the challenges that the SWCNT community has faced in make practical high-quality devices. For all of these reasons, SWCNT have found their way into a number of practical applications a few of which are illustrated in Figure 1-5. Examples include computer chips with SWCNT transistors [226], conductive reinforced materials such as SWCNT yarns [188], size-selective membranes with high water flow rates [97], near-IR photovoltaics for energy capture [111], and biomedical sensors [45, 269].

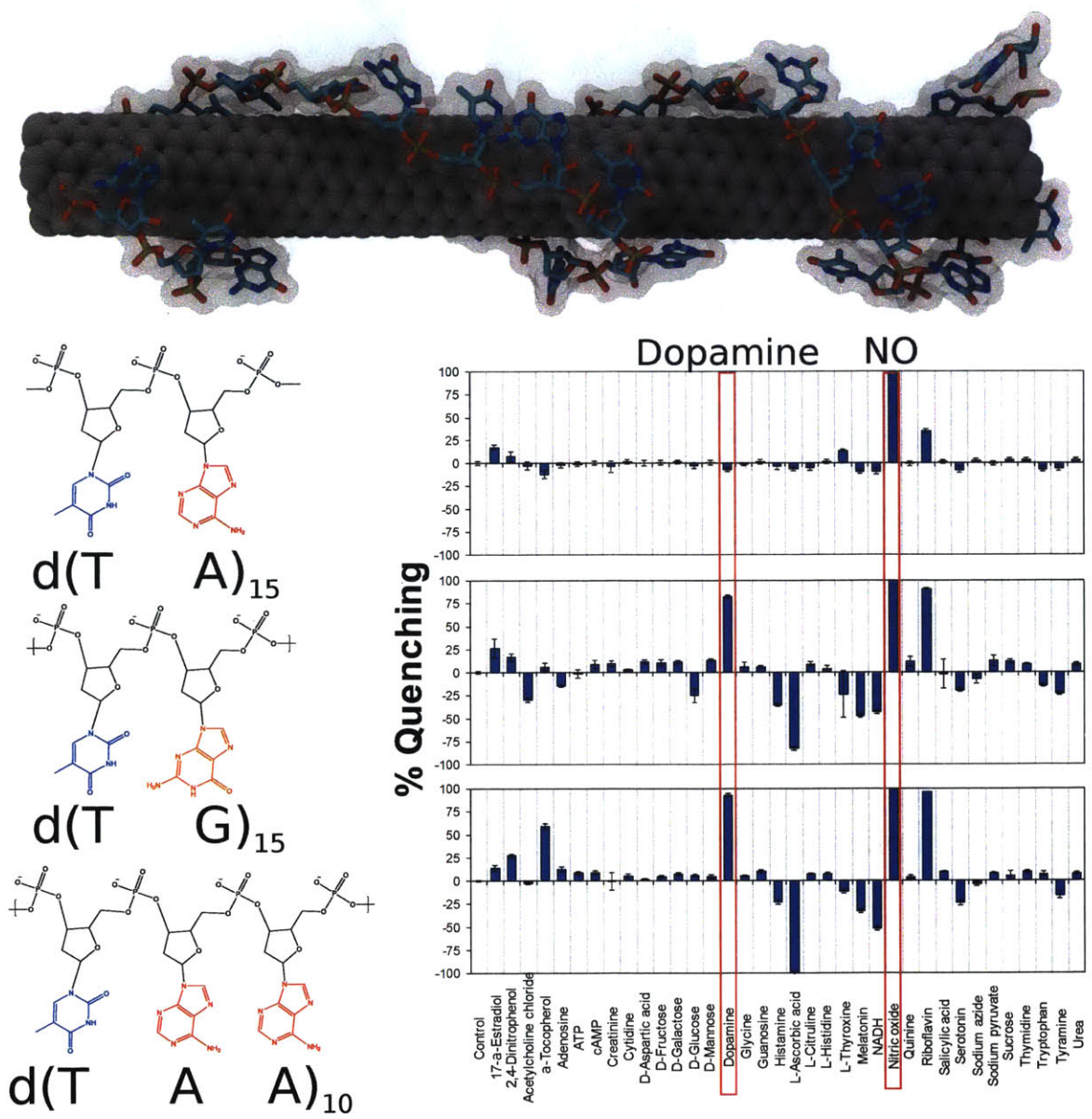

Figure 1-4: Selective detection of small molecules with various sequences of single-stranded DNA adsorbed to a SWCNT surface. (top) Cartoon of a $d(AT)_{15}$ sequence of single-stranded DNA wrapped helically around a SWCNT. (bottom) Selectivity profile for the change in intensity of a (6,5) SWCNT wrapped with three different DNA sequences upon exposure to a screen of a number of small-molecules [269]. $d(AT)_{15}$ has the highest selectivity to nitric oxide (NO) of the three sequences.

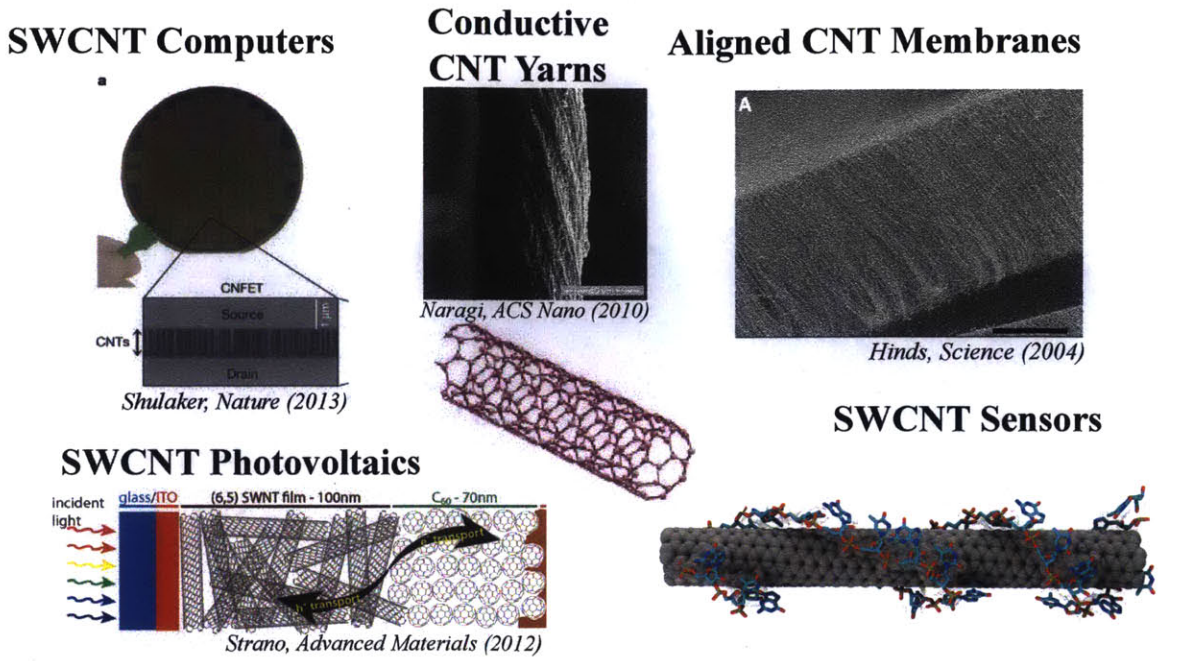

Figure 1-5: A selection of the applications of SWCNT currently under investigation, including the development of SWCNT-based transistors [226], electrically-conductive SWCNT yarns [188], selective SWCNT membranes with high flow rates, SWCNT-based solar cells for near-infrared photovoltaics, and sensors based on functionalized SWCNT [45, 269].

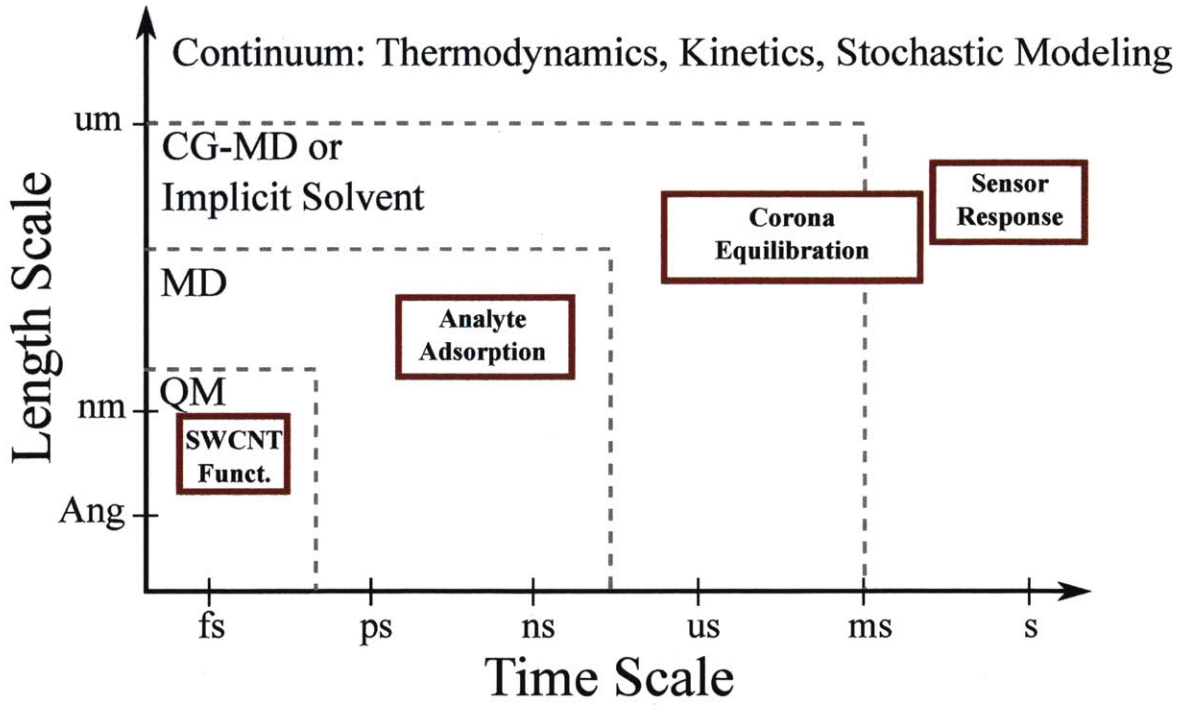

Figure 1-6: Modeling and simulation from SWCNT devices, from the electronic to the device scale. At the largest length scales, continuum or stochastic models are necessary to describe sensor collections. Selectivity is mostly determined by classical interactions near the SWCNT surface. The actual quenching process is a fundamentally electronic effect.

1.3 Thesis Objectives

This thesis explores a number of interesting phenomenon related to SWCNT sensors, with the goal of providing insight into the physical mechanisms at work and providing targets for further engineering of these materials. In many cases, it is impossible to fully characterize these devices with experimental techniques such as spectroscropy, atomic force microscopy, and scanning electron microscropy. In these situations, the models and simulations presented in this work form our most complete picture of the molecular structure and behavior of these devices. By exploring how devices behave at a variety of scales, we can form a more complete picture of how to improve and engineer new functionality in the future.

Part I of this thesis considers how we can use SWCNTs for sensing of small molecules in complicated environments such as cancerous cells:

1. Chapter 2 discusses the challenges related to state-estimation at the nanoscale, especially in the presence of stochastic fluctuations.

2. Chapter 3 presents analytical results for how a collection of stochastic sensors, such as $d(AT)_{15}$-wrapped SWCNT responsding to nitric oxide, will respond to a signal. Methods of estimating chemical concentrations are discussed and an optimal method for estimation is presented along with analytical results for the uncertainty in these estimations.

3. Chapter 4 shows how we can use DNA-wrapped SWCNT sensors for nitric oxide concentration detection inside of cancerous cells. The results are the first measurements of nitric oxide at sub-cellular length scales and at biologically-relevant time scales.

4. Chapter 5 presents a molecular thermodynamic model for predicting how the wrappings of SWCNT impact the sensitivity towards various small molecules of interest. This work paves the way to new adsorbed phases by providing relevant molecular properties to engineer and providing a method to screen wrappings that are unlikely to be useful.

Part I thus forms a more complete picture of how these SWCNT sensors behave, from the molecular scale, to the device scale, to actual biological applications.

Part II of this thesis explores another class of devices that allow for the study of transport and pore-blocking withing individual SWCNTs:

1. Chapter 6 discusses the experimental challenges in making devices with verified transport through the interior of nanoscale pores. Flow at these scales necessarily leads to stochastic transort fluctuations and can be used as an indication of interior flow.

2. Chapter 7 presents the first measurements of transport rates through individual SWCNT with known diameter. A physical mechanism for the observed diameter dependence is presented which explains the maximum in transport rates observed at 1.6 nm.

Due to the challenges in making a large number of these devices in reasonable time scales, further study was limited by the development efforts in the group to design a new class of more reliable devices.

Finally, Part III of this thesis explores the properties of a new class of materials that our group has pondered for several years: chainmail structures made out of interlocking graphene rings. This work aimed to clarify the possible benefits of these materials, before others in the lab undertook the challenge of synthesizing these materials. In the process of investigating these possibilities we realized these membranes should have interesting mechanical properties. However, the literature on similar fluctuating surfaces could not answer the practical ranges over which these properties would persist, so we developed simulations to answer these questions.

Part I

Modeling and Design of SWCNT-based Corona Phase Molecular Recognition Sensors

Chapter 2

Control of nano and microchemical systems

This work originally appeared as: Zachary W. Ulissi, Michael S. Strano, and Richard D. Braatz. Control of nano and microchemical systems. Computers & Chemical Engineering, 51(SI):149-156, 2013.

2.1 Abstract

Many advances in the development of nano and microchemical systems have occurred in the last decade. These systems have significant associated identification and control challenges, including high state dimensionality, limitations in real-time measurements and manipulated variables, and significant uncertainties described by non-Gaussian distributions. Some strategies for addressing these challenges are summarized, which include exploiting structure within the stochastic Master equations that describe molecular interactions, manipulating molecular bonds at system boundaries, and manipulating molecules and nanoscale objects through magnetic and electric fields. The strategies are illustrated in a variety of applications that include the estimation of nucleation kinetics of protein and pharmaceutical crystals within fluidic devices, the estimation of two-dimensional concentration fields using DNA-wrapped single-walled carbon nanotube-based sensor arrays, the simultaneous control of nanoscale geometry and electrical activation during thermal annealing in a semiconductor material, and the control of nanostructure formulation using electric or magnetic fields. Promising directions for research and technology development are identified for the next

decade.

2.2 Introduction

Remarkable advances have been made in the last decade on technologies for *nano and microchemical systems*, which are systems in which chemistry is carried out at nano- to microliter volumes [236, 171]. The objective of using these technologies to manufacture high quality products has motivated a growing literature on the identification and control of these systems. The focus of this article is on the control of chemical systems that have key components with dimensions at the nano or microscale, expanding upon previous reviews on microscale systems [139]. Atomic force microscopy, thin film deposition, and multiscale systems are minimally covered, as these topics are already described in past reviews (e.g., see [229, 257, 44, 27, 26, 29, 178] and citations therein). A summary of challenges that arise when solving control systems tasks for nano and microchemical systems is followed by a description of promising directions for addressing those challenges.

2.3 Challenges and Requirements

In a macroscopic system, the measured outputs are stochastic due to measurement noise and unknown disturbances arising from fluctuations in the environment in variables such as temperature and pressure. If the measurement noise and unknown disturbances for a macroscopic system could be completely removed, the measured outputs would be deterministic. This underlying deterministic character of the relationships between process inputs to states and outputs enables macroscopic systems to be described by deterministic models with isolated stochastic terms to account for measurement noise and unknown disturbances [18, 162]. Much of the phenomena that occur at the nano and microscale are stochastic in a way that is very different from the fluctuations typically observed in a macroscopic system. In particular, phenomena at the molecular scale are inherently stochastic, so that a repeated experiment can produce vastly different outputs even if the overall system has no measurement noise and no unknown disturbances.

As an example of such a phenomenon, consider the nucleation of crystals in droplets of solution, for which a large number of high-throughput microfluidic platforms have been developed over the past decade for the crystallization of organic compounds including amino

acids, proteins, and active pharmaceutical ingredients (e.g., see Figure 2-1 and [88, 275, 236, 242, 10, 149]). These microseparation systems enable the efficient high-throughput search for solvents, molecular additives, and dynamic operating conditions that nucleate and grow high quality protein and pharmaceutical crystals for subsequent analysis via X-ray or neutron crystallography, and enable the investigation of crystallization kinetics for a much wider range of conditions than achievable at the macroscale [247, 256, 79]. Such applications have the potential to impact structure-function analysis, pharmaceuticals design, bioseparations, controlled drug delivery, treatment of protein condensation diseases, and study of human degenerative conditions [32, 256, 197]. The measured output for a single droplet is the *induction time*, which is the time in which the first crystal nucleates. The measured induction time can vary by a factor of two or more, even when the experiment is designed to have negligible disturbances and measurement biases and noise, due to the very small volume of each droplet and that the very small number of crystals in a droplet (e.g. [247, 109]). In such a system, treating the measured output as "*the* induction time" is not appropriate, and the true measured output is represented in terms of an induction time distribution or a cumulative induction time distribution (see Figure 2-2). Quantities derived from such distributions, such as the measured mean induction time or the standard deviation of the induction time, contain much less information than the entire distribution. For nano and microscale systems, the distributions of process outputs are typically not Gaussian, so that the assumption of an underlying Gaussian distribution parameterized by a mean and a variance is not appropriate.

As phenomena at the molecular scale are inherently stochastic, the measured outputs of nano and microscale systems that are a direct consequence of those molecular scale dynamics are also inherently stochastic. Stochastic dynamics with continuous states are typically described by Langevin dynamics or the Fokker-Planck equation [71, 205]. However, when there are only a discrete number of states, stochastic dynamics are described by Master equations [128, 69]:

$$\frac{dP(\sigma,t)}{dt} = \sum_{\sigma'} W(\sigma',\sigma)P(\sigma',t) - \sum_{\sigma'} W(\sigma,\sigma')P(\sigma,t) \tag{2.1}$$

where $P(\sigma,t)$ is the probability that the system is in configuration σ at time t, and $W(\sigma',\sigma)$ is the rate of transitions between configuration σ' and σ (in units of inverse time). Each

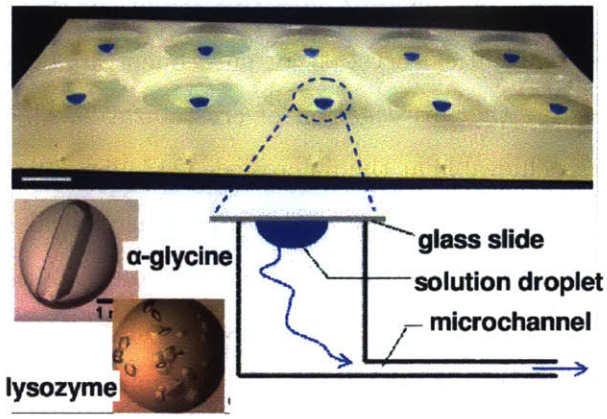

Figure 2-1: A microfluidic platform that uses evaporation to induce nucleation in microliter droplets [125, 126]. The evaporation rate in each droplet is specified by the partial pressure of water at the droplet surface, the area and length of each channel that connects the droplet to external air, and the humidity of the external air.

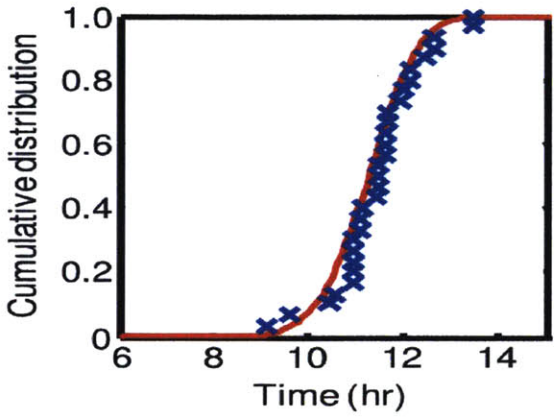

Figure 2-2: Cumulative induction time distributions for droplets containing lysozyme and sodium chloride in aqueous solution: experimental data ($\times$), and model (line) in Eq. 3 fit to the data [125, 126]. The measured induction times range from about 9 to 14 hr for the same experimental conditions.

Master equation is the conservation equation for the probability of a configuration (accumulation = in − out), with the overall system described by writing Eq. 2.1 for every possible configuration in the system. For example, for the nucleation of crystals in droplets, one configuration is the droplet containing no crystals, another configuration is the droplet containing one crystal, etc. The structure of Eq. 2.1 is relatively simple, being linear in the probabilities $P(\sigma,t)$, each of which lie in the interval between 0 and 1. The probabilities can be stacked into a single state vector $x(t)$ and the transition rates collected into a matrix $A(t;\theta)$ that enables Eq. 2.1 to be written in state-space form:

$$\frac{d}{dt}x(t) = A(t;\theta)x(t) \tag{2.2}$$

where $A(t;\theta)$ depends on additional variables such as temperature or concentrations of species external to the system that can vary with time, and on a vector of first-principles model parameters θ such as chemical kinetic, adsorption, or desorption rate constants; surface diffusion coefficients; and equilibrium constants. As an example, the nucleation of crystals in droplets for the microfluidic platform in Figure 2-1 can be modeled by the Master equations

$$\frac{dP_0(t)}{dt} = -\kappa(t)P_0(t), \tag{2.3}$$

$$\frac{dP_n(t)}{dt} = \kappa(t)(P_{n-1}(t) - P_n(t)), \quad n = 1, 2, \ldots, \tag{2.4}$$

where $P_n(t)$ is the probability that the number of crystals is equal to n at time t and $\kappa(t) > 0$ is the transition probability of nucleation in units of inverse time, which depends on the solubility, crystallization kinetics, evaporation rate, and initial droplet volume and solution concentrations [79, 115]. In most applications, the initial number of crystals in a droplet is equal to zero, which is described by the initial conditions $P_0(0) = 1$ and $P_n(0) = 0$. The number of possible configurations in the above model, as well as the number of states in Eq. 2.2, is infinite.

As another example, consider the Master equation for adsorption and desorption of molecules on a DNA-wrapped single-walled carbon nanotube used for single-molecule sensing (see Figure 2-3). A standard approach for reducing the number of configurations is by defining equivalence classes (e.g. [194]), which for this application involves ignoring which

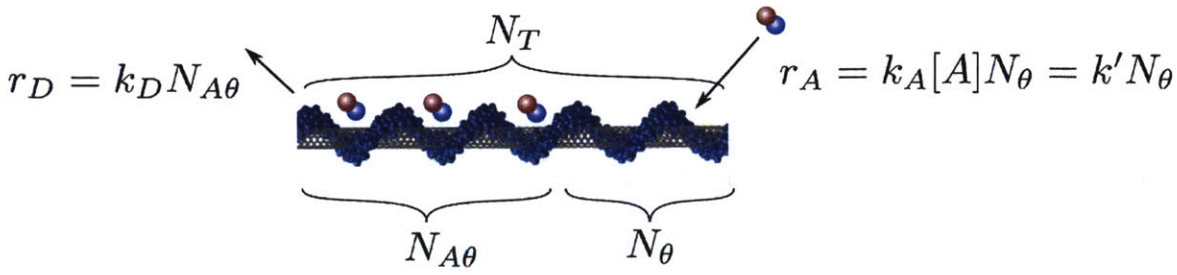

Figure 2-3: Schematic of adsorption and desorption on a DNA-wrapped single-walled carbon nanotube (Ulissi et al., 2011). The arrow points to an open adsorption site.

sites on the nanotube contain the adsorbed molecules. This representation produces the simplified Master equations [250]

$$\frac{dP_0(t)}{dt} = -k'_A N_T P_0(t) + k_D P_1(t), \tag{2.5}$$

$$\frac{dP_i(t)}{dt} = k'_A \left(N_T - (i-1)\right) P_{i-1}(t) \tag{2.6}$$

$$- \left(k_D i + k'_A (N_T - i)\right) P_i(t) \tag{2.7}$$

$$+ k_D (i+1) P_{i+1}(t), \quad i = 1, ..., N_T - 1, \tag{2.8}$$

$$\frac{dP_{N_T}(t)}{dt} = k'_A P_{N_T - 1}(t) - k_D N_T P_{N_T}(t), \tag{2.9}$$

where N_T is the number of potential sites for adsorbed molecules on the nanotube, P_i is the probability that the nanotube has i molecules adsorbed somewhere on its surface, k_D is the desorption rate constant, and k'_A is the adsorption rate constant, which is proportional to the concentration of the adsorbing species in the surrounding solution. Both rate constants can vary with time, due to time-varying temperature during sensing. The nanotube-based sensor computes the latter concentration by real-time estimation of the adsorption rate constant k'_A from the measured adsorption and desorption events [22]. The matrix A in the state equation (Eq. 2.2) has row and column dimensions equal to the number of potential adsorption sites plus one, which is high for long nanotubes (carbon nanotubes have been grown that are longer than 10 centimeters, [272]).

The main challenge with implementing control systems tasks for process models described by Master equations is that the number of states is usually very large, often higher than 10^{10}. For this reason, few chemists and chemical engineers have attempted to solve Eq. 2.1 directly, but instead employ kinetic Monte Carlo (KMC) simulation, which follows a single

realization of the Master equation by calling a random number generator to select among the possible transitions with probabilities defined by the kinetic rate laws for each allowed kinetic event. At most one kinetic step can be taken during each time step of the KMC algorithm, with the time step (typically on the order of 1 ns) selected so that the time simulated in the KMC algorithm corresponds to real time [69]. Although a KMC simulation is usually much faster than exactly solving the Master Eq. 2.1 for each possible configuration, a KMC simulation for a process of practical importance is typically on the order of a day using a personal computer of 2011. Further, if an entire state or output distribution is of interest, a large number of KMC simulations are needed to generate even an approximation for the distributions. If the control objective only depends on some statistic of the output distribution, then a feedback controller can be designed based on a low-order "equation-free" model fit to the results of one or more KMC simulations (e.g. [129, 228]). Alternatively, black-box models can be used to replace a full model with a simplified one [194]. In both equation-free and black-box models, the physicochemical relationships between the states and controlled variables on the manipulated variables are no longer transparent.

Another challenge is that nanoscale systems typically have few variables at the nanoscale available for real-time manipulation by a digital control system. For example, multilayered polyelectrolyte nanofilms for the spatially localized release of molecules to kill tumor or bacteria cells or promote tissue regeneration are surgically implanted into the macroorganism so that no real-time variables are available for manipulation (e.g. [164, 207]). The only parameters available for optimization to produce a desired time profile of molecular release are specified during the manufacture of the polyelectrolyte nanofilm. As another example, the only variable that typically can be manipulated in real-time during the rapid thermal annealing of a nano or microstructure is the time-varying power to heating lamps. A sparsity of variables for real-time manipulation limits the degrees of freedom available for control.

Reduced availability of manipulated variables tends to be less of an issue for microscale systems than for nanoscale systems. For example, consider that the variables available for real-time manipulation in the microfluidic platform in Figure 2-1 are the temperature and evaporation rate, which can be implemented by enclosing the entire microfluidic system within a box instrumented with feedback control of temperature and humidity. These manipulated variables, although specified at the macroscale, have a direct effect on the solution concentrations within each droplet. Although it is difficult to specify a different temperature

in each droplet in a single device due to the high surface area-to-volume ratio, the evaporation rate can be specified to be different in each droplet by selecting different areas and/or lengths for the channel connecting each droplet to the exterior air (see Figure 2-1). The selection of temperature, channel areas and lengths, and controlled time-varying evaporation rate enables the direct specification of dynamic conditions within each droplet.

Another control challenge is that limited real-time measurements are available for most nanoscale systems. Sensors require a certain quantity of material to be able to produce useful information. For example, no real-time sensors are available for measuring the solution concentrations in nanoliter droplets. As another example, no real-time sensors are available for measuring the interior pH or concentrations within multilayered polyelectrolyte nanofilms used for the release of growth factors, hormones, or pharmaceutical compounds [164, 207]. The limited real-time sensors make both identification and control challenging.

Models for nano and microscale systems have significant uncertainties. The distributions of measured outputs for nano and microscale systems are often non-Gaussian, as will be seen in the next section, which is incompatible with the most common parameter estimation and stochastic control systems techniques [18, 37]. The non-Gaussian distributions of the measured outputs as well as nonlinearities in the models imply that the probability distributions on the model parameters computed from a rigorous parameter estimation procedure will typically be non-Gaussian.

2.4 Promising Research Directions

This section describes some promising approaches for addressing the aforementioned challenges to the control of nano and microscale systems. While any sufficiently general set of systems engineering methods developed for multiscale systems automatically applies to molecular, nanoscale, and microscale systems, which has been discussed in detail in past reviews [27, 26], general approaches for multiscale systems can fail to take advantage of the underlying structure of specific classes of nano- and microscale systems that can be exploited to greatly facilitate control systems tasks such as parameter estimation, experimental design, and feedback control.

A significant effort has been directed in the last decade on exploiting time-scale separation inherent in many physicochemical systems to accelerate KMC simulations (e.g.

[212, 214, 34, 36, 277, 237] and citations therein). Rather than basing the completion of control systems tasks on running large numbers of KMC simulations to approximate the dynamics of Master equations, some recent efforts have been towards direct solution of the Master equations that explicitly exploit their sparse and highly structured character. One approach is the direct numerical solution of Eq. 2.1 using sparse ordinary differential equation solvers [3], which is applicable for systems with up to tens of millions of configurations. Further reductions in computational cost can be obtained using methods that project the state vector in the Master equation to a lower dimensional space or employ other model reduction algorithms design for direct application to the Master equations (e.g., see [201, 66, 67, 62] and citations therein). Although there is a limit to the complexity of the Master equations that can be solved using these numerical methods, this approach is feasible for many nanoscale systems of practical importance, and numerical algorithms are expected to continue to improve over the next decade.

Another approach for addressing specific classes of systems described by Master equations is by the derivation of analytical or semi-analytical solutions of Eq. 2.1 by exploiting the structure of the equations. While this approach is not applicable to all nano/microsystems, analytical solutions can be derived for many applications. For example, while the number of states for the nucleation in droplets is infinite, with the matrix A in Eq. 2.2 having infinite row and column dimensions, the matrix A is highly structured, being both bidiagonal and Toeplitz. For this microfluidic system, a probability-generating function [128] can be used to derive a semi-analytical solution to Eq. 2.4 that describes the dynamics of crystal nucleation in droplets as

$$P_n(t) = \frac{1}{n!}\left[\int_0^t \kappa(s)ds\right]^n e^{-\int_0^t \kappa(s)ds} \tag{2.10}$$

for all positive integers n [79]. Numerical evaluation of Eq. 2.10 only requires a small number of algebraic operations and the computation of an integral whose computational cost at time t can be reduced by incorporating the integral computed at the last previous time instance for which the integral was computed:

$$\int_0^t \kappa(s)ds = \int_0^{t-\Delta t} \kappa(s)ds + \int_{t-\Delta t}^t \kappa(s)ds \tag{2.11}$$

The function $\kappa(t)$ and its derivative vary by more than six orders-of-magnitude in a typical

induction time experiment, whose dynamics can be efficiently handled by employing an ordinary differential equation solver with adaptive time-stepping,

$$I(t) := \int_0^t \kappa(s)ds \quad \Rightarrow \quad \frac{dI}{dt} = \kappa(t) \tag{2.12}$$

The above analytical solutions have been applied to the solution of systems engineering problems, such as the identification of parameters in nucleation rate expressions [79] and the determination of upper and low bounds on nucleation rates (basically, a state estimation problem, [38]).

As an example of a different approach in exploiting structure, the state matrix A in Eq. 2.2 corresponding to Eq. 4 for modeling the adsorption of molecules on a nanotube is tridiagonal and highly structured. Equations 2.9 can be equivalently formulated in terms of two discrete population balances, with one population being the number of adsorbed molecules and the other population being the number of open sites [110]. This reformulation facilitates the derivation of analytical solution that is the convolution of binomial distributions with parameters N_T and $\bar{N}_{A\theta}$, the latter of which is described by

$$\frac{d\bar{N}_{A\theta}}{dt} = k'_A(N_T - \bar{N}_{A\theta}) - k_D\bar{N}_{A\theta} \tag{2.13}$$

for suitably defined initial conditions [250]. As in Eq. 2.10, the computational cost of computing the semi-analytical solution of Eq. 2.13 only requires a small number of algebraic operations and the numerical determination of an integral. This approach has been applied to the (i) maximum estimation of adsorption rates, which have been used to estimate nitric oxide concentration near the carbon nanotube, (ii) the quantification of uncertainties in these estimates, and (iii) the reconstruction of two-dimensional nitric oxide concentration fields from arrays of carbon nanotubes [250].

Many methods are available for exploiting the structure of linear ordinary differential equations to derive numerical, analytical, or semi-analytical solutions that can be applied to the Master equations that arise in nano- and microscale systems. For example, the Master equations for some nanoscale systems have an A matrix that is symmetric circulant, in which case the real Fourier matrix can be used to diagonalize the equations, which can be exploited for carrying out systems tasks including robust optimal control design (e.g., see [251], and citations therein). Research is expected to continue on fast methods for the analysis of

Master equations, both in terms of general methodology and in addressing specific classes of applications, as these methods enable facile application of systems engineering.

Many methods have been developed in recent years for addressing the sparsity of real-time manipulating variables available in most nanoscale systems. One approach is to modify the system boundaries at the molecular scale to create desirable feedback interactions during manufacturing [222, 221]. This approach of embedded feedback is the application at the molecular scale of the autoregulatory feedback paradigm investigated for macroscale processes many decades ago and investigated more recently in tissue engineering and other biomedical systems (e.g., see [28, 135] and citations therein). Another interesting recent approach is to employ action-at-a-distance magnetic or electric fields for real-time manipulation of molecular motion or nanoparticles [233, 234, 3, 172]. This approach provides many more degrees of freedom than relying solely on the selection of initial conditions and self-assembly to attempt to produce a desired positioning or structural arrangement of molecules (e.g., such as in [65, 64, 160] and citations therein). One of the applications of localized feedback or action-at-a-distance fields of high interest has been in combining drug targeting with surface-modified nanoparticles with light to cause the nanoparticles to release their payloads or greatly increase their temperature, often for the purpose of detecting or killing tumor cells [195, 196, 204, 78, 154, 209]. Methods have been developed for the robust optimal control of spatial fields [133, 134, 135, 136], for which the manipulated variable is a spatial field. There may be potential in applying these methods to determination optimal fields for the real-time manipulation of molecular motion or nanoparticles [233, 234, 3]. Finally, passive control of microscale systems can be achieved by appropriate design of the active volume [171].

Sensor technologies are being developed that greatly expand the number and quality of real-time measurements in nanoscale and microscale systems. For example, DNA-wrapped single-walled carbon nanotube-based sensors have been developed that are able to measure the adsorption and desorption of single molecules [22]. These sensors can be arranged into a two-dimensional (2D) array, to enable the real-time measurement of the 2D spatial variation of molecules in nano- and microscale systems. The nanotubes can be chemically modified or coupled with strong-binding enzymes or fluorescent dyes to measure in real-time the spatial concentration fields of different molecules (e.g. [6, 92, 250] and citations therein).

A strategy for improved estimation of model parameters from limited sensors in nanoscale

systems is to abstract additional information from the noise statistics. For example, the estimation of two model parameters from repeating the exact same experiment with only one datum per experiment has been demonstrated for the high-throughput device in Figure 2-1 [79]. The two model parameters were associated with a nucleation rate described by classical nucleation theory and the single datum per experiment was the measured induction time. In a macroscale system, it is usually impossible to estimate two model parameters from repeated experiments in which only one datum is measured during each experiment, as the measurement noise and unmeasured disturbances characterize the differences in the measured value in each experiment, and their effects on the measured value are stochastically different in each experiment. In such systems, extra experiments improve the accuracy of the stochastic model for the measurement noise and disturbances but do not provide information on the nominal model.

The situation is very different at the molecular scale, in which phenomena are inherently stochastic. For these systems, stochastic variations in experimental measurements can be separated into two types of sources: (1) intrinsic variability, which arises simply as a consequence of the stochastic nature of molecular events, and (2) extrinsic variability, which is a consequence of variability in the external environment. Characterization of the intrinsic variability through numerical or analytical solutions of the Master Eqs. 2.1 makes it is possible 1to distinguish between the two types of sources of variability. Our group has applied such an approach to separate the variability due to imperfections in our experimental setups from variability associated with molecular events for the detection of single-molecule adsorption and desorption of nitric oxide on DNA-wrapped carbon nanotubes [250]. Such an approach is expected to be useful in many systems in nanoscale science and technology.

For these systems, the intrinsic stochastic variations in the measured values are direct functions of the physicochemical parameters, and hence contain information on those parameters. In the crystallization experiments, the analytical solution for the stochastic variation as a function of the nucleation model parameters can be derived from the Master Eq. 2.4, so that the model parameters can be estimated accurately by fitting the distribution of induction times obtained by repeating the exact same experiment multiple times (Figure 2-2). In principle this approach of improving the estimation of physicochemical parameters from the stochastic fluctuations in the measurements can be applied to any molecular system described by Master equations, regardless of whether the Master equations are solved

analytically, such as for the micro-crystallization process and the single-molecule sensing system in Figure 2-3 described by Eq. 2.9 or solved numerically either by direct solution of the Master equations or by indirect solution via kinetic Monte Carlo simulation. Parameter estimates in the process model are estimated from the distribution of measurements rather than mean values. In some sense, instead of trying to filter away the noise as in a macroscale system, the model parameters in many nanoscale systems can be estimated from the noise. The potential improvement in the accuracy of the parameter estimates obtained by exploiting the additional information in the "noise" will depend on the details of the particular system.

Many high-value applications of carbon nanotubes such as in nanoelectronics require the separation of nanotubes in terms of their chirality, as this molecular structure is directly related to their electronic structure, adsorption kinetics, and chemical reactivity (e.g. see [187, 186, 61, 240, 223, 40, 39, 155] and citations therein). Typically the nanotubes are separated by the addition of surfactants followed by centrifugation, which produces a gel with each position along the gel corresponding to a different mixture of chiralities. Various spectroscopic methods are applied to each position, with the objective of estimating the concentrations of nanotubes with each chirality. The amount of peak overlap in the spectra is very high and while advances have been made in the deconvolution of the spectra (e.g., see [185] and citations therein), more advances are needed to reduce the large uncertainty in some of the estimated concentrations. Advanced control of many nanosystems will require significant advances in sensor calibration that exploit all aspects of the sensor physics, such as the effect of defects in carbon nanotubes on their spectra, while carefully quantifying uncertainties in the estimates.

Polynomial Chaos Expansions (PCEs) is an approach for uncertainty analysis that is applicable to dynamical systems described by continuum models with model parameters that belong to non-Gaussian distributions [263, 202]. In recent years PCE-based systems and control methods have been developed (see [183, 184, 70, 246] and citations therein), that extend techniques such as robust nonlinear control and model predictive control to handling non-Gaussian distributions. As such distributions also appear in nano and microscale chemical systems, it seems likely that some of the PCE-based methods will be useful for addressing their associated systems and control problems.

2.5 Conclusions

Challenges in the control of nano and microchemical systems are high model state dimensionality, limitations in real-time measurements and manipulated variables, and significant uncertainties described by non-Gaussian distributions. Promising directions for dealing with these challenges include exploiting model structure of the stochastic model equations, employing molecular modification at system boundaries to create desirable feedback interactions within the material, and manipulation via magnetic and electric fields. These approaches included the numerical or analytical solution of Master Eqs. 2.1 for

(i) distinguishing between fundamental intrinsic variability and extrinsic variability, and

(ii) abstracting information on fundamental model parameters from the intrinsic variability or "noise."

Methods were reviewed for the numerical and analytical solution of the Master Equation that commonly arises when modeling nano- and microscale chemical systems, with the analytical methods being (i) matrix exponentials, (ii) probability generating functions, (iii) reformulation as discrete population balance equations, and (iv) exploiting symmetries. While these approaches will not apply to all nano- and microscale systems, our experiences is that the methods apply to a surprisingly large number of chemical systems, with some examples of such systems given in this paper. All of the approaches used for directly solving Master equations can be directly applied to any systems problem, such as parameter estimation, quantification of uncertainties in model parameters, state and output estimation, optimal design, and optimal state feedback control. This paper described some of these applications of systems engineering to nano- and microscale chemical systems, including to carbon nanotube-based devices and microfluidic systems. Many more applications of systems engineering to nano- and microscale chemical systems by direct solution of Master equations are expected in the near future.

One of the messages of this paper is to embrace the non-Gaussian stochastic phenomena that occur in nano- and microchemical systems; that stochasticity if understood fundamentally can be more an asset than a hindrance. A way to develop this fundamental understanding of intrinsic variability is to direct numerical or analytical solution of the stochastic equations (Eq. 2.1) that describe the kinetic phenomena at these length scales. For problems

in which such direct methods are not applicable, polynomial chaos expansions was suggested as a potential approach for addressing non-Gaussian distributions during state and output estimation and optimal feedback control design.

Chapter 3

Applicability of Birth-Death Markov Modeling for Single Molecule Counting using Single-Walled Carbon Nanotube Fluorescent Sensor Arrays

This work originally appeared as: Zachary W. Ulissi, Jingqing Zhang, Ardemis A. Boghossian, Nigel F. Reuel, Steven F. E. Shimizu, Richard D. Braatz, and Michael S. Strano. Applicability of birth-death Markov modeling for single-molecule counting using single-walled carbon nanotube fluorescent sensor arrays. Journal of Physical Chemistry Letters, 2(14):1690-1694, 2011. It has been edited to include the supporting information in-line.

3.1 Abstract

In recent work, we have shown that $d(AT)_{15}$ DNA-wrapped single-walled carbon nanotubes (SWCNT) are able to detect the adsorption and desorption of single molecules of nitric oxide (NO) from the surface by quenching of the near-infrared fluorescence [269]. A central question is how to estimate the local concentration from stochastic dynamics for these types of sensors. Herein, we employ an exact solution to the Birth-Death Markov model to estimate the local analyte concentration from the stochastic dynamics. Conditions are derived for the intrinsic variance displayed by identical sensor elements and the homogeneity of the

environment is assessed by comparing experimental sensor-to-sensor variance with this limit. We find that $d(AT)_{15}$ DNA-wrapped SWCNTs demonstrate variances that are close to the idealized limit at relatively high NO concentrations (19.4 μM). At 780 nM, the sensor-to-sensor variance is approximately double the idealized value indicating marginal variation in the SWCNT array. An NO adsorption coefficient of $2.6 \times 10^{-4}[s^{-1}\mu M^{-1}]$ is identified and we outline how to predict the local analyte concentration from the sensor dynamics.

3.2 Introduction

An important development in nanotechnology is the emergence of sensor transducers capable of single molecule resolution at room temperature. Single-walled carbon nanotubes alone account for at least three sensor types capable of this important property. One sensor type is an electrically contacted field effect transistor (FET) with a single electrochemically induced catalytic defect, inducing a defection in the channel current in response to reactions at the defect site [46, 48, 47]. A second sensor type uses the interior of the SWCNT as a nanopore for Coulter detection of single cations [145]. A third sensor type consists of a near-infrared fluorescent semiconducting SWCNT where adsorption and desorption of a fluorescence quencher causes a discretized and stochastic fluctuation of the intensity from the single nanotube. We have developed several near-infrared fluorescent SWCNT sensors selective for glucose [14, 13, 15, 16], DNA [91, 113, 118, 114], ATP [130], H_2O_2 [116, 117], and recently NO [131, 269]. For H_2O_2 and NO, we first introduced the idea of a selective sensor interface able to count single analyte molecules, following the pioneering experiments of Cognet and Weismann demonstrating stochastic fluorescence quenching of SWCNT excitons [45]. A central challenge in the theory of these single molecule sensors is how to relate intensity fluctuations to the local analyte concentration of interest and/or its flux to the sensor. We have used recently, without rigorous proof, a Birth-Death Markov model to accomplish this. This letter develops a mathematical test for the agreement of molecular adsorption dynamics for this Markov process.

When molecules bind to the surface of a SWCNT, the fluorescence is partially quenched resulting in a step decrease in intensity. Similarly, the intensity increases when molecules unbind from the surface. By counting the transient change in the number of step changes in intensity, the number of adsorption and desorption events, the total number of adsorbed

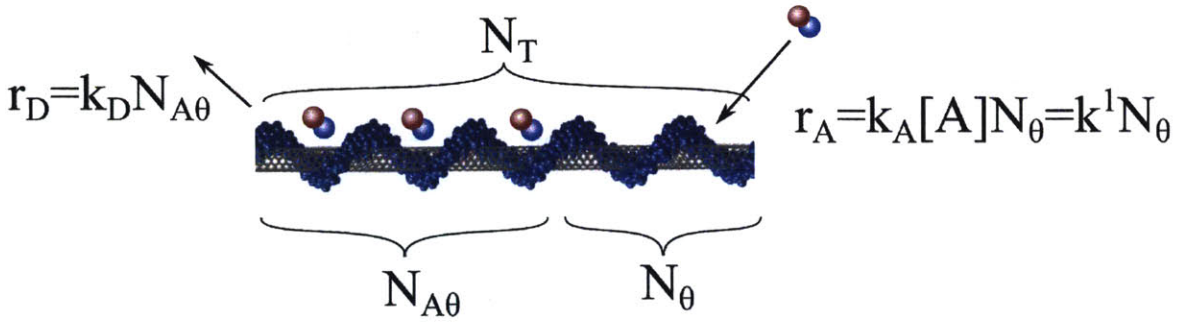

Figure 3-1: Model of the SWCNT sensor, with rates of chemical adsorption and desorption.

molecules, and the incident flux can be estimated.

Exciton quenching by adsorbed analyte molecules limits the number of observable adsorption and desorption states. For a typical SWCNT sensor, the number of states will be about 10, based on a mean nanotube length of 1μmand an estimated exciton diffusion length of 100 nm [269]. More detailed physical models of exciton dynamics propose that the diffusion length is limited by pre-existing or static defects [89], but the analysis of adsorption and desorption kinetics in this work applies to these physical models as well. Due to this small number of observable states, adsorption and desorption events will be stochastic, which results in a deviation in the observed number of bound analyte molecules from the number predicted by the continuum approximation, or average sensor. These stochastic deviations can cause the apparent reaction rates to be different for various SWCNTs even when the underlying rates are the same (i.e. the nanotubes are chemically identical).

3.3 Results

Each sensor is modeled as a surface with a fixed total number of adsorption sitesN_T, as shown in Figure 3-1. The most recent theory of exciton dynamics on a pristine SWCNT assumes that there is no limit to the number of adsorption/quenching events and these can happen anywhere along the length [89]. In practice it is believed that either the matrix or tethering chemistry divides the SWCNT into isolated segments each of which can be quenched completely through an adsorption event, in agreement with recent experimental studies [116, 117, 131, 269]. Further work is necessary to reconcile these two physical models.

Free analyte molecules in the surrounding liquid A (concentration, $[A]$ M) are assumed to bind to an empty nanotube segment, θ, (number,$N_\theta \in [0, N_T]$) to form bound molecules

Table 3.1: Notation

k_D	Desorption coefficient
k_A	Adsorption coefficient
k'_A	Pseudo first order coefficient (e.g. $k_A[A]$)
$N_{A\theta}$	Number of bound molecules
$\bar{N}_{A\theta}$	Continuum number of bound molecules
$\tilde{N}_{A\theta}$	Fraction of bound molecules ($N_{A\theta}/N_T$)
N_θ	Number of free sites
N_T	Total number of Sites
$\mathcal{L}$	Likelihood
θ	Vector of parameters
$\mathbf{W}$	Transition matrix
$\mathbf{P}$	Probability vector

(number,$N_{A\theta} \in [0, N_T]$) through the reversible reaction

$$A + \theta \rightarrow A\theta$$

where $k_A[M^{-1}s^{-1}]$ and $k_D[s^{-1}]$ are coefficients for adsorption and desorption respectively. Although these coefficients are often constant, they could change with external stimuli such as temperature and thus could be time dependent.

Assuming mass action kinetics, the net adsorption rate in the continuum limit is

$$r = r_A - r_D = k_A[A]\bar{N}_\theta - k_D\bar{N}_{A\theta} = k'_A(t)\bar{N}_\theta - k_D\bar{N}_{A\theta} \tag{3.1}$$

where rates are given in $s^{-1}$and $k'_A(t) = k_A[A(t)][s^{-1}]$ is a pseudo-first-order rate coefficient for when the concentration of A in the liquid phase can be considered independent of adsorption events. If the reaction rate is not first order in liquid concentration, which is a plausible scenario at low concentrations, the definition for the pseudo-first-order constant can be adjusted (e.g., $k'_A = k_A[A]^{1/2}$) without affecting any other results. If the reaction rate is not first order in the number of sites, the stochastic solution presented below will

not be applicable and a more complicated stochastic solution will be necessary. A final algebraic relation can be obtained through a balance on the number of adsorption sites, $N_T = N_\theta + N_{A\theta}$. The continuum solution is found by solving the appropriate ordinary differential equation

$$\frac{d\bar{N}_{A\theta}}{dt} = r = k'_A\bar{N}_\theta - k_D\bar{N}_{A\theta} = k'_A\left(N_T - \bar{N}_{A\theta}\right) - k_D\bar{N}_{A\theta} \tag{3.2}$$

With initially empty ($N_{A\theta}^{t=0} = 0$) surface and constant rate coefficients, the analytical solution is

$$\tilde{N}_{A\theta}^E(t) = \frac{\bar{N}_{A\theta}^E(t)}{N_T} = \frac{1 - \exp[-(k'_A + k_D)t]}{1 + k_D/k'_A}, \text{for} \bar{N}_{A\theta}^0 = 0. \tag{3.3}$$

The corresponding solution for an initially full ($N_{A\theta}^0 = N_T$) surface is

$$\tilde{N}_{A\theta}^F(t) = \frac{\bar{N}_{A\theta}^F(t)}{N_T} = \frac{1 + \exp[-(k'_A + k_D)t]k_D/k'_A}{1 + k_D/k'_A}, \quad \text{for } \bar{N}_{A\theta}^0 = N_T. \tag{3.4}$$

For rate coefficients that change over time (due to changing analyte concentration or temperature), alternative analytic solutions to Eq. 3.2 can be derived by applying the integrating factor $\exp\left[k'_A(t) + k_D(t)\right]$.

How does the individual sensor-to-sensor response vary within a collection of sensors? This variation can be due to the chemical or physical environment, or due to imperfections on the CNTs themselves. We call this type of variation extrinsic. Alternatively, because the sensors count single molecules, we expect some intrinsic stochastic variation among even perfectly identical sensors. One important question to ask is if the variances in the sensor responses are within this intrinsic limit (indicating that the sensors are nearly identical) or if the variance is much larger (perhaps due to a spatially inhomogeneous environment).

This question can be addressed by analysis of the stochastic chemical master equation (CME), which is a system of differential equations that describes the probability of each possible state in the system at each time t. The chemical master equation (CME) is formed by writing differential equations for each possible state of the system. Each state can be characterized by the number of adsorbed molecules $N_{A\theta} \in [0, N_T]$, resulting in $N_T + 1$ total states. The probability of each state is denoted by $P_{i=N_{A\theta}} = \Pr(N_{A\theta} = i) \in [0, 1]$ so that i is the number of adsorbed molecules. By definition, all probabilities must sum to 1. The

chemical master equation, along with appropriate boundary equations, is

$$\begin{aligned}
\frac{dP_i}{dt} &= -P_i\left[k_D i + k'_A\left(N_T - i\right)\right] + P_{i-1}\left[k'_A\left(N_T - (i-1)\right)\right] + P_{i+1}\left[k_D(i+1)\right], \\
\frac{dP_0}{dt} &= -P_0\left[k'_A N_T\right] + P_{i+1}\left[k_D\right], \\
\frac{dP_{N_T}}{dt} &= -P_{N_T}\left[k_D N_T\right] + P_{i-1}\left[k'_A(N_T - 1)\right].
\end{aligned}$$

These equations form a system of first-order linear ordinary differential equations:

$$\frac{d}{dt}\mathbf{P} = \frac{d}{dt}\begin{bmatrix} P_0 \\ \vdots \\ P_{N_T} \end{bmatrix} = \mathbf{W}(t)\mathbf{P}$$

where $\mathbf{W}(t)$ is the transition matrix. The initial conditions for these $N_T + 1$ differential equations can be defined either deterministically or in terms of a probability distribution. If the number of adsorbed molecules at $t = 0$ is known to be $N^0_{A\theta}$ (a deterministic initial condition), then the initial condition is $P_i(t = 0) = \delta_{i,N^0_{A\theta}}$. The CME is simple to solve numerically when the number of states is not too large, especially when using sparse matrices and when $\mathbf{W}(t)$ is a constant.

For the birth-death model, the SWCNT sensor states [269] can be characterized by the number of adsorbed molecules, resulting in $N_T + 1$ total states, each with a probability $\Pr(N_{A\theta} = i) \in [0, 1]$. Solving the CME directly for the birth-death model requires the solution of $N_T + 1$ordinary differential equations, which is feasible for moderate N_T but not convenient. Instead, analytical solutions for probability distributions are sought and verified with the CME.

Probability distributions for the number of empty (N_θ) and bound ($N_{A\theta}$) sites are derived instead of solving the standard CME. This first-order adsorption/desorption system is essentially identical to the isomerization example (Example 5.2) in [110]. The system is first order and closed, that is, can be written as $d\mathbf{P}/dt = \mathbf{W(t)P} + \mathbf{B}(t)$ with $\mathbf{B}(t) = \mathbf{0}$, so it is known that an initially multinomial distribution will stay multinomial for all time (Proposition 1 [110]). For convenience, a multinomial distribution $\mathcal{M}$ is defined for this

system as

$$\mathcal{M}(\mathbf{x}, N, \mathbf{p}) = \begin{cases} \frac{N!(1-|\mathbf{p}|)^{N-|\mathbf{x}|}}{(N-|\mathbf{x}|)!} \prod_{k=1}^{n} \frac{p_k^{x_k}}{x_{k!}}, & \text{for } |\mathbf{x}| \leq N \\ \mathbf{0}, & \text{otherwise.} \end{cases}$$

$$\mathcal{M}\left(\mathbf{x} = \begin{bmatrix} N_{A\theta} \\ N_\theta \end{bmatrix}, N = N_T, \mathbf{p} = \begin{bmatrix} \tilde{N}_{A\theta} \\ \tilde{N}_{A\theta} \end{bmatrix}\right) =$$

$$\begin{cases} \frac{N_T!(1-|\mathbf{p}|)^{N_T-|\mathbf{x}|}}{(N_T-|\mathbf{x}|)!} \left(\frac{\left[\tilde{N}_{A\theta}\right]^{N_{A\theta}}}{N_{A\theta}!}\right)\left(\frac{\left[\tilde{N}_\theta\right]^{N_\theta}}{N_\theta!}\right), & \text{for } |\mathbf{x}| \leq N_T \\ \mathbf{0}, & \text{otherwise.} \end{cases}$$

Since $1 - |\mathbf{p}| = 0$, the necessary condition for the multinomial to be nonzero is $|\mathbf{x}| = N_T$ (this simply recovers the site balance). The multinomial simplifies then to

$$\mathcal{M}\left(\mathbf{x} = \begin{bmatrix} N_{A\theta} \\ N_\theta \end{bmatrix}, N = N_T, \mathbf{p} = \begin{bmatrix} \tilde{N}_{A\theta} \\ \tilde{N}_\theta \end{bmatrix}\right) = N_T!\delta_{N_T,|\mathbf{x}|}\left(\frac{\left[\tilde{N}_{A\theta}\right]^{N_{A\theta}}}{N_{A\theta}!}\right)\left(\frac{\left(1-\tilde{N}_{A\theta}\right)^{N_T-N_{A\theta}}}{(N_T-N_{A\theta})!}\right)$$

$$= \text{Bin}\left(N_T, \tilde{N}_{A\theta}\right)$$

Proposition 1 [110] further states that the parameter vector will evolve according to the continuum model, which in this case yields

$$\frac{d\mathbf{p}}{dt} = \begin{bmatrix} -k'_A & k_D \\ k'_A & -k_D \end{bmatrix}\mathbf{p},$$

$$\frac{d}{dt}\begin{bmatrix} \tilde{N}_{A\theta} \\ \tilde{N}_\theta \end{bmatrix} = \begin{bmatrix} -k'_A\tilde{N}_{A\theta} + k_D\tilde{N}_\theta \\ k'_A\tilde{N}_{A\theta} - k_D\tilde{N}_\theta \end{bmatrix}.$$

This system of differential equations is precisely the same as that solved in the continuum model 3.2, so the system is fully specified for an initially full or empty surface (as described above). For a deterministic number of bound molecules as discussed above, Theorem 1 [110] can be used. This solution can be verified with the CME by solving for P_{i+1} and P_{i-1} in terms of P_i using the binomial solution and then substituting into the CME above. The P_i terms will cancel, along with the other terms on the right hand side of the CME.

The number of adsorbed molecules $N_{A\theta}$ at a time t is a random variable distributed as a binomial with number of trials N_T and probability $\tilde{N}_{A\theta}$ from solving the continuum problem

3.2 with the appropriate initial condition for the average fraction of initially occupied sites 3.3,

$$N_{A\theta} \sim \text{Bin}\left(N_T, \tilde{N}_{A\theta}(t)\right),$$
$$\Pr(N_{A\theta} = i) = \left(\begin{array}{c} N_T \\ i \end{array} \right) \left(\tilde{N}_{A\theta}(t)\right)^i \left(1 - \tilde{N}_{A\theta}(t)\right)^{N_T - i}. \tag{3.5}$$

When the initial state is an entirely empty ($N_{A\theta} = 0$) or full ($N^0_{A\theta} = N_T$) sensor and the rate coefficients are constant, the initial binomial distribution becomes deterministic and

$$\Pr\left(N_{A\theta} = i \,|N_{A\theta}(t=0) = 0\right) = \begin{cases} \delta_{i,0} & \text{for } t = 0, \\ \left(\begin{array}{c} N_T \\ i \end{array} \right) \left(\tilde{N}^E_{A\theta}(t)\right)^i \left(1 - \tilde{N}^E_{A\theta}(t)\right)^{N_T - i} & \text{for } t \geq 0, \end{cases} \tag{3.6}$$

where $\delta_{i,j}$ is the Kronecker delta function (1 if $i = j$ and 0 otherwise) and $\tilde{N}^E_{A\theta}(t)$, $\tilde{N}^F_{A\theta}(t)$ are the continuum solutions in Eq. 3.3. The analogous probability distribution for a sensor starting with an arbitrary number of initial adsorbed molecules is a convolution of the solutions for initially empty and full sensors (see Eq 3.9). The continuum and stochastic solutions for an empty initial condition are presented in the main text. Solutions for the full initial condition can be derived in exactly the same manner, and are included here for convenience. The continuum solution for an initially full sensor analogous to Eq 3.3 is

$$\tilde{N}^F_{A\theta}(t) = \frac{\bar{N}^F_{A\theta}(t)}{N_T} = \frac{1 + \exp[-(k'_A + k_D)t]k_D/k'_A}{1 + k_D/k'_A}, \quad \text{for } \bar{N}^0_{A\theta} = N_T.$$

The probability distribution for an initially full sensor analogous to Eq 3.6 is

$$\Pr\left(N_{A\theta} = i| \, N_{A\theta}(t=0) = N_T\right) = \begin{cases} \delta_{i,N_T} & \text{for } t = 0, \\ \left(\begin{array}{c} N_T \\ i \end{array} \right) \left(\tilde{N}^F_{A\theta}(t)\right)^i \left(1 - \tilde{N}^F_{A\theta}(t)\right)^{N_T - i} & \text{for } t \geq 0. \end{cases}$$

The solution for an initially empty surface ($\tilde{N}^0_{A\theta} = 0$) at several times is shown in Figure 3-2, along with sample experimental distributions from previous studies [269]. Reasonable agreement is seen between the birth-death model and the experimental data. Less agreement

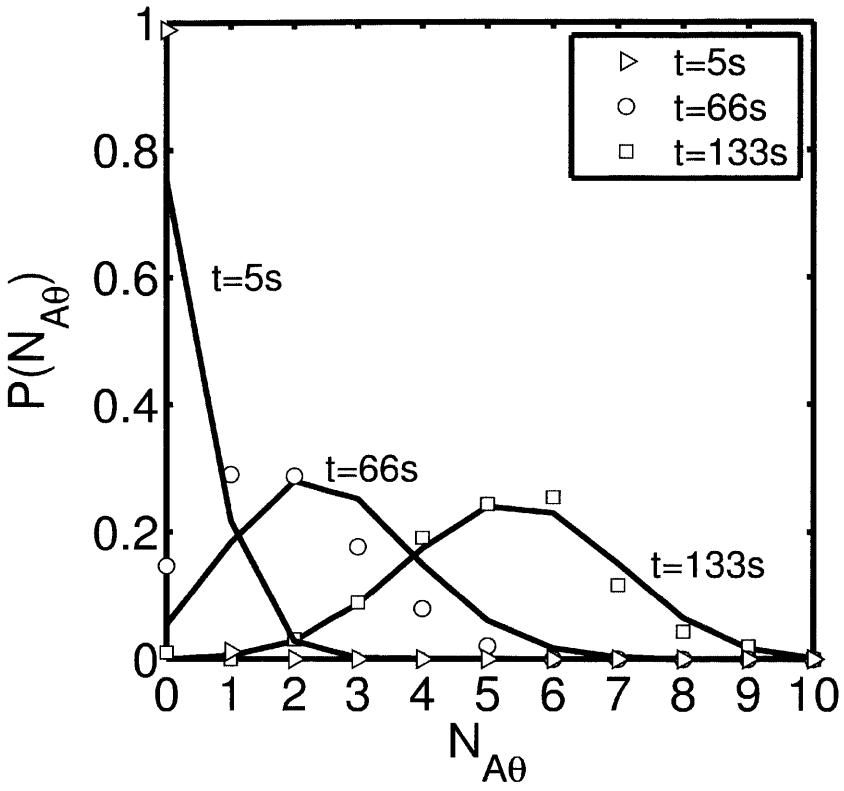

Figure 3-2: Plot of the probability distribution over time for the binomial solution (solid lines) as well as for representative experimental data (open shapes) from a previous study for a SWCNT sensor exposed to 19.4μMNitric Oxide [269]. The parameters used in the model are fits with the exact numerical MLE, with values $k'_A = (5.5 \pm 0.5) \times 10^{-3}$ [1/s], $k_D = (3.9 \pm 2.1) \times 10^{-4}$ [1/s].

is seen at small times, where transient effects from introducing analyte into the experimental system may play a role. For an initial state with an arbitrary number of bound sites $N^0_{A\theta}$, the distribution of the number of bound molecules will simply be the convolution ($*$) of the distributions for the initially empty and full portions [110]

$$N_{A\theta} \sim \text{Bin}\left(N^0_{A\theta}, \bar{N}^F_{A\theta}(t)\right) * \text{Bin}\left(N_T - N^0_{A\theta}, \bar{N}^E_{A\theta}(t)\right). \tag{3.7}$$

With knowledge of the full distribution as a function of time, the time-dependent properties of the distribution can be calculated by substituting values into known formulae for the binomial distribution. An initially empty surface with constant rate coefficients (as is

typical for previous experiments [269]) has mean and variance

$$\langle N_A \rangle (t) = N_T p = N_T \left(\frac{1 - \exp\left[-(k'_A + k_D)t\right]}{1 + k_D/k'_A} \right), \tag{3.8}$$

$$\mathrm{Var}\left[N_A\right](t) = \sigma^2 = N_T p(1-p) = N_T \left(\frac{k_D/k'_A + (1 - k_D/k'_A)\exp[-(k'_A + k_D)t]}{(1 + k_D/k'_A)^2} \right). \tag{3.9}$$

This suggests a characteristic relationship between the variance in measurements of the number of adsorbed molecules and the average number of adsorbed molecules for the birth-death process. Figure 3-3 shows the observed relationship between the mean and variance of the number of occupied sites for experimental SWCNT sensor arrays at various analyte concentrations compared to the birth-death model with varying numbers of sites. The model assumes that all sensors have identical properties, even though this is probably not the case experimentally. Thus, the model stochastic variance forms a lower bound on the variance observed in experimental processes that follow this simple birth-death model assuming identical properties for all sensors (i.e. there will be more sensor-to-sensor variation if sensor properties are also varied). An observed variance much larger than this characteristic value would indicate either a large amount of experimental error, variations in the underlying parameters, or a breakdown with the birth-death model. The model with $N_T = 10$ provides a good fit to the high NO concentration data. Lower NO concentrations behave similarly for low coverage, but exhibit increased variance at higher coverage, which may be an indication of environmental inhomogeneity (lower NO concentrations should take more time to diffuse uniformly throughout the liquid film, for example).

Knowing the exact probability distribution for the system allows for straightforward fitting of model parameters for an array of SWCNT sensors instead of analyzing sensors individually [269, 68, 127]. The likelihood of a set of parameters θ given a series of system measurements is defined [68] as $\mathcal{L}(\theta) = \Pr(x_1, x_2, \ldots, x_n)$. The Maximum Likelihood Estimator (MLE) is obtained by identifying the set of parameters θthat maximizes the likelihood. In previous studies of an array of SWCNT sensors, adsorption and desorption coefficients in the birth-death model were estimated by averaging parameters obtained by applying the MLE to each trace individually. Here this method is shown to yield incorrect parameter fits. The exact MLE can be calculated for the entire sensor array simultaneously using the above analytical results 3.7.

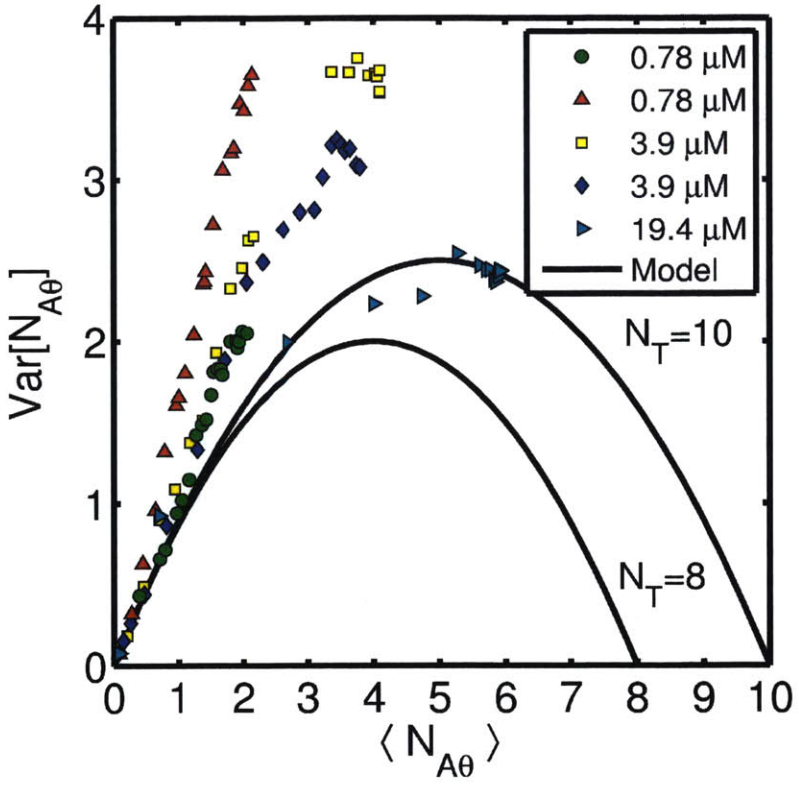

Figure 3-3: Comparison of the birth-death model with experimental data for five arrays of SWCNT sensors exposed to solutions of varying NO concentration from a previous study [269]. Model results were obtained by plotting the variance, $N_T\tilde{N}_{A\theta}\left(1-\tilde{N}_{A\theta}\right)$ versus the mean, $N_T\tilde{N}_{A\theta}$, with two values of N_T.

The exact birth-death MLE for a SWCNT sensor array can be calculated to provide substantially more accurate results than previous methods. When multiple sensors are observed independently, each measurement will be dependent on the data in its own trace but independent of the measurements in all other traces. Thus, the likelihood function, $\mathcal{L}(\theta)$ for N_Q independent SWCNT sensors with measurements $x_i^j, i \in [1, N_j], j \in [1, N_Q]$ (each measurement composed of the number of bound molecules $N_{A\theta}^{i,j}$ at times$t^{i,j}$) is

$$\begin{aligned} \mathcal{L}(\theta) &= \prod_{j=1}^{N_Q} \left[\Pr\left(x_1^j \,|\theta\right) \prod_{i=2}^{N_j} \Pr\left(x_i^j \,|x_{i-1}^j, \theta\right) \right] = \prod_{j=1}^{Q} \left[\prod_{i=2}^{N_j} \Pr\left(x_i^j \,|x_{i-1}^j, \theta\right) \right], \\ \log \mathcal{L}(\theta) &= \sum_{j=1}^{N_Q} \left[\log \Pr\left(x_1^j \,|\theta\right) + \sum_{i=2}^{N_j} \log \Pr\left(x_i^j \,|x_{i-1}^j, \theta\right) \right], \end{aligned} \tag{3.10}$$

where $\Pr\left(x_1^j|\theta\right)$is the probability of the first measurement of $N_{A\theta}$for the jth sensor and $\Pr\left(x_i^j|x_{i-1}^j, \theta\right)$ is the probability of the ith measurement of $N_{A\theta}$ for the jth sensor given the measurement immediately preceding it in time. $\Pr\left(x_1^j|\theta\right)$ is unity as our experiments started with clean SWCNTs free of analyte molecules. Calculating likelihoods usually involves the multiplication of many small numbers, so the log-likelihood is calculated as a sum instead. Since the full probability distribution is known, the likelihood 3.10 can be directly calculated using the above exact results 3.7, with $\Pr\left(x_i^j|x_{i-1}^j, \theta\right) = \Pr\left(N_{A\theta}^{t=t_i^j - t_{i-1}^j} = N_{A\theta}^{i,j} \,|N_{A\theta}^{t=0} = N_{A\theta}^{i-1,j}\right)$ and parameters $\theta = (k'_A, k_D)$. The problem is computationally tractable since each probability evaluation is simply an algebraic evaluation. The Matlab constrained optimization algorithm fmincon is used to minimize the log likelihood over all positive values with initial guesses based on the incorrect analytical method above.

Data for the number of adsorbed molecules on SWCNT sensors can be analyzed using an analytical MLE for the birth-death model [269, 127]

$$\hat{k}'_A = \frac{B_t}{N_T t - S_t} \qquad\qquad \hat{k}_D = \frac{D_t}{S_t}, \tag{3.11}$$

where B_t is the number of adsorption events ("Births"), D_t is the number of desorption events ("Deaths"), $t$is the total observation time, and $S_t = \int_0^t N_{A\theta} dt$ is the integrated number of adsorbed molecules. Our previous study derived this equation for a single SWCNT sensor and fit parameters by averaging the MLE parameters estimates for each tube [269]. The

analytical MLE for a collection of SWCNT sensors observed at uniform time increments Δt was calculated by analytically equating $\partial \log \mathcal{L}/\partial k'_A = \partial \log \mathcal{L}/\partial k_D = 0$, expanding in powers ofΔt, and solving for $\hat{k}'_A, \hat{k}_D$. Keeping the zeroth and first-order terms, corresponding to continuously observed SWCNTs, yielded 3.11 except that B_t, S_t, D_t,and t were summed for all sensors

$$\lim_{\Delta t \to 0} \hat{k}'_{A,MLE} = \frac{\sum B_t^j}{N_T \sum t^j - \sum S_t^j} \neq \left\langle \frac{B_t^j}{N_T t^j - S_t^j} \right\rangle, \lim_{\Delta t \to 0} \hat{k}_{D,MLE} = \frac{\sum D_t^j}{\sum S_t^j} \neq \left\langle \frac{D_t^j}{S_t^j} \right\rangle \tag{3.12}$$

The remaining terms ($O[\Delta t]^2$ and higher) represent deviations in the exact MLE 3.10 from the continuous observation limit. The magnitude of higher order contributions was calculated for previous experiments [269] to be less than 3% of the zeroth and first-order contributions. Note that averaging the MLE estimates for individual traces, indicated as the bracketed terms, yields incorrect parameter estimates.

The confidence bounds on the parameter estimates provided by 3.12 can be estimated by calculating the bounds in the continuous observation limit ($\Delta t = 0$). The 95% error bounds can be derived by linearizing the log likelihood function around the MLE-fitted parameter vector $\theta = (k'_A, k_D)$ and using a χ^2 test with two free parameters

$$\left(\theta - \hat{\theta}\right)^T \nabla_{\theta\theta}[-\log \mathcal{L}] \left(\theta - \hat{\theta}\right) \leq \chi_2^2(0.95) \tag{3.13}$$

The middle term $\nabla_{\theta\theta}[-\log \mathcal{L}]$ can be calculated exactly for the continuous observation limit

$$\lim_{\Delta t \to 0} \nabla_{\theta\theta}[-\log \mathcal{L}] = \begin{pmatrix} \frac{N_{\text{ads}}^{\text{obs}}}{\hat{k}_A'^2} & 0 \\ 0 & \frac{N_{\text{des}}^{\text{obs}}}{\hat{k}_D^2} \end{pmatrix} \tag{3.14}$$

where $N_{\text{ads}}^{\text{obs}}$and $N_{\text{des}}^{\text{obs}}$are the number of adsorption and desorption events observed for all sensors. Since the two parameters are uncoupled in this limit (covariances are zero), the

95% confidence intervals can be easily calculated

$$\hat{k}'_A - \hat{k}'_A\sqrt{\frac{\chi_2^2(0.95)}{N_{\text{ads}}^{\text{obs}}}} \leq k'_A \leq \hat{k}'_A + \hat{k}'_A\sqrt{\frac{\chi_2^2(0.95)}{N_{\text{ads}}^{\text{obs}}}}, \tag{3.15}$$

$$\hat{k}_D - \hat{k}_D\sqrt{\frac{\chi_2^2(0.95)}{N_{\text{des}}^{\text{obs}}}} \leq k_D \leq \hat{k}_D + \hat{k}_D\sqrt{\frac{\chi_2^2(0.95)}{N_{\text{des}}^{\text{obs}}}}. \tag{3.16}$$

This result explains the variations in observed coefficients that we reported previously as rate constant histograms [269], and gives a bound for the observation time needed to obtain accurate parameter estimates. In order to achieve 10% accuracy in either the adsorption or desorption coefficient, roughly 600 event observations are required. The rate constant histograms reported previously are not rigorous because they convolute the intrinsic and extrinsic variances for the collection of sensors. However, the above methods require the assumption of a collective concentration above the sensor array, and do not allow for an examination of single sensor dynamics, even though this limit is the most compelling for nanosensor applications.

The fitting capability of the new exact MLE was compared to the previous method for individual SWCNTs using results for SWCNT nanotube sensors exposed to aqueous solutions at an NO concentration of 0.78 μM [269], shown in Figure 3-4. Contour lines represent the true log-likelihood surface, which would be unfeasible to calculate without the new method. The analytical MLE was first applied to the trace for each nanotube resulting in a range of fitted parameters previously reported as rate coefficient histograms. Two approximate methods for calculating the rate coefficients using all of the data were considered as well: (a) averaging the parameters obtained using the analytical MLE on each sensor as in [269], and (b) applying the continuous observation limit analytical MLE to all of the traces simultaneously (summing observation times, births, deaths, and sites for all sensors). Finally, the exact numerical MLE was calculated by optimizing the log likelihood function. The continuous observation limit MLE was not quite equal to the true MLE, due to the $O[\Delta t]^2$ error. The fit using the new method is $k'_A = (8.2 \pm 1.1) \times 10^{-4}$ [1/s], $k_D = (2.1 \pm 0.47) \times 10^{-3}$ [1/s]. These are lower than the values that we estimated previously from considering single sensor dynamics, $k'_A = 1.2 \times 10^{-3}[1/s]$ [269]. The current analysis also provides the quantification of the uncertainty.

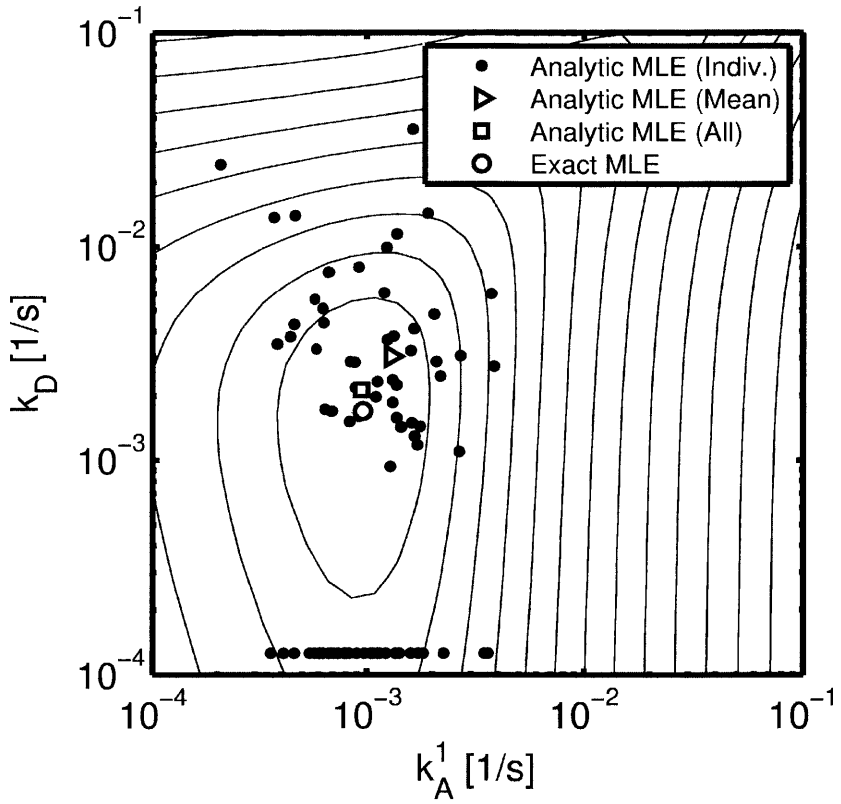

Figure 3-4: Comparison of four different methods for fitting rate coefficients to data from a previous study for a SWCNT sensor array exposed to a 0.78 μM nitric oxide solution. Methods include: (filled circles) applying the analytic MLE to individual sensors, (open triangle) averaging the results of the analytic MLE applied to each trace, (open square) applying the analytic MLE to all traces, and (open circle) using the exact MLE based on the full solution. When no desorption events are observed, the MLE estimate yields $k_D = 0$, and these points are included at the bottom.

3.4 Conclusion

The analytical probability distribution for the birth-death model has allowed for the expansion of previously published results for the case where a uniform concentration appears above the sensor array. The intrinsic stochastic impact of the system was derived and used to calculate the experimentally observed [269] sensor-to-sensor variance. The exact solution was also used to improve parameter estimation and provide uncertainty estimates on the fitted parameters. Finally, the more general maximum likelihood estimator presented here 3.11 will be useful for the interpretation of results from sensors in spatially or temporally inhomogeneous environments. We expect that these tools will be useful for the interpretation of future adsorption/desorption based stochastic sensors.

Chapter 4

Spatiotemporal Intracellular Nitric Oxide Signaling Captured using Internalized, Near Infrared Fluorescent Carbon Nanotube Nanosensors

This work originally appeared as: Zachary W. Ulissi, Fatih Sen*, Xun Gong*, Selda Sen, Nicole Iverson, Ardemis A. Boghos- sian, Luiz Godoy, Gerald Wogan, D. Mukhopadhyay, and Michael S. Strano. Spatiotemporal intracellular nitric oxide signaling captured using internalized, near infrared fluorescent carbon nanotube nanosensors. Nano Letters, 2014. It has been edited to include the supporting information in-line.*

4.1 Abstract

Fluorescent nanosensor probes have suffered from limited molecular recognition and a dearth of strategies for spatial-temporal operation in cell culture. In this work, we spatially imaged the dynamics of nitric oxide (NO) signaling, important in numerous pathologies and physiological functions, using intracellular near-infrared fluorescent single-walled carbon nanotubes (SWCNT). The observed spatial-temporal NO signaling gradients clarify and refine the ex-

isting paradigm of NO signaling based on averaged local concentrations. This work enables the study of transient intracellular phenomena associated with signaling and therapeutics.

4.2 Introduction

Nitric oxide (NO) is integral to the vascular system as a vasodilator, the nervous system as a neurotransmitter and the immune system as a defensive agent [103, 166] but it also plays an integral role in pathology, specifically for inflammatory diseases, vascular diseases, diabetes and cancer [50, 57, 181, 74]. Currently, NO detection in tissues is limited to assays developed to detect downstream products of NO. However, these assays fail to elucidate the implications of fluctuating intracellular NO levels.

Many techniques have been developed to quantify nitric oxide levels in biological settings. Two common approaches are the use of small-molecule labeling dyes [17, 20, 151, 176, 177, 220, 261] and specially coated electrodes [161, 163, 245, 255, 264]. Dyes are usually delivered intracellularly or in the interstitia where they bind reactive species and indicate species concentration through either fluorescence or chemiluminesce. However, dyes such as the widely used 4,5-diaminofluorescein respond to all species that nitrosate the substrate, including many NO decomposition products. Such dyes can also react with dehydroascorbic acid and ascorbic acid to yield emission products with similar emission wavelengths, interfering with NO detection [273]. Such dyes are also non-reversible, suffer from chemical photo-bleaching inherent to small-molecule fluorophores, and generally cannot be resolved at a sufficient level to measure NO at sub-cellular spatial resolution. Electrochemical measurement, however, is capable of detecting absolute NO levels but it cannot map the subcellular space. Hence, none of these methods to date have enabled the detection of intracellular NO dynamics.

Molecular sensors based on nanoscale structures are well suited to address many of these limitations, with examples including sensors based on quantum dot FRET probes [8], graphene oxide probes [259], aggregating gold nanorods and nanoparticles [173], and single-walled carbon nanotube (SWCNT). Single-walled carbon nanotubes (SWCNT) have been shown to be particularly well-suited as intracellular nitric oxide sensors. SWCNT have a very strong photoluminescence (PL) response, absorbing and emitting in the visible and near-infrared (nIR) spectrums respectively. Small-molecule analytes can interrupt the PL emission by providing a site for generated excitons to recombine destructively. This

results in an easily observable quenching and in the case of NO, single-molecule detection as individual molecules adsorb to the surface [269]. Various polymers or DNA corona phases can wrap the outer surface of the SWCNT to enable selective molecular detection of other analytes by restricting molecular access to the SWCNT surface. With this method, we have designed sensors specific for glucose [14, 13, 15, 16], DNA [91, 113, 114, 118], ATP [269], H_2O_2 [116, 132], and NO [269, 14]. Such sensors have also been demonstrated for whole-animal measurements [107], but have not been studied for their ability to do spatiotemporal sensing at the sub-cell length scale.

In this work, we utilize the SWCNT-based NO sensor and a new methodology to study NO generation and intracellular signaling for the first time. Such sensors are readily internalized by A375 melanoma cells through macropinocytosis [21], exhibit low background signals, and have a high signal to noise ratio that allows for real time detection of intracellular spatiotemporal NO. NO generation and subsequent intracellular signaling was assayed using the nitric oxide releasing anticancer drug JS-K in the A375 melanoma cells. Endogenous NO generation from vascular endothelial growth factor (VEGF) stimulation of human umbilical vein endothelial cells (HUVEC) was also measured. We show that the resulting spatial and temporal fluctuations can only arise from two or more asynchronous NO sinks within the cell that are spatially distinct. This finding provides a more in-depth understanding of intracellular NO and illustrates just one use of these nanosensor probes and their capability to expand the knowledge of biological molecules and their intracellular distribution.

While it is currently believed that the local average concentration of NO governs its pathophysiology, some studies have indicated the importance of intracellular NO localization [108]. With the novel SWCNT sensor for NO we demonstrate that NO concentration is dynamically modulated at an intracellular level, leading to a more complex picture of NO signaling and biochemistry. It is shown that spatiotemporal fluctuations can only be a consequence of temporally varying NO sinks within the cell, and that two or more asynchronous sinks must be present to model the observations. These results offer new possibilities to explore and understand NO signaling. For our future work, the unique PL emissions of different SWCNT chiralities can be utilized for simultaneous study of multiple substrates and their dynamic interactions.

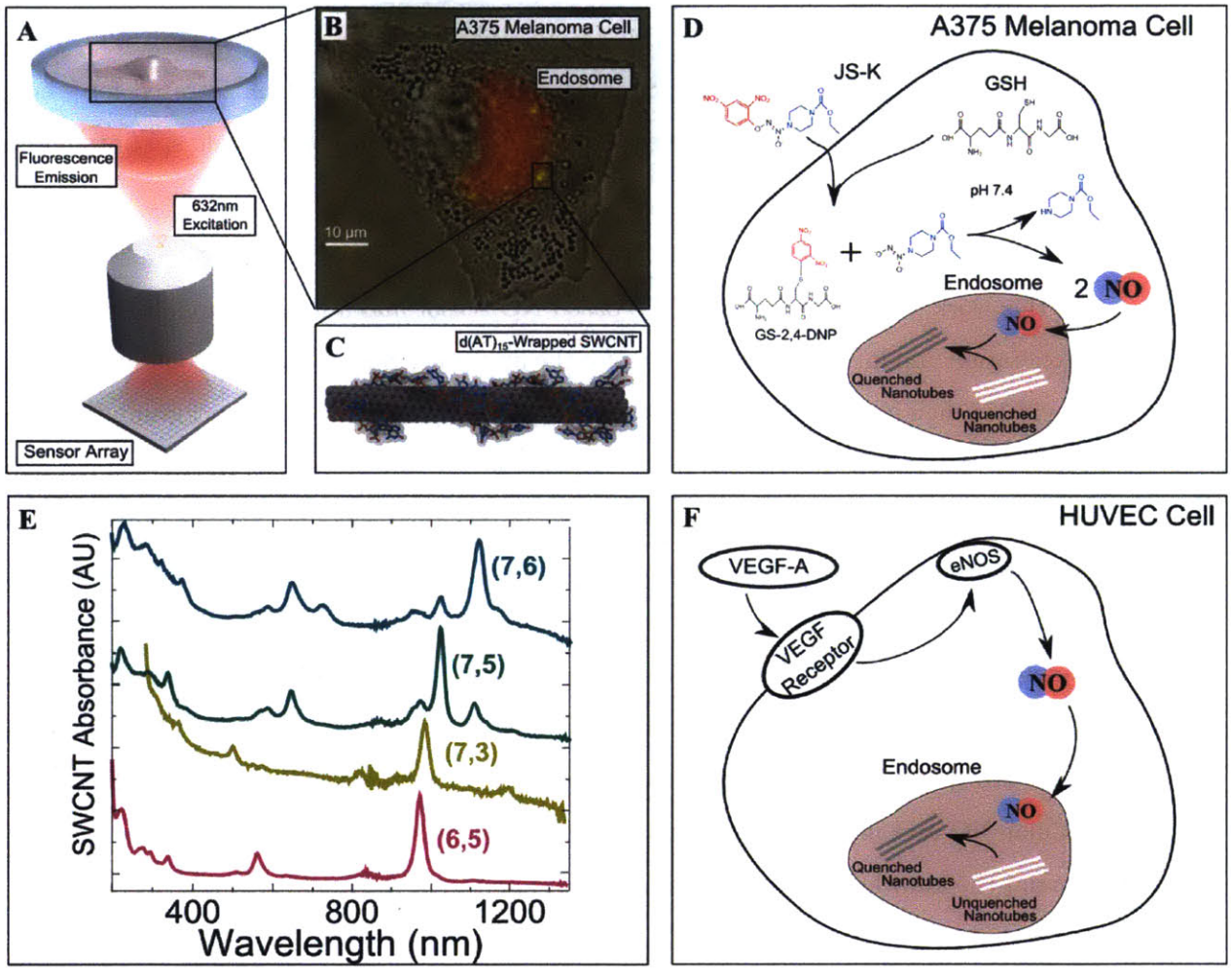

Figure 4-1: Experimental setup for the detection of intracellular NO. Experimental setup for the detection of intracellular NO. (A) The fluorescence setup, with an A375 melanoma cell of interest located on a petri dish, a 632 nm excitation source, and a NIR sensor array. (B) Co-localization of the SWCNT sensors (yellow) with the cell endosomes (red) as indicated using LysoTracker Red. (C) A cartoon of a DNA(AT15)-wrapped SWCNT capable of detecting NO. (D) Chemical pathway for the penetration and decomposition of JS-K, resulting in increased NO concentrations in the endosome. (E) Absorbance spectra for three SWCNT chiralities. (F) Chemical pathway for the binding of VEGF-A to VEGF receptors on HUVEC cells, causing a release of NO from eNOS bound to the cell membrane.

4.3 Results

4.3.1 SWCNT Uptake and Colocalization in Melanoma Cells.

$d(AT)_{15}$-DNA wrapped SWCNT previously found to selectively detect nitric oxide in vitro [269] were prepared and introduced to cultures of A375 melanoma cells (see Methods in section 4.6). The SWCNT concentration was quantified via absorbance spectroscopy, and a concentration of 2ug/ml was diluted into media for cellular uptake. After introduction of the SWCNT and a 12 hour incubation, the cells were found to have internalized the SWCNT. SWCNT PL was observed using a previously described nIR fluorescence microscope setup [269] (Fig. 4-1A). Briefly, SWCNT were excited with a 632nm laser (CrystaLaser, CL660-100, 100mW), and fluorescent emission wasmonitored in an inverted microscope (Carl Zeiss, Axiovert 200) using a 100x TIRF objective and a 2D liquid nitrogen-cooled InGaAs near-infrared sensor array (Princeton Instruments OMA 2D. nIR images were saved every 0.2 s over the course of an experiment. The absorbance spectra for three SWCNT chiralities [249] is shown in Fig. 4-1E.

The intracellular presence and location of the SWCNT was confirmed through optical and fluorescent microscopy. The SWCNT nIR emission was observed in the peri-nuclear region, indicative of a late endosome and lysosome localization. This was further confirmed through incubation with LysoTracker Red, which co-localized with the nIR image (Fig. 4-1B). SWCNT sensors were shown to respond through the direct administration of nitric oxide to the cell medium (see Appendix A), but this method was not used extensively because of the short diffusion length, roughly 20 um [41], and cellular barriers from large nitric oxide concentration gradients in and near cells. MAHMA NONOate was also attempted for NO introduction (see below), but release occurred outside of the cell diluting its effect. Instead, we relied on the production of intracellular nitric oxide using the nitric oxide pro-drug JS-K.

4.3.2 Nitric Oxide Signaling Dynamics in Response to the Glutathione Activated Donor JS-K.

The nitric oxide pro-drug JS-K [225] [O2-(2,4-dinitrophenyl)1-[(4-ethoxycarbonyl)piperazin-1yl]diazen-1-ium-1,2-diolate] was utilized to exogenously generate intracellular NO concentrations and signaling. JS-K reacts with intracellular glutathione (GSH) to produce an intermediate (4-Carbethoxy-PIPERAZI/NO) that then releases two parts NO for each JS-

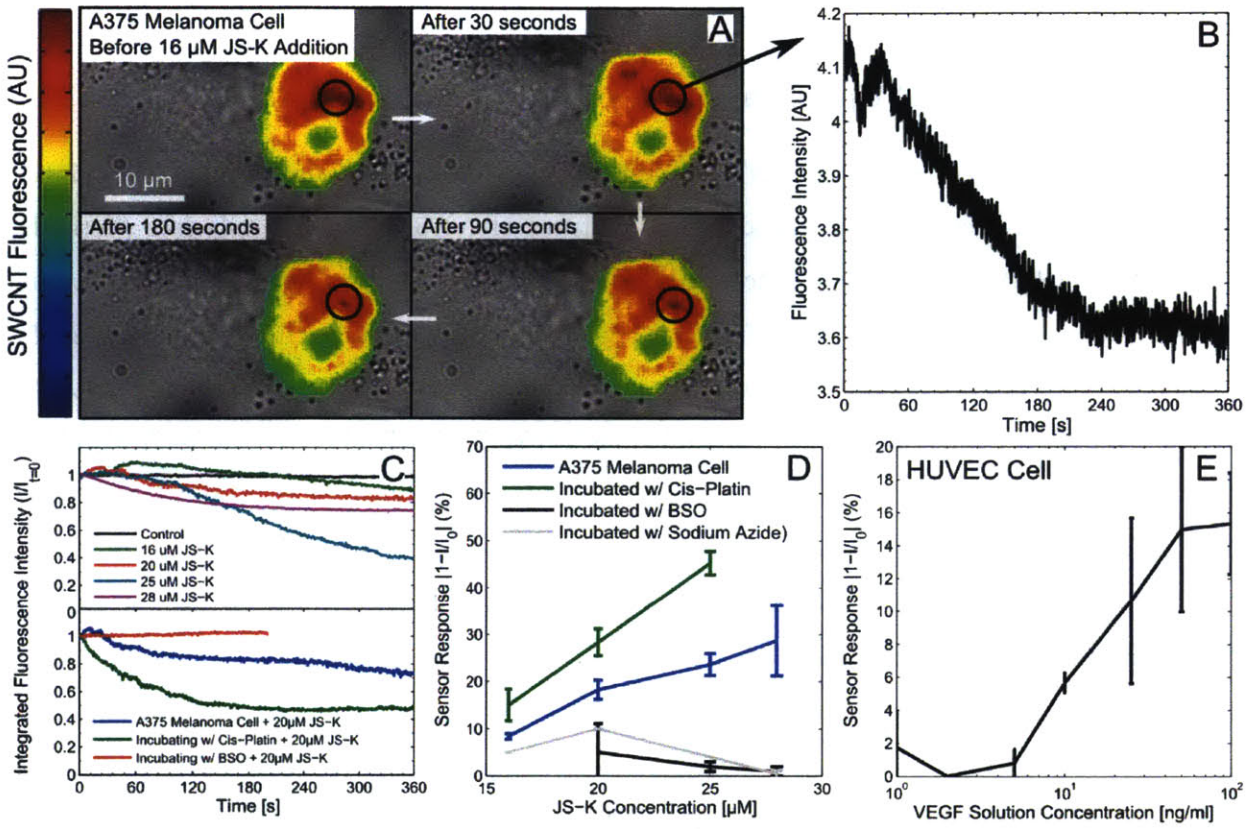

Figure 4-2: Confirmation of Intracellular NO Detection. (A) NIR intensity profiles of the endosome region over three minutes after exposure to JS-K, showing gradual intensity quenching. (B) Intensity of a single point over time showing rapid quenching followed by a settling to a new steady state intensity. (C) Quenching profiles for several JS-K concentrations, and confirmation of the included literature JS-K pathway by promoting the intermediate reagent GSH with Cisplatin or reducing GSH with buthionine sulfoximine (BSO). (D) Calibration curves showing the final quenching response to various JS-K concentrations after incubation with Cisplatin, BSO, or sodium azide. (E) A similar calibration curve for a HUVEC cell exposed to vascular endothelial growth factor (VEGF).

K molecule (Fig. 4-1D). This additional nitric oxide can then freely diffuse throughout the cell and their intracellular location detected with our SWCNT sensors. This mechanism was verified first by modulating the JS-K concentration, and then modulating the intracellular GSH concentrations to alter net nitric oxide production.

The degree of SWCNT quenching in A375 melanoma cells was found to increase with increasing JS-K concentrations in the range of 16 µM to 28 µM (Fig 4-2). For a given JS-K concentration, the baseline integrated SWCNT PL intensity of a target cell was observed for 400s. JS-K was then added to the cell medium, and the PL levels of the same cell was imaged over another 400s, which was typically sufficient for the quenching to reach steady

state (Fig. 4-2A). The PL at local maxima (central SWCNT positions) was also found to decrease in a similar manner (Fig. 4-2B). Data for each JS-K concentration represent the results of 3 replicates unless otherwise stated. Examples of the PL changes over 3 minutes for each tested JS-K concentration (16, 20, 25, and 28 μM) are shown in Fig 4-2C, and the final quenched intensity for each concentration is shown in Fig 4-2D. To ensure that the introduction of JS-K was releasing nitric oxide that was being detected by the intracellular SWCNT sensors, several alternative methods were used. First, prepared NO solution (see Materials and Methods in section 4-7 for procedure) was introduced directly to cell medium. An observable quenching effect was observed as demonstrated in Figure A-1. However, this protocol was less favorable than the final JS-K protocol due to the short diffusion length of free NO in solution, resulting in decreased delivery to the cell interior. Second, MAHMA NONOate was added to the cell medium. MAHMA NONOate releases NO at pH 7, but not under acidic conditions. MAHMA NONOate solution was prepared at pH 2 (see methods in main text) and added to the cell medium, resulting in a quenching effect of interior SWCNT, as shown in Figure A-1. However, the degradation method (only internal to the cells) was preferred to this method. Finally, to ensure that the injection protocol (JS-K in DMSO solution) was not inherently affected the SWCNT PL, a stock DMSO solution without JS-K was added to cell medium. No PL effect was observed upon this addition (see Figure A-1). The protocol for JS-K administration and NO release was qualitatively confirmed through the administration of the commercial NO-sensitive fluorescent dye DAF-FM. To ensure that NO released by JS-K successfully made it to the SWCNT interior, a commercial DAF-FM NO detection kit was used (see section 4.6 for protocol). The NIR emission at 515nm is shown in Figure 4-5 for five minutes after the introduction of JS-K to the cell medium, resulting in a broad increase in fluorescence within the cell. Figure 4-6 includes 5 minutes of NIR images taken before the introduction of JS-K, showing the DAF-FM was stable over that time scale to intracellular nitric oxide release. It is important to note that in contrast to diaminofloureceins, SWCNT NO sensors react with NO directly and do not involve reactive oxygen species or NO byproducts.

We investigated NO dynamics in the presence of both elevated and suppressed GSH. Intracellular GSH levels were measured using a GSH assay (see Methods), with a measured concentration of 1.3 ± 0.3 mM inside the A375 melanoma cells. Incubating the cells with Cisplatin (see Methods), a chemo-therapeutic agent that cross-links DNA increasing

cellular stress and GSH production [123], resulted in an increased GSH concentration of 3.2 ± 0.4 mM and increased PL quenching for each concentration of JS-K tested (Fig 4-2D). Conversely, incubating the cells with buthionine sulphoximine (BSO), an inhibitor of gamma-glutamylcysteine synthetase that reduces GSH concentrations [63], resulted in a decreased GSH concentration of 0.71 ± 0.24 mM and less PL quenching (Fig. 4-2D). Finally, administering sodium azide disabled aerobic metabolism in the melanoma cells and effectively removed their ability to produce GSH. Subsequent addition of JS-K resulted in no observable quenching of the SWCNT PL (Fig. 4-2D).

4.3.3 Application to Vascular Endothelial Growth Factor and HUVEC Cells.

To examine our hypothesis in a different system, vascular endothelial growth factor (VEGF)-mediated NO production was monitored in endothelial cells. HUVEC cells were observed to uptake the SWCNT sensors using the same incubation protocol as the A375 melanoma cells. Introducing VEGF activates endothelial nitric oxide synthase (eNOS) [140] resulting in an increase in intracellular NO concentration and a detectable quenching of the SWCNT PL, as illustrated in Fig 4-1D. PL quenching was tested for VEGF treatments ranging from 1 ng/ml to 100 ng/ml. Responses were observed at the widely accepted treatment concentration of 10 ng/ml (Fig 4-2E). Furthermore, VEGF stimulated NO release occurs more rapidly with larger intracellular gradients, illustrating the differences between physiological and pharmacological NO release (see Appendix A).

4.3.4 Spatio-Temporal Mapping of Intracellular Nitric Oxide.

To interpret the resulting novel data sets, we developed a absorption/scattering image processing algorithm for allowing spatial and temporal data to be extracted from movies of cellular quenching during NO signaling, which we demonstrate for the case of an A375 melanoma cell responding to JS-K. The $d(AT)_{15}$-DNA wrapped SWCNT sensors allow for spatiotemporal resolution of nitric oxide concentrations not possible with previous NO detection mechanisms. Inside the cell, the SWCNT are localized to multiple endosomes resulting in multiple effective sensors within the cell. Each SWCNT bundle within an endosome functions as a point source of photoluminescent light in the NIR scattering and absorbing cell, effectively illuminating the surrounding region (Fig. 4-2A and 4-2B). The SWCNT centers

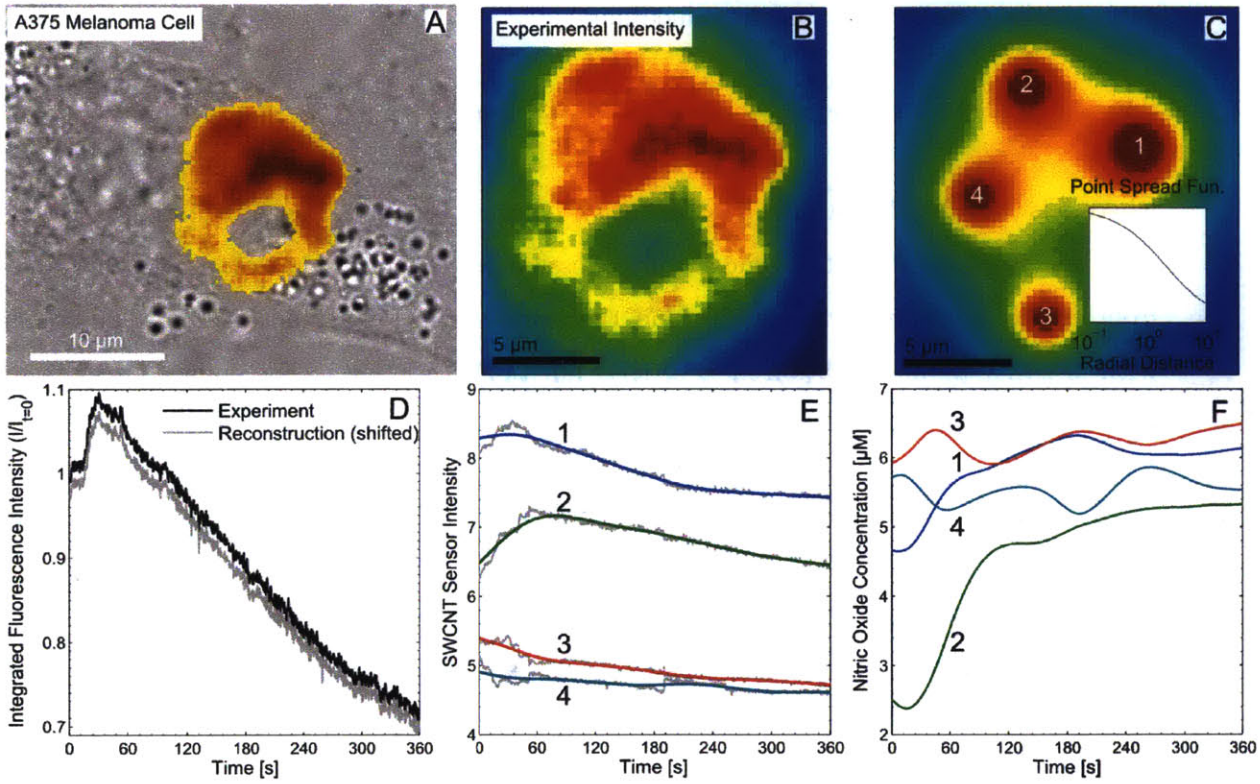

Figure 4-3: Calculation of intracellular nitric oxide concentration through observations of SWCNT fluorescence. A) Fluorescence intensity of SWCNT in A375 melanoma cell. B) Experimental intensity profile. C) Reconstructed intensity profile after fitting a small number of point illumination sources with point spread functions indicated in the inset. D) Demonstration that point-source process retains the same total intensity information from Figure 4-2E) Intensity for each point source, before and after removal of high frequency noise with a smoothing spline. F) Calculated nitric oxide concentration for each point source using a kinetic model for the adsorption/desorption of nitric oxide on SWCNT.

and intensities were reconstructed using a simple NIR scattering/absorption model, and the resulting intensity traces were analyzed to calculate the observed nitric oxide signal using known kinetics for SWCNT PL quenching by NO.

Each SWCNT bundle is treated as a point illumination source. The propagation of NIR light in tissue and cells is effectively modeled at steady state by solving the Helmholtz equation for a scattering/absorbing medium,

$$\mu_a \phi(\mathbf{r}) - \frac{1}{3(\mu_a + (1-g)\mu_s)} \nabla^2 \phi(\mathbf{r}) = \text{Source Term}, \tag{4.1}$$

where ϕ is the spatially varying light intensity, μ_a, μ_s, g are the tissue absorption, scattering, and anisotropy coefficients tissue at the emission wavelength, approximated with values from *in vivo* melanoma tissue [75], and the source term for a point illumination source with intensity ϕ^0 and location r_1 is a delta function $\phi^0 \delta(r - r_1)$. For point sources in an unbounded medium, the Green's function is

$$G(\mathbf{r}) = \frac{3(\mu_a + (1-g)\mu_s)}{4\pi} \frac{\exp\left[-3\mu_a(\mu_a + \mu_s(1-g))\,|\mathbf{r}|\right]}{|\mathbf{r}|} \tag{4.2}$$

and the resulting spatiotemporal intensity for the illumination from all SWCNT point sources is a summation over the Green's function for each point source

$$\phi(\mathbf{r}, t) = \sum_k \phi_{0,k}(t) G\left(\mathbf{r} - \mathbf{r}_k(t)\right), \tag{4.3}$$

where $\phi_{0,k}(t), r_k(t)$ are the time-dependent intensity and position of the kth SWCNT bundle. A point source was initially placed at every local maximum in the first frame of a NIR experimental movie and the closest sources combined until the minimum point separation was below a threshold distance of 5 um (the length scale of interest). At each time frame T, we minimize the error between the frame pixels $I^T_{x,y}$ and the calculated intensity by adjusting the point intensity and locations

$$\min_{\phi_1^0(T), r_1(T), \phi_2^0(T), r_2(T), \ldots} \sum_{x,y} \left[I^T_{x,y} - \phi\left(\mathbf{r} - (x,y), T\right)\right]^2. \tag{4.4}$$

An example of the resulting intensity field $\phi(\mathbf{r}, t)$ is shown in Figure 4-3C, as well as the point spread function $G(\mathbf{r})$ in the inset. Summation of the intensity field at each time point

(Fig. 4-3D), resulted in the same integrated information as discussed in Figure 4-2.

The local nitric oxide concentration at each sensor location can be calculated by considering the reversible interaction of NO with an unoccupied site on the SWCNT surface, forming the NO-SWNCT complex that results in a quenched emission state at that site, as we have shown previously in the case of single molecule detection [22] of NO. The adsorption and desorption of nitric oxide can be described by a first order reversible process, NO + SWCNT $\longleftrightarrow$ NO - SWCNT leading to the rate expression:

$$\frac{d[\text{NO - SWCNT}]}{dt} = k_f[\text{NO}][\text{SWCNT}] - k_r[\text{NO - SWCNT}], \tag{4.5}$$

where k_f, k_r are the forward and backward rate constants, respectively, and calculated from previous *in vitro* single-SWCNT experiments [269] to be $k_f = 8.68 \times 10^{-4}$ (μM s)$^{-1}$ and $k_r = 3.18 \times 10^{-3}$ s^{-1} . These were calculated from previous measurements of nitric oxide quenching of isolated SWCNT [269]. d(AT)$_{15}$-wrapped SWCNT films were prepared and exposed to solution with various nitric oxide concentrations. Rate coefficients were calculated as described in previous work, by fitting both continuous and stochastic kinetics models to the experimental intensity traces. The SWCNT PL intensity is proportional to the fraction of unoccupied sites, [SWCNT], or I/I_0 = [SWCNT]/[SWCNT]$_0$. The value of I_0 was set to correspond to the minimum initial NO concentration for the calculated concentrations to be positive, or $I_0 = I_{(t=0)}\left[1 + \frac{k_f}{k_r}C_0\right]$, where $C_0 = 5\mu$M. The number of sensor sites are conserved with the conservation relation [SWCNT]$_0$ = [SWCNT] + [NO - SWCNT]. Making this substitution and rearranging, the concentration of NO can be calculated directly from the local intensity and its time-derivative

$$[\text{NO}] = \frac{1}{k_f}\frac{I_0}{I}\left[k_r\left(1 - \frac{I}{I_0}\right) - \frac{1}{I_0}\frac{dI}{dt}\right]. \tag{4.6}$$

The finite imaging detector frame rate introduces noise into the calculation of the intensity derivative, potentially amplifying the fluctuations in the excitation source. Hence, each intensity trace is smoothed using a FFT low-pass filter prior to differentiation (Fig. 4-3E). This method yielded similar results as compared to regularized differentiation [238] at a fraction of the computation cost. The resulting nitric concentrations are shown in Figure 4-3F for each of the SWCNT groupings in Figure 4-3C. Full analysis for each of the

experimental conditions is included in Appendix A. These NO concentrations fall within the same range as those reported in previous studies [41]. Complete analysis of nitric oxide concentration for all experimental conditions are included in the supplement.

Previous work has shown that DNA-wrapped SWCNT enter the cell through macropinocytosis [21]. We found that the majority of A375 melanoma cells displayed fluorescent SWCNT in multiple endosomes after a three hour incubation. These allowed for the measurement of the heterogeneity of intracellular nitric oxide generation and decay (Fig. 4-4). At each observed time point, the concentration difference between each pair of SWCNT sensors was calculated and normalized by their spatial separation. All of the observed differences over the course of an experiment were used to build a probability density of concentration differences (Fig. 4-4A). Before stimulation with JS-K, difference values of approximately 0.1 µM/um were observed, corresponding to baseline intracellular NO heterogeneity. When 28 µM of JS-K was added, NO differences increased to 1 µM/um. This change is potentially due to a combination of variations in JS-K diffusion into the cell and intracelluar glutathione (see Fig. 4-4F). Over time, the observed differences returned to their values before JS-K addition.

The diffusion of nitric oxide has been very well studied. For a diatomic gas with a diffusion coefficient of $10^{-7}cm^2/s$, equilibrium can be achieved on the order of 10 milliseconds. However, our setup detects intracellular concentration differences persisting over seconds. We demonstrate below that such spatial and temporal fluctuations can only occur from the asynchronous modulation of two or more spatially distinct NO sinks within the cell. These results can be understood with a simple numerical model for JS-K diffusion and reaction to produce nitric oxide within the cell.

4.3.5 Numerical Model for the Response of Intracellular SWCNT to an External JS-K Stimulus.

To understand the implications of the nitric oxide gradients reported by our sensors under a variety of conditions, we constructed a simple numerical 2D model for the diffusion of JS-K into the cell and the reaction with GSH to form NO according to the scheme presented in Figure 4-1D. We also consider various models for spatially heterogeneous production and consumption of intracellular NO which have not yet been considered due to the lack of NO sensors with sufficient spatial resolution.

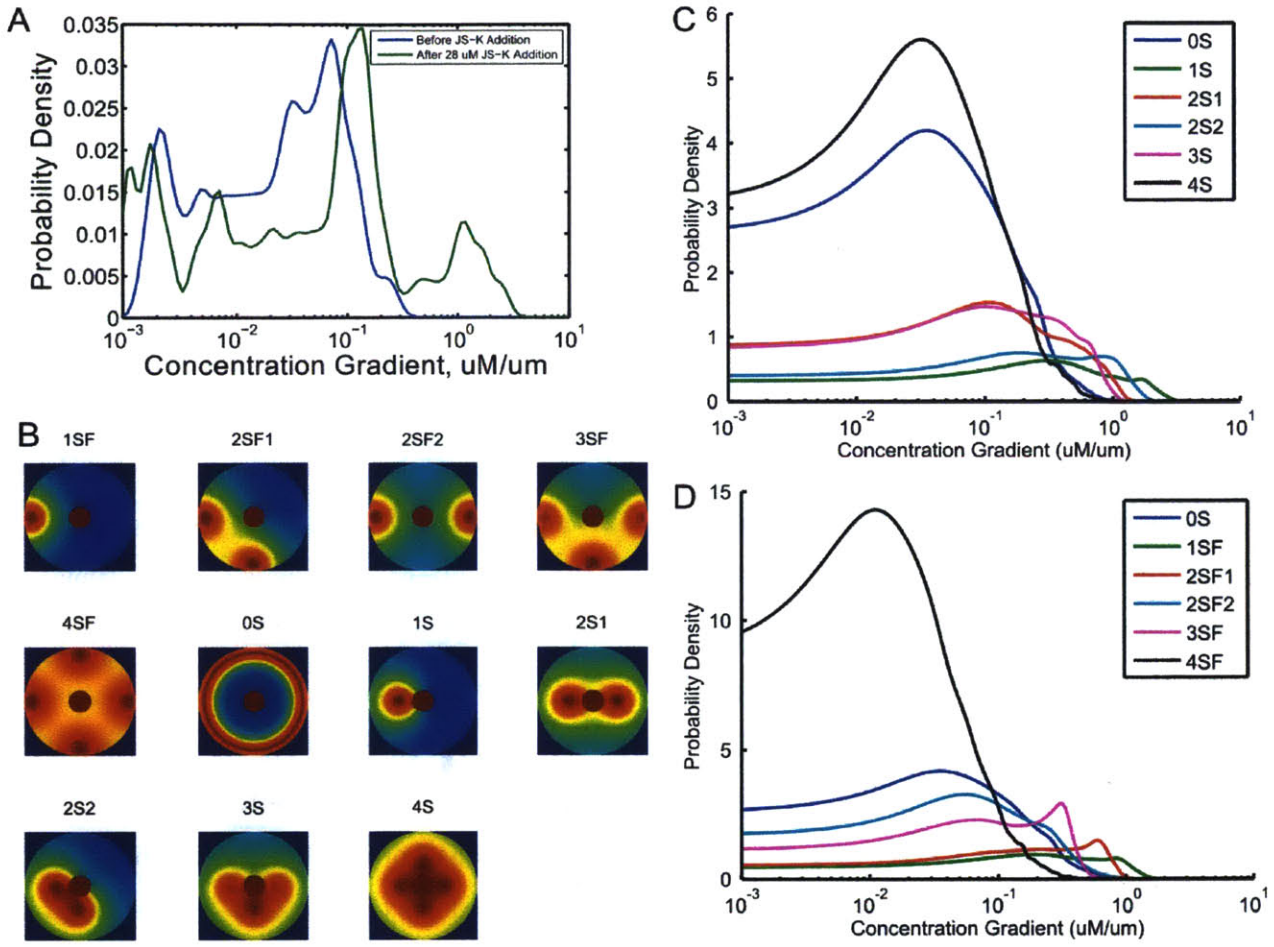

Figure 4-4: Observed intracellular NO gradients and a numerical model for the release of NO by JS-K addition. A) Typical observed NO concentration gradients between sensor regions before and after the introduction of 28 µM JS-K. Baseline concentration differences are approximately 0.1 µM/um. A second peak in the histogram at approximately 1 µM/um occurs at the beginning of the experiment, before the SWCNT settle to a new equilibrium. B) Diffusion-reaction model simulation of intracellular NO formation with 16µM JS-K addition. Zero to four sources of intracellular GSH is places in various locations. The system is optimized such that NO concentration is approximately 4 µM, and the gradient is studied. C-D) For each scenario in B, gradient is calculated as the concentration difference collected at random pairs of locations within 3 µm of the nucleus normalized by distance. A probability density distribution is then plotted. Results show that at least 1 source is required to reproduce the concentrations and gradients.

We construct a diffusion and reaction model to simulate intracellular nitric oxide (NO) concentrations from JS-K treatment (see Table 4.1) for model parameters and section 4.5 for full details of the model). The geometry of the system simulates the cytosol with a 10 µm diameter circle and a nucleus at the center with a 2 µm diameter impermeable boundary (Fig. 4-4). The outer boundary of the cytosol was permeable to JS-K and NO, but impermeable to GSH. The concentration of JS-K was set outside the cell to the various levels used in the experiments (16-28 µM). The reaction of JS-K with GSH to form NO was included with literature rate data [225]. Intracellular NO production and first-order consumption was modeled both homogeneously and heterogeneously with sources and sinks as two-dimensional sinusoidal functions (i.e. proportional to $[\sin(x/X)\sin(y/Y)]^a$, where we control the sharpness and position of the function with a, x and y). The magnitudes of these functions were adjusted to obtain the experimental concentrations of NO and the resulting intracellular spatial differences were compared. COMSOL™ was used to solve for the resulting NO concentrations, each simulation ran until equilibrium is reached, typically 10 seconds.

We performed the simulation for combinations of 4 potential sources placed either proximal or distal to the nucleus (Figure 4-4B). Random pairs of points were used to calculate the gradient in the peri-nuclear region, defined as between 1 and 3 µm to the center of the simulated cell. A kernel density estimation of the gradient probability density distribution was constructed to compare with the experimental readings (Figure 4-4C-D). At least one sink that caused a polarization of the intracellular NO concentrations was required to result in gradients similar to those reported by our intracellular sensors. Furthermore, while proximal sources created higher gradient readings, probability density function shapes from sources further away from the nucleus more closely resembled the data. We hypothesize that the sensors are detecting multiple GSH sources at different intracellular locations during the experiment. Future work will focus on the identification and characterization of cellular sources of NO. As SWCNT sensors can be modified to detect a variety of species, this intracellular detection schema can be used to understand the distribution and modulation of other biological molecules.

The role of NO in human physiology and pathology is paradoxical not only in its contributions to vasodilation, neurotransmission, and intercellular signaling but also its implications in DNA damage, lipid oxidation and cancer progression. One prevailing hypothesis explain-

ing this paradox attributes the NO associated pathway and outcome to local concentrations on the tissue or cellular scale. It is important to note that current detection systems potentially yielding such spatial information either do not have the required resolution or fails to measure NO directly. Therefore, the field currently lacks the appropriate tools to test the above hypothesis.

The method we developed in this work along with our findings calls into question the notion of an average cellular concentration of NO. We show clear evidence for persistent gradients within the cell. These gradients are observed with both exogenous (JS-K) and endogenous (VEGF $\rightarrow$ eNOS) NO sources. We believe that these gradients are a result of sources and sinks non-uniformly distributed within the cell. With gradients of the magnitude that we observe, regions of the cell will experience NO concentrations at orders of magnitude higher than others. This phenomena and its regulation can be important in NO signaling and is not reflected in current bulk detection systems. Even more importantly, we show that this gradient fluctuates in tens of seconds and that this can only arise from temporal modulations in the source and sink pathways for NO. As biological signaling is often modulated via duration and frequency, deciphering intracellular NO dynamics can prove to be instrumental in studying the mechanism of NO action for its various biological functions.

4.4 Conclusion

We use $d(AT)_{15}$-DNA in this work to demonstrate the intracellular detection of NO. In comparison with other techniques, the preparation of SWCNT probes is relatively simple and does not require organic synthesis. These sensors are stable for prolonged periods of time and do not photo bleach with repeated excitation at high frequency. Furthermore, nIR imaging allows for minimal signal attenuation in biological environments which also lends itself to tissue analysis in addition to in vitro culture. For the first time, we were able to achieve intracellular spatial and temporal NO resolution. In addition to only concentration, we show that location and frequency of NO signals can now be detected and may play a major role in intra- and extra-cellular communication.

Overall, this technology allows for the study of NO which will further our understanding of its function in cellular signaling and equilibrium. It can also be readily expanded for the detection of other species and multiplexed for multiplex applications. In this case,

investigation of NO dynamics can extend to applications such as the early detection of endothelial dysfunction and the study of tumor progression and response to treatment. As a unique tool to query cellular states, these sensors provide new and valuable information in both the basic understanding and potential toward novel clinical diagnostics.

4.5 Numerical NO Reaction/DiffusionModel

A diffusion reaction model system was constructed in COMSOL (COMSOL, Inc., Burlington, MA) to simulate intracellular nitric oxide (NO) concentration following JSK treatment. Model parameters are included in Table 4.1.

The geometry of the system simulates the cytosol through a 10 Îijm diameter circle. The outer boundary of the cytosol is setup so that JSK is permeable, GSH is impermeable and NO permeable with an appropriate partition coefficient. The nucleus is 2 μm in diameter at the center of the cell with impermeable boundary.

The model uses the simple two dimensional diffusion-reaction equation for each of the three species (NO, GSH and JSK):

$$\frac{\partial c_i}{\partial t} + \nabla(-D_i \nabla c_i) = R_i$$

c is the concentration, D is the diffusion coefficient, and R the change in concentration due to reaction, which is modeled through first-order kinetics:

$$\text{JSK} + \text{GSH} \rightarrow 2\,\text{NO} + \text{Products}$$

A fine free triangular mesh is utilized for optimal solving efficiency and resolution. The simulation is solved until the system reaches equilibrium or until 60 seconds (which never was necessary). To simulate distinct sources and sinks of NO, two-dimensional sine functions of varying sharpness were used $[\sin(x/X)\sin(y/Y)]^a$. The magnitude of these functions were adjusted appropriately so that the simulations obtain the experimental concentrations of NO at equilibrium. The number and locations of the sources and sinks are varied to reproduce the intracellular gradients measured.

Table 4.1: Numerical Simulation Parameters

Parameters	Values	Reference
JSK-GSH Reaction Rate	0.154[m^3/(mol*s)]	Kumar et al. [141]
NO Degradation	7.1[1/s]	Chin et al. [41]
JSK Diffusion Coefficient	5.813e-10[m^2/s]	Chemspider[4]
GSH Diffusion Coefficient	6.7e-10[m^2/s]	Wu et al.[265]
NO Diffusion Coefficient	1.0e-10[m^2/s]	Chin et al. [41]
Intracellular GSH Concentration	5.5[mol/m^3]	Hallbrink et al. [85]
Intracellular NO Concentration	1e-3[mol/m^3]	Lewis et al.[146]

4.6 Materials and Methods

A375 Melanoma Cell Culturing. A375 melanoma cells were cultured to confluence in 75 cm_2 cell culture flasks under culture conditions of 5% CO_2 at 37°C. The cells were grown in DulbeccoâĂŹs modified EaglesâĂŹ media (DMEM) supplemented with 10% fetal bovine serum (FBS), 2 mM L-glutamine, 1 mM sodium pyruvate, 100 IU/ml penicillin, and 100 μg/ml streptomycin.

$d(AT)_{15}$-SWCNT Suspension. Single walled carbon nanotubes were wrapped with $d(AT)_{15}$ oligonucleotides using a previously published method [8, 13]. Briefly, HiPCO SWCNT purchased from Unidym were suspended with a 30-base (dAdT) sequence of ssDNA (Integrated DNA Technologies) in a 2:1 DNA:SWCNT mass ratio in 0.1 M NaCl. A typical DNA concentration was 2 mg/mL. Samples were sonicated with a 3 mm probe tip (Cole-Parmer) for 10 min at a power of 10 W, followed by benchtop centrifugation for 180 min (Eppendorf Centrifuge 5415D) at 16,100 RCF. Afterwards, the supernatant was collected and the pellet was discarded. APTES was not used since sensor-glass adhesion was not necessary as in previous studies. The average SWCNT length was 1-2 Âţm, well under the scale of cell length [8].

Uptake of $d(AT)_{15}$ by A375 Melanoma Cells. The $d(AT)_{15}$-SWCNT suspension (10mg/L) was added to melanoma cells dispersed in 2 ml DMEM and then incubated for 12 hours at 37°C, enabling the cells to adhere to the glass bottom of a petri dish and take up the SWCNT. Before fluorescence experiments (addition of JS-K, etc), the cells were washed

with PBS several times. Two ml of fresh DMEM medium and 1 ml PBS (1x) was added and the cells were incubated for 30 min. The fluorescence response within the cells was then monitored using a NIR fluorescence microscope.

nIR Fluorescence Microscope Setup . SWNCT were excited with a 660nm laser (CrystaLaser, CL660-100, 100mW) and fluorescent emissions were monitored with an inverted microscope (Carl Zeiss, Axiovert 200) using a 100x oil immersion objective (alpha Plan-Apochromat 100x/1.46) and a 2D liquid nitrogen-cooled InGaAs near-infrared sensor array (Princeton Instruments OMA 2D) (Fig. 4-1A). nIR images were saved every 0.2 s over the course of an experiment.

NO Solution Preparation. NO solution was obtained using a method similar to one reported previously [118]. Briefly, 3 mL of phosphate buffer saline (PBS, 1x) was introduced into a 5 mL round-bottom flask and sealed with a septum inserted with two needles to provide an inlet and an outlet. After initially purging the syringe apparatus with argon gas (Airgas) before use, argon was introduced to the buffer for 2 h to remove all dissolved oxygen Nitric oxide gas (99.99 %, Electronicfluorocarbons) was then introduced for 20 min at an outlet pressure of 2 psi. NO concentration was determined by using the horseradish peroxidase assay.

JS-K Solution Preparation. To prepare the JS-K solution for administration to cells, 0.38 mg JS-K was dissolved in 1 ml DMSO to obtain a 1 mM stock solution.

Verification of Intracellular NO Production with DAF-FM After Administration of JS-K. A375 melanoma cells were incubated for 12 hours at 37°C to allow for adherence to the culture dish. After the 12 hour incubation, the medium was changed to 1 ml fresh DMEM, and DAF-FM (4-amino-5-methylamino- 2',7'-difluorescein) was added to the culture at a final concentration of 20 ÂţM. After a 30 minute incubation at 37°C, the medium was changed to L15 medium and DAF-FM at a final concentration of 20 μM. After taking a visible image on the microscope, JS-K was added and an image was taken every few minutes.

Incubation of A375 Melanoma Cells to Alter Intracellular Glutathione Levels. GSH Inhibitor (BSO) Pre-treatment. 0.166 mg L-Buthionine-(S,R)-sulfoximine (BSO), purchased from Enzo Life Sciences, was dissolved initially in a small amount of DMEM medium and added to A375 cells cultured in 75 cm^2 culture flasks. The final culture volume was brought up to 15 ml, resulting in a 50 μM BSO solution. These A375 and BSO cultures were incubated for 48 hours at 37°C with 5% CO2.

Cisplatin Pre-treatment. A375 melanoma cells were incubated with 5 μM Cisplatin for 8 hours under normal cell culture conditions.

GSH Measurements. The intracellular GSH concentration was measured using a CHEMICON Glutathione Detection Kit. Fluorescence was measured using a Varioskan plate reader, and results were calibrated using a dilution series of 5 GSH concentrations: 0.625 mM, 1.25 mM, 2.5 mM, 5 mM, and 10 mM. The calibration is shown in Figure 4-7.

Sodium Azide Solution and Cell Incubation. 0.3 M sodium azide was prepared by dissolving 19.5 mg sodium azide in 1 ml water under sterile conditions. Cells were incubated with a final concentration of 2 mM sodium azide for 4 hours prior to NIR fluorescence measurements.

Human Umbilical Vein Endothelial Cells (HUVEC) Cell Culture and Proliferation Assay. HUVEC were cultured in F-12K medium supplemented with 10% FBS, 1% endothelial cell growth factor (100x, Sigma), 100 IU/ml penicillin, and 100 Âţg/ml streptomycin. Tissue culture plates were initially coated with endothelial cell attachment factor (ECAF) to promote cell adherence. To detect NO production by eNOS in stimulated HUVEC cells, $d(AT)_{15}$-SWCNT suspensions (10mg/L) were incubated with the cells for 12 hours at 37°C to promote SWCNT uptake. After several washes with PBS to remove dead cells and excess nanotubes, 2ml of F-12K medium was added. After an additional 30 minute incubation, the fluorescence response within the cells was monitored using the NIR microscope.

MAHMA NONOate Solution Preparation and Administration. Stock 1 mM MAHMA NONOate solution was prepared by dissolving 0.20 mg MAHMA NONOate 10 ml phosphate buffer (pH 12). MAHMA NONOate solution was injected through a fine hole (with an argon-purged syringe) to the petri dish that contain cells and cell medium. Upon contact with the pH 7 cell medium, MAHMA NONOate began to release NO. 150 L of MAHMA NONOate solution was added, corresponding to a final NO concentration of approximately 50 μM.

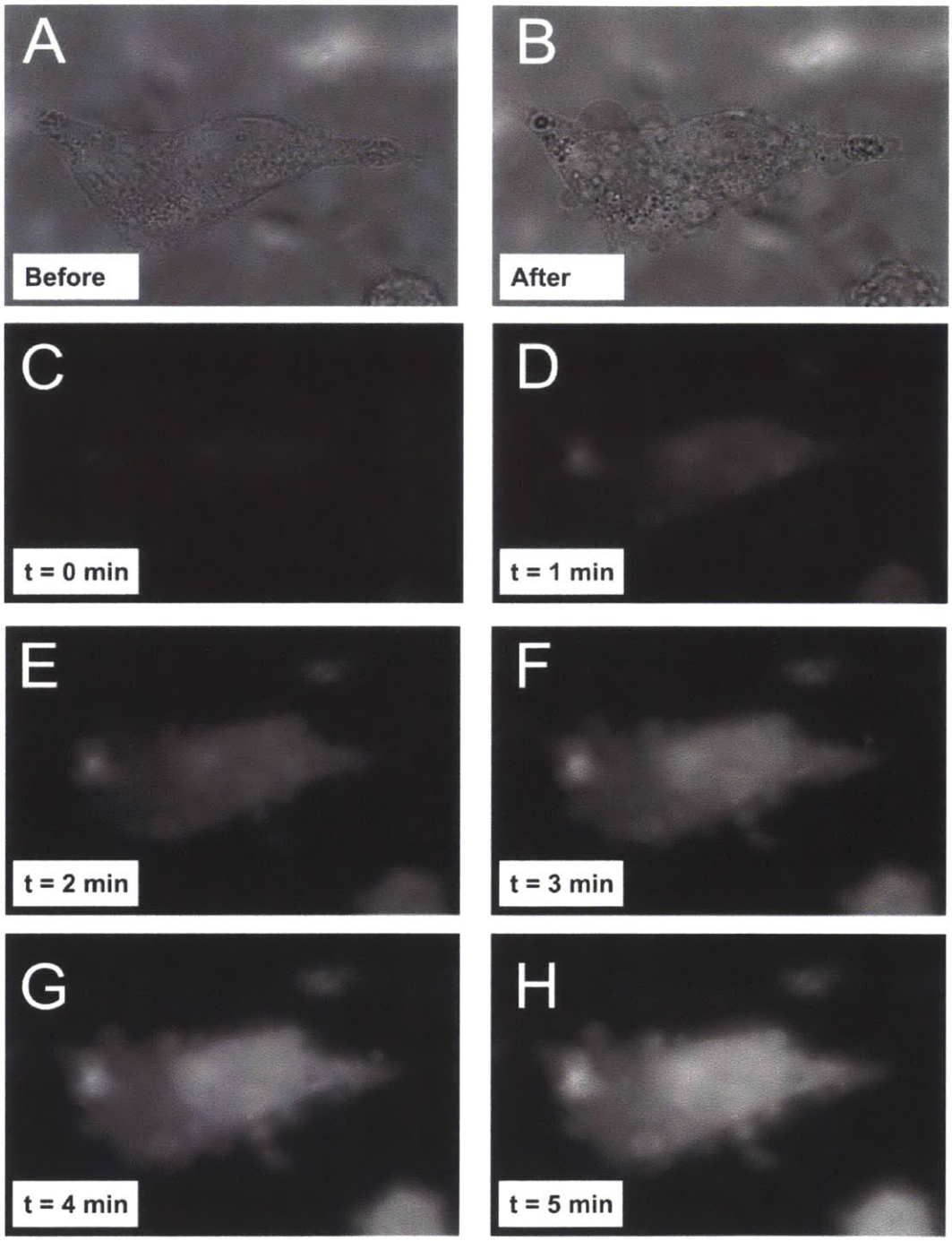

Figure 4-5: Confirmation of intracellular NO release in an A375 Melanoma cell upon addition of extracellular JS-K. (A) Visible image of the cell before incubation with DAF-FM. (B) Visible image of the same cell after incubation with DAF-FM. (C-H) Fluorescence signal at 515nm, in response to stimulation at 495nm (the excitation/emission peaks of DAF-FM), collected every minute after addition of JS-K. The fluorescence signal saturated after approximately 5 min.

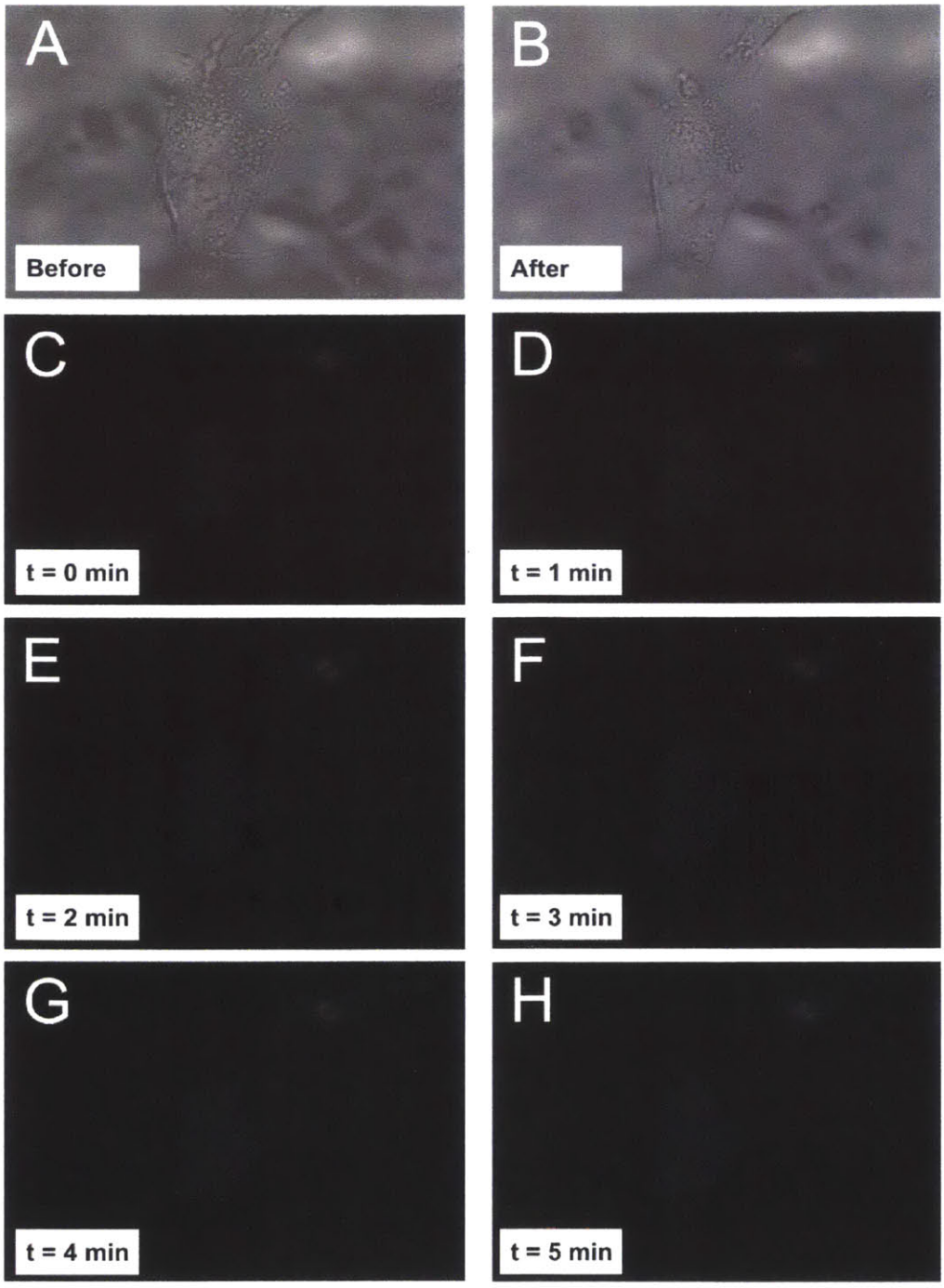

Figure 4-6: Stability of intracellular nitric oxide in an A375 melanoma cell without JS-K measured using DAF-FM. (A-B) Visible images of the cell before and after incubation with DAF-FM. (C-H) Fluorescence emission at 515nm with 495 excitation collected over 5 min, showing stable baseline DAF-FM fluorescence.

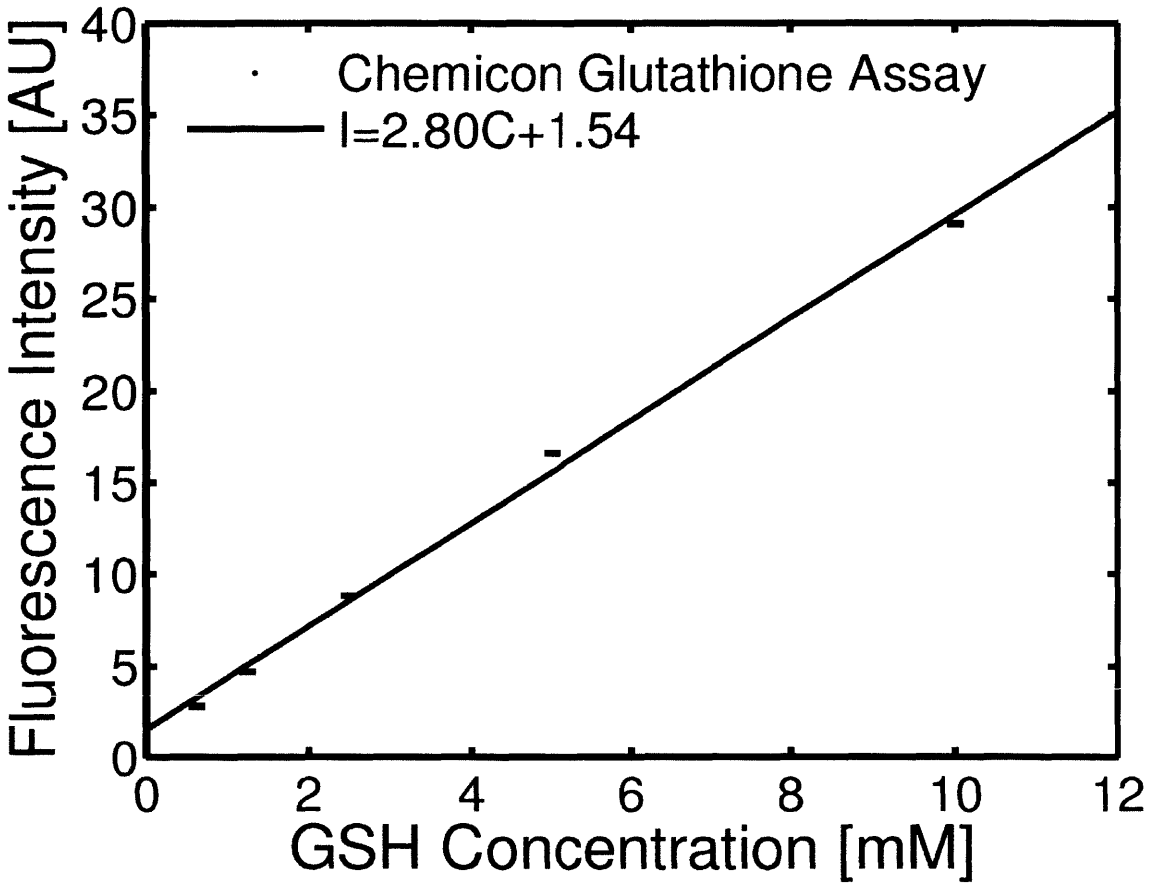

Figure 4-7: Calibration of the CHEMICON GSH assay against five solutions of known GSH concentration. Results were repeated in triplicated, and error bars shown. The fluorescence intensity was approximately linear with the known GSH concentration.

Chapter 5

A 2D Equation-of-State Model for Corona Phase Molecular Recognition on Single- Walled Carbon Nanotube and Graphene Surfaces

This work originally appeared as: Zachary W. Ulissi, Jingqing Zhang, Vishnu Sresht, Daniel Blankschtein, and Michael S. Strano. A 2D Equation-of-State Model for Corona Phase Molecular Recognition on Single-Walled Carbon Nanotube and Graphene Surfaces. Langmuir, 2014. It has been edited to include the supporting information in-line.

5.1 Abstract

Corona Phase Molecular Recognition (CoPhMoRe) has been recently introduced as a means of generating synthetic molecular recognition sites on nanoparticle surfaces. A synthetic heteropolymer is adsorbed and confined to the surface of a nanoparticle, forming a corona phase capable of highly selective molecular recognition due to the conformational imposition of the particle surface on the polymer. In this work, we develop a computationally predictive model for analytes adsorbing onto a polymer corona phase around a single-walled carbon nanotube (SWCNT) surface using a 2D equation of state that takes into consideration the analyte-polymer, analyte-nanoparticle, and polymer-nanoparticle interactions using param-

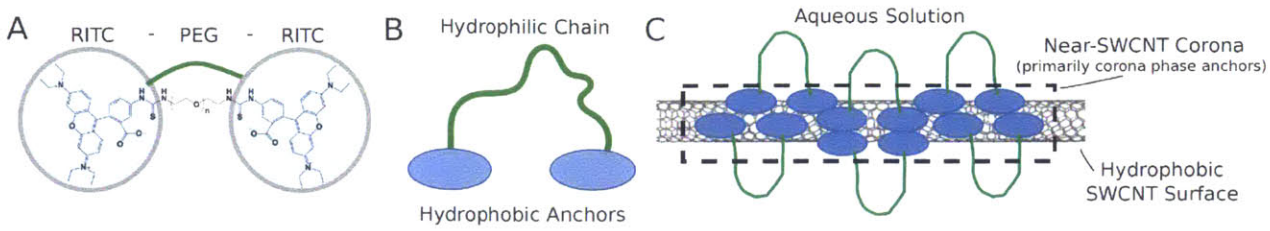

Figure 5-1: Illustration of a Corona Phase Molecular Recognition (CoPhMoRe) sensor using a single-walled carbon nanotube (SWCNT) and an amphiphilic polymer (hydrophobic and hydrophilic regions). (A) An example studied here of rhodamine isothiocyanate (RITC) segments connected with a polyethylene glycol (PEG) chain, referred to as RITC-PEG-RITC. (B) Cartoon of the same RITC-PEG-RITC polymer, illustrating the hydrophobic corona phase anchors and the hydrophilic chain connection. (C) Schematic of a RITC-PEG-RITC configuration on the SWCNT surface, with the hydrophobic corona phase anchors preferentially adsorbed to the hydrophobic SWCNT surface and the hydrophilic chain extending out into solution.

eters determined independently from molecular simulation. The SWCNT curvature is found to contribute weakly to the overall interaction energy, exhibiting no correlation for three of the corona phases considered, and differences of less than 5% and 20% over a larger curvature range for two other corona phases, respectively. Overall, the resulting model is able to correctly predict 83% of an experimental 374 analyte-polymer library, generating experimental fluorescence responses within 20% error of the experimental values. The modeling framework presented here represents an important step forward in the design of suitable polymers to target specific analytes.

5.2 Introduction

Corona Phase Molecular Recognition (CoPhMoRe) is an emerging experimental platform for the detection of various small molecules by engineering the adsorbed phase on single-molecule fluorophores such as Single-Walled Carbon Nanotubes (SWCNTs). Examples of experimentally-studied adsorbed phases on SWCNTs include single-stranded DNA [217, 269], small molecule surfactants such as sodium dodecyl sulfate (SDS) or sodium cholate (SC) [131], and complex polymers with various hydrophobic and hydrophilic regions [271], as illustrated in Figure 5-1. Specific small molecules can induce changes in the corona phase of the SWCNT, modulating the fundamental fluorescence signal of the SWCNT and providing experimentally-detectable fluorescence. In many cases, target analytes replace part of the corona phase, leading to a change in the local environment of the SWCNT and changing the

SWCNT fluorescence efficiency, as evidenced by single-molecule imaging studies [269] and simulations of the adsorption process [153]. The selectivity and response of the sensors to specific molecules is determined by the specific corona phase. From an applied standpoint, CoPhMoRe allows for the development of highly-selective sensors [13, 131] without relying upon known biological recognition sites, such as antibodies or aptamers.

Experimentally, changes in the corona phase have been shown to modulate the band gap fluorescence of the SWCNT in the near-infrared (870-1400 nm, nIR) [193]. Mechanisms for this include solvatochromism [42], exciton quenching [219], and bleaching of valence-band electrons [192]. Accordingly, SWCNTs have been used as biological sensors for β-D-glucose6, nitric oxide [269, 131], and the protein avidin [219], among many others. SWCNTs have advantages as sensors, especially for biological applications, since near-infrared fluorescence excitation and emission do not overlap with the natural auto-fluorescence or absorption of cell media, blood, or tissue. SWCNTs also have photo-stable emission [193, 218]; and single-molecule sensitivity to certain analytes of interest [269, 45, 116, 117, 231, 230]. Hence, they are an ideal platform for the study of the CoPhMoRe mechanism. The prospect that other nanoparticle surfaces can exhibit CoPhMoRe remains an open question.

The selectivity of adsorbed phases to specific target molecules has been studied experimentally but is poorly understood and not easily predicted, motivating this work. The corona phase can interact with a target molecule through several mechanisms, including steric hindrance [269], van de Waals interactions, or electrostatic interactions [271]. Recent work explored this concept by screening fluorescence intensity changes of various polymer-SWCNT CoPhMoRe sensors against a panel of molecules [271]. Figure 5-1 illustrates one such CoPhMoRe sensor composed of an amphiphilic polymer with two hydrophobic rhodamine isothyocyanate (RITC) connected by a hydrophilic poly-ethylene glycol (PEG) chain ($\sim$5kDa in size). We refer to such a corona phase as RITC-PEG-RITC, with experimentally observed selective recognition to estradiol [271], a hormone molecule in the human body as shown in Figure 5-2. This particular example has been studied using molecular simulations [153]. The structures of the various corona phase polymers used in the present study are included in Figure 5-8. Changing the hydrophobic portion of the corona phase from RITC to fluorescein isothyocyanate (FITC), referred to as FITC-PEG-RITC, changes the recognition capabilities to a non-selective recognition profile [271], shown in Figure 5-2. The difference exhibited in the responses for the two corona phases is very interesting due to

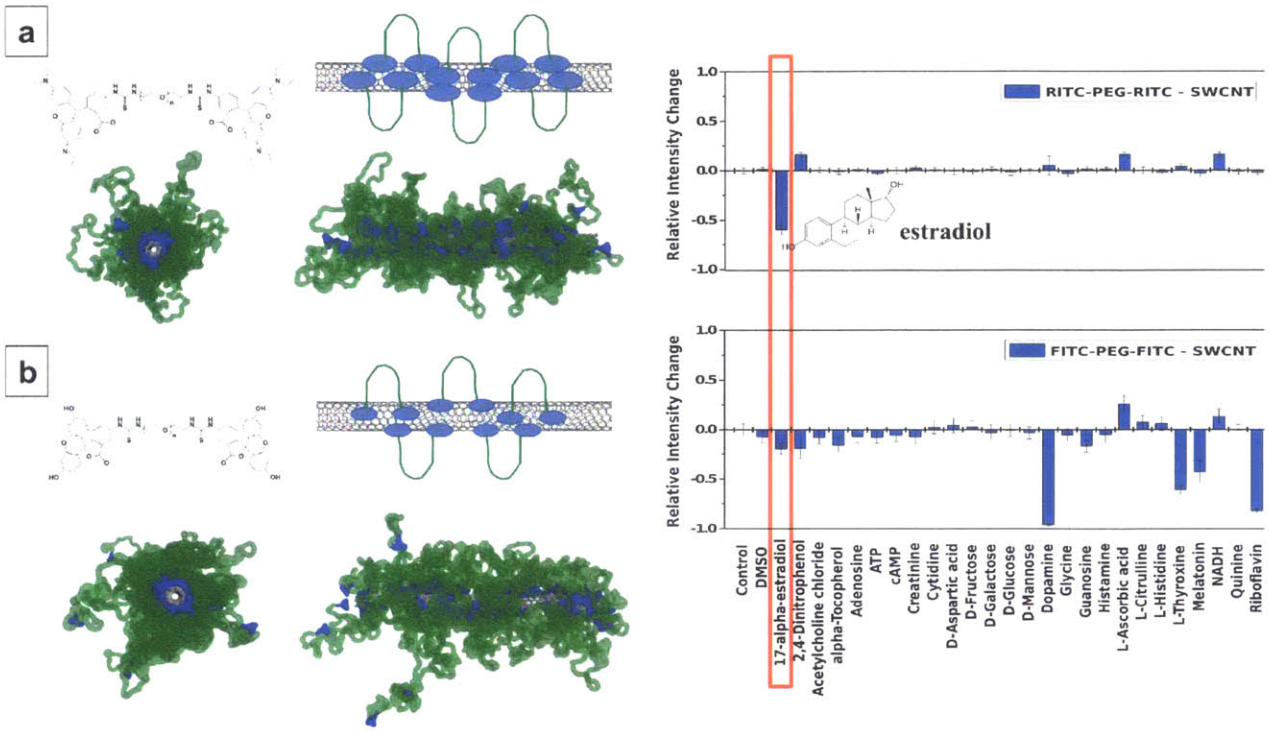

Figure 5-2: Structure and analyte-response profile of two CoPhMoRe sensors using polymer – SWCNT complexes. (a, b) Polymer structure, schematics of polymer-SWCNT complex, and front and side views calculated from coarse-grained MD simulation for (a) rhodamine isothiocyanate segments connected with polyethylene glycol (RITC-PEG-RITC), and (b) fluorescein isothiocyanate segments connected with polyethylene glycol (FITC-PEG-FITC). The schematics are deduced from a combination of polymer molecular structure and finger-printed response profile, supported by MD results. (c, d) Bar charts that show intensity changes of RITC-PEG-RITC (c) and FITC-PEG-FITC (d) against a panel of 35 biological molecules. RITC-PEG-RITC shows selective quenching response upon addition of 100 μM estradiol, but FITC-PEG-FITC shows a non-selective response profile.

their structural similarities, and demonstrates the need for detailed thermodynamic models and simulations.

In this work, we introduce the first comprehensive thermodynamic model for CoPhMoRe sensors where competitive adsorption at the SWCNT interface is dominant. We develop a simple, albeit practical, theoretical platform that is able to describe the adsorbed phase created by a large library of polymer-SWCNT constructs, and to provide insight on the distinct fluorescence responses. The predictions of this platform are compared to previous semi-empirical models of small-molecule adsorption on carbon materials. Finally, the influence of the SWCNT chirality on model predictions is investigated, an important consideration for developing multi-functional sensors using multiple SWCNT chiralities with

different corona phases.

5.3 Theory

5.3.1 Structure of Corona Phase Molecular Recognition Sensors

Understanding the selectivity of CoPhMoRe sensors towards analytes requires an understanding of the structure of the corona phase on the nanoparticle of interest, including how such a phase is influenced by target analytes. Predicting the structure of an arbitrary adsorbed corona phase on nanoparticles is an unsolved problem in the literature. Despite many advances in the capabilities of molecular simulations, the large systems sizes (well over 100,000 atoms) and long time scales (microseconds) required to equilibrate the adsorption of the long (>5 kDalton) polymer chains used to construct the corona phases in recent work [271] makes such an approach currently computationally prohibitive. Furthermore, deriving accurate force fields for arbitrary polymers is an active research area, making the accuracy of such simulations difficult to gauge. Other approaches have been attempted in the literature to model polymer chains attached to various surfaces using statistical polymer theories1 [193, 179, 203], Monte Carlo simulations [83, 84], or the adsorption of larger diblock copolymers [182], but these do not provide the molecular description of the surface necessary to determine if small-molecule analytes can adsorb. Most literature efforts to simulate SWCNT corona phases have therefore focused on scenarios with established parameter sets, including DNA adsorbed on a SWCNT [217, 276, 175, 169, 119, 216, 266], or the adsorption of small molecules like surfactants [152, 264, 11, 258], or coarse-grained block copolymers [227, 189]. Even in these limited cases, it is difficult for these studies to reach the timescales necessary to reach full adsorption equilibrium, requiring making assumptions about the coverage of molecules on the surface. Most importantly, these studies do not describe the wide range of corona phases that have been created experimentally [271].

For a class of studied corona phases, constructed with amphiphilic polymers composed of hydrophobic anchors tethered together with hydrophilic chains, the resulting polymer corona phase is much simpler to model. Figure 5-1 illustrates one example of such a polymer: hydrophobic rhodamine isothiocyanate (RITC) molecule connected with a hydrophilic poly-ethylene glycol (PEG) chain. Molecular dynamics simulations confirm that the hydrophobic RITC molecules form a corona phase on the SWCNT surface, while the PEG

chains loop out into solution. Sufficiently hydrophobic anchors will adsorb directly to the hydrophobic SWCNT surface, and the hydrophilic connections will extend out into solution. The corona phase directly adsorbed at the SWCNT surface is therefore composed entirely of the adsorbed hydrophobic anchors. For analytes to influence the SWCNT fluorescence, some of these hydrophobic anchors must be removed and replaced with analyte molecules, a process that does not require knowledge of the hydrophilic polymer structure. This process can be observed and confirmed experimentally by attaching small-molecule fluorophores to the corona phase-polymers that quench in close proximity to the SWCNT. Introducing target analytes causes both the quenching of the SWCNT and the restoration of the fluorophore emission, suggesting that part of the original corona phase has detached from the SWCNT surface [271]. Furthermore, changing the length of the hydrophilic part of the polymer does not dramatically affect the recognition selectivity of the sensor [271]. This scheme motivates focusing solely on the hydrophobic anchor regions of the corona phase competing with analyte molecules for access to the SWCNT surface, and the assumption of negligible selectivity contribution from the hydrophilic polymer regions. This process can be modeled thermodynamically as competitive adsorption of the hydrophobic anchors and the analytes of interest onto the SWCNT surface.

5.3.2 Thermodynamic Model of Competitive Adsorption at the Hydrophobic SWCNT Surface

We model the competitive adsorption of corona phase aanchors and analytes onto the SWCNT surface using a 2D equation of state developed previously for surfactant adsorption at air-water interfaces [180]. That model accounted for the thermodynamic equilibrium between surfactant molecules adsorbed at the air-water interface and those present in the bulk aqueous solution. The same model is used here to describe the competitive adsorption of the hydrophobic polymer anchors and analyte molecules onto the SWCNT surface, as illustrated in Figure 5-3. The SWCNT is treated as a single layer of graphene, essentially neglecting the curvature effects to further simplify the problem. This is reasonable, because for each polymer, multiple SWCNT chiralities show similar responses (although the extent of each response may vary). Note that the neglect of curvature effects is investigated below through the study of the curvature dependence for a small number of representative corona phases and analytes.

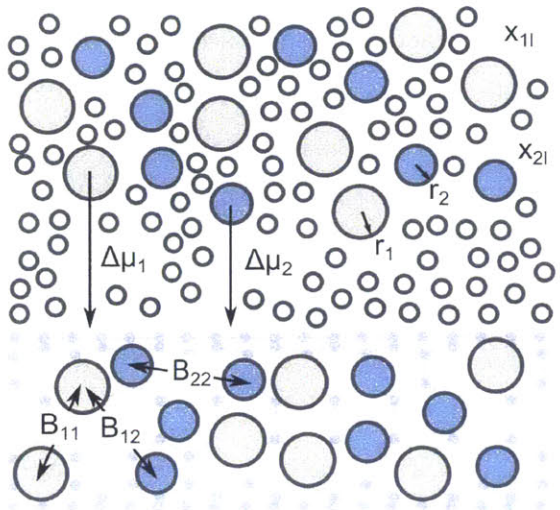

Figure 5-3: Equilibrium of polymer "anchors" (**1**) and the analyte molecules (**2**) adsorbing on the SWCNT surface. Each species on the surface is in thermodynamic equilibrium with the same species in the bulk solution.

We designate species 1 as the polymer anchor and species 2 as the analyte molecule. The fractional surface coverage of each species is designated by θ_i. Adsorbing molecules are modeled as adsorbing hard discs with molecular radius r_i and area a_i, in equilibrium with a bulk monomer with molar fraction x_i^b. The free-energy difference between molecules on the surface and in the bulk is controlled by the standard-state adsorption free energy $\Delta\mu_i^0 = \mu_i^{\sigma,0} - \mu_i^{b,0}$, the van der Waals interactions between molecules on the surface (captured with the second-order virial coefficient B_{ik}), and the hard-sphere interactions with other molecules on the surface. Note that B_{11} and B_{22} describe the self-interactions of the molecules, whereas B_{12} (and equivalently B_{21}) describe interactions between the analyte and the corona phase anchors. Electrostatic effects could be considered in future work with an enhanced understanding of the corona phases dielectric properties.

Thermodynamic equilibrium between the analytes in the bulk solution and at the air-water interface is described by the following equation of state:

$$\ln\left(x_i^b\right) = \frac{\mu_i^{\sigma,0} - \mu_i^{b,0}}{k_B T} + \ln\left(\frac{x_i^s}{a - \sum_k x_k^s a_k}\right) + \frac{a_i + 2\pi r_i \sum_k x_k^s r_k}{a - \sum_k x_k^s a_k} + \frac{\pi a_i \left(\sum_k x_k^s r_k\right)^2}{\left(a - \sum_k x_k^s a_k\right)^2} + \frac{2}{a}\sum_k B_{ik} x_k^s, \tag{5.1}$$

$$\{1\} = \quad \{2\} \quad + \quad \{3\} \quad + \quad \{4\} \quad + \quad \{5\} \quad + \quad \{6\} \tag{5.2}$$

where x_i^s represents the molar fraction of species i on the surface, a is the area occupied per adsorbed surfactant molecule, $\Delta\mu_i^0 = \mu_i^{\sigma,0} - \mu_i^{b,0} = f\left(D^{\mathrm{SWCNT}}\right)$ defines the standard-state chemical potential difference of surfactant molecules of type i at the surface and in the bulk solution and is potentially a function f of the SWCNT diameter D^{SWCNT}. Although this EOS does not explicitly consider surface curvature, the possible curvature dependence of the adsorption free energy is investigated below and found to be weak. Equation 5.2 describes a simple thermodynamic equilibrium between the solution phase (left-hand side, LHS) and the surface phase (right-hand side, RHS). On the LHS, term {1} is the ideal (entropic) solution chemical potential contribution. On the RHS, term {2} is the empty-surface adsorption free energy, term {3} is the entropic chemical potential contribution for the surface configuration, terms {4} and {5} account for the hard-sphere repulsions of the molecules adsorbed on the surface, and term {6} represents the van der Waals interactions between the molecules adsorbed on the surface. It is important to note that the units for the $\ln\left(\frac{x_i^s}{a-\sum_k x_k^s a_k}\right)$ term are accounted for by an adjustment of $\Delta\mu_i^0$ by approximately 6 kcal/mol, corresponding to the units of square angstroms for the molar surface area $a44$. The system of equations in 5.2 represents one equation for each species present – in our case, two species - with the additional constraint that all molar fractions must add to unity, that is, that $\sum_i x_i^s = 1$. Specifically, the following three equations apply:

$$\ln\left(x_1^b\right) = \frac{\Delta\mu_1^0}{k_B T} + \ln\left(\frac{x_1^s}{a-\left(x_1^s a_1 + x_2^s a_2\right)}\right) + \frac{a_1 + 2\pi r_1\left(x_1^s r_1 + x_2^s r_2\right)}{a-\left(x_1^s a_1 + x_2^s a_2\right)} + \tag{5.3}$$

$$\frac{\pi a_1 \left(x_1^s r_1 + x_2^s r_2\right)^2}{\left(a-\left(x_1^s a_1 + x_2^s a_2\right)\right)^2} + \frac{2}{a}\left(B_{12} x_2^s + B_{11} x_1^s\right), \tag{5.4}$$

$$\ln\left(x_2^b\right) = \frac{\Delta\mu_2^0}{k_B T} + \ln\left(\frac{x_2^s}{a-\left(x_1^s a_1 + x_2^s a_2\right)}\right) + \frac{a_2 + 2\pi r_2\left(x_1^s r_1 + x_2^s r_2\right)}{a-\left(x_1^s a_1 + x_2^s a_2\right)} + \tag{5.5}$$

$$\frac{\pi a_2 \left(x_1^s r_1 + x_2^s r_2\right)^2}{\left(a-\left(x_1^s a_1 + x_2^s a_2\right)\right)^2} + \frac{2}{a}\left(B_{21} x_1^s + B_{22} x_2^s\right), \tag{5.6}$$

$$1 = x_1^s + x_2^s, \tag{5.7}$$

Equations 5.4, 5.6, and 5.7 need to be solved simultaneously for the three unknowns: the surface mole fractions x_1^s, x_2^s on the SWCNT, and the average area per molecule, a. The bulk molar fractions x_1^b, x_2^b are known from our experiments. For surfactants such as SDS and SC, bulk solutions were prepared with total surfactant concentrations above the critical micelle concentration (CMC), such that the monomer concentrations x_{li} are approximately equal to

the CMC. Molecular volumes for each molecule are accessible using either experimentally-determined parameters from the van der Waal equation of state, or estimated from the molecular structure (using VMD and default van der Waals radii). r_i and a_i are computed using molecular volumes under the assumption that the molecules are spherical. B_{11}, B_{22}, B_{12}, and $\Delta\mu_1^0, \Delta\mu_2^0$ can be estimated using molecular simulations, as discussed below.

5.3.3 Adsorption Free-Energy Estimates Using Molecular Simulations

It then follows that for each pair of polymer and analyte, we can solve for (x_1^s, x_2^s, a) given the parameters $(r_1, r_2, a_1, a_2, B_{11}, B_{12}, B_{22}, \Delta\mu_1^0, \Delta\mu_2^0)$ by solving simultaneously Eqs. 5.4, 5.6, and 5.7. Once (x_1^s, x_2^s, a) are determined, the analyte surface coverage θ_{cal} is calculated as follows:

$$\theta_{cal} = \frac{a_2 x_2^s}{a}. \tag{5.8}$$

To calculate the analyte surface area θ_{cal}, it is necessary to estimate $\Delta\mu_1^0, \Delta\mu_2^0, B_{12}, B_{11}, B_{22}$, which were computed using a series of all-atomistic molecular dynamics simulations. The simulations were run in the software NAMD, with CHarMM. Force-field parameters for the sp2-carbon atoms in nanotube/graphene were obtained from previous work [262], and parameters for the large variety of analytes and polymers considered were obtained automatically by the CGenFF force field (version 2b7 and parameterization tool version 0.9.6) [253, 254, 252]. The tool compares the molecule of interest with existing molecules in the database, searching for the most accurate parameters for the simulation. However, the CGenFF force field was unable to automatically type some of the molecules considered in this study, which include one analyte molecule, sodium azide, and two wrapping "anchors", boronic acid, and $d(GT)_{15}$ single-stranded DNA. Because sodium azide was not observed experimentally to quench the SWCNTs [271], it was excluded from the results presented here. We also did not include $d(GT)_{15}$ single-stranded DNA, since DNA is not handled by CGenFF and instead needs to be modeled using existing biological parameter sets (i.e., established CHarMM parameter sets). In addition, DNA has been shown to wrap SWCNTs in a way that nearby bases interact strongly through the helical structure, so adsorbed bases are not adsorbed independently [217, 169, 119]. DNA would thus not be well-characterized using this thermodynamic model. CGenFF does not currently support molecules with boron

atoms, and therefore, for boronic acids, we approximated the boron atom using nitrogen. In many cases, the CGenFF analogy was poor, but the molecular parameters were used as a first approximation. It should be noted that such methods represent the current state-of-the-art for automatic parameterization methods of small-molecule organic compounds. Planned improvements to the CGenFF methods, such as automatic refinement with supplemental quantum mechanical simulations, will allow for more accurate simulations.

The free energy of adsorption, $\Delta\mu_i^0$, was computed using an adaptive biasing force simulation in NAMD. Specifically, the molecule of interest was placed in between two (3nm x 3nm) graphene sheets (corresponding to SWCNTs with no curvature) at a 6 nm separation, with periodic boundary conditions in all directions (Figure 5-4a). TIP3P water molecules then solvated the system, which was taken from an equilibrated water sample at room temperature and a pressure of 1 bar, and excess charge in the system was neutralized with counterions (Na^++ or Cl^-) depending on the simulation (with no set overall NaCl concentration). The system was then equilibrated under the NVT ensemble at room temperature for another 100 ps. The potential of mean force for the molecule of interest between the two graphene sheets was then computed using an adaptive biasing force (ABF) simulation [51, 94], allowing the molecule to freely move. The potential of mean force was expected to converge when it became nearly symmetric (due to the symmetry of the system), and the energy minimum near the graphene surface was sufficiently resolved (Figure 5-4c). The full simulation details are provided in section 5.5. The calculated adsorption free energies,$\Delta\mu_i^0$, are summarized in Table 5.1. Molecules with more aromatic groups tend to have higher adsorption energies. This is due to an optimal alignment of the aromatic group with the SWCNT hexagonal lattice. This effect, an affinity between aromatic groups, is normally referred to as $\pi - \pi$stacking, although in this simulation is not explicitly due to overlap in electronic structure.

Calculating adsorption energies in between two graphene sheets rather than on SWCNTs was preferable due to the simpler simulation geometry, faster convergence, and reduced number of simulations. This simplification was tested for five of the molecules which were shown experimentally to participate in selective detection, RITC, FITC, estradiol, riboflavin, and FMOC, by performing similar adsorption simulations onto SWCNTs of various chiralities corresponding to diameters between 0.7 and 1.8 nm, in a TIP3P water box of 5nm x 5nm cross section, and length of approximately 5nm corresponding to the nearest mul-

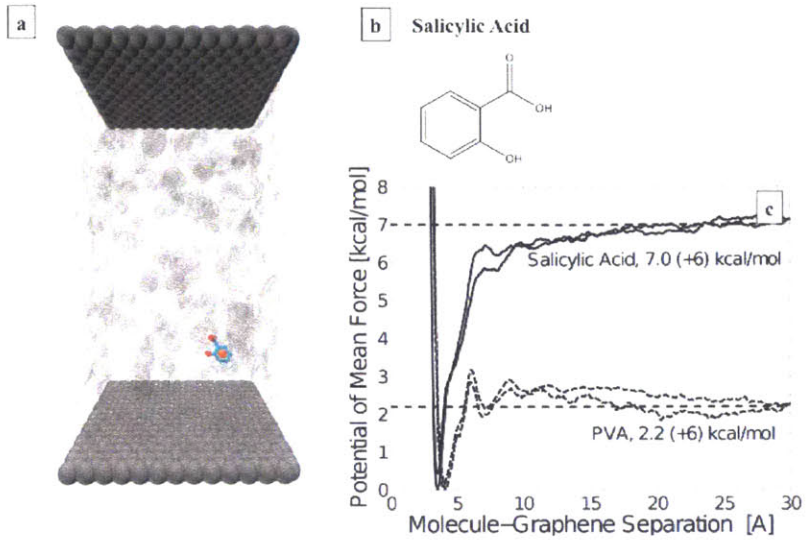

Figure 5-4: Molecular simulation of the molecules of interest. (a) Simulation cell of a salicylic acid molecule surrounded by water in between two graphene sheets. (b) The chemical structure of salicylic acid. (c) Two examples of a $\Delta\mu_i^0$ calculation: $\Delta\mu_i^0$ calculated from the simulation as a function of distance from the graphene surface for salicylic acid, and PVA.

tiple of the SWCNT unit cell for each chirality. Simulation convergence was worse than for the graphene simulations, resulting in only a modest number of simulations with significantly higher variance in the calculated adsorption energy, shown in Figure 5-8. Two of the molecules, RITC and riboflavin, had adsorption free energies that correlated significantly ($p>0.95$) with SWCNT diameter, with a range of approximately 6 kcal/mol between the smallest and the largest diameters, and approximately 3 kcal/mol between moderate diameter SWCNTs and those closest to the zero-curvature limit of graphene. The high computational cost for these simulations made a treatment of this type impractical for all the molecules considered in the current study, but could be plausible for future studies with greatly increased computational resources.

The adsorption free energies calculated correlate favorably with previous studies of organic small-molecule adsorption from water onto heterogeneous activated carbon surfaces based on Quantitative Structure-Activity Relationship (QSAR) methods [213, 270, 53]. Activated carbon surfaces have a distribution of pore sizes and adsorption sites, and therefore, increasing solution concentrations allows for adsorption to higher energy sites, in contrast to our thermodynamic model which relates solution concentrations to surface coverage for a uniform surface. The quantum QSAR method empirically predicts the solution concentra-

tion, $\log(C_E)$, in equilibrium with a commercial activated carbon filter. This concentration implies a free-energy difference between small molecules in the bulk solution and those adsorbed on the activated carbon surface as described in the Polanyi adsorption theory [206, 168]:

$$\Delta\mu^{\text{eff}} = RT \ln \frac{C_s}{C_e}, \tag{5.9}$$

where $\Delta\mu^{\text{eff}}$ is the effective free-energy difference, $C_s$is the saturation concentration, and $C_e$is the predicted solution concentration as described above. This free-energy difference is not identical to the adsorption free energy calculated separately in this work, which represents the adsorption free energy onto an empty pristine graphene surface, but is nevertheless strongly correlated to it, because both reflect adsorption onto graphitic surfaces. Therefore, the quantum QSAR approach, relating experimental loadings of small molecules onto a commercial activated carbon surface to quantum-mechanical calculations of the molecular polarizability α, the HOMO-LUMO band-gap energy, and the mean atom charge, was used to independently verify the predictions in this work. The isotropic polarizability and HOMO-LUMO bandgap were calculated for 43 of the CoPhMoRe anchors and analytes considered in this study using Gaussian 09 at the DFT-B3LYP/6-311g(d) level. Two molecules were excluded due to computational limitations (NADH, acetylcholine chloride), and L-thyroxine could not be treated without an additional basis set for the iodine atom. The saturation concentrations of each analyte/anchor in water were taken from literature studies or from estimates from commercial samples, as indicated in Table 5.5. Figure 5-5 compares this effective partition free energy to the adsorption chemical potential deduced from our MD studies, and a correlation is observed between the two. The variance observed in the correlation is similar to the variation observed between predictions from different QSAR methods for activated carbon [270].

5.3.4 Estimation of van der Waals Interactions using Molecular Simulations

B_{ik} captures the van der Waals interactions between molecules i and k, or self-interactions, and is defined as a correction to the hard-sphere model of intermolecular interactions. B_{ik}

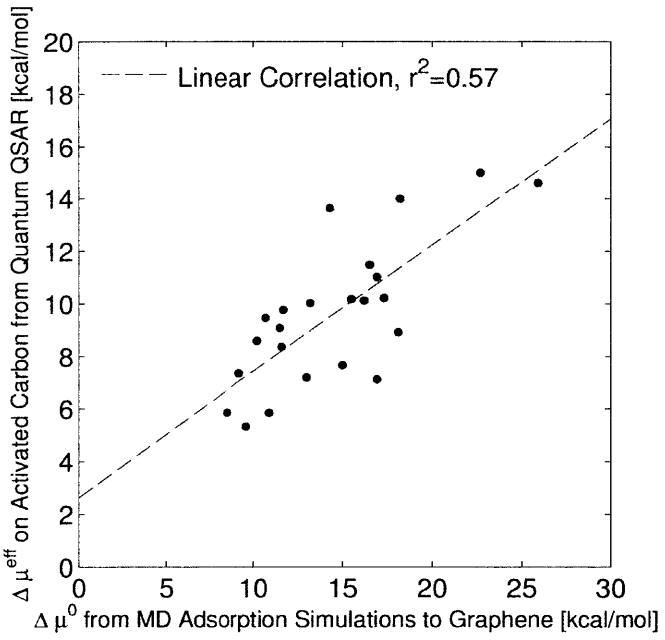

Figure 5-5: Comparison of the free energy of adsorption calculated from molecular dynamics simulations, $\Delta\mu^0$, with the effective partition free energy between solution and a commercial activated carbon filter, $\Delta\mu^{eff}$, as listed in Table 5.5. A linear correlation is included as a guide. The indicated r^2 value is similar to that observed during the fitting of the QSAR model and the experimental data [53].

is defined [191] as follows:

$$B_{ik} = \pi \int_{r_i+r_k}^{\infty} \left[1 - \exp\left(-\frac{u_{ij}(r)}{kT}\right)\right] r dr, \tag{5.10}$$

where $u_{ik}(r)$is the interaction energy between molecules i and k relative to infinite separation (no interaction), and r_i, r_k are the appropriate hard-sphere radii given above. Note that $u_{ik}(r)$ is affected by the environment, because the ensemble average of the potential at a given distance depends on the local environment and water solvation (making certain molecule-molecule orientations more or less likely). However, as a first approximation to these parameters, we calculated the energy between various molecules in vacuum for distances ranging from 3Å to 100Å for a single set of molecular orientations using the same CHarMM/CGenFF force-field parameters as above. The resulting B_{ik} parameters are summarized in Table 5.3. Future work is necessary to compare the potential curves measured in this way to those obtained from solvated simulations. Parameters including r_i, a_i, and B_{12} are provided as Tables 5.2, 5.3, and 5.4.

5.3.5 Model Behavior after Complete Adsorption or Desorption of the Corona Phase

If one of the species adsorbs at the interface much more strongly than the other, computationally, this results in $(x_1^s \approx 1, x_2^s \approx 0)$or $(x_1^s \approx 0, x_2^s \approx 1)$. The latter case indicates that it is possible that addition of analytes replaces the corona phase anchors almost completely on the SWCNT surface. Experimentally, this indicates that the SWCNT suspension would be no longer stable, and aggregates would form in solution. However, this was not observed experimentally. In our model, we treated corona phase anchors as individual molecules, and as if they are not connected by the backbone of the polymer. Therefore, if adsorption of certain analytes is predicted to be much stronger than that of the corona phase anchors, the model indicates that the anchors are expected to be pushed off the SWCNT surface. Single-molecule imaging of SWCNTs during adsorption events confirms that this is the case for some systems, such as FITC and RITC anchors connected by long PEG chains [271]. However, polymer wrappings with more anchors per unit length would exhibit a kinetic trapping phenomenon, since the desorption of nearby anchors is correlated, rather than independent as assumed in this model. In other words, the model here does not account for

this kinetic-trapping effect of the polymer in some cases. In those extreme situations where either ($x_1^s \approx 1, x_2^s \approx 0$)or ($x_1^s \approx 0, x_2^s \approx 1$)is predicted by the model, we compared values of $\frac{a_1}{a}$ of the polymer anchor and the competing analyte, assuming that only one of them is present in the bulk, and then selected the one with the larger value to be the species present on the SWCNT surface. This criterion is consistent with the adsorption free-energy calculations shown in Figure 5-4. In other words, when the model predicts that the "anchors" of the polymers completely desorb from the surface as a result of strong analyte binding, we simply consider ($x_1^s = 1, x_2^s = 0$) to avoid numerical problems in the calculation.

5.3.6 Experimental Fitting of the Analyte Quenching Coefficient

The optical fluorescence modulation (intensity increase or decrease) of a SWCNT sensor shown in Figure 5-2 ($\Delta I/I_0$) is approximately proportional to the analyte coverage on the SWCNT surface, θ, that is,

$$\frac{\Delta I}{I_0} = \beta\theta, \tag{5.11}$$

where β is the coefficient that correlates the relative intensity change of the SWCNT fluorescence to the surface coverage of a specific analyte-polymer pair. Adsorption of certain analytes modulates the photoemission of the SWCNT to a greater extent than others, leading to a more significant optical change and to a larger value ofβ. The mechanisms of how analytes modulate SWCNT fluorescence have been described by three major routes: bleaching of valence-band electrons [13, 192], quenching of excitons [219], and solvatochromism [42]. Ideally, for the first two mechanisms, β can be estimated by calculating the overlap between the density of states of the SWCNT and the molecular orbitals and vibrational states of the analyte molecule [170, 96]. The electronic states of those molecules can potentially be estimated from density functional theory. However, SWCNTs are exitonic in nature, and therefore, the actual calculation of β will in fact involve proper estimation or measurement of the excited-state lifetime [235], which is corona phase dependent. In addition, the polymer wrapping also fundamentally affects the redox level of the SWCNT53, complicating the estimation of β. In practice, there is no way to readily estimate β with confidence. Therefore, we experimentally determined the value of β once, assuming that it is unique to each analyte and is polymer-independent. Specifically, we chose two reference

polymers, polyvinyl alcohol and FITC-PEG-FITC (Figure 5-2), a combination which provides a relatively complete response profile for all the analytes in our library. We used a response-weighted estimate, that is,

$$\overline{\beta} \equiv \frac{\beta_{PVA}(\Delta I/I_0)_{PVA} + \beta_{FITC-PEG-FITC}(\Delta I/I_0)_{FITC-PEG-FITC}}{(\Delta I/I_0)_{PVA} + (\Delta I/I_0)_{FITC-PEG-FITC}}, \tag{5.12}$$

since a large intensity response is a more reliable indicator of β. The value of β was only computed once using the two reference polymers, and all other polymer-SWCNT construct predictions used this same estimated β. Calculated values of β for each of the corona phase polymers are included as Table 5.3.

5.3.7 Model Comparison to Literature Experimental Data

The accuracy of the model was tested by comparing the model response $\beta\theta_{cal}$ to the experimental fluorescence modulation for a library of analytes and SWCNT wrappings [271], shown in Figure 5-6. Using this model, 83% of the fluorescent responses (374 data points) were predicted to within 20% error of their experimental values (purple area in Figure 5-6). However, for a small subset of cases (3.7%, grey area in Figure 5-6), the model was found to underpredict the experimental intensity modulation by more than 20%. Therefore, our 2D EOS-based model captures the physics underlying the competitive adsorption between the analytes and the corona phase anchors reasonably well, and represents the first fully-predictive model for this type of problem. Previous simulation efforts were able to capture the interactions between the corona phase and analyte molecules with higher resolution using coarse-grained molecular dynamics [153], but due to the high computational costs, were only able to do so for a single corona phase and under an assumed non-equilibrium surface coverage.

A further test of the model is its ability to model the adsorption isotherm of the analyte, illustrated in Figure 5-7. Binding isotherms of estradiol to RITC-PEG-RITC and of L-thyroxine to Fmoc-Phe-PPEG8 are shown in Figure 5-7, where we were able to fit the isotherm with our model using B12 and β as fitted parameters.

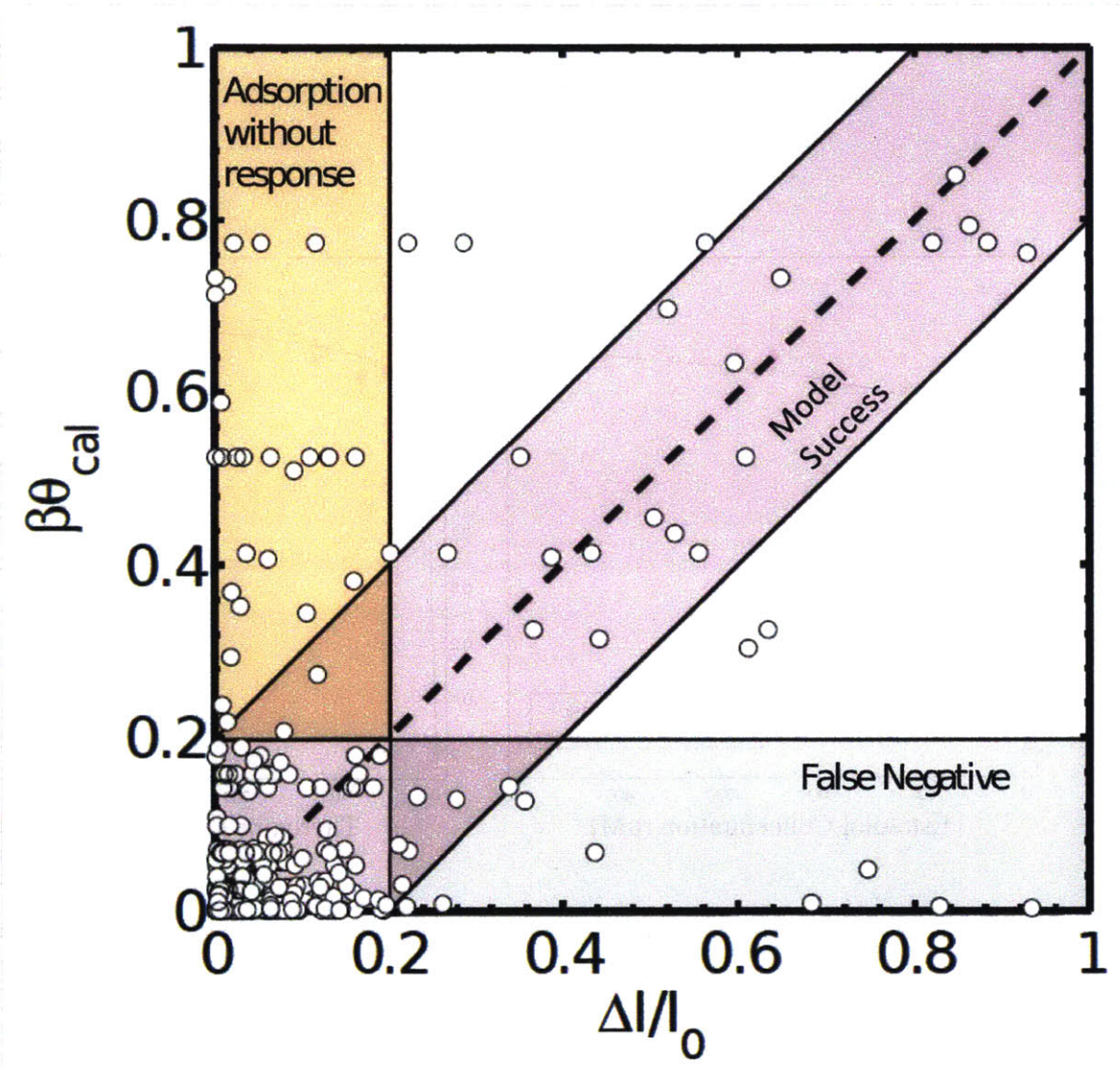

Figure 5-6: Calculated intensity of fluorescent response, $\beta\theta_{cal}$, as a function of experimental intensity modulation, $\Delta I/I_0$, for 11 distinct CoPhMoRe phases responding to a library of 34 analyte molecules. The purple region indicates that modeled responses are within 20% error of the actual responses, which accounts for 83% of the total number of polymer-analyte trials. Orange indicates the "false positive" region (13.1%), where the model overpredicts over 20%. Gray indicates gray the "false negative" region (3.7%), where the model underpredicts the response more than 20%.

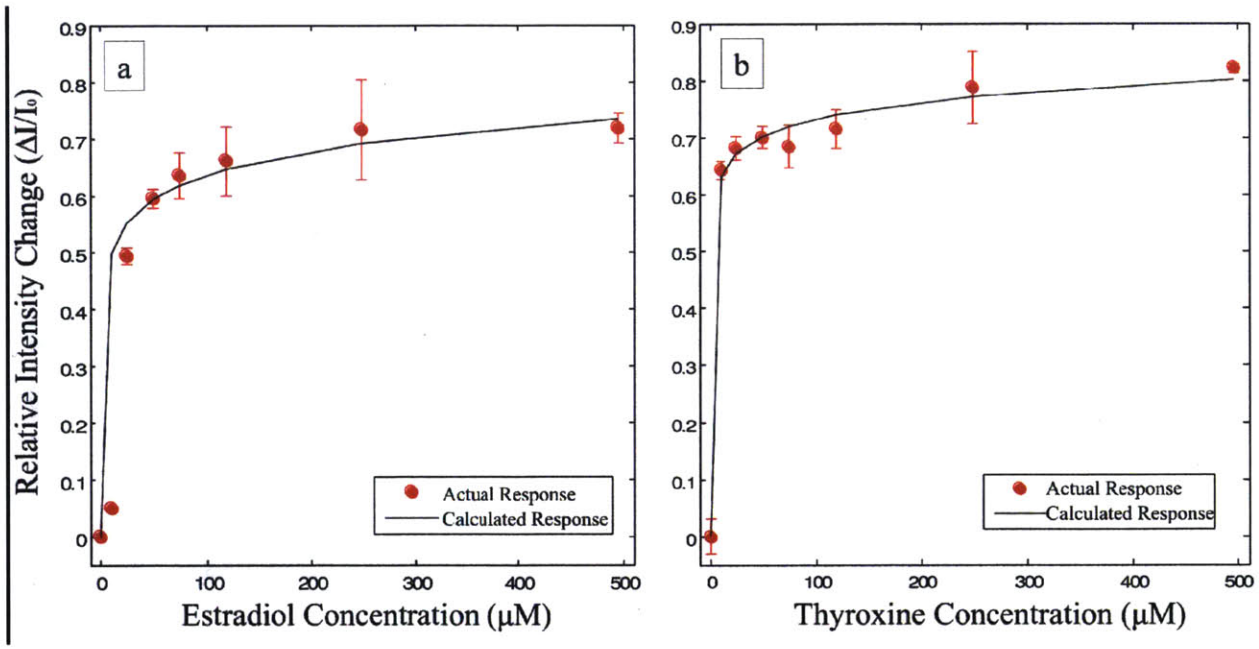

Figure 5-7: Comparison between calculated and experimental CoPhMoRe adsorption isotherms (a) Fluorescence quenching of (7,5) chirality of RITC-PEG-RITC – SWCNT as a function of estradiol concentration (red). The dashed black lines are fits of the data to the 2D EOS model with β=1 and B_{12} of -400 Å^2. (b) Fluorescence quenching of (7,5) chirality of Fmoc-Phe-PPEG8 – SWCNT as a function of thyroxine concentration (red). The dashed black lines are fits of the data to the surface-adsorption model with β=3.2 and B_{12} of -1150 Å^2. Data were taken with three replicates, and error bars are 2 standard deviations.

5.4 Conclusion

Future work is necessary to extend our thermodynamic model to more accurately reproduce the experimental findings, and to improve the accuracy of the necessary molecular parameters through more detailed simulations. Further consideration should be given to the effect of hydrophilic connections between the corona phase anchors, which inhibit the free adsorption of the anchors onto the SWCNT surface. In some cases, the assumption of a molecular monolayer on the SWCNT surface may not be accurate, especially if the polymer chains are able to hinder analyte access to the SWCNT surface. In addition, the force-field parameters used here were determined automatically through CGenFF, and require further refinement and verification. Finally, we anticipate that the evaluation of β using quantum-mechanical calculations may be possible in the future, and that doing so would allow the model to be fully predictive (i.e., without an experimental determination of β from two reference polymers). Experimental advances in understanding and imaging the structure of CoPhMoRe phases would also assist in developing models that have a stronger molecular basis.

5.5 Simulation Details

5.5.1 Adsorption Energy Calculations

The workflow for the calculation of the adsorption energy of the various small molecule analytes to graphene surface, as described in the manuscript, was as follows:

1. The small molecule PSF/PDB was generated in accordance with the CGenFF/Paramchem.

2. A single copy of the small molecule was placed at the centerline between two parallel graphene sheets (size 30 angstroms by 30 angstroms). The graphene sheets were 60 angstroms apart. The simulation cell was set to be periodic in the X and Y directions (the directions of the graphene sheet). The cell was also periodic in the Z direction (perpendicular to the sheets), but with a cell distance of 150 angstroms so that 90 angstroms of vacuum separated each unit cell from the next in the periodic Z direction.

3. The simulation cell was solvated using the default settings in the VMD solvate plugin. Ions (Na or Cl) were added to neutralize the simulation cell if the small molecule analyte was charged.

4. The simulation cell was minimized for 100ps in an NVT ensemble with a 1fs time step, with the temperature set to 300 K. The position of the graphene atoms were fixed to preserve the hexagonal lattice.

5. The simulation was run using an adaptive biasing force on the z-position of the center of mass of the small molecule for 24hrs on NICS/Kraken using 24 cores (two nodes) in an NPT ensemble. Various lower-bounds on the ABF were used (from 3 to 4.5 angstroms) to prevent the simulation spending too much time resolving the highly repulsive potential as the molecule was pushed against the graphene surface. The position of the graphene atoms were fixed.

5.5.2 Radial Adsorption Energy Calculations

The workflow for the calculation of adsorption energy of the various small molecule analytes to single-walled carbon nanotubes with various chiralities, as described in the manuscript, was as follows:

1. The small molecule PSF/PDB was generated in accordance with the CGenFF/Paramchem.

2. A single-walled carbon nanotube of approximately 50 angstroms with the appropriate chirality was generated. The length was approximate, as an integer number of unit cells was necessary to have a periodic cell.

3. A single copy of the small molecule was placed 15 angstroms radially from the SWCNT surface (measured from the center or mass of the SWCNT to the center of the small molecule).

4. The simulation cell was set to be periodic in all directions. The unit cell length in the X/Y directions (perpendicular to the SWCNT) were set to 50 angstroms, and the cell length in the SWCNT direction was set to the SWCNT length plus one angstrom.

5. The simulation cell was solvated using the default settings in the VMD solvate plugin, to a final size of 50 angstroms in the X/Y directions. Ions (Na or Cl) were added to neutralize the simulation cell if the small molecule analyte was charged.

6. The simulation cell was minimized for 100ps in an NVT ensemble with a 1fs time step, with the temperature set to 300 K.

7. The simulation was run using an adaptive biasing force on the radial position of the center of mass of the small molecule for 24hrs on NICS/Kraken using 24 cores (two nodes) in an NPT ensemble, resulting in a total simulation time of approximately 15ns. The lower-bounds on the ABF wasset to the SWCNT radius plus 4 angstroms to prevent the simulation spending too much time resolving the highly repulsive potential as the molecule was pushed against the graphene surface.

5.5.3 van der Waals Interaction Calculations

The workflow for the calculation of van der Waals interactions between small molecules and hydrophobic monomers was as follows. For each pair of analyte and anchor unit, and each analyte and anchor unit with themselves:

1. The two molecules were separated by distances from 2A to 30A (measured from the center of mass of each) using VMD.

2. The energy was calculated using the CGenFF forcefield in NAMD. The dielectric constant was set to 80 to simulate intermediate water. The cutoff for interactions was set to 100A to ensure that all interactions were captured even at large separations.

Table 5.1: Calculated standard-state chemical potential difference of surface adsorbed surfactant with bulk, $\Delta\mu_i^0$, for the corona-phase anchors and analytes in the library (the data highlighted in red is less accurate than the rest of the data due to convergence problems in the simulation).

$\Delta\mu_i^0\,(kcal/mol)$			
Corona Phase Anchors			
BA-PhO-Dex	12.7	SDS	18.0
PhO-Dex	11.6	PVA	8.8
RITC-PEG-RITC	16.0	Fmoc-Phe-PPEG8	15.3
FITC-PEG-FITC	15.6	Fmoc-Phe-PPEG4	15.3
PE-PEG	16.9	NH_2-PPEG8	8.1
SC	16.5		
Analytes			
17-alpha-estradiol	16.9	Histamine	10.7
2,4-Dinitrophenol	15.0	L-Ascorbic acid	13.2
Acetylcholine chloride	11.5	L-Citrulline	10.5
alpha-Tocopherol	25.9	L-Histidine	10.2
Adenosine	15.5	L-Thyroxine	15.4
ATP	22.7	Melatonin	20.3
cAMP	16.5	NADH	30.9
Creatinine	10.9	Quinine	18.2
Cytidine	16.0	Riboflavin	24.7
D-Aspartic acid	9.6	Salicylic acid	13.0
D-Fructose	11.5	Serotonin	14.0
D-Galactose	10.7	Sodium pyruvate	9.0
D-Glucose	11.7	Sucrose	14.3
D-Mannose	17.3	Thymidine	16.9
Dopamine	13.1	Tryptophan	16.2
Glycine	8.5	Tyramine	11.6
Guanosine	18.1	Urea	9.2

Table 5.2: r_i,B_{ii} values of analyte molecules and polymer "feet".

Chemical	r_i (Å)	B_{ii} (Å^2)	Chemical	r_i(Å)	B_{ii}(Å^2)
17-alpha-estradiol	4.55	-71.50	Melatonin	4.26	-92.20
2,4-Dinitrophenol	3.62	-42.80	NADH	4.95	-2715.10
Acetylcholine chloride	3.97	-32.20	Quinine	4.78	-327.90
alpha-Tocopherol	5.63	-103075.40	Riboflavin	4.84	-904.90
Adenosine	4.05	-1626.30	Salicylic acid	3.43	-34.60
ATP	4.66	-453.20	Serotonin	3.89	-42.70
cAMP	4.17	-520.30	Sodium pyruvate	2.94	-20.40
Creatinine	3.36	-38.90	Sucrose	4.35	-960.40
Cytidine	3.96	-139.00	Thymidine	3.99	-372.30
D-Aspartic acid	3.37	-41.40	Tryptophan	3.99	-47.60
D-Fructose	3.54	-125.70	Tyramine	3.67	-30.30
D-Galactose	3.54	-76.40	Urea	2.59	-21.00
D-Glucose	3.53	-326.30	BA-PhO-Dex	3.67	-29.02
D-Mannose	3.54	-137.60	PhO-Dex	3.59	-22.20
Dopamine	3.72	-33.80	RITC-PEG-RITC	5.52	-96.40
Glycine	2.93	-15.70	FITC-PEG-FITC	4.98	-98.70
Guanosine	4.42	-903.80	PE-PEG	4.72	-37.20
Histamine	3.31	-30.20	SC	4.81	-641.04
L-Ascorbic acid	3.44	-59.00	SDS	4.64	-32.29
L-Citrulline	3.78	-38.20	PVA	3.3	-22.80
L-Histidine	3.51	-70.80	Fmoc-Phe-PPEG8	4.07	-238.20
L-Thyroxine	4.84	-83.70	Fmoc-Phe-PPEG4	4.07	-238.20
			NH2-PPEG8	4.37	-8.20

Table 5.3: B_{ij} values for pairs of analytes and corona phase monomers.

	BA-PhO-Dex	PhO-Dex	RITC-PEG-RITC	FITC-PEG-FITC	PE-PEG	SC	SDS	PVA	Fmoc-Phe-PPEG8	Fmoc-Phe-PPEG4	NH2-PPEG8
17-alpha-estradiol	54.1	43.2	400.0	73.5	42.5	164.5	41.6	42.9	121.6	121.6	22.7
2,4-Dinitrophenol	37.9	31.0	48.9	54.8	31.4	157.1	30.0	31.5	84.1	84.1	18.0
Acetylcholine chloride	30.6	26.1	40.2	46.1	27.3	107.9	23.7	26.1	66.8	66.8	14.4
alpha-Tocopherol	287.2	154.9	215.5	305.1	135.9	10755.5	111.5	162.5	769.1	769.1	93.4
Adenosine	81.9	69.1	88.6	114.9	56.9	1275.4	55.1	80.7	295.6	295.6	40.4
ATP	76.9	64.6	131.8	178.6	104.2	1102.3	61.9	60.6	194.6	194.6	33.3
cAMP	148.1	125.4	131.9	215.0	102.0	662.2	78.0	147.4	590.4	590.4	53.9
Creatinine	42.5	29.8	39.2	45.4	24.9	133.4	24.1	30.3	85.3	85.3	17.6
Cytisine	54.1	46.3	66.4	80.8	43.3	392.1	40.9	49.4	145.2	145.2	26.5
D-Aspartic acid	35.5	26.1	33.3	39.3	21.6	111.4	21.2	27.1	75.4	75.4	15.7
D-Fructose	54.3	42.2	52.8	63.3	33.6	222.3	35.2	45.9	144.4	144.4	26.4
D-Galactose	43.3	34.8	47.7	55.7	30.2	188.1	30.0	36.8	103.6	103.6	22.1
D-Glucose	71.0	47.5	55.5	71.5	36.6	385.8	35.3	51.8	244.8	244.8	33.7
D-Mannose	47.1	38.8	51.2	60.6	32.3	244.7	32.6	42.9	121.8	121.8	24.9
Dopamine	32.3	26.9	43.6	46.7	26.4	128.8	27.8	27.0	65.4	65.4	15.3
Glycine	21.8	18.2	23.0	27.6	15.4	80.7	15.1	19.8	52.6	52.6	12.0
Gramine	190.6	154.7	132.8	243.1	96.0	1127.2	84.8	270.6	493.8	493.8	104.6
Histamine	29.7	22.7	33.9	38.8	20.7	96.6	21.5	23.2	59.3	59.3	13.6
L-Ascorbic acid	42.6	32.2	46.1	54.1	30.1	169.9	28.4	32.6	92.4	92.4	20.3
L-Citrulline	32.5	26.6	41.0	49.3	27.9	124.9	24.1	26.1	68.2	68.2	14.9
L-Histidine	70.7	41.5	50.9	61.0	30.4	182.0	33.2	42.9	137.9	137.9	26.6
L-Thyroxine	41.2	37.8	77.0	80.1	51.2	169.4	46.4	35.4	1150.0	1150.0	19.3
Melatonin	90.4	53.0	76.9	88.2	47.3	356.7	41.6	50.2	167.9	167.9	31.7
NADH	600.4	460.5	259.0	1788.5	890.3	75321.8	290.4	500.5	1019.6	1019.6	122.9
Quinine	783.2	664.6	239.1	773.2	190.9	1119.4	168.8	328.7	370.5	370.5	155.6
Riboflavin	500.0	450.0	189.5	414.4	150.6	1223.9	154.9	264.2	492.3	492.3	97.8
Salicylic acid	30.6	26.2	38.6	43.9	24.8	123.8	24.5	27.0	66.3	66.3	15.7
Serotonin	37.0	31.4	46.6	55.3	30.1	145.7	28.7	31.9	79.1	79.1	17.7
Sodium pyruvate	24.8	20.2	26.1	31.2	17.4	87.1	17.1	21.6	57.7	57.7	13.0
Sucrose	182.2	108.7	121.4	145.2	67.2	766.2	81.3	117.3	585.1	585.1	55.2
Thymidine	80.4	52.9	71.4	93.8	46.7	472.1	41.0	53.3	192.8	192.8	32.3
Tryptophan	37.5	31.0	48.4	55.3	30.6	131.3	28.7	31.1	74.7	74.7	17.1
Tyramine	28.4	24.9	40.0	42.9	24.5	114.6	24.5	24.9	56.2	56.2	13.4
Urea	25.0	20.1	22.4	28.7	14.9	85.5	15.1	22.7	65.1	65.1	12.7

Table 5.4: Values of β for each analyte molecule.

β			
17-alpha-estradiol	3.76	NADH	0.58
2,4-Dinitrophenol	0.24	Quinine	0.02
Acetylcholine chloride	4.12	Riboflavin	0.91
alpha-Tocopherol	0.14	Salicylic acid	0.05
Adenosine	0.06	Serotonin	16.05
ATP	0.09	Sodium azide	NaN
cAMP	0.06	Sodium pyruvate	0.96
Creatinine	1.10	Sucrose	0.03
Cytidine	0.04	Thymidine	0.08
D-Aspartic acid	50.86	Tryptophan	0.13
D-Fructose	0.03	Tyramine	14.43
D-Galactose	0.08	Urea	0.30
D-Glucose	0.02		
D-Mannose	0.04		
Dopamine	3.96		
Glycine	1.94		
Guanosine	0.19		
Histamine	4.97		
L-Ascorbic acid	1.68		
L-Citrulline	31.48		
L-Histidine	5.41		
L-Thyroxine	1653.12		
Melatonin	0.52		

Table 5.5: QSAR Parameters. Properties computed with Gaussian 09, the corresponding QSAR predictions, and the adsorption free energies computed using molecular dynamics as described in the main text.

Molecule	Computed with Gaussian09 (this study)			Quantum QSAR Prediction			Adsorption Potential (this work) [kcal/mol]	Aqueous Solubility Citation, Temp, and Note
	Molecular Polarizability [10^{-24} cm^3]	Mean Atom Charge [C]	Homo-Lumo Gap [eV]	log(C_w)	Aqueous Solubility [g/g H_2O]	Effective Adsorption Potential, Eq (6) [kcal/mol]		
17-alpha-estradiol	33.6	2.88E-06	7.4	-11.6	0.0015	7.1	16.9	[1], 25C
2,4-Dinitrophenol	19.1	2.78E-06	5.3	-6.4	0.69	7.7	15.8	[1], 25C
alpha-Tocopherol	57.3	2.95E-06	7.9	-21.7	0.0209	14.6	25.9	[2], 33C
Adenosine	26.2	3.22E-06	6.8	-8.7	5.1	10.2	15.5	[1], 25C
cAMP	29.9	3.65E-06	6.5	-10.4	7.8	11.5	16.5	[3], 20C, in Phosphate Buffer
Creatinine	10.9	4.08E-06	10.0	-0.3	14.0	5.9	10.9	[4], 20C
D-Aspartic acid	9.9	4.16E-06	8.9	-0.5	4.9	5.3	9.6	[1], 25C, L-Aspartic Acid
D-Fructose	13.8	3.37E-06	8.6	-2.3	450.0	9.1	11.5	[1], 20C, β-D-Fructose
D-Galactose	13.7	3.24E-06	8.2	-2.6	684.0	9.5	10.7	[1], 20C
D-Glucose	13.7	3.26E-06	8.2	-2.5	1200.0	9.8	11.7	[1], 30C
D-Mannose	13.7	3.24E-06	8.7	-2.3	3189.4	10.2	17.3	[5], 25C
Glycine	5.6	4.16E-06	10.9	2.4	227.0	5.9	8.5	[1], 25C
Guanosine	26.8	3.61E-06	7.0	-8.8	0.5000	8.9	18.1	[1], 25C
L-Ascorbic acid	14.5	3.53E-06	5.5	-4.2	357.0	10.0	13.2	[1], 25C
L-Histidine	14.3	3.33E-06	6.2	-3.8	43.5	8.6	10.2	[1], 25C
Quinine	42.9	2.59E-06	4.3	-17.3	0.5700	14.0	18.2	[1], 25C
Salicylic acid	14.7	3.21E-06	5.1	-4.6	1.9	7.2	13.8	[1], 25C
Sucrose	27.2	3.13E-06	8.8	-8.5	2040.0	13.6	14.3	[1], 20C
Thymidine	23.5	3.43E-06	6.4	-7.7	54.0	11.0	16.9	[1], 25C
Tryptophan	24.1	3.15E-06	7.1	-7.6	13.2	10.1	16.2	[1], 25C, L-Tryptophan
Tyramine	16.8	3.83E-06	6.2	-4.9	10.4	8.4	11.6	[1], 15C
Urea	4.0	5.11E-06	7.9	1.6	1200.0	7.4	9.2	[1], 25C
Molecules for which aqueous solubilities not readily available								
ATP	39.2	4.75E-06	6.4	-14.5			22.7	
Cytidine	23.1	3.43E-06	6.4	-7.6			16.0	
Dopamine	17.5	3.28E-06	5.7	-5.5			13.1	
Histamine	12.0	2.97E-06	10.0	-0.8			10.7	
L-Citrulline	15.9	3.94E-06	6.8	-4.2			10.5	
Melatonin	27.8	3.24E-06	1.0	-12.4			20.3	
Riboflavin	77.9	3.46E-06	2.3	-33.6			24.7	
Serotonin	6.7	3.59E-06	5.5	-0.9			14.0	
Sodium pyruvate	20.6	3.10E-06	1.7	-9.0			9.0	
BA-PhO-Dex	13.7	2.67E-06	7.6	-2.8			12.7	
PhO-Dex	13.3	2.61E-06	8.7	-2.1			11.6	
RITC-PEG-RITC	27.5	3.08E-06	0.7	-12.5			16.0	
FITC-PEG-FITC	47.0	2.97E-06	1.6	-20.5			15.6	
PE-PEG	37.4	2.98E-06	8.5	-12.6			16.9	
SC	45.4	2.98E-06	6.4	-17.2			16.5	
SDS	28.1	3.27E-06	9.0	-8.4			18.0	
PVA	8.4	3.17E-06	8.6	0.0			8.8	
Fmoc-Phe-PPEG8	27.8	2.13E-06	5.9	-9.9			15.3	
Fmoc-Phe-PPEG4	27.8	2.13E-06	5.9	-9.9			15.3	
NH2-PPEG8	2.9	4.45E-06	16.5	6.6			8.1	
Molecules for which QSAR results could not be computed								
GT15								
Sodium azide								
NADH								
L-Thyroxine								
Acetylcholine chloride								

Table 5.5: QSAR Parameters (continued).

[1] CRC Handbook of Chemistry and Physics. 95th ed.; CRC Press.

[2] Dubbs, M. D.; Gupta, R. B. Solubility of Vitamin E (α-Tocopherol) and Vitamin K3 (Menadione) in Ethanol-Water Mixture. Journal of Chemical & Engineering Data 1998, 43 (4), 590-591.

[3] Dworkin, M.; Keller, K. H. Solubility and diffusion coefficient of adenosine 3':5'-monophosphate. Journal of Biological Chemistry 1977, 252 (3), 864-5.

[4] JÃd'ger, R.; Purpura, M.; Shao, A.; Inoue, T.; Kreider, R. Analysis of the efficacy, safety, and regulatory status of novel forms of creatine. Amino Acids 2011, 40 (5), 1369-1383.

[5] Gabas, N.; Carillon, T.; Hiquily, N. Solubilities of D-xylose and D-mannose in water-enthanol mixtures at 25.degree.C. Journal of Chemical & Engineering Data 1988, 33 (2), 128-130.

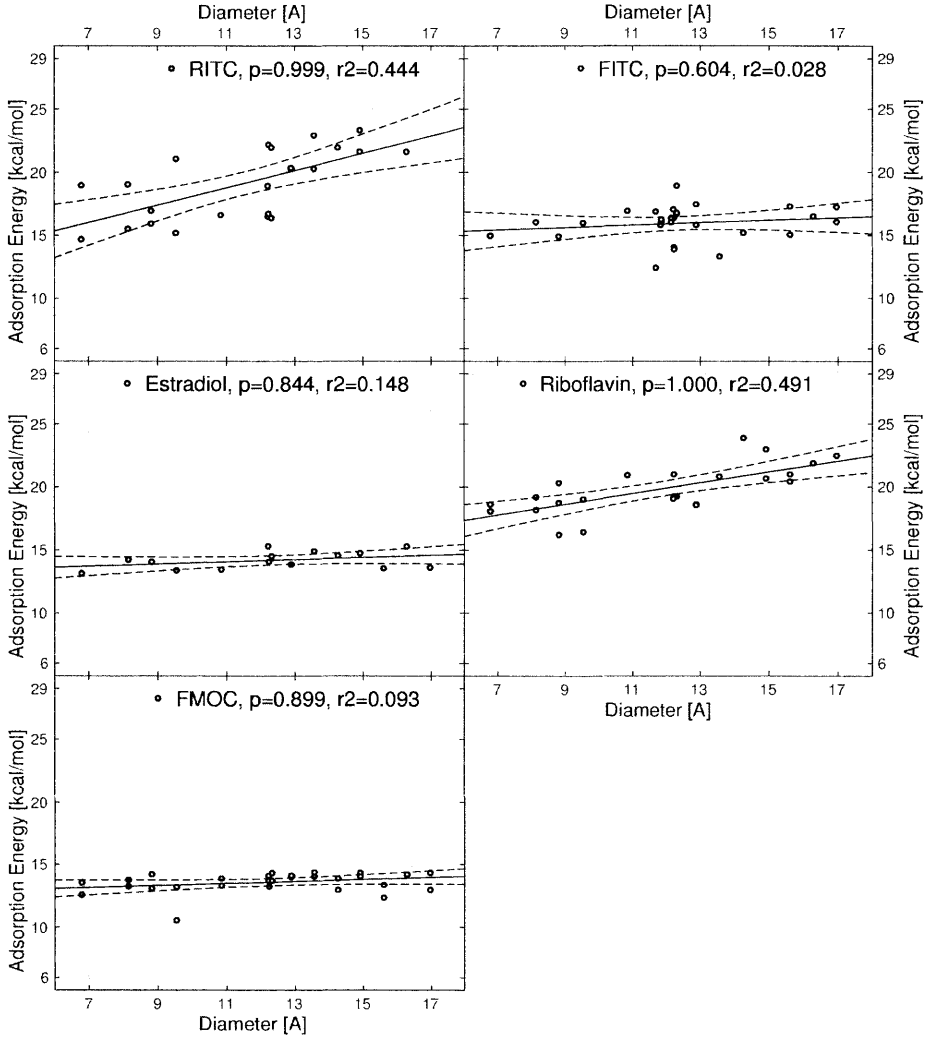

Figure 5-8: Molecular adsorption energies on SWCNTs of various diameters for five selected molecules. p-values in the legend indicate the significance of the correlation between adsorption energy and diameter ($p>0.95$ is significant). Linear fits, their corresponding r2 values, and corresponding shaded 95% confidence intervals are included as visual guides. Two molecules, RITC and riboflavin, have adsorption energies that depend significantly on diameter.

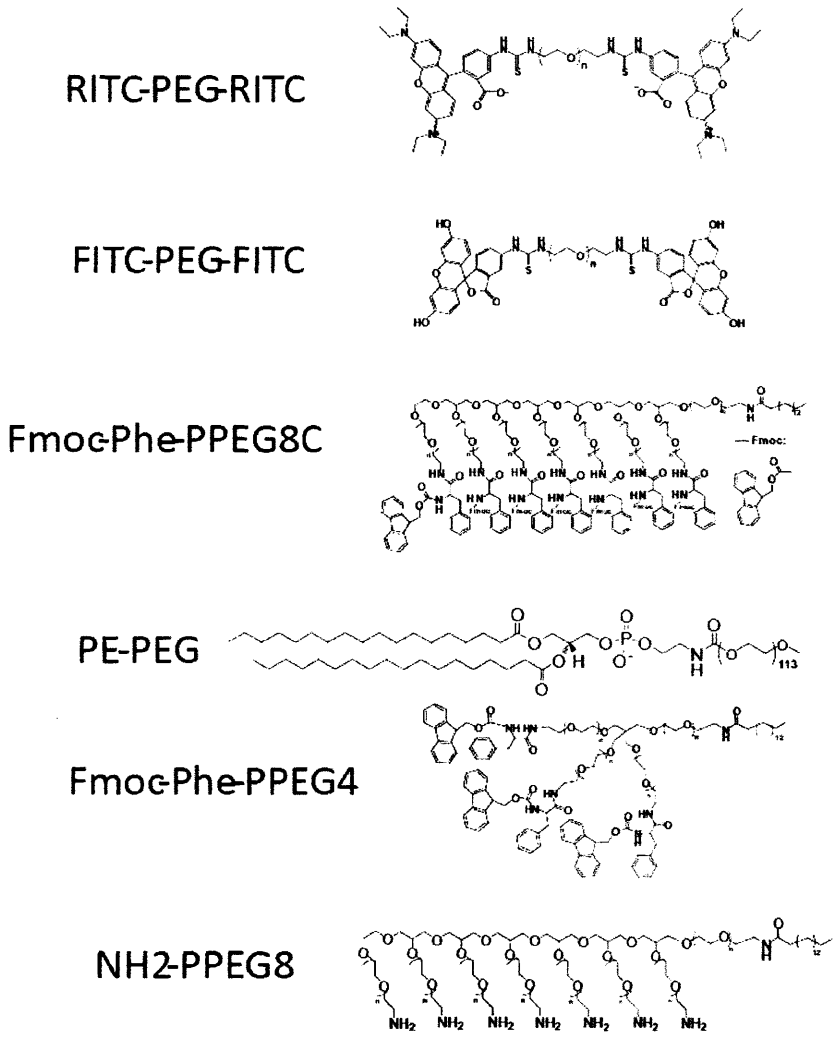

Figure 5-9: Structures of the polymers that were used to suspend SWCNT.

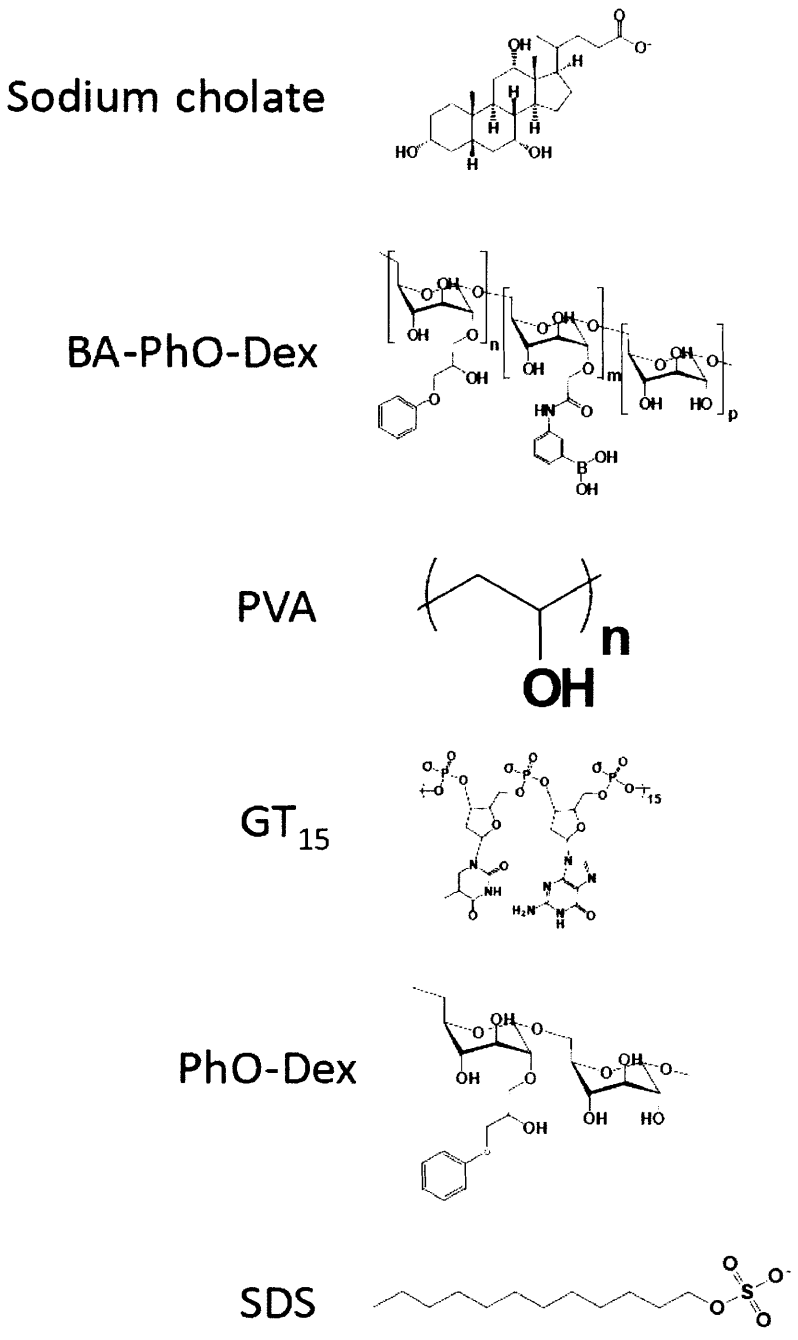

Figure 5-9: (continued) Structures of the polymers that were used to suspend SWCNT.

Part II

Stochastic Transport Inside of SWCNTs

Chapter 6

Carbon Nanotubes as Molecular Conduits: Advances and Challenges for Transport through Isolated Sub-2nm Pores

This work originally appeared as: Zachary W. Ulissi, Steven Shimizu, Chang Young Lee, and Michael S. Strano. Carbon nanotubes as molecular conduits: Advances and challenges for transport through isolated sub-2 nm pores. Journal of Physical Chemistry Letters, 2(22):2892-2896, 2011.

6.1 Abstract

Devices that explore transport through the narrowest diameter single-walled carbon nanotubes (SWCNTs) have only recently been enabled by advances in SWCNT synthesis methods and experimental design. These devices hold promise as next generation sensors, platforms for water desalination, proton conduction, energy storage, and to directly probe molecular transport under significant geometric confinement. In this perspective, we first describe this new generation of devices, and then highlight two important concepts that have emerged from recent work. First, the most reliable way to identify transport is to borrow techniques from the biological and silicon nanopore communities and analyze the discrete

stochastic events caused by molecules blocking the SWCNT channel. Second, it is nearly impossible to isolate mass transport within a SWCNT without a substantial suppression of leakage transport and around the SWCNT. To highlight this, we discuss experiments showing water transport along the exterior of SWCNTs. Finally, we describe some further innovations to these devices in the near future that will allow for a more complete understanding of confined molecular transport.

6.2 Introduction

Recent experimental advances have led to several systems capable of directly monitoring transport through the interior of sub-2nm, isolated single walled carbon nanotubes [43, 145, 211, 33, 90, 159]. In this perspective, we identify nanopores of this size as having properties that are distinct from larger multi-walled conduits that have been used as Coulter detectors for sub-micron particles [106]. Carbon nanotube (CNT) membranes have been studied extensively in literature [73, 100, 97, 167] but provide less insight into transport physics compared with single nanotube devices [43, 145, 211, 33, 90, 159], and we direct the reader to recent reviews of membranes for details [99]. This perspective focuses on the emergence of single nanotube pores or collections of pores, since they are ideal systems to validate theoretical predictions of nanopore transport [102, 60] and to elucidate new ones [43, 145]. In this size regime of sub-2nm pores, there has been extensive investigation of isolated transmembrane proteins, silicon nanopores, and others (see reviews [101, 58]). It is noteworthy that very few silicon nanopores have been fabricated and studied with diameters comparable to that of SWCNTs [93, 98, 260, 174]. The simple geometry and large aspect ratio of SWCNT devices appear to result in transport regimes that are distinct from these other systems, motivating our currentperspective.

Single-SWCNT devices will be able to address the validity and predictions of what is now an extensive literature on SWCNT molecular simulations [95]. Computational studies and physical models of transport through SWCNT nanopores [102] were developed before the original CNT membrane experiments [100, 97, 167] and these results will apply directly to single-SWCNT devices. Most importantly, the hydrophobic nature of the SWCNT internal surface suggests that decreasing SWCNT diameter should increase the ordering of internal water [138]. This ordering is predicted to increase fluid flow rates [248], proton transport

rates [60], and ion transport rates [19]. A complete listing of simulation predictions and results can be seen in recent reviews [99, 95]. However, spectroscopic studies and experiments with CNT membranes have not been able to confirm many of these predictions. Additionally, simulations have not yet predicted the pore-blocking effects that we have observed experimentally [145] and that are present in other nanopores [101]. Electrochemical and fluid models [142] have also been proposed but do not yet quantitatively explain all of the device characteristics seen experimentally or in simulation (e.g. continuum/sub-continuum transitions [248]). Data from single-SWCNT devices will improve our simulations of confined flows and lend more insight into biological nanopores and many-SWCNT membranes.

6.3 Experimental Devices in Literature

Several studies on devices with individual SWCNTs have been reported due to advances in synthesis techniques and the application of standard methods of analysis and verification such as Coulter states. Last year, our group demonstrated for the first time the detection of single ion translocation events and coherent resonance in SWCNT pores through the analysis of stochastic state-switching known as the Coulter effect. Other studies have reported devices with significantly larger multi-walled nanotubes (MWNT) [105], devices with a single SWCNT for the detection of DNA [90, 159], devices for the analysis of SWCNT electronic structure upon water filling [33], and a device for the measurement of water transport rate through a single SWCNT [211]. However, across many different size regimes, the signature of a single, isolated nanopore of any type continues to be the observation of stochastic pore blocking by a guest molecule or particle comparable in size. Even for membrane systems, pore size is characterized with respect to transport and the size of rejected molecules, and not by electron microscopy. Therefore, studies relying on the mere presence of a carbon nanotube in a barrier or physical characterization have not adequately proven that observed transport is through a single nanopore.

Our laboratory recently demonstrated the device illustrated in Figure 6-1 capable of analyzing the Coulter states of a single SWCNT [145]. Devices were made by growing parallel centimeter-long SWCNTs on a silicon substrate and forming an epoxy barrier covering the SWCNTs between two reservoirs with various electrolyte solutions. Upon the application of electrical potential between the two reservoirs, we observed stochastic current fluctuations

which were attributed to the entrance and exit of cations within a single SWCNT, for several reasons. First, we observed that increasing the ionic concentration led to a decrease in current measurements, suggesting ions interfere with current through the nanopores. Second, reducing the pH of solution increased the current measurements, suggesting that protons are the majority carriers of current across the nanopores. Thirdly, we noticed that using various cations led to different dwell times and pore-blocking currents. Finally, in order to determine that the cations were the blockers, as opposed to the chloride ions, we showed in our previous work [145] hat a large cation electrolyte (tetramethylammonium chloride) does not produce any pore-blocking characteristics. For a subset of conditions, we also observed coherent current oscillations when pore blocking events coordinated with diffusion limited proton aggregation at the pore mouth. In a further study [43], we studied the importance of end-group electrostatics and made devices with multiple functioning SWCNTs that demonstrated additional Coulter states.

A recent study by another group involved a single-SWCNT microfluidic device for the purpose of DNA detection [159]. Short (2μm) SWCNTs were grown on a silicon surface and a microfluidic device was built on top using PMMA as the barrier material. Devices were first tested with aqueous salt solutions and an applied potential difference. Upon the introduction of DNA on one side of the SWCNT, some devices demonstrated periods of greatly enhanced current, and DNA was observed on the other side upon PCR amplification. However, Coulter states from ion pore-blocking were not observed indicating that the SWCNT may not be solely responsible for the observed electro-osmotic current or DNA transport. In a further study [90], the translocation of individual nucleotides and DNA sequences of various lengths was investigated.

In subsequent work, the same group monitored the effect of water filling on the conductance of a single SWCNT field-effect transistor (FET) [33]. A single-SWCNT was grown on a silicon surface, and gold electrodes were attached to create a FET with a connecting SWCNT. The FET was covered with a PMMA photoresist connecting two aqueous reservoirs. Importantly, control studies showed a difference in FET characteristics between nanotubes with internal or external water. Upon internal filling with water, the FET was disabled, presumably caused by large water dipole moments. The results were consistent with electronic calculations of SWCNTs with and without internal water, however, the Coulter effect was not demonstrated.

Different authors report a single-SWCNTdevice for the measurement of internal water flow [211]. A single SWCNT was grown over several parallel FETs and a water droplet placed on one end. This device had no matrix or shielding to prevent parallel or otherwise external transport. The water flow rate was measured by observing the arrival time to the various FETs. External transport was thought to be negligible since addition of a thin spin-coated hydrophobic film over the SWCNTs did not significantly change the reported flow rates, however, the majority of the measurements were performed using the uncovered device. We demonstrate below that external electro-osmotic flow along a nanotube is significant, and that a barrier is required to observe internal transport only.

The primary experimental method for analyzing either synthetic or biological nanopore systems has historically been the use of patch-clamps to isolate a section of membrane with a single active nanopore or small collection of nanopores [86]. A single nanopore is then characterized by observing the stochastic fluctuations in transport properties. For biological trans-membrane proteins like aquaporins or α-hemolysin [101], these states might correspond to various protein conformations induced by local changes in the environment. Similar effects are observed in synthetic nanopores when the nanopores are blocked by the translocation of a small molecule or particle (e.g. DNA in silicon nanopores [174], or if precipitation occurs at the entrance regions [208]. This blocking effect is known as Coulter states [101], illustrated in Figure 6-2.

Coulter states play an important role in characterizing synthetic nanopores and checking for other sources of mass transport in the system. The rate of stochastic switching between states (or equivalently the dwell time during blocking events) is related to mass transport rates through a nanopore, as well as molecular entrance and exit kinetics, as illustrated in Figure 6-2A,B. Based on studies of silicon nanopores and our own experiments [43, 145, 93, 98, 174], we expect that most experimental systems consisting of a single nanopore with molecule-scale diameters (e.g. less than 2nm for aqueous systems), a smaller, fast-translocating species, and a larger atomic or molecular species capable of entering the nanopore should exhibit Coulter states. Under these conditions, a lack of switching between stochastic states could indicate that any observed electrical resistance is the result of many parallel channels. Note that for detection experimentally, a state must persist for a threshold period of time, set by the resolution of typical voltage clamp equipment which is of order microseconds. For any nanopore system, one should find a blocking species and

conditions such that the Coulter effect is observed. When analyzing our own nanopore devices, we do not attribute transport measurements to a nanopore unless we can observe well-defined Coulter states, proving that single, isolated nanopores are observed.

Coulter states are often straightforward to identify since the change in conductance between two states is usually significant compared to experimental noise, as shown in Figure 6-2C. Furthermore, the timescale for moving from one state to another is usually much faster than the time spent in each state, resulting in sharp changes in the conductance signal. If multiple independent nanopores are observed simultaneously, these stochastic fluctuations become more complicated with multiple possible states of the system. However, since small current fluctuations for each pore will generally be additive, the electrical noise in a system with many nanopores may conceal stochastic switching events. Devices with a single functional SWCNT are thus the most useful for initially studying and characterizing a nanopore device.

A variety of other experimental methods can be used to further characterize nanopore-based devices but none offer the unambiguous discrete nature of the Coulter effect. The most common method for analyzing electrochemical devices is to measure the electrical current across the nanopore as a function of an applied voltage difference, but it is difficult to separate current passing through the nanopore from leakage current through the barrier. Spectroscopy of the SWCNTs during translocation events would also be useful as an independent confirmation of transport. Several groups have used spectroscopy to probe the ordering of internal water, but none have done time-resolved spectroscopy. It may also be possible to measure either the effect of internal molecules on the SWCNT radial breathing mode, or vibrations of the molecules themselves.

An enabling advance in analyzing single-SWCNT devices has been the adoption of thicker and larger sealant barriers to eliminate background and leakage impedance. To measure a blockade current from a single nanopore, the background current or leakage current must be reduced by appropriate sealing of the device. Various materials have been used, such as SU-8 epoxy [43, 145] or PMMA [33, 90, 159]. Both of these materials invariably have small imperfections and cracks arising from the curing process making the width of the barrier apparently very important. Most recent devices have used sealant barriers of various widths [43, 145, 33, 90, 159], although a recent study used uncovered SWCNTs [211]. We have found that the barrier presence and width can have a large impact on the observed transport

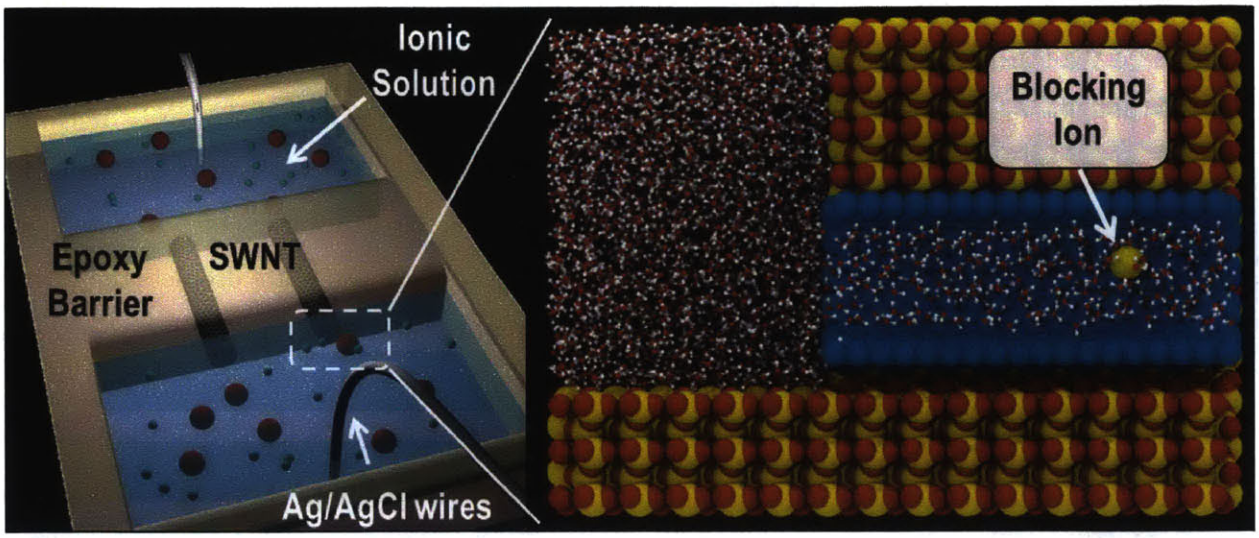

Figure 6-1: Illustration of a single-SWCNT device [43, 145], with a blocking sodium ion.

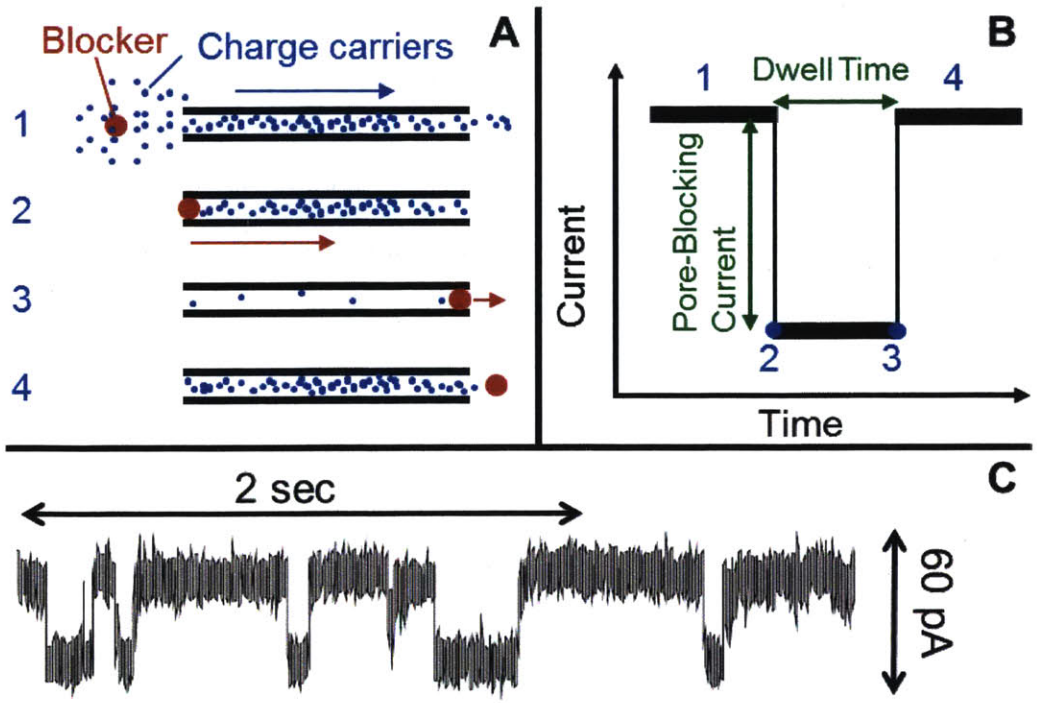

Figure 6-2: Demonstration of Coulter States, which are characteristic of nanopores with diameters similar to analyte molecules in solution. A) Stages of a blocking event, B) characteristic current profile, and C) current profile for a SWCNT device with a 3M KCl solution [145].

characteristics due to the possibility of flow external to the SWCNTs.

We learned the importance of barrier design while performing preliminary experiments [144] for our recent study [145], illustrated in Figure 6-3A. Parallel SWCNTs were first grown on a silicon substrate. A droplet of aqueous salt solution was placed on one end of the SWCNTs, and a droplet of de-ionized water was placed on the other end. A voltage was applied across the two droplets and upon contact between the two water droplets the current increased dramatically, as shown in Figure 6-3B. After the droplets evaporated, we confirmed mass transport by showing residual NaCl with energy dispersive X-ray spectroscopy (EDX) on the region with initially pure water. Using scanning electron microscopy (SEM) on the sample (Figure 6-3C), we noted that there was a significant build-up of NaCl crystals around the SWCNTs, indicating external mass transport. The SEM images show the SWCNT as well as the NaCl crystals, which were deposited quite far from the SWCNT. On subsequent devices, we introduced either metal or silica covers over some of the SWCNTs, as shown in Figure 6-3D. SWCNTs that were covered had a lower conductance and did not show NaCl buildup on the pure water side of the device, while uncovered SWCNTs again showed salt crystallization along the SWCNT length. Thus, a barrier is required to eliminate mass transport external to the SWCNTs. Our experience indicates that without such a barrier, the bulk of electro-osmotic flow is invariably from the exterior of the SWCNT.

The trend in isolated SWCNT literature seems to be towards wider barriers to completely remove excess transport. The effect of barrier width on leakage current can be seen in Figure 6-4, using control devices similar to Figure 6-1, but without a SWCNT. As expected, without the presence of a SWCNT these devices showed no stochastic pore-blocking. The leakage current and barrier conductance is observed to decrease roughly exponentially as a function of barrier width. If conduction through the barrier was through a uniform network of pores, the current would be expected to vary inversely proportional to the width. However, conduction through the barrier should occur along networks of cracks and defects, making this a complex percolation problem, and suggesting that the current will decrease more rapidly than a 1/width dependence. Although this plot is not representative of all the different materials that could be used to construct the barrier, it illustrates the necessity of understanding the proper barrier resistance required in order to minimize leakage enough so that stochastic pore-blocking events will not be masked by leakage currents. We expect further improvements to be made in barrier construction in the future.

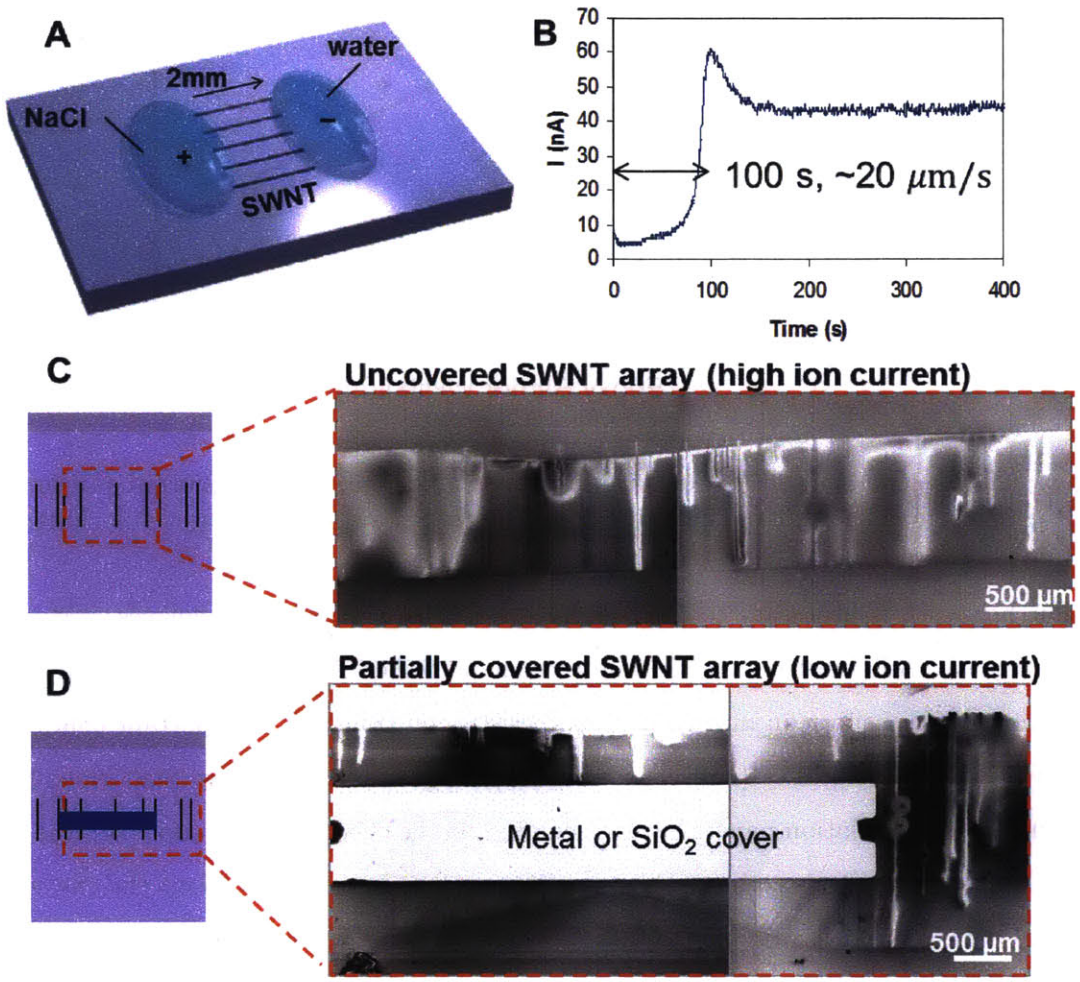

Figure 6-3: Demonstration of water and NaCl transport along the outside of uncovered SWCNTs. A) Device design, with a voltage applied between across the two droplets. B) Typical current trace after droplet deposition, showing a sharp increase in current upon water translocation. C) SEM image of device after water/NaCl translocation and water evaporation, with bright areas indicating NaCl deposited external to the SWCNTs. D) SEM image of a device with a barrier. *Reproduced with permission [144]*

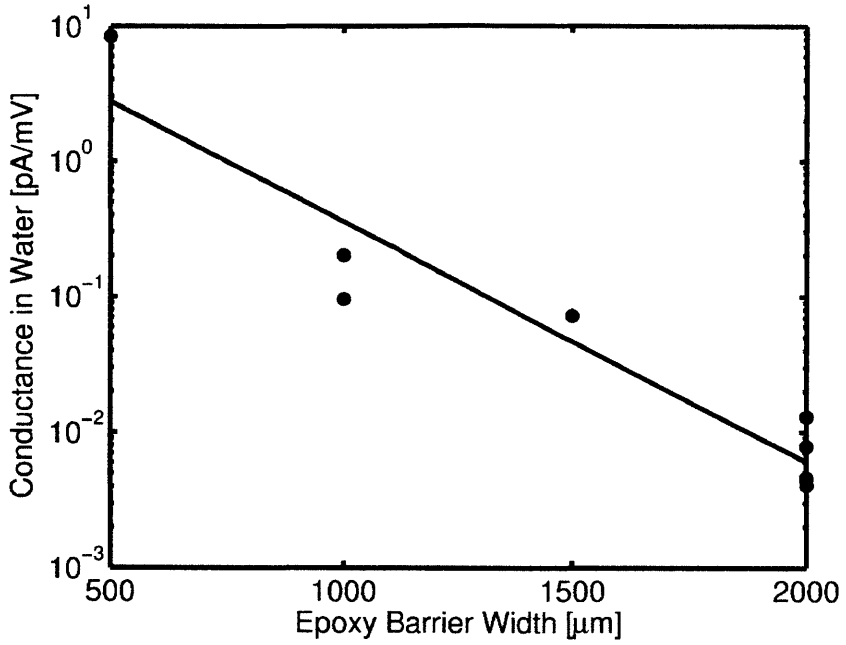

Figure 6-4: The conductance of devices with water in both reservoirs is plotted as a function of SU-8 epoxy barrier width. These devices all did not show stochastic pore-blocking.

Further work is necessary to fully understand these new SWCNT devices. Most importantly, SWCNTs must be tested using these new methodologies to determine the precise dependence of transport on nanotube characteristics on transport. Important characteristics to test are the chirality (and thus diameter), length, and end-group functionalization. Although a few simulation papers have speculated on the effect of end-groups [76], the effect in single nanopores needs to be studied experimentally. Information about the end-groups would also ensure that errant effects that may be mistaken for translocation events like salt precipitation [208] and nanobubble formation [232] are not occurring at the entrance and exit regions.

6.4 Conclusion

We see a need for convergence between the current simulation methods, results for single SWCNT devices, and the extensive SWCNT membrane literature, all of which describe the same fundamental phenomena under different conditions. Once simulations can predict transport properties for arbitrary SWCNT chiralities, membranes could be modeled statistically using known chirality distributions from synthesis methods. These devices could

clarify the rates and mechanism of proton transport under confinement, which have been simulated [60, 145] but not completely tested experimentally. Convergence of these methods would be an exciting advance since these transport systems are one of the few available that can be completely simulated by modern molecular simulations. The success (or failure) of these simulations could also help clarify if the force fields developed for bulk materials are sufficient to model confined environments.

Finally, we see many possibilities for new devices with enhanced construction and further analysis methods available. A completely enclosed microfluidic system could be used to apply a pressure gradient across the SWCNT expanding upon the measurements conducted recently [211]. An enclosed system could also be used for the study of new materials with high vapor pressures, and allow for the accurate control of temperature in the system. The possibility of DNA sequencing suggests that new devices will soon be designed with built-in spectroscopic probes that will identify larger molecules as they translocate across the SWCNT.

Chapter 7

Diameter Dependent Ion Transport through the Interior of Single Isolated Single Walled Carbon Nanotubes

This work originally appeared as: Wonjoon Choi, Zachary W Ulissi*, Steven F. E. Shimizu, Darin O. Bellisario, Mark D. Ellison, and Michael S. Strano. Diameter-dependent ion transport through the interior of isolated single-walled carbon nanotubes. Nature Communications, 4, 2013. It has been edited to include the supporting information in-line.*

7.1 Abstract

Nanopores that approach molecular dimensions demonstrate exotic transport behavior and are theoretically predicted to display discontinuities in the diameter dependence of interior ion transport due to structuring of the internal fluid. No experimental study has been able to probe this diameter dependence in the 0.5 - 2nm diameter regime. Herein, we observe a surprising 5-fold enhancement of stochastic ion transport rates for SWCNT centered at a diameter of approximately 1.6 nm. An electrochemical transport model informed from literature simulations is used to understand the phenomenon. We also observe rates that scale with cation type as $Li^+ > K^+ > Cs^+ > Na^+$ and pore blocking extent as $K^+ > Cs^+ > Na^+ > Li^+$ potentially reflecting changes in hydration shell size. Across several ion types, the pore-blocking current and inverse dwell time are shown to scale linearly at low electric

field. This work opens up new avenues in the study of transport effects at the nanoscale.

7.2 Introduction

Various types of nanopores and nanochannels have attracted significant interest in recent years [30]. Examples include silicon-based nanopores [72, 239, 148, 35, 7, 147], which achieve selectivity primarily through size-exclusion of macromolecules, and biological nanopores [56, 165, 278, 124, 55], which manipulate their shape or present a specific pore-opening to allow the passage of only specific ions such as potassium [165], calcium [56], or sodium [56]. Single-walled carbon nanotubes (SWCNTs) are promising candidates for nanopore studies [159, 104, 80, 102, 122, 210, 199, 200, 198] since they can match the well-defined diameter and high aspect ratios of traditional silicon nanopores with sub-2 nm diameters and hydrophobic interior that allows for ion selectivity. These properties potentially allow for interesting desalination [73] and DNA-sequencing applications [159], as well as the ability to probe basic fluid structure properties at the smallest of possible scales. For this reason, a large number of molecular simulations have demonstrated interesting diameter-dependent phenomena such as ion selectivity [80, 73], rapid proton conduction [210, 60] that can be caused by the unique water structures and geometric confinements [31, 145, 49], and altered water-ice phase behavior [241]. However, most studies have focused on theoretical simulations, and their experimental verification is still a subject of debate [167, 100, 211, 248].

In previous work [43, 145] we demonstrated pore-blocking transport phenomena through the interior of multiple parallel SWCNTs with lengths of approximately 1 mm. We attributed discrete stochastic changes in the measured current to the blocking of a large proton current by translocating ions based on a number of experimental observations. First, we noticed a large dependence of the blocking current on the solution pH, suggesting that protons were the majority charge carriers. Second, we only observed pore-blocking phenomena in electrolyte solutions (e.g. KCl, as opposed to water or HCl) and only with relatively small cations, suggesting that cations, not anions, were responsible for the pore-blocking phenomena. Finally, we noted that the pore-blocking phenomena are quantitatively altered with various cation species, an observation which we further explore in this work with new single-SWCNT devices. In follow-up work, we were able to further demonstrate pore-blocking phenomena through multiple parallel SWCNTs resulting in a stochastic three-state

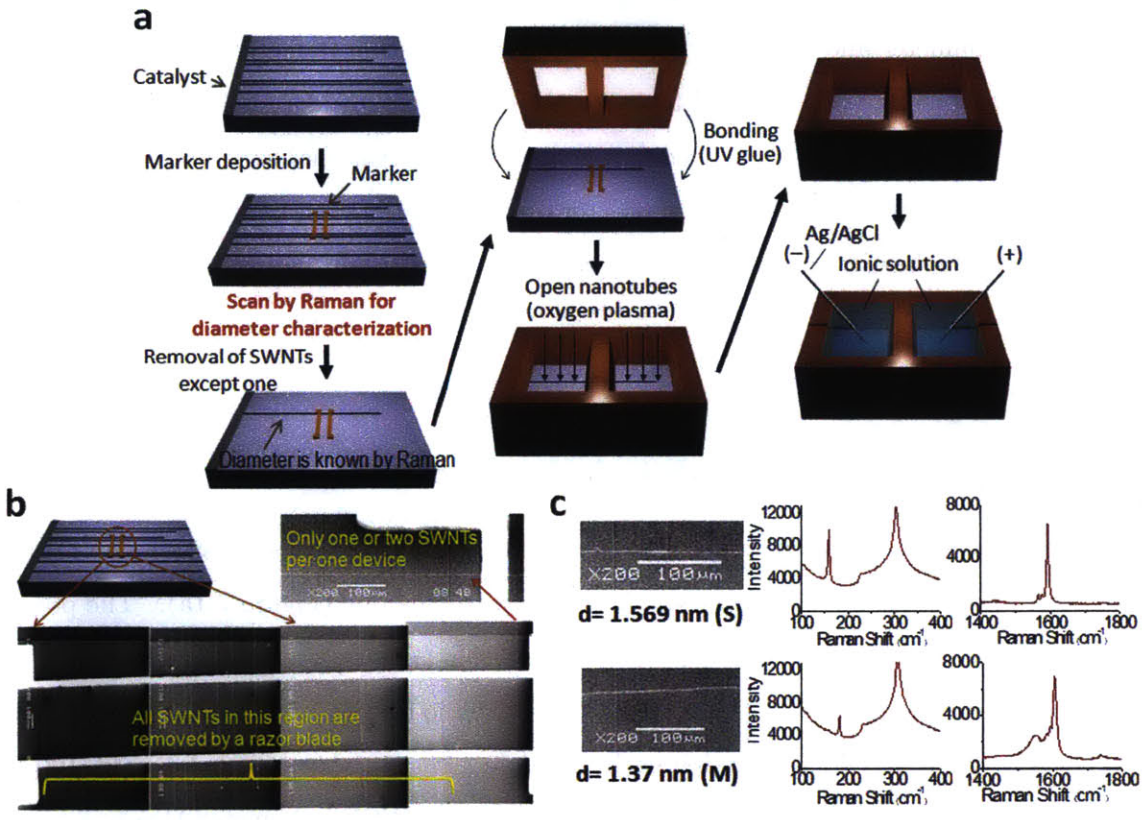

Figure 7-1: Experimental method for manufacturing characterized single-SWCNT devices. (a), Aligned single-walled carbon nanotubes (SWCNTs) are grown on a silicon wafer, identified with a marker, diameter-characterized with Raman spectroscopy, all but one or a few SWCNT removed with a razor blade, a two-reservoir epoxy structure bonded to the wafer, SWCNT ends opened with oxygen plasma etching, and finally devices are tested with Ag/AgCl electrodes with various electrolyte solutions. (b), Example of scanning electron microscope (SEM) identification of all aligned SWCNT grown on a device with the chosen SWCNT for study marked. Scale bar for the SEM indicates 100 um. (c), SEM microscope images of two representative 1.569 nm, 1.37 nm SWCNTs (left), scale bar for the SEM indicates 100 um. Raman characterization of the diameter of the chosen SWCNT based on the radial breathing mode, and metallic/semiconductor nature based on G-peak (right).

system [43]. Other groups have studied transport through larger collections of SWCNTs [73, 167, 100] or with much shorter lengths [30, 198], but stochastic pore-blocking was not observed under these conditions.

In this work, we employ a modified version of the platform introduced earlier [145] for explicit study of cation transport through single, isolated SWCNT, that are measured and assigned a diameter and electronic type using single molecule Raman spectroscopy. These diameter-assigned devices are used to probe the diameter dependence of pore-blocking phenomena for the first time. We then rationalize the observations using an electrochemical transport model drawing from previous literature simulations. Finally, we report the dependence of stochastic transport rates on cation type and temperature.

7.3 Results

7.3.1 Fabrication and Characterization of Single-SWCNT Devices

Aligned SWCNTs were grown on a silicon wafer by chemical vapor deposition (CVD) as in previous work [145] and characterized via Raman spectroscopy (Figure 7-1a). The position of each SWCNT was marked with e-beam evaporation (Figure 7-1b). Raman spectra were then collected for each identified SWCNT (See Methods, Figures 7-2,7-3, 7-4 and Table 7.1). The position of the radial breathing mode ω_{RBM}, a sharp peak between 100 and 300 cm^{-1} shown in Figure 7-1c, was used to assign the SWCNT diameter D_{SWCNT} via the empirical literature relation $\omega_{RBM}=(248/D_{SWCNT})$ [120]. The metal/semiconductor nature of the SWCNT was determined by analyzing the shape of the G peak. A strong second peak (Figure 1c, lower) in the G peak region indicated a metallic SWCNT and the absence of such a peak (Figure 1c, upper) indicated a semiconductor SWCNT. To prevent the use of SWCNTs in a substantial narrowing that can affect the observation of the transport phenomena, we measured raman spectra for over 2 or 3 positions along its length axis. The distance between measured points was at least 100 μm.

After characterization of all SWCNT on each wafer, one, two, or three SWCNT were chosen for study, all remaining SWCNT were removed with a razor blade, and a microfluidic platform was fabricated on top as in previous work [145], (Figure 7-1a). Briefly, the wafer was covered by an epoxy structure constructed from SU-8 negative photoresist with defined reservoirs and a 1 mm barrier region perpendicular to the SWCNT alignment. The exposed

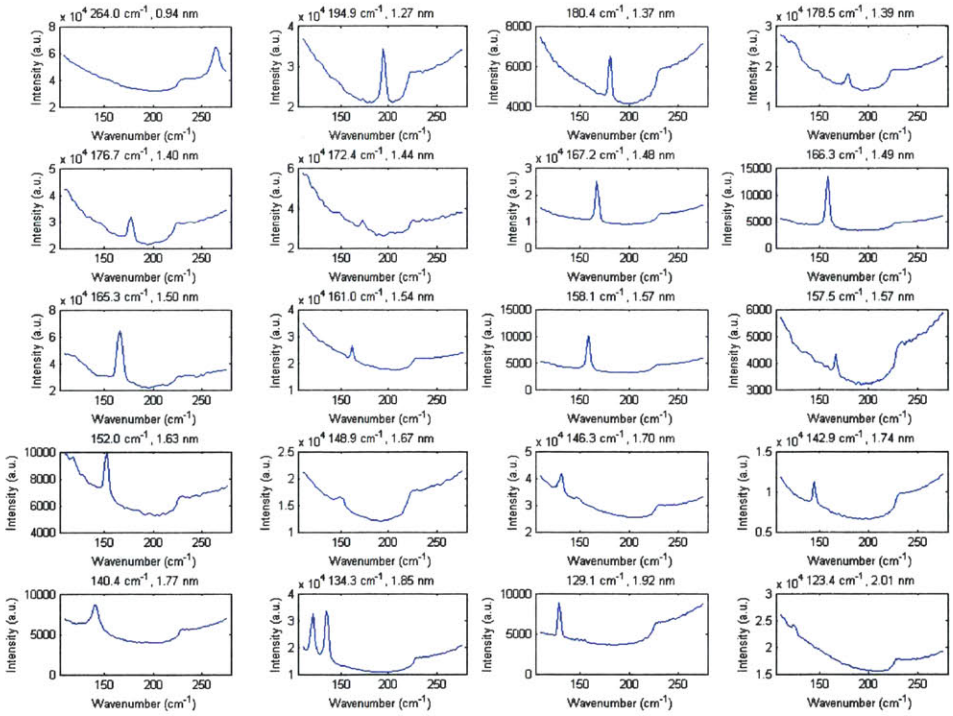

Figure 7-2: Plots of Raman spectra showing the radial breathing mode (RBM) feature for all carbon nanotubes from devices used in the diameter study, sorted in order of increasing diameter. The position of the RBM and corresponding tube diameter are listed above each plot. The sample at 1.85 nm actually has 2 RBMs observed, indicating the presence of DWNT; the corresponding diameter was calculated using the inner tube RBM.

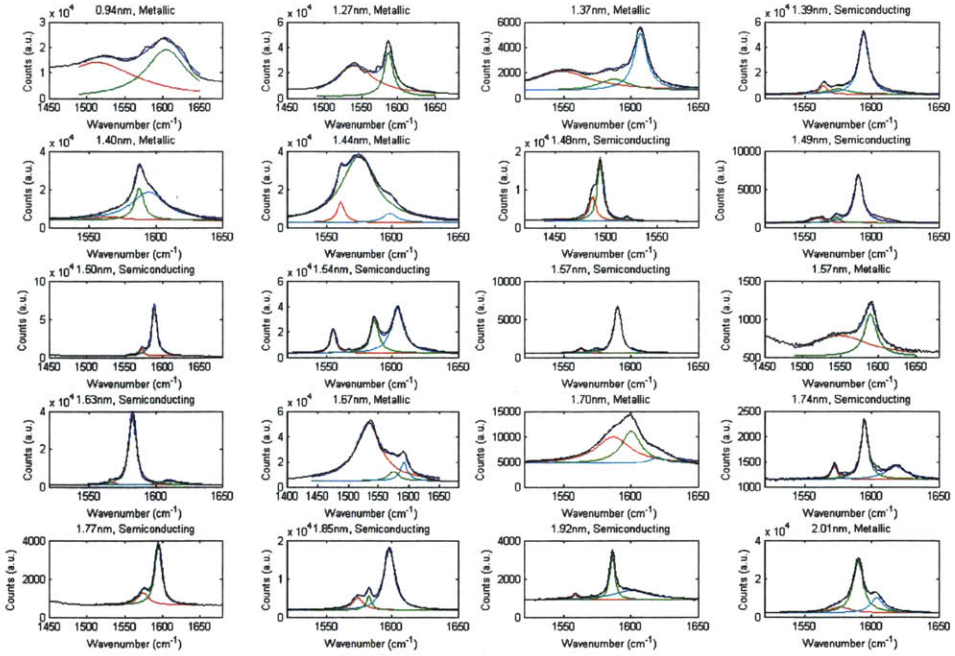

Figure 7-3: Plots of Raman spectra showing G peak features for all carbon nanotubes from devices used in the diameter study, sorted in order of increasing diameter. The diameter and metallicity of each tube are listed above each plot.

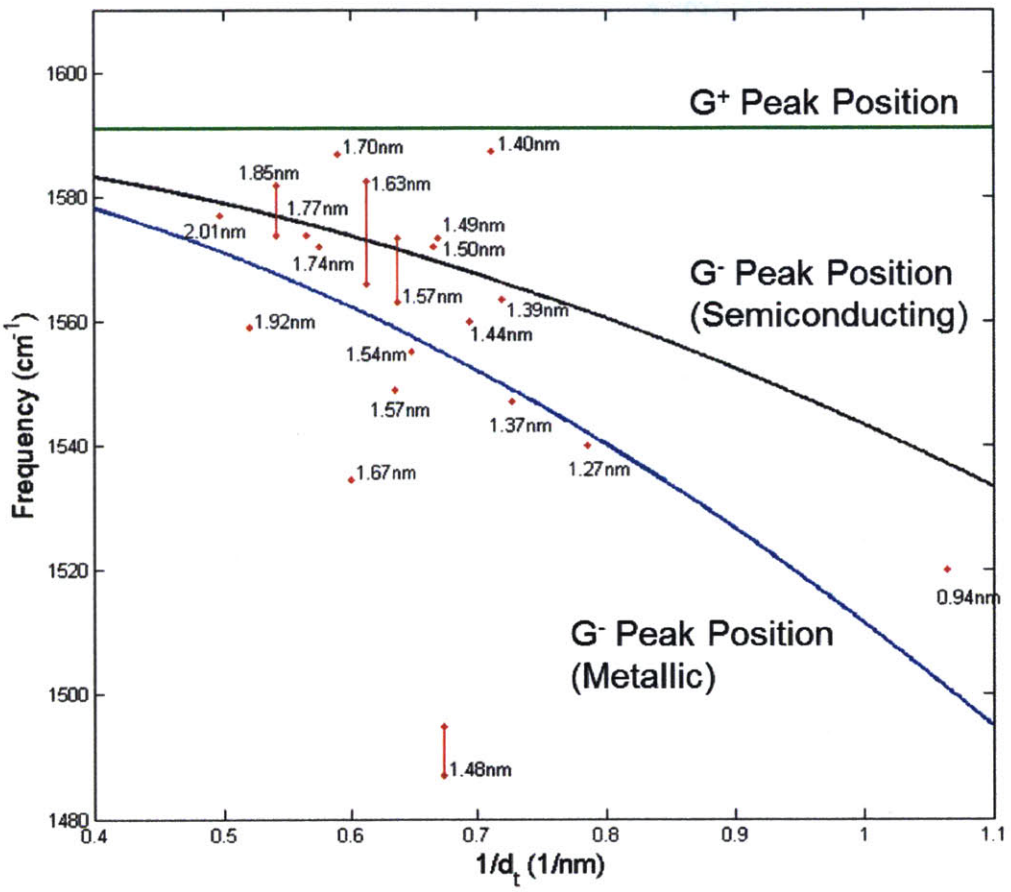

Figure 7-4: G^- peak positions are plotted against inverse tube diameter. The lines are plotted according to the empirical fit found by Jorio et al. [121] The lines indicate the position of the G- peaks for metallic and semiconducting tubes. For reference, the constant G+ peak position is also shown. Each red point corresponds with a single nanotube used in the diameter study. Vertical red lines connecting two points are for samples which had two possible G- peaks.

Table 7.1: Calculated diameters and corresponding metallicity assignment

Diameter (nm)	Nanotube Metallicity (M = metallic, S = semiconducting)
0.94	M
1.27	M
1.37	M
1.39	S
1.4	M
1.44	M
1.48	S
1.49	S
1.50	S
1.54	S
1.569	S
1.575	M
1.63	S
1.67	M
1.7	M
1.74	S
1.77	S
1.85*	S
1.92	S
2.01	M

*Diameter and metallicity are for the inner tube of this DWNT

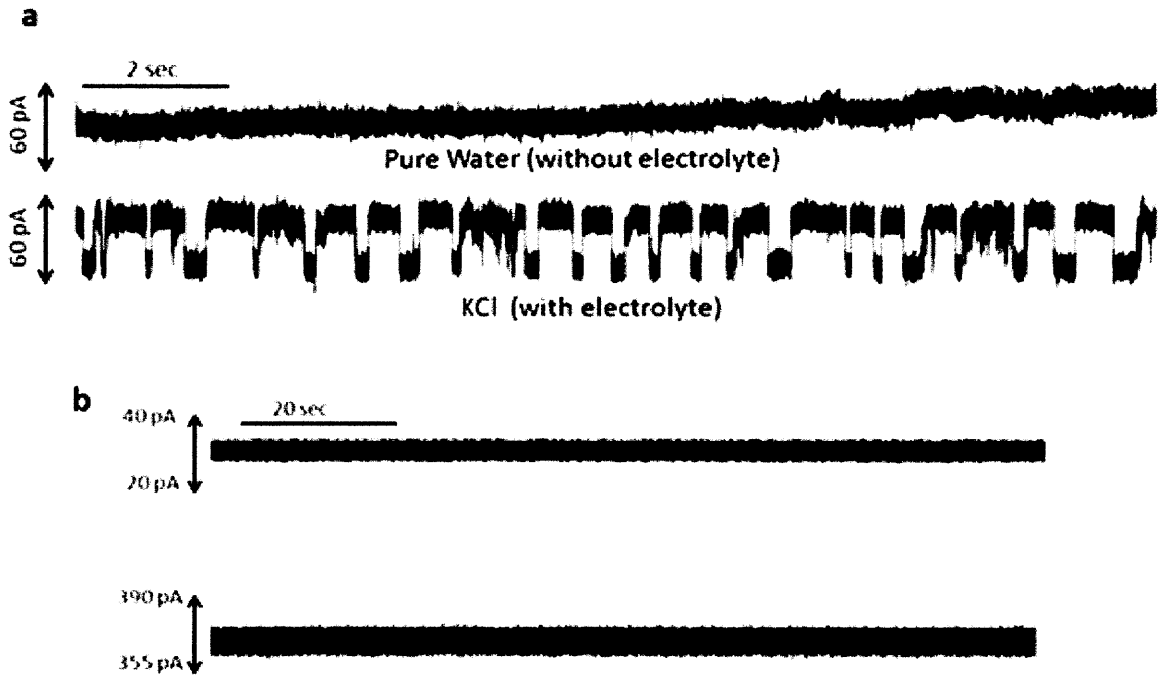

Figure 7-5: Comparison of current traces before and after adding electrolyte solutions and baseline current with and without SWCNTs in devices. a) Comparison between pure water (without electrolyte) and KCl 3M ionic solutions (with electrolyte). b) Comparison of the absolute magnitude of the current level in the devices without (top) SWCNTs and (bottom) with SWCNTs constructed by the epoxy structure in same batch.

ends of the SWCNT were removed using oxygen plasma leaving open SWCNTs that spanned the epoxy barrier. The reservoirs were then filled with electrolyte solutions and Ag/AgCl electrodes added to determine the ionic current between the reservoirs at fixed voltage differences. Electrolyte solutions were all slightly acidic from exposure of DI water-based solution to air. Approximately 200 such devices were fabricated in this manner with a controlled number of SWCNT and SWCNT diameters spanning 0.94 to 2.1 nm. We observed a roughly similar successful device yield – defined as the observation of regular stochastic current fluctuations in response to the application of both an electric field and electrolyte solutions to both reservoir – of approximately 10%.

To confirm ion transport through SWCNTs, we checked the current traces before and after adding electrolyte solutions (Figure 7-5a). Before adding the electrolyte solutions, the current trace is flat with low intrinsic noise (typical RMS noise level). However, after adding electrolyte solutions like KCl and NaCl, within several minutes, the clear Coulter effect was shown with relatively large blockade current compared to the intrinsic noise. Also, it seems

that there was some regular time interval of each pore blocking events like the events in biological ion channels. The flat baseline current without electrolyte were constructed by proton flux through CNTs. However, with electrolyte, the cation was the blocker for the path of proton flux, and the repetitive penetrations made this rhythmic current change.

Devices using epoxy structures in the same batch, in general, maintained similar background and leakage current levels in control devices. To investigate the effects of SWCNTs on the baseline current, devices with SWCNTs are compared to those without SWCNTs fabricated by epoxy structures in the same batch. Figure 7-5b illustrates that the device with many SWCNTs (13) obtain a higher current level than that of the device without SWCNTs. Impurities in the device or the defect appearing during fabrication could make permanently or instantly blocked SWCNTs. However, the baseline current upto 365 pA in a device with SWCNTs is much larger than 32 pA in a device without SWCNTs. It shows that a flow current through the interior of SWCNTs is added to the background and leakage path in sealant barriers. Figure 7-6 summarizes the water baseline current, KCl baseline current and pore-blocking current for 23 devices. In most cases, there is a moderate increase in baseline current upon addition of electrolyte solution, which includes leakage current through the epoxy structure and UV glue.

In pore-blocking events, fast proton flux [60] through the interior of SWCNT results in a high current level, depleting the proton concentration in the near-pore region and increasing the concentration of cations near the pore mouth (Figure 7-1a). Next, cations enter the SWCNT and obstruct the proton flux, resulting in a low current level (Figure 7-1b). Once the blocker emerges from the other side, the high current level is rapidly restored due to the high proton concentration near the pore mouth [145] (Figure 7-1c).

7.3.2 Cation Dependence and Voltage Scaling of Transport Phenomena

We first investigated the influence of ion type and applied voltage on the observed stochastic transport phenomena using several single-SWCNT devices with an unassigned diameter. Figure 7-8a shows typical, unprocessed current traces for a voltage stepping experiment using 3M KCl solution. At an applied voltage of 900 mV, stochastic current fluctuations are observed with a dwell time of 0.16 s and a pore-blocking current I_{BC} of 28 pA. After increasing the applied voltage to 1000 mV, stochastic pore blocking is re-established but with a decreased τ of 0.10 s and an increased I_{BC} of 50 pA. This testing process was repeated

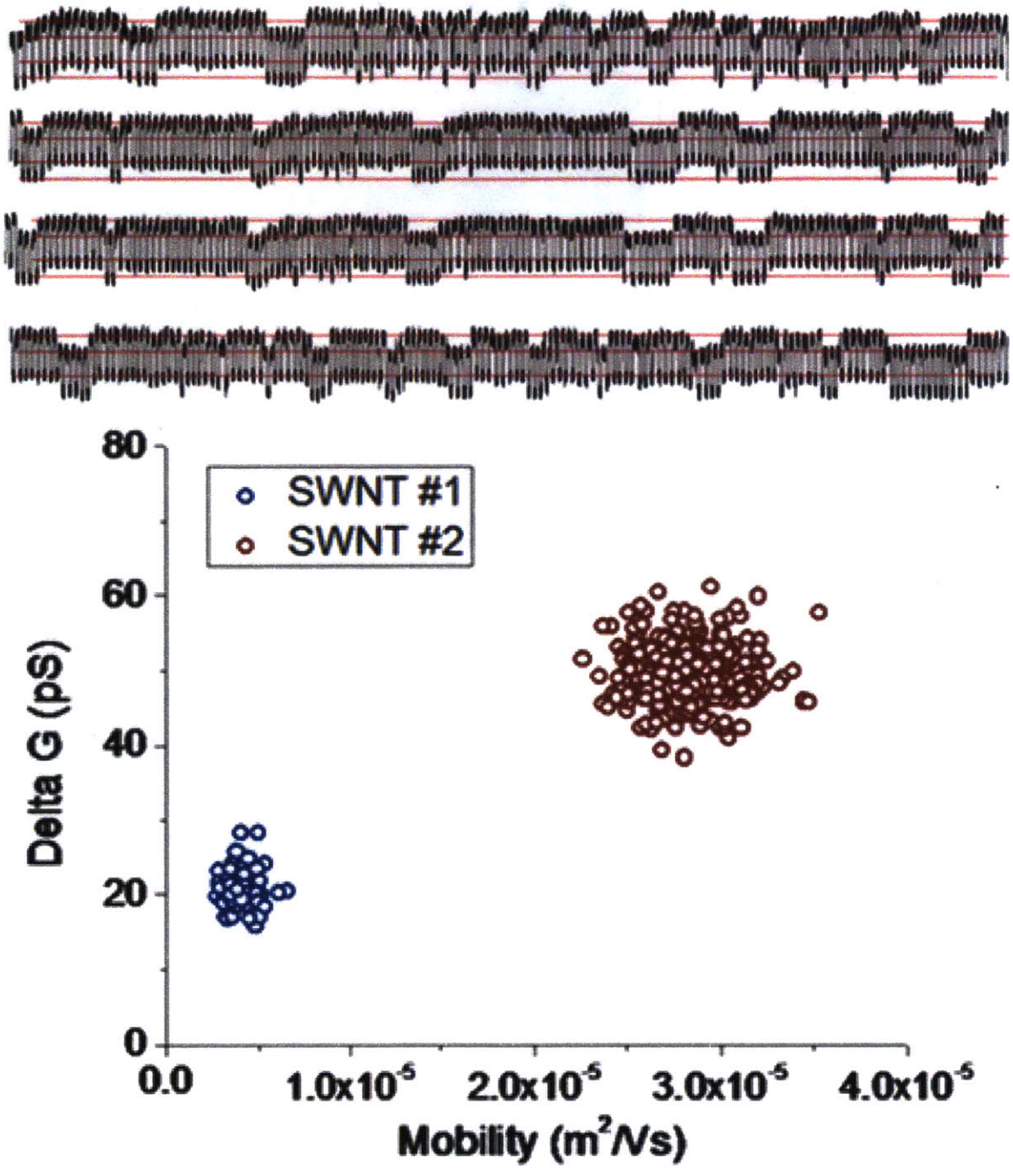

Figure 7-6: Additional examples of two SWCNTs undergoing coherence resonance simultaneously (top) and The conductance change with blocking, ΔG and ion mobilities of two SWCNTs constructing coherence resonance (#1 and #2) (bottom).

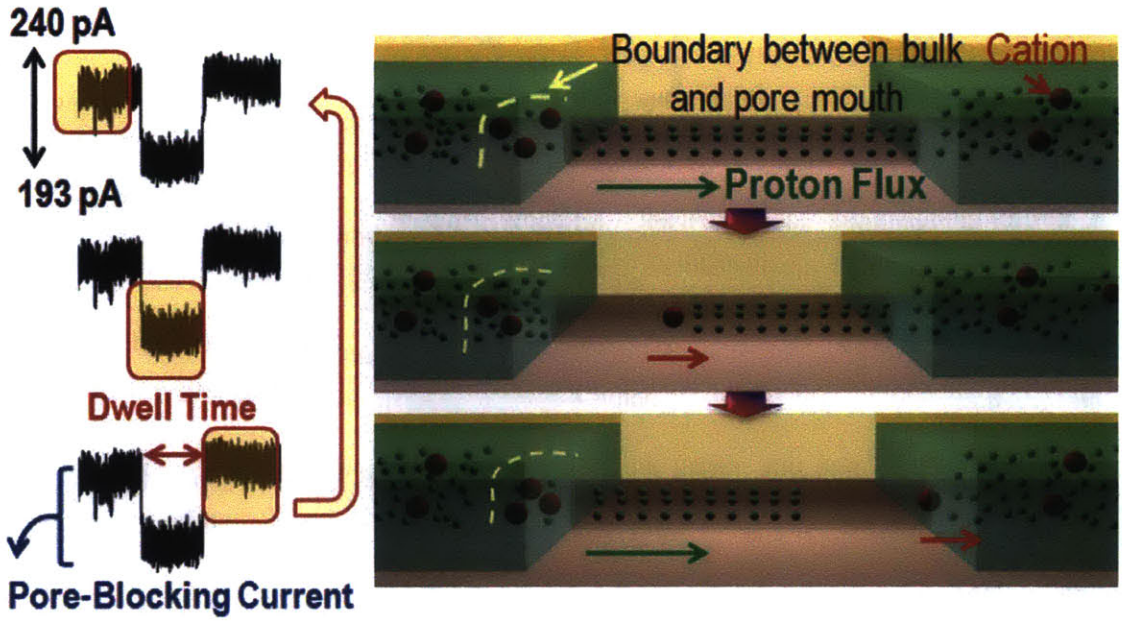

Figure 7-7: Schematic illustration of ion transport and pore-blocking in SWCNTs. (a), Proton flux, (b), ion insertion (blocked by cations), and (c), recovery of proton flux.

for a range of voltages between 500 mV and 1000 mV, and for both K^+ and Cs^+ cations through the same tube, illustrated in Figure 7-8b. The average pore-blocking current and dwell time for K^+ and Cs^+ cations in another SWCNT device were tabulated as a function of applied voltage for each cation and shown in Figure 7-8c and 7-8d, respectively. The average pore-blocking current increased monotonically with applied voltage with a linear low-voltage regime described by our model of pore-blocking below with non-linear, convex deflection at large voltages, while the dwell time decreases monotonically. From a simple scaling analysis, we expect that the pore-blocking current will scale linearly with the electric field inside the tube, calculated as the potential drop per unit length or $\Delta I \propto (\Delta V - \Delta V_t)/L$, where ΔV is the applied voltage difference across the two reservoirs, ΔV_t is the threshold voltage loss across the pore observed previously [43] and the minimum voltage to observe pore-blocking phenomena, and L is the length of the connecting SWCNT. Similarly, we expect that the dwell time will scale as, $\tau = L/[(\Delta V - \Delta V_t)\,\mu_{eff}]$ where μ_{eff} is an effective ion mobility taking into account both diffusive and convective effects. These relations can also be recovered using a series expansion of the nonlinear model below to first order for small electric fields. The minimum voltage ΔV_t to observe stochastic blocking is larger for cesium ions (800mV) than for potassium ions (500 mV), consistent with an electrostatic

barrier to pore transport, as observed earlier [43]. We show similar measurements for a divalent cation, Ca^{2+}, in Figure 7-8e/7-8f, which shows a ΔV_t of 200 mV, and follows similar scaling relationships (solid line). Also, it should be noted that lower concentration of salt (K^+, Cs^+, Ca^{2+}) caused the long unblocked durations and the pore-blocking events would be rare events because this condition would decrease the probability of the penetration of blockers inside of SWCNTs.

The cation type (K^+, Cs^+, Li^+, Na^+) was then varied for a single device with a single anion type (Cl^-) resulting in regular stochastic fluctuations with a range of dwell times and pore-blocking current, shown in Figure 7-8g. Interestingly, the average pore-blocking currents and dwell time, shown in Figure 7-8h/7-8i, exhibit a non-intuitive scaling with $K^+ > Cs^+ > Na^+ > Li^+$ for the former and $Li^+ < K^+ < Cs^+ < Na^+$ for the latter. The rapid transport of Li^+ seems to be consistent with our previous observations [145], despite its larger bulk ionic radius [150]. The unique scaling of these transport parameters may reflect changes in hydrated radius from bulk to a nano-confined environments, induced by shedding its hydration shells of ions to enter the molecular confined nanochannels and suggest future theoretical studies on the solvation structure of cations within SWCNTs. We note that the strong dependence of blocking phenomena on cation type reinforces our understanding that the cation is central to the blocking mechanism, as we have previously observed [43, 145].

7.3.3 Diameter Dependence of Transport Phenomena

Differences in stochastic pore-blocking phenomena for 12 devices with a single connecting SWCNT of varying diameter reveal the first direct experimental demonstration of strongly non-monotonic diameter dependence. Figure 7-9 shows current traces and dwell time / pore-blocking current histograms for two single-SWCNT devices, one with a diameter of 1.74 nm (top) and the other with a diameter of 1.67 nm (bottom)), both using a 3M KCl solution and applied voltage of 1000 mV. The device with the smaller 1.67 nm diameter shows qualitatively different pore-blocking phenomena and has a much larger pore-blocking current (95 pA compared to 53 pA) and much smaller dwell time (9 ms compared to 16 ms). Despite the small difference in diameter, there is a large disparity in blockade current, contrary to a simple hypothesis that transport rates increase monotonically with diameter, as would be expected for a larger nanopore with bulk-like transport [239, 58].

Exploring this disparity further, the dependence of transport phenomena on SWCNTs

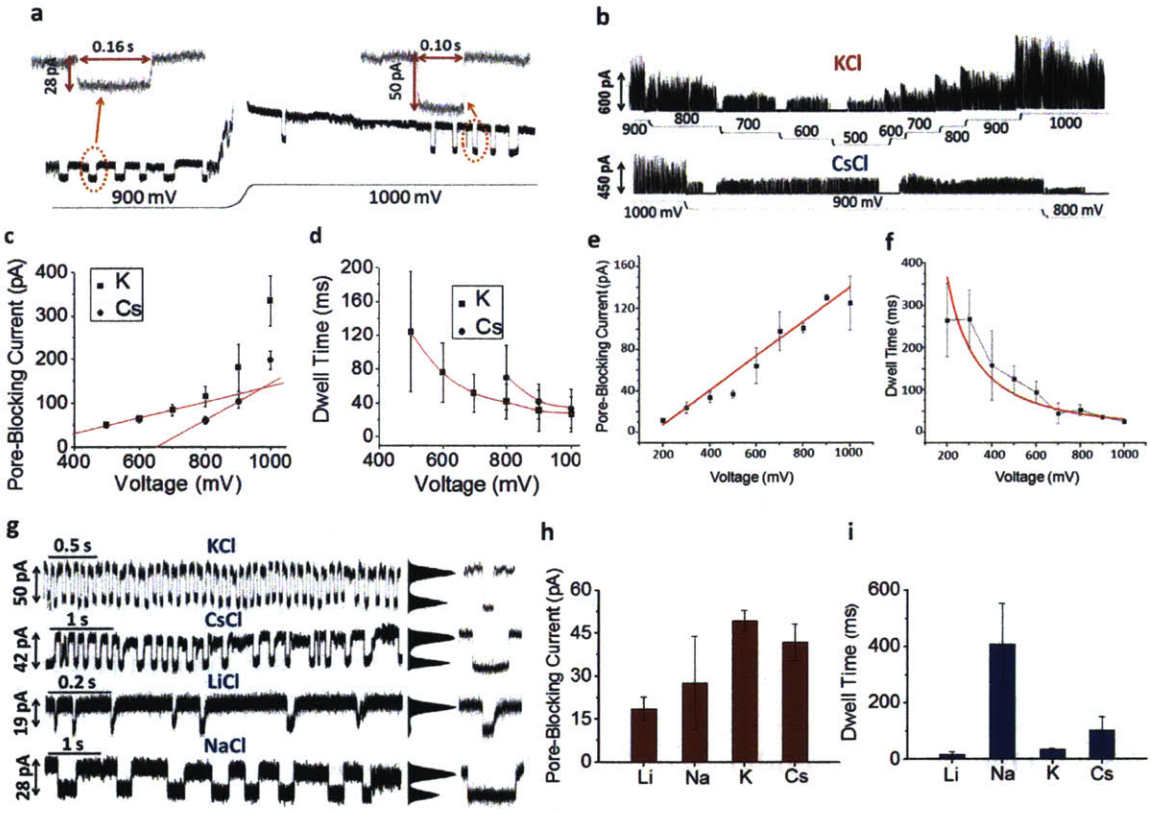

Figure 7-8: The effect of cation type on pore-blocking phenomena. (a), Example of pore-blocking phenomena tested with 3M KCl at two applied voltages. (b), Voltage-scanning experiment for a single SWCNT with two cation types at several voltages. (c/d), Tabulated data for the effect of voltage on dwell time and pore-blocking current for potassium and cesium ions. (e/f), Effect of voltage on dwell time and pore-blocking current for a divalent cation, calcium. (g), Qualitative demonstration of the impact of four cation types on pore-blocking phenomena (left), as well as current histograms clearly demonstrating two-state oscillations. The expanded raw data (right) shows distinctive pore blocking current and dwell time behavior as cation types are changed. (h/i), Tabulated data for the effect of cation type on observed dwell time and pore-blocking current.

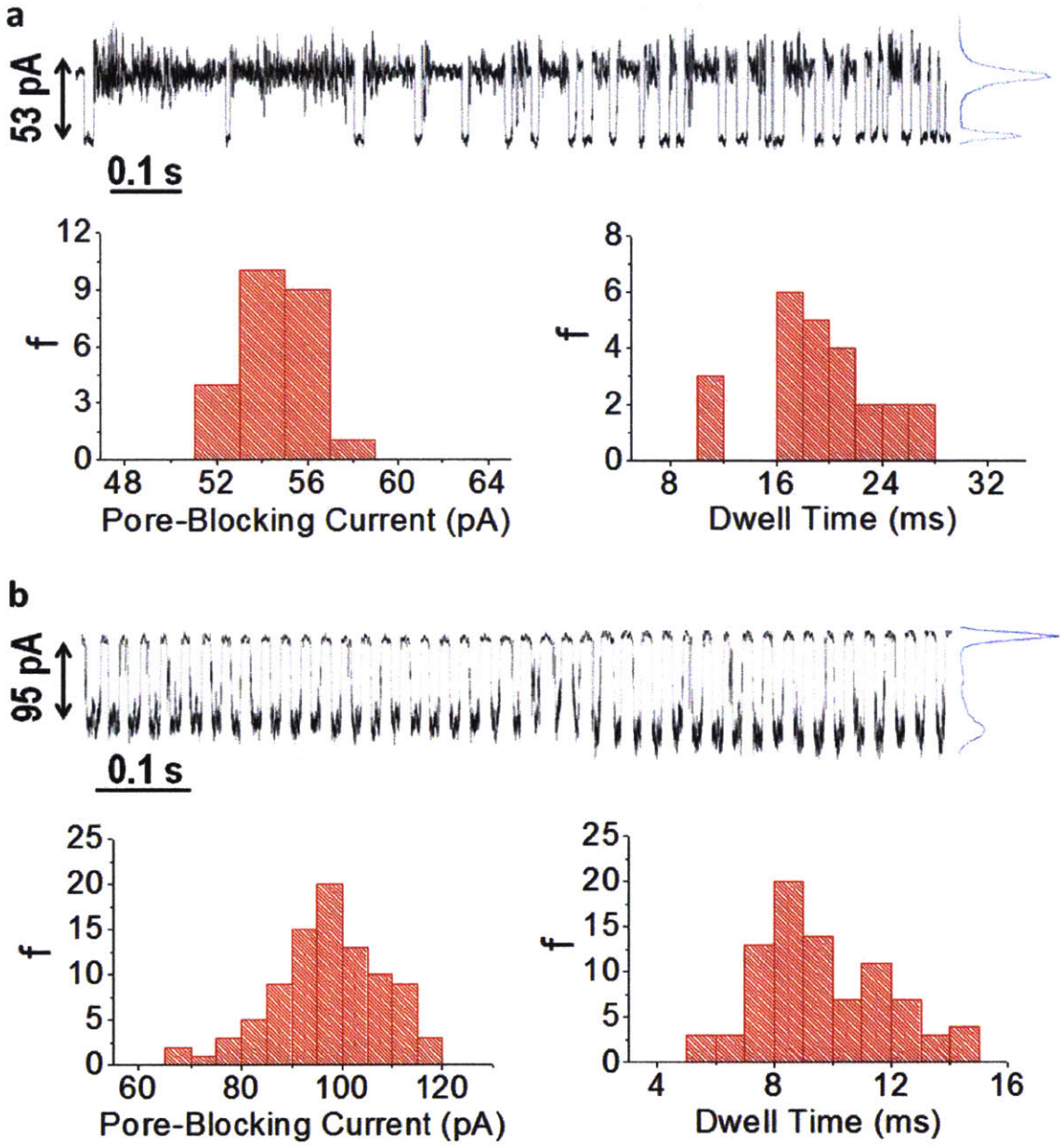

Figure 7-9: Pore-blocking for two single-SWCNT devices with different SWCNT diameters. (a), 1.74 nm, (b) 1.67 nm, tested at the same applied voltage (1V) and electrolyte solution (3M KCl).

with diameters between 0.94 nm and 2.01 nm is presented in Figure 7-13a, revealing that proton transport in SWCNTs is at a local maximum at approximately 1.6 nm. Data collected from single-SWCNT devices are shown in blue, while data from devices intentionally containing two or three SWCNT are depicted in black, all using a 3M KCl solution and applied voltage of 1,000 mV, and identical fabrication conditions. The scatter plot from single SWCNT devices was constructed first. From an analysis of only single-SWCNT containing devices, there is a statistically significant enhancement at 1.63 nm (a Student t-test suggests that the maximum at 1.6 nm is statistically significant from the other devices with $p<10^{-6}$). We note a main peak at 1.6 nm (Fig 7-13b), and two significant but smaller increases in pore-blocking current at the limits of the diameter range (0.94 and 2.01 nm), but no clear maximum in the dwell time (Fig 7-13c). Our device fabrication techniques can selectively choose a SWCNT diameter for the platform, and it can be used to explore the unique trend near 1.6 nm range. Two devices fabricated to have multiple-SWCNT channels show similar enhancement with each containing one SWCNT in the vicinity of 1.6 nm (1.57 nm and 1.58 nm), further supporting the trend. Using the observed maximum, it was possible to assign blocking events to specific individual SWCNTs. For example, a device with two SWCNTs of diameter 1.6nm and 1.8nm that exhibited two sets of stochastic behavior with very different pore-blocking currents, could be assigned with the knowledge that there is a strong peak in pore-blocking current at 1.6nm. We used this data to supplement the trends in the single-device data. The assignment of metallic or semiconducting of each SWCNT was determined from Raman characterization, but somewhat surprisingly, the designation does not seem to correlate with observed transport characteristics. All data points from each device are shown as scatter plots (See Figures 7-10, 7-11, 7-12).

7.3.4 Temperature Dependence of Transport Phenomena

The temperature dependence of pore-blocking can shed light on the transport mechanism, and determine the influence of structured, solid water as suggested in simulations [241, 87]. Reversibly heating the platform (Fig 6a) to 50°C while recording I_{BC} was used to explore three single SWCNT devices of unassigned diameter (See the Methods and section 7.8). Room temperature I_{BC} data suggests that one SWCNT (red) lies near 1.6 nm and the other two do not. I_{BC} decreases with an Arrhenius dependence (Figure 7-14b) for all three with apparent activation energies of 6, 11, 15, kcal/mol (see Table 7.2). These values are larger

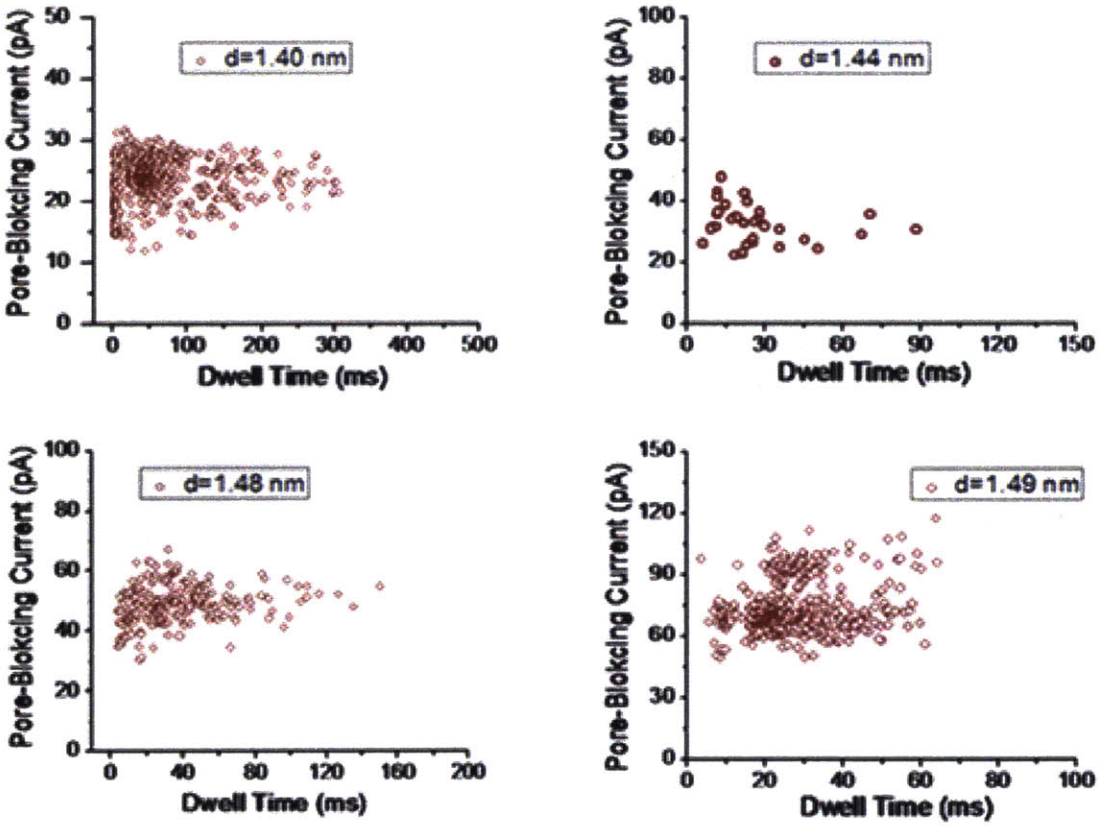

Figure 7-10: Scatter plots of pore-blocking currents versus dwell times for nanotubes used in the diameter study (0.9 nm-1.49 nm).

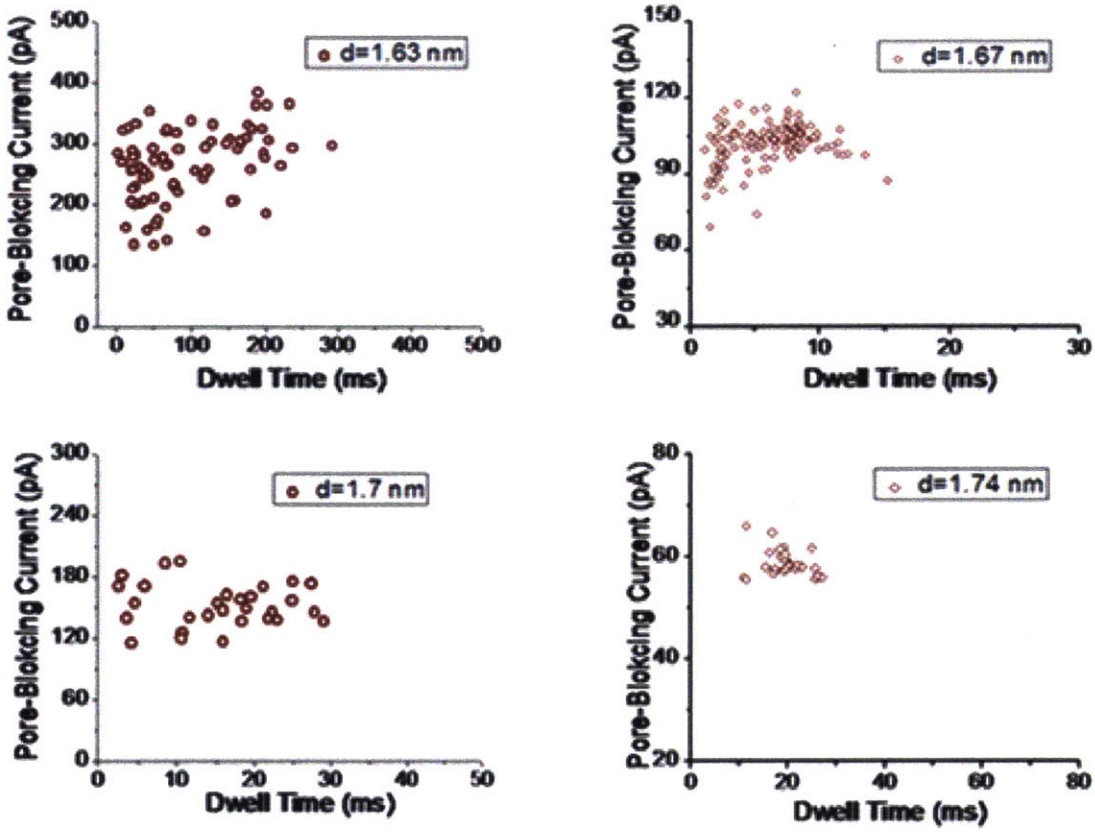

Figure 7-11: Scatter plots of pore-blocking currents versus dwell times for nanotubes used in the diameter study (1.5 nm-1.74 nm).

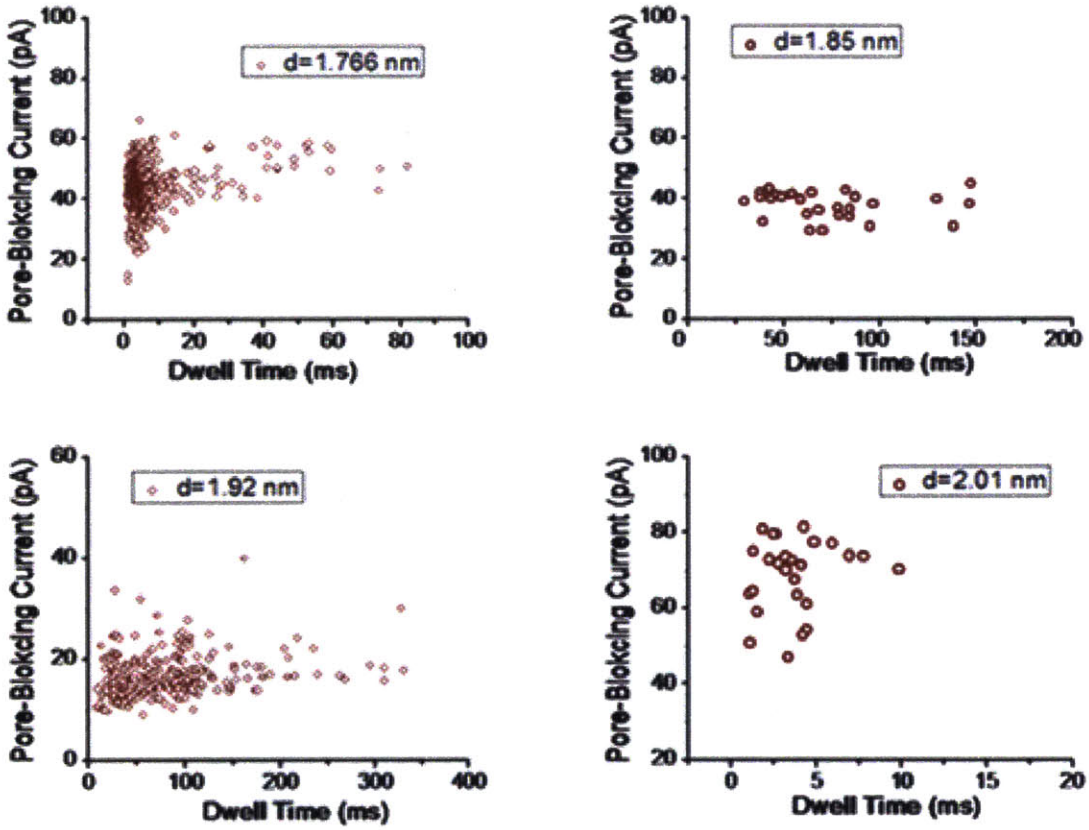

Figure 7-12: Scatter plots of pore-blocking currents versus dwell times for nanotubes used in the diameter study (1.766 nm-2.01 nm).

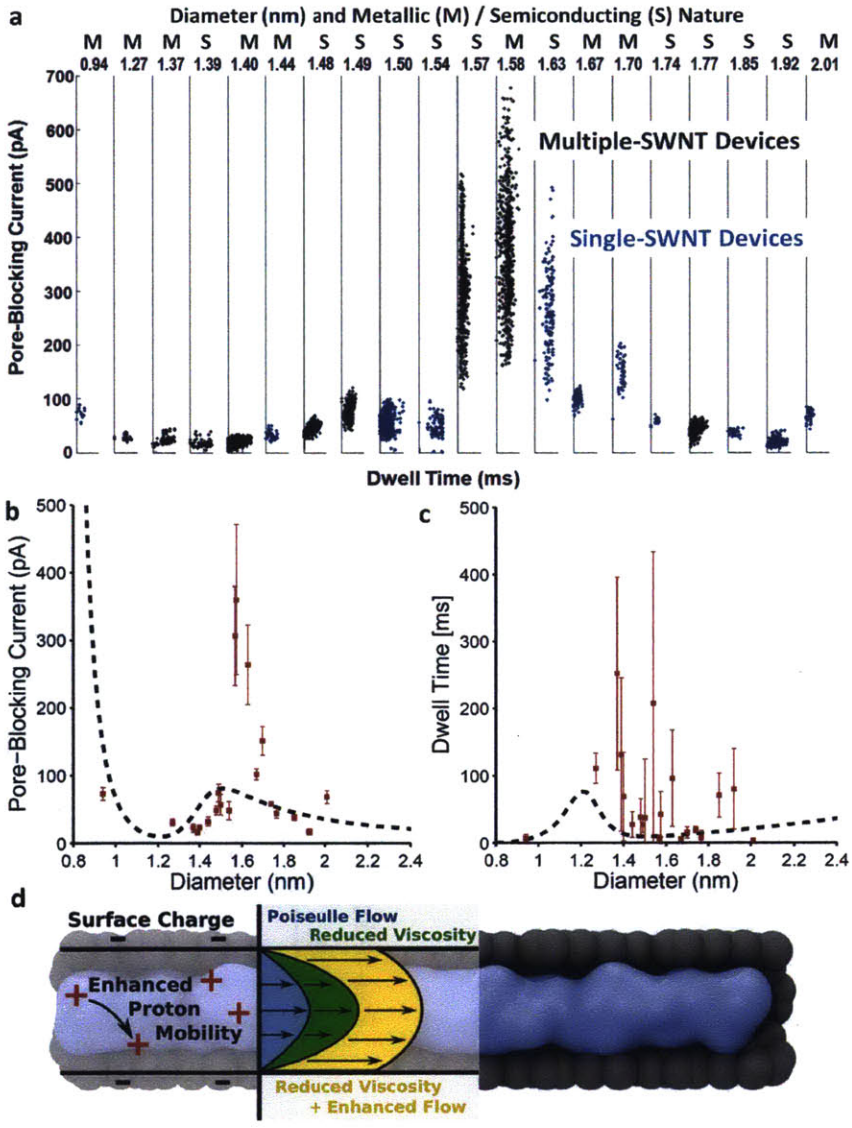

Figure 7-13: Diameter dependence of ion transport phenomena. (a) Pore-blocking current for each device separated by observed dwell time, with diameter and metallic/semiconductor nature marked. x-axis is displayed on a log scale (10^0-10^3 (milliseconds)), all tested with 3M KCl and 1V applied voltage. (b,c), Observed pore-blocking current and dwell time as a function of SWCNT diameter, along with the results from the electrochemical model. Error bars represent the range of measurements over the many stochastic events for each SWCNT. (d), Illustration of the physical effects accounted for in the electrochemical model.

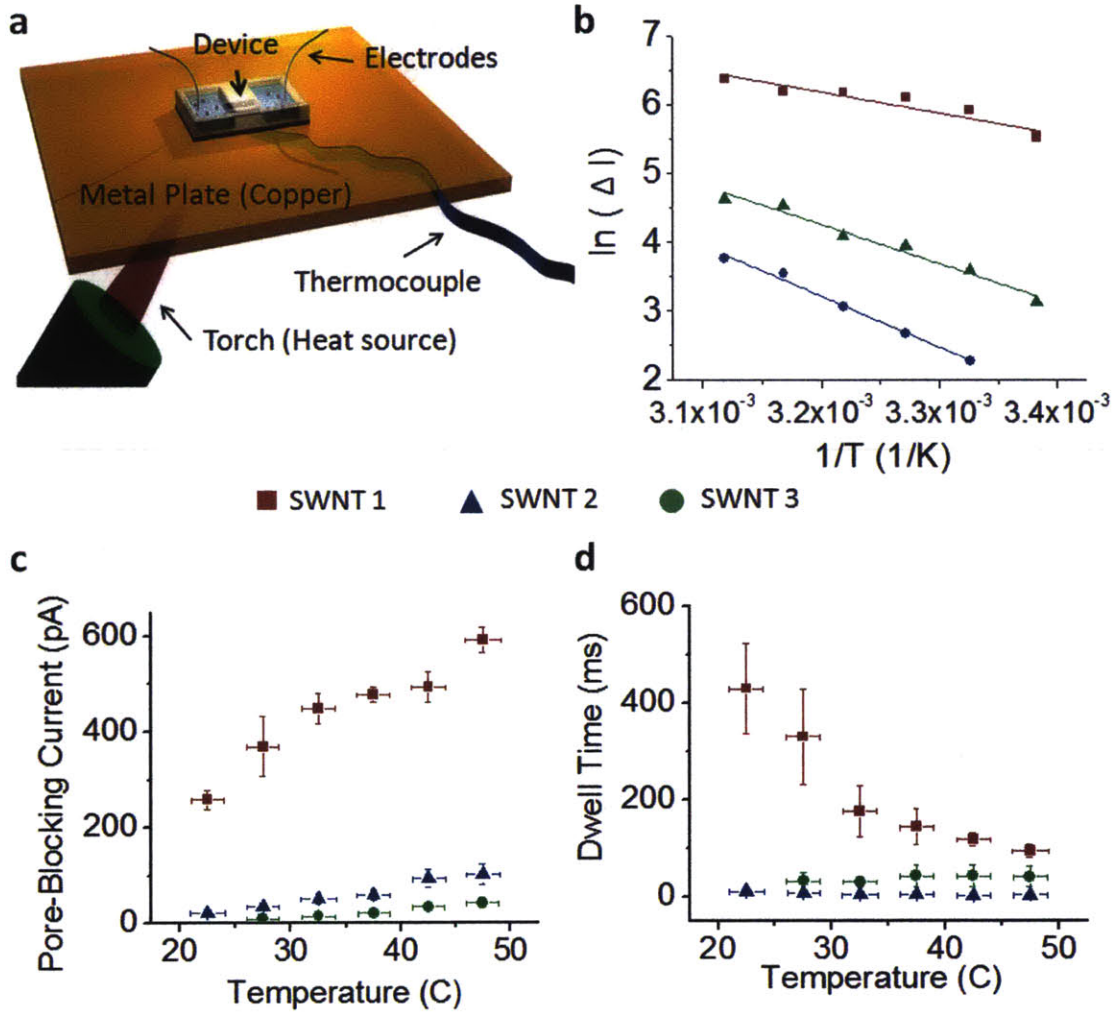

Figure 7-14: Temperature dependence of ion transport for three single-SWCNT devices. (a), Illustration of the modified setup for temperature-dependent measurements. (b), Arrhenius plot of the pore-blocking current for the three devices. (c/d), Pore-blocking current and dwell time for each device over the range of tested temperatures. Error bars represent the range of transport measurements for each SWCNT at each temperature.

Table 7.2: Arrhenius plot parameters from temperature scaling experiments.

	Slope ($-E_a/R$)	Intercept ($\ln\Delta I$)	E_a (kJ/mol)
SWNT 1	-3075	16.02	25.57
SWNT 2	-5696	26.89	61.53
SWNT 3	-7401	22.48	47.46

than the activation energies necessary for accelerated proton transport via the Grotthus mechanism alone, which is estimated at only 2-3 kcal/mol [56, 5]. Possible sources of this activation energy are the presence of an energy barrier at the SWCNT entrance or exit region, or a secondary effect from temperature dependence of the proton-water equilibrium [137]. Especially, the energy barrier near the entrance might be due to the desolvation of a cation species in going into one SWCNT [19], with an activation energy of about 12 kcal/mol activation [59]. Also, transition of atomic water density structures depending on temperature changes [87] might affect the requirement of energy to occupy the nanoscale channels by the blockers. Most interesting is that there is not a discontinuity indicative of a phase transition, suggesting that a liquid water phase is present throughout our diameter range. Similar temperature scaling data is shown in Figure 7-13d for the dwell time, with the SWCNT near 1.6 nm (red) decreasing as temperature increases. The trend for the other two is opposite. Such diverse behavior is perhaps anticipated by the non-monotonic trends with diameter uncovered in this work, motivating further study of SWCNT transport in this range.

7.4 Discussion

Our results are easily understood within a simple electrochemical model building upon previous theoretical studies on the diameter dependence of transport through SWCNTs. Water confined in nanopores of diameter similar to its molecular size demonstrate slip-flow at the walls [248], reduced viscosity [268], and increased proton transport rates [60]. Both protons and blocking ions within a SWCNT will feel these effects and our simple model, illustrated in Figure 7-13d, builds upon these studies to reproduce the transport maximum

that we observe experimentally. We note that previous transport models proposed to explain similar effects [198] do not explicitly contain the diameter dependencies in all parameters.

First, we assume a fitted diameter-independent linear charge density on the SWCNT, similar to that of previous works [198], that results in a net positive proton concentration in the SWCNT interior. With the much larger aspect ratio, we expect a more linear electric field throughout most of the length of our device than previous studies [198], resulting in convective proton transport as well as diffusive proton transport if the SWCNT is not blocked with a larger cation. If the protons are unable to interact directly with the SWCNT walls, the energy being dissipated at steady state from the electric field must be dissipated to the surrounding fluid in the SWCNT. We model this proton driving force as an effective pressure that drives water convection. At steady state, the energy required for hydrodynamic flow (lhs) is balanced by the energy of proton transport through the electric field (rhs), hence:

$$32\frac{\bar{v}^{\mathrm{O}}\eta\left(D\right)}{\varepsilon\left(D\right)}=4\frac{eC_{\mathrm{H}}^{\mathrm{O}}E_{\mathrm{f}}}{\pi}\left(\frac{\mu_{\mathrm{H}}\left(D\right)E_{\mathrm{f}}}{\bar{v}^{\mathrm{B}}}+1\right) \tag{7.1}$$

for the open channel state and

$$32\frac{\bar{v}^{\mathrm{B}}\eta(D)}{\varepsilon(D)}=4\frac{eC_{\mathrm{H}}^{\mathrm{B}}E_{f}}{\pi}\left(\frac{\mu_{\mathrm{H}}\left(D\right)E_{\mathrm{f}}}{\bar{v}^{\mathrm{B}}}\right) \tag{7.2}$$

for the blocked state. Here $\bar{v}^{O}$, $\bar{v}^{B}$ are the mean fluid velocity in the SWCNT in the open and blocked states respectively, η is a diameter-dependent water viscosity [268], D is the SWCNT diameter, C_{H}^{O}, C_{H}^{B} are the proton concentration (balancing the SWCNT charge) in the open and blocked states respectively, $\mu_{H}\left(D\right)$ is the diameter-dependent proton mobility, E_{f} is the uniform electric field magnitude, and ε is a diameter-dependent enhancement factor fitted to smoothly represent literature simulation results[31] that represents deviations in fluid transport from an ideal Poiseuille flow through a pipe of equivalent diameter (See section 7.7 and Figure 7-15). We approximate the proton mobility with an exponential interpolation between the small diameter enhanced rate mobility [60] and bulk transport rates [52]. We note that most of the properties are strongly diameter-dependent, currently not well-understood, and with varying values in literature, since only simulation results have been available to date without an experimental platform for validation. The proton concentration is assumed to be diameter independent and influenced by whether the SWCNT is blocked by a translocating ion. After solving for the open and blocked fluid velocities, $\bar{v}^{O}$

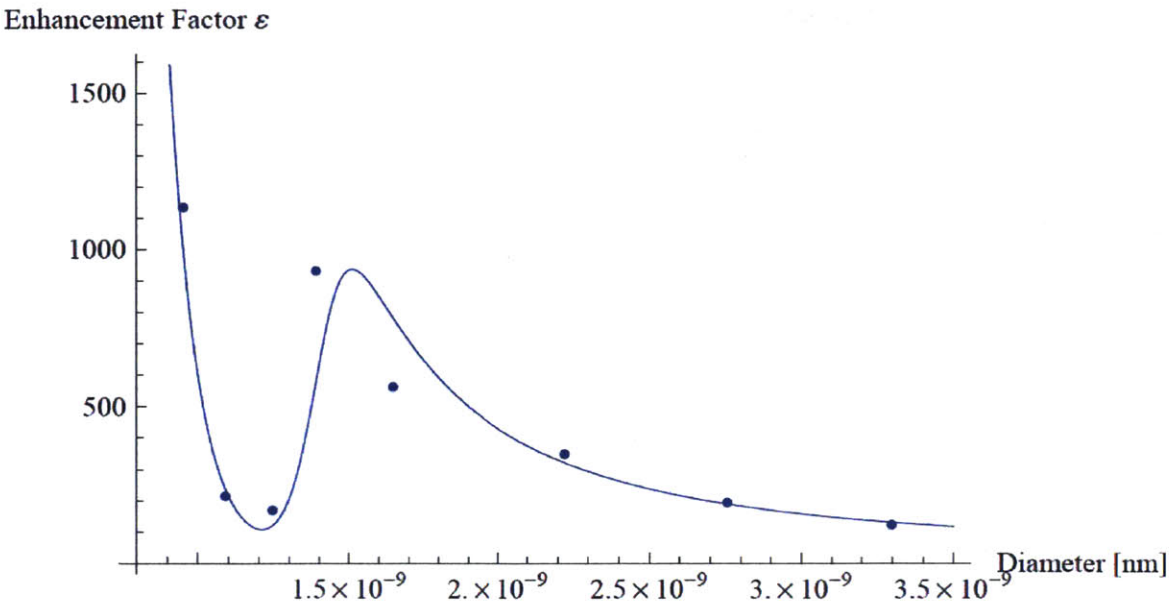

Figure 7-15: Diameter dependent flow enhancement factor ε. Closed circles are taken from literature31, and the smooth line is a fit of the form $\varepsilon(D) = \alpha e^{\beta D} + \gamma e^{\kappa D}$.

and $\bar{v}^B$, the key experimentally-observable quantities can be calculated: $I_{BC} = e(C_H^O \bar{v}^O + \mu_H E - C_H^B \bar{v}^B)$ and, assuming the ion is carried in the convective flow, the dwell time $\tau = L/\bar{v}^B$, where L is the length of the SWCNT. Although our model uses two fitted parameters as in previous literature studies [198], the SWCNT surface charge in the open and closed state, C_H^O, C_H^B, these quantities affect only the magnitude of the pore-blocking current and dwell time and not the characteristic diameter dependence we report here.

A comparison of our experimentally determined diameter dependence and this electrochemical model are shown in Figures 7-13b and 7-13c. Critically, we note that the position of the local maximum in Figure 7-13b is approximately reproduced at 1.5 nm compared to 1.6 nm observed, primarily through the strong diameter-dependence of ε. There is an increasing trend of I_{BC} as diameter decreases for D<1.2 nm as the water structure becomes more important and at large diameters (D>1.9 nm) as transport approaches the bulk (Poiseuille) case. The overall trend of I_{BC} is similar since it is fitted through the proton concentrations, but the model predicts a smaller peak in the blockade current at the 1.6 nm local maximum found experimentally. There is less agreement between this model and the observed dwell times, but the predicted times are within an order of magnitude. Also, there is a hypothesis about the change of coordination number of ions near this critical diameter. It is well known that the bulk hydration radius is not the same as that in the nano-confined

structures. However, it is not known which channel sizes tend to shed hydration shells and change hydrated radius to accept the specific ions. Changing the cation type could alter the precise location of this transition region based on the ion hydration structure, but this is unexplored in this work aside from noting the ionic dependence on the blockade current and dwell time.

7.5 Conclusion

In conclusion, the first experimental support for non-monotonic diameter-dependent transport in single-walled carbon nanotubes is demonstrated and analyzed. We expect further simulation and theoretical study to elucidate the precise mechanisms behind these effects. These results highlight several outstanding issues that prevent the prediction of these phenomena from first-principles. An obvious extension to a quantitative understanding of these effects would be the design of functionalized SWCNT with specific diameters to optimally transport or filter new molecules of interest.

7.6 Methods

7.6.1 Growth of Ultra-Long Aligned SWCNTs.

The platform is constructed using an epoxy structure that acts as both an oxygen plasma mask for the opening of the nanotube ends, and to form two liquid reservoirs at either side. The SWCNT are synthesized and aligned using by methane CVD in a horizontal quartz tube furnace with an inner diameter of 22 mm (CVD furnace : Thermo Fisher Scientific Lindberg/Blue M * 1100°C, TF55035A, Mass flow controller : Aalborg SDPROC Microprocessor Driven Command Module). After a catalyst layer, 0.5 nm-thick Fe, was deposited on a Si/SiO_2 wafer by electron beam evaporation, the substrate was placed in the quartz tube. Methane (CH_4) was used as the carbon source. Hydrogen (H_2) and argon (Ar) were used as catalysts and carrier gases, respectively. The flow rate was 3 sccm of H_2 during increase of temperature up to 950°C for 46 minutes, and the temperature and the flow rate were maintained for 30 minutes. Next, the temperature was increased up to 1015°C for 33 minutes. After these steps, CH_4 was introduced into the furnace at 1015°C and 1 atm, and ultra-long aligned SWCNTs were grown for 3 h 30 minutes.

7.6.2 Characterization of a Single SWCNT by Raman Spectroscopy.

The diameter and metallicity of each carbon nanotube used in devices for the diameter study was characterized using Raman spectroscopy (Horiba LabRAM HR). In order to locate individual single-walled carbon nanotubes (SWCNT), optically-observable markers were placed on the substrate and imaged in a scanning electron microscope (SEM), which can be used to image carbon nanotubes. The relative distance between the marker and SWCNT were used to locate the SWCNT in the Raman's optical microscope. A 633 nm laser excitation source was predominantly used to identify the SWCNT, although a 532 nm laser excitation source was also used in some cases.

From the Raman spectrum, the radial breathing mode (RBM) peak position has been found to be inversely related to the carbon nanotube diameter through the following relation: $d_t = 248/\omega_{RBM}$, which is valid for isolated SWCNT sitting on a silicon oxide substrate [120]. The Raman RBM spectra for all 20 different nanotube diameters are shown in Figure 7-3. One device actually contained a double-walled carbon nanotube (DWNT) as indicated by the presence of two RBM peaks; in this case, the smaller, inner tube's diameter was used.

The G band of the carbon nanotube corresponds to tangential vibrations of the carbon atoms in the carbon nanotube, and it is observed at higher wavenumber shifts (~1550-1600 cm^{-1}) in the Raman spectrum. The G band contains two peaks, the G^- and G^+ peaks, where the G^+ peak stays mostly constant around 1591 cm^{-1} and the G^- peak is at lower wavenumber shifts and changes more dramatically. The shape of the G^- peak gives evidence of the metallicity of the tube. Metallic tubes have broader G^- peaks that are softened compared to those of semiconducting tubes. Metallic G^- peaks can also be fitted to a Breit-Wigner-Fano (BWF) lineshape, compared with a Lorentzian lineshape for those of semiconducting tubes [121]. The deconvoluted Raman G band spectra for all 20 different nanotube diameters are shown in Figure 7-3, with the G^- peak fitted to a BWF or Lorentzian (depending on whether the nanotube was determined to be metallic or semiconducting), and the G^+ peak fitted to a Lorentzian. In several cases, an additional peak was observed, which was thought to be due to amorphous carbon around the SWCNT from the growth process.

The criteria used to determine the metallicity of the tube was by first looking for distinctly broad or sharp G^- peaks, which would indicate that the nanotube was metallic or semiconducting, respectively. For tubes whose assignment was still ambiguous, the posi-

tion of the G^- peak was used to determine the metallicity, as metallic tubes have softened G^- phonon modes relative to semiconducting tubes. The empirical fits from Jorio et al. were used to assign metallicity to the ambiguous tubes, as shown in Figure 7-4 [121]. The diameters and metallicity of all the nanotubes are summarized in Table 7.1.

7.6.3 Device Fabrication and Measurement of Pore-blocking

Horizontally-aligned SWCNT were grown using chemical vapour deposition. The specific markers that indicate the position of SWCNTs on silicon wafer were deposited by E-beam evaporation technique. At this stage, SWCNTs on the specific area were characterized by Raman spectra, which would give the information of diameters and types (metal or semiconducting) of SWCNTs. According to the collected information, the only one SWCNT was chosen and remained as the specific nanochannel in the device, whereas all other SWCNTs were removed by a razor blade etching process. SU-8 photoresist was used to fabricate the epoxy structure for reservoirs of ionic solution and a mask against plasma etching, A constant-volume-injection method with spin-coating was used to construct an ultra-thick SU-8 epoxy structure. The epoxy structure was glued onto the silicon wafer containing one ultra-long aligned SWCNT using a UV-curing optical adhesive (Norland) to form a tight seal. The plasma etch removes an exposed SWCNT leaving 1 mm across the protected section, and opens both ends at the bottom of epoxy reservoirs. The duration of oxygen plasma etching was optimized to remove the exposed parts of a SWCNT and not to etch out the nanofluidic part of a SWCNT underneath the epoxy wall. SEM images were recorded during the process, repeatedly. With both compartments filled with ~ 15-60 µL aqueous ionic solution (KCl, LiCl, NaCl, CsCl, $CaCl_2$) ion current across the reservoirs was monitored using Axopatch 200B (Molecular Devices, 2 kHz Bessel low-pass filter, 250 kHz acquisition frequency). Ag/AgCl electrodes are used to apply electric field across the reservoirs.

7.6.4 Successful Device Manufacturing Rate.

A number of devices with one, two or three SWCNTs were fabricated and tested for ion translocation with a voltage clamp setup. A higher failure rate has been observed in a device with a single SWCNT compared to multi-SWCNTs devices. In the previous work, multiple SWCNTs in one device were fabricated to increase the probability of the observation of ion transport during experiments. Many SWCNTS in multi-SWCNTs devices were

permanently blocked by impurities or defects from CVD or fabrication processes. Moreover, SWCNTs with a high aspect ratio might be bent or damaged during the fabrication, and these uncertain obstructions could block the paths of ions. An applied electric field (max 1000 mV) may also be below the necessary field to begin ion translocation by cleaning the blocking species or to overcome the potential barrier (threshold voltage) near the pore mouth. Therefore, many devices were fabricated and tested. Pore-blocking events were identified in about 15 devices out of over 100 devices.

7.6.5 Temperature Dependence Experiments.

In order to determine the effect of temperature on observed transport characteristics, the devices were heated during a typical voltage clamp experiment. Because of the low currents being measured (picoamps), a butane torch was used as the heating device, as opposed to a hot plate, which produced too much interfering electrical noise. Figure 7-17 is a photo of the temperature scaling setup. The torch is fixed to the optical table and directed toward the sample, which is placed on a thermally-conductive surface. A thermocouple placed close to the sample is used to record the temperature in real-time. During the experiment, the torch was turned on when regular pore blocking events are observed, using the same 3M KCl solution as in the diameter experiments. Figure 7-16 shows the typical temperature response from application of the torch. The temperature during this experiment was kept under 50 ^{o}C to avoid excessive evaporation. According to the calibration process, we found that applying heat from the torch for 7 seconds would increase the temperature up to 50°C. Due to the heat transfer delay, the temperature reaches the maximum after 20 seconds of stopping the torch. After the maximum temperature is reached, the system cools down slowly through heat transfer to the environment. During this time, ion transport events are monitored using the voltage clamp apparatus and correlated to specific temperatures.

7.7 Electrochemical Model for Diameter-Dependent Pore-Blocking

We start by considering the scenario when the tube is in the "open" state - that is, there is no blocking ion. Furthermore, we consider the case when there is a net fluid velocity in the tube, with some amount of slip at the walls (the precise velocity profile is not so important).

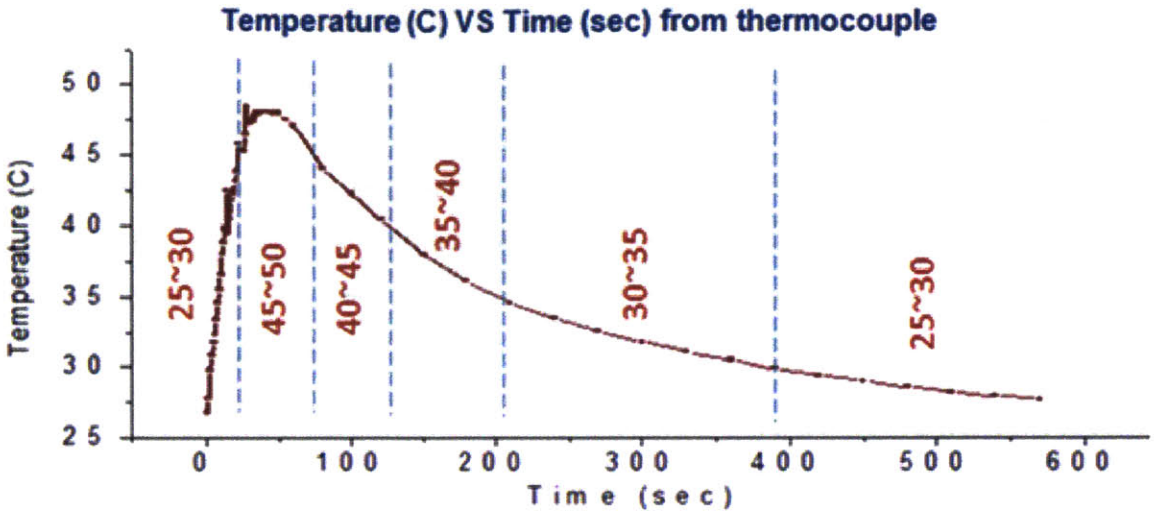

Figure 7-16: Temperature (Celcius) vs time (sec) plot during the heating by torch and subsequent cooling.

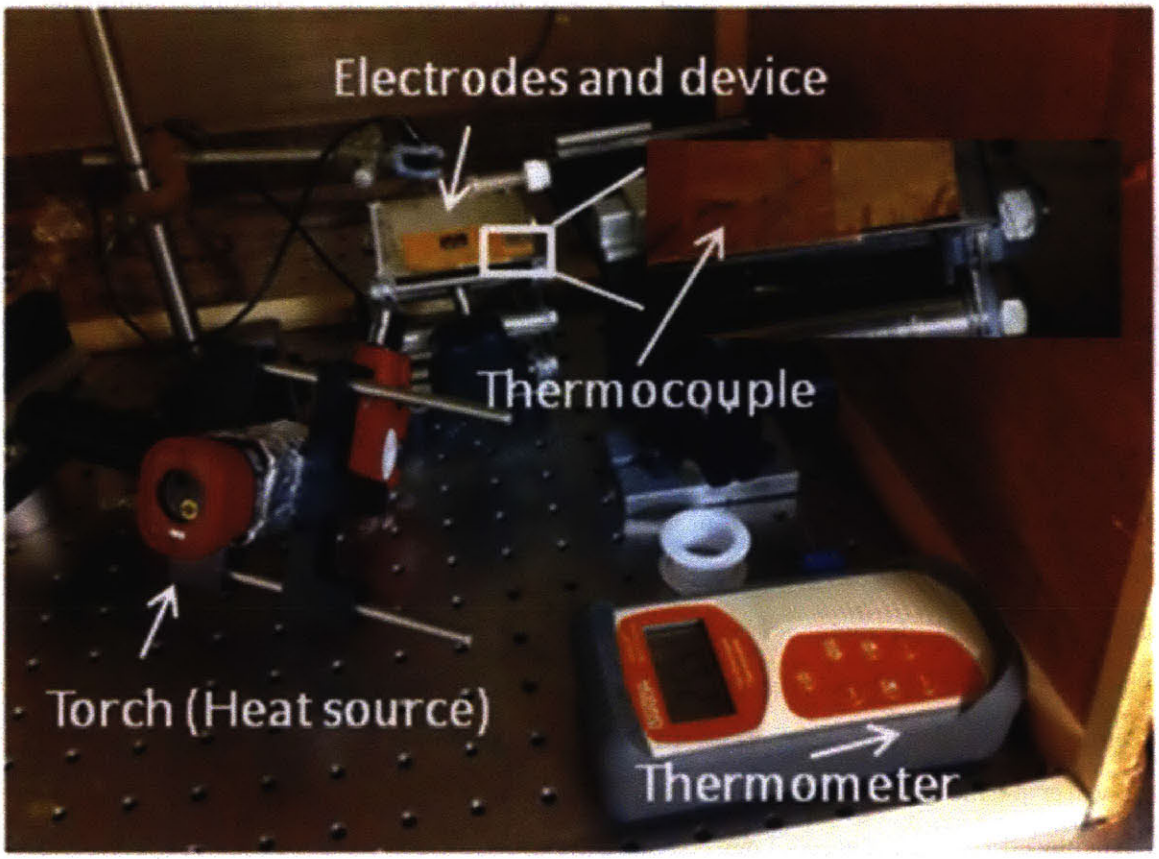

Figure 7-17: Picture of temperature scaling experimental setup.

The net current in this case is

$$I_{open} = eE(mu_H C_H^{open} - \mu_{OH} C_{OH}^{open}) + ev(C_H^{open} - C_{OH}^{open})$$

where e is the electron charge, μ_H and μ_{OH} are the proton and hydroxide mobilities which are strongly dependent on diameter, $\bar{v}^o$ is the average fluid velocity in the open state, and C_H and C_{OH} are the number of protons and hydroxides per unit length in the nanotube. We assume that there is a net negative charge on the SWCNT that from the environment (similar to previous studies) that results in a dominant proton concentration so that the open current simplifies to

$$I_{open} = eE\mu_H C_H^{open} + e\bar{v}^o C_H^{open}$$

When a large cation has entered the tube, proton hopping is limited to the rate at which the large cation moves through the tube (we assume a large energy barrier to approaching and passing the cation in a confined space). For very small diameter nanotubes, the large cation maybe not be able to easily pass water molecules, and cation movement is reduced to pushing water through the nanopore. The current in the closed state is thus approximated as the convective carrying of protons, $I_{closed} = eC_H^{closed}\bar{v}^b$. The pore-blocking current can then be calculated as

$$\Delta I = I_{open} - I_{closed} = eE(\mu_H C_H^{open}) + e\bar{v}^o(C_H^{open}) - eC_H^{closed}\bar{v}^b.$$

The electrical energy imparted to protons through the electric field is transferred to the water molecules through which it passes, effectively dragging water molecules in the axial direction. Due to the significant current $\sim 10^8$ protons/s and the low resistance to water transport in small diameter carbon nanotubes, this leads to a non-negligible flow velocity. The rate of water transport in small diameter carbon nanotubes has been extensively studied in literature [248] which used standard MD potentials and methods to carefully calculate the water permeation rate as a function of nanotube size. In these papers, water transport is calculated through Darcy's law

$$\bar{v}\gamma\frac{\Delta P}{L} = \gamma G$$

where G is the pressure gradient and γ is a coefficient that contains all of the flow physics. γ is further related to the no-slip coefficient under no-slip conditions $\gamma_n s$ via a flow-enhancement factor ε, yielding $\gamma = \varepsilon\gamma_n s$. The no-slip coefficient is obtained through the standard equation for Poiseulle flow

$$\gamma_{ns} = \frac{D^2}{32\eta}$$

where D is the SWCNT diameter and η is a cross-section averaged water viscosity. Since no theory is available to predict the precise form of the flow-enhancement factor, we adopt values from literature simulations [248] and fit it to a simple double-exponential continuum curve for convenience, shown in Figure 7-12. A sharp discontinuity is seen at approximate 1.4 nm as ordering in the water structure becomes more important.

Further diameter-dependence is introduced since the proton mobility and water viscosity are also diameter dependent. The water viscosity η is adopted from literature simulation studies [268]. The proton mobility is known to be enhanced at small diameters [60], but the precise diameter dependence is not known. It is thus assumed to be of a simple exponential form,

$$\mu_H(D) = \mu_H^{bulk}\left(1 + 39\exp\left(-\frac{D - 0.81nm}{0.33nm}\right)\right),$$

to match the literature simulations at a diameter of 0.81 nm and the bulk value at large diameters.

The flow velocity during proton transport can be calculated by equating the energy dissipation necessary to sustain the flow (LHS) and the electrical energy lost through ion translocation (RHS),

$$\bar{v}^o\frac{\pi D^2}{4}G = eC_H^{open}(\mu_H E + \bar{v}^o)E$$

It is possible to solve directly for the open fluid velocity $\bar{v}^o$. The blocked fluid velocity can be obtained through a simpler equation, since there is assumed to be only convective proton transport

$$\bar{v}^o\frac{\pi D^2}{4}G = eC_H^{open}(\bar{v}^b)E$$

All terms in these equations are known functions of diameter as described above, so the open and blocked velocities can be solved for and the pore-blocking current and dwell time calculated. The results and comparison to experimentally observed values can be seen in Figure 7-9b and 7-9c of the main text.

7.8 Correlation between proton concentration and temperature change

Because the temperature scaling experiments do not show any discontinuities in the pore-blocking currents, and assuming water is in the liquid phase at 50°C, these experiments confirm that the water inside the nanotube at room temperature is in the liquid phase, as opposed to an ice phase.

The proton concentration in solutions are related to the water dissociation constants, K_w. The water dissociation constants have been explored experimentally, but there is no completed theoretical analysis up to date. The following empirical formula can be used to determine this dissociation constant across a range of temperatures [121],

$$K_W = 8.754 \times 10^{-10} \exp\left(\frac{-1.01 \times 10^6}{T^2}\right)$$

where T is the absolute temperature in Kelvin. The water dissociation constant as a function of temperature is plotted in Figure 7-18a. Since proton concentration is proportional to $\sqrt{K_w}$, or

$$\text{Proton Concentration} \propto \left(\exp\left(\frac{-1.01 \times 10^6}{T^2}\right)\right)^{\frac{1}{2}}$$

This relationship is used to plot proton concentration as a function of temperature (Figure 7-18b). The range of interest is between 293 K and 323 K. The proton concentration at 323 K is about 3 times larger than that at 293 K (8.3×10^{-8} M vs 2.35×10^{-7} M). Assuming the proton concentration near the pore mouth and inside the SWCNTs also exhibit this trend with temperature, one would expect the pore-blocking current to increase roughly by a factor of 3 between 298 K and 323 K.

Figure 7-19 is a direct comparison between the blockade current in experiments and the calculated proton concentration. The factor of increase in the blockade current across

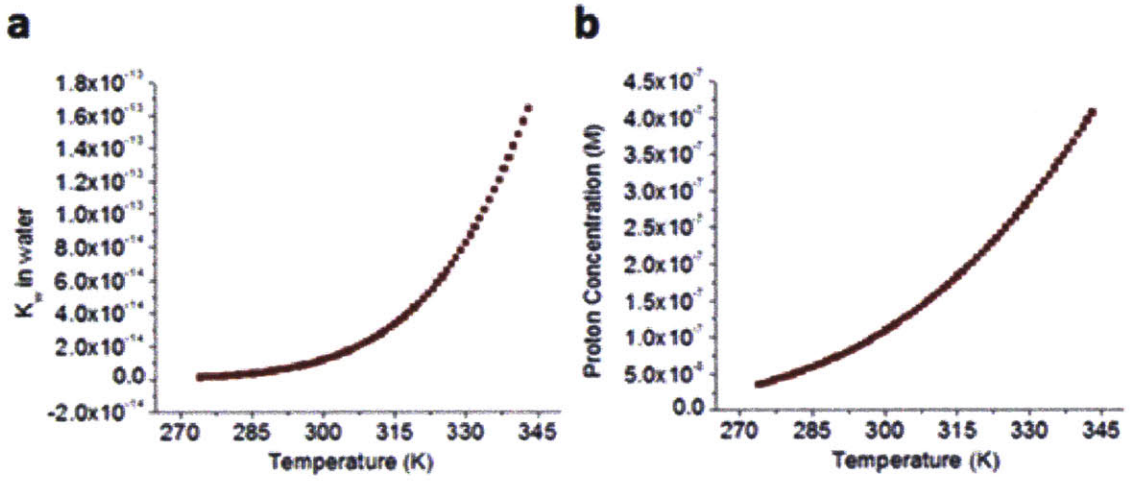

Figure 7-18: Temperature dependence of (a) water dissociation constant and (b) proton concentration.

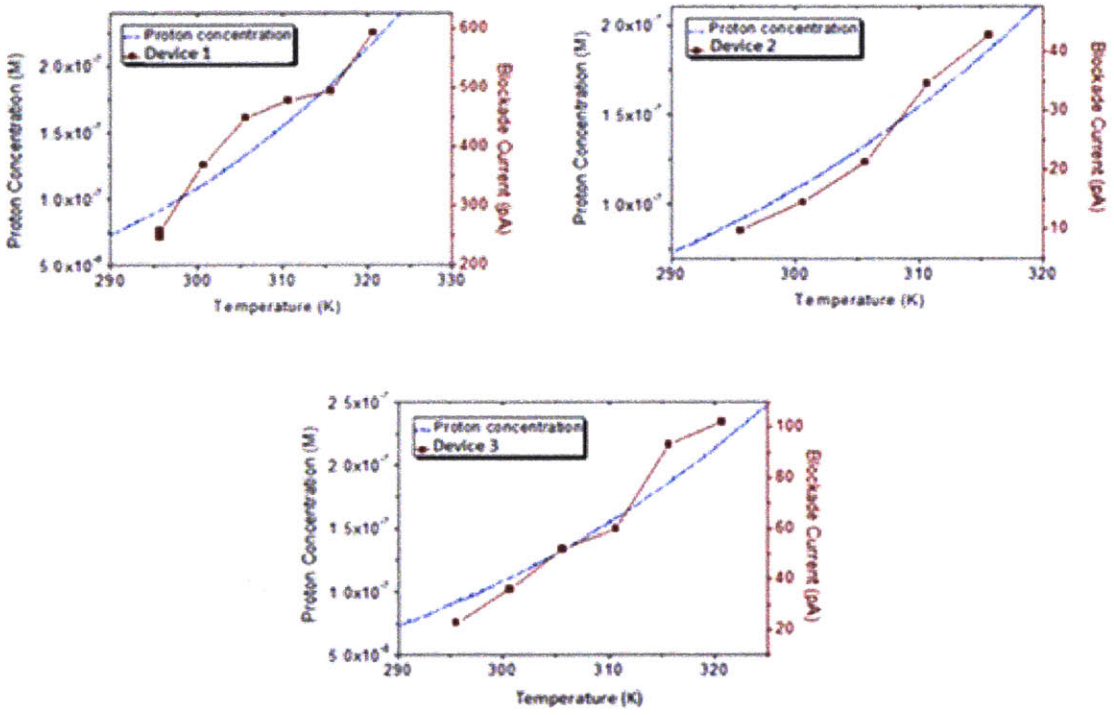

Figure 7-19: Comparison of the blockade current of experimental dataset from SWCNTs and calculated proton concentration.

the temperature range (298 K to 232 K) is between 2.5 and 4 times. Furthermore, the overall pore-blocking current trend with temperature roughly follows the same trend of proton concentration, as shown in Figure 7-19. The increase in pore-blocking current may be due to an increase in the proton concentration near the pore mouth. Another possible mechanism is the increase in the D defects in water chain structures inside the SWCNT [56]. To explain this, the Grotthus mechanism predicts that protons are transferred along water chains, where the proton transfer is regarded as the transfer of defects along the water chains. The flux of protons should be determined by the number of defects (called D defects) occupied by protons [56]. Thus, increasing the number of defects by increasing the temperature would allow for a higher flux of protons traveling through the SWCNT.

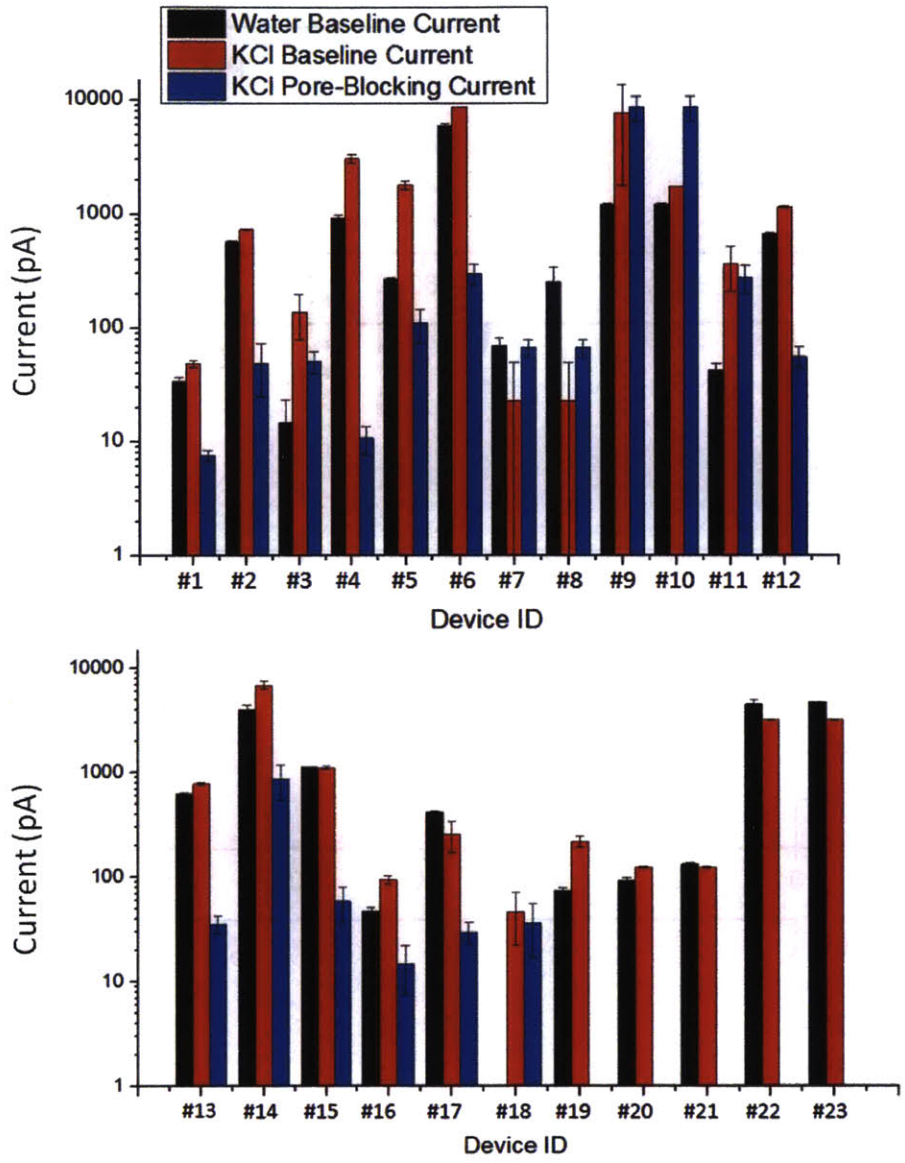

Figure 7-20: Analysis of baseline current of water and ionic solutions. Comparison among water baseline current, KCl baseline current (opened channel) and pore-blocking current (closed channel) for 23 devices. All devices werer tested using 3M KCl, except #14 and #3, which used 1M KCl.

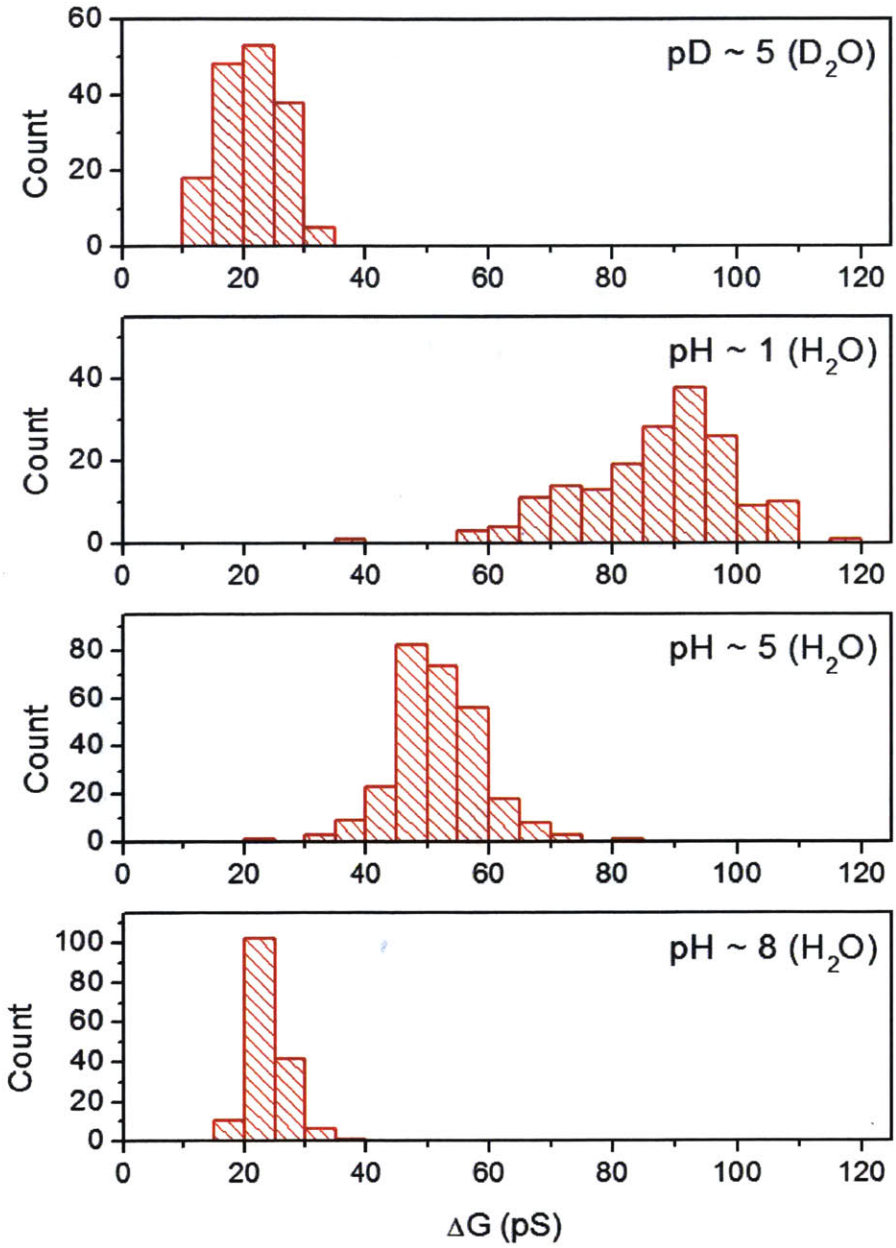

Figure 7-21: ΔG values from 3M KCl at different pH. The value is smaller in D_2O than in H_2O. Larger ΔG at acidic pH verifies that protons are the major charge carriers.

Part III

Material Properties of Fluctuating Membranes

Chapter 8

Persistently Auxetic Materials (PAMs): Engineering the Poisson ratio of 2D Self-Avoiding Membranes with Finite Anisotropic Strain

8.1 Abstract

Entropic surfaces such as fluctuating 2D membranes are predicted to have desirable mechanical properties when unstressed, including a negative Poisson's ratio. We present measurements of the strain-dependent Poisson ratio of self-avoiding membranes. We show that finite size membranes with free boundary conditions in fact have a positive Poisson ratio due to spontaneous non-zero mean curvature, which can be suppressed with an explicit bending rigidity in agreement with literature. Applying longitudinal strain to this system suppresses this mean curvature and entropic out-of-plane fluctuations, resulting in a negative Poisson's above a critical strain, with Poisson ratios significantly more negative than the zero-strain limit for infinite sheets. We find that this auxetic behavior persists to surprisingly high strains (over 20% for the smallest surfaces), and finite size effects are actually desirable in producing a surface with a negative Poisson ratio over a wide range of strains. These results give clues to designing surfaces with a tunable negative Poisson ratio by using materials with a set amount of initial applied strain or adjusting the surface rigidity.

8.2 Introduction

Materials with a negative Poisson's ratio, known as auxetics, contract in transverse directions when strained. This property is highly desirable in several applications, such as impact mitigation where material failure is caused by a thinning of the materials in the impact region, and for sealants, where it is desirable to materials to expand to fill regions as anisotropic pressure is applied. A negative Poisson ratio can be engineered at the macroscopic scale with carefully designed lattice structure [267], but there are limited ways to create molecular structures with a tunable Poisson's ratio. At the microscopic scale, it is well established that fluctuating membranes should, in the zero-strain limit, possess a negative Poisson ratio. Applying anisotropic in-plane strain to a self-avoiding 2D membrane suppresses out-of-plane roughness, which allows the material to expand in the transverse direction [190]. This effect has been confirmed with simulations in the zero-strain limit for simple inter-connected beads with periodic boundary conditions [274] and with triangular lattices with small bending rigidity with free boundary conditions [25, 23, 24].

Experimental realizations of these predictions for microscopic surfaces have shown limited success. For example, graphene should exhibit these properties as it can be modeled as a 2D self-avoiding fixed connectivity membrane. However, the significant bending rigidity of graphene suppresses most out-of-plane fluctuations leading to no measurable transverse expansion in detailed molecular simulations [156, 82]. A recent study proposed the introduction of atomic vacancies into the lattice to promote out-of-plane structure that could be suppressed [81]. The difficulties in determining the Poisson ratio of graphene illustrates an important problem that has been overlooked in the more general literature of 2D entropic surfaces: how do we design materials with a negative Poisson's ratio over a range of relevant strains, and what properties affect how persistent these properties are. The increasing complexity of nanoscale devices suggest that there may be many new materials with these properties that can be engineered. Possible routes to surfaces with desirable functionality include 2D DNA origami surfaces, 2D materials more flexible than graphene, and interlocking molecular structures.

In this work, we present the first simulations of the strain-dependent behavior of 2D self-avoiding fixed connectivity surfaces, starting with a simple model studied in the zero strain limit in previous literature. We show that membranes with free boundary conditions and

without an explicit bending rigidity actually possess a positive Poisson ratio at zero-strain due to a non-zero mean curvature of the surface. After suppression of this curvature, the material becomes auxetic (a negative Poisson ratio) and this persists over a large range of applied strains for small surfaces. Larger surfaces or those with more significant bending rigidity show a smaller window for a negative Poisson ratio. At very large strains the membrane connectivity becomes limiting and the membrane begins to contract, placing an upper limit on the window for auxetic behavior.

8.3 Background Theory

The Hamiltonian for a strained continuum elastic surface with small out-of-plane fluctuations in the harmonic approximation coupled to an external stress source [215] is

$$F[\mathbf{u}, h, \tau_{\alpha\beta}] = \frac{1}{2}\int d^2r \left[\kappa\left(\nabla^2 h\right)^2 + 2\mu u_{\alpha\beta}^2 + \lambda u_{\alpha\alpha}^2 + \tau_{\alpha\beta}u_{\alpha\beta}\right] \tag{8.1}$$

where $\mathbf{u}$ is the strain tensor for in-plane strain, h is the membrane height, $\tau_{\alpha\beta}$ is the in-plane stress tensor $\tau_{\alpha\beta} = \lambda\delta_{\alpha\beta}u_{\alpha\beta}^{ext} + 2\mu u_{\alpha\beta}^{ext}$, κ is the bending rigidity, λ is the first Lame coefficient, and μ is the shear modulus. For an unstrained membrane, $u_{\alpha\beta}^{ext} = 0$. The internal strain tensor of a thin membrane, to first order, is

$$u_{\alpha\beta} = \frac{1}{2}\left(\partial_\alpha u_\beta + \partial_\beta u_\alpha + \partial_\alpha h \partial_\beta h\right). \tag{8.2}$$

This internal strain is important for understanding the state of the system. This system has been studied in detail, especially in the case of no external strain. We can also define a local 2D strain for the membrane projected onto the mean surface

$$u_{\alpha\beta}^P = \frac{1}{2}\left(\partial_\alpha u_\beta + \partial_\beta u_\alpha\right). \tag{8.3}$$

This definition is valuable for considering how the local strain contributes to the macroscopic strain for the entire membrane, and is related to angle between the local surface tangent and the mean plane of the membrane. Key measurables that have been described for 2D self-avoiding membrane with fixed connectivity based on this Hamiltonian include the RMS out-of-plane fluctuations $\langle h^2 \rangle$, the radius of gyration R_g, the induced bending rigidity from

self-avoidance κ. The most interesting property of the systems is the prediction of a universal Poisson ratio σ, defined as the ratio of transverse to longitudinal strain. In this study, we consider a practical macroscopic definition of the Poisson ratio

$$\sigma^L = \frac{\partial u_{yy}}{\partial u_{xx}} \frac{u_{xx}}{u_{yy}}, \tag{8.4}$$

$$\sigma^M = \frac{\delta W/W}{\delta L/L}. \tag{8.5}$$

The first definition σ^L is based on the strain definition presented in Eq 8.2, and represents the local Poisson ratio on the membrane surface including out-of-plane fluctuations. The macroscopic Poisson ratio σ^M is defined as the center-of-mass distance between the membrane edges in the longitudinal/strained direction L and the transverse/free direction W. σ^M is the Poisson ratio we would observe for the entire sheet if we only probed it through interactions at the membrane edges, and the most important for consideration of practical experiments. It is important to note that all of these definitions are highly strain-dependent, as their properties depend on out-of-plane fluctuations that can be suppressed or enhanced through external strain. Interestingly, the local Poisson ratio σ^L has been predicted to be approximately -1/3 in the limit of no external strain. This follows analytical theory using renormalization group theory [143], and numerical simulations for finite sized membranes [274, 23]. The Poisson ratio in this limit of zero strain appear to be nearly universal and independent of the precise connectivity geometry or tethering, under the presence of periodic boundary conditions or explicit bending rigidity.

In this study, we report the first strain-dependent measurements of the Poisson ratio in 2D self-avoiding fixed connectivity membranes. These membranes exhibit a transition from previously reported universal limits to a positive Poisson ratio at a size-dependent critical strain. Further, we show that this critical strain decreases with membrane size suggesting that maintaining a small membrane size is actually beneficial for maintaining a negative Poisson ratio over a large regime. In addition, we show that other experimentally-relevant measureables, such as the RMS out-of-plane fluctuations undergo nonlinear transformations at similar strains. We show that this transition is necessary as the behavior transitions from being dominated by entropic fluctuations of the membrane to enthalpic interactions in the strained lattice.

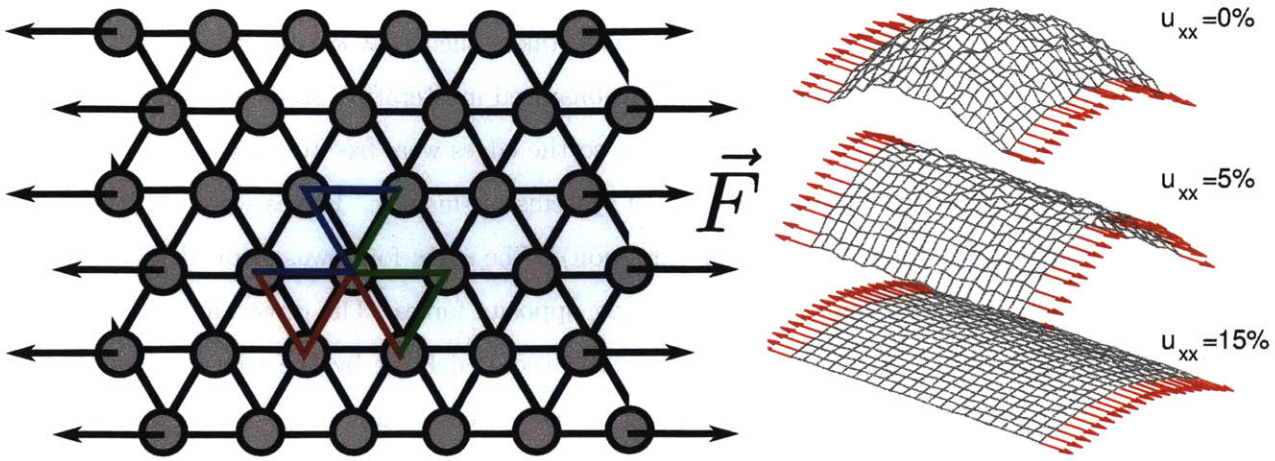

Figure 8-1: Example geometry for a 6x6 mesh. (left) Forces were added to edge beads in the longer (longitudinal) direction. Actual mesh sizes were much larger (minimum 28x28, up to 150x150). Example improper dihedrals, used to increase the bending rigidity of the sheet, are also indicated for a single central atom, as shown with the red/green/blue connections. The direction of the applied forces were updated periodically based on the orientation of the membrane. (right) Cartoon of the effect of applying longitudinal strain for a sheet without explicit rigidity. At $u_{xx} = 0$, there is a non-zero mean curvature in both directions. At small extensions, the curvature in the longitudinal direction is quickly suppressed, but the transverse curvature increases slightly. For large extensions, curvature in both directions is suppressed and the surface becomes more flat.

8.4 Simulation methods:

We performed molecular dynamics simulations of self-avoiding fixed connectivity membranes in the NVT ensemble with varying external anisotropic strain. For easy comparison to previous studies, we adopted a literature physical model [274]. Square NxN lattices of beads were connected in a triangular mesh (i.e. connectivity of 6), as illustrated in Figure 8-1. All beads interacted via a truncated self-avoiding Lennard Jones potential of the form

$$U_{LJ} = \begin{cases} 4\epsilon \left[\left(\frac{\sigma}{r}\right)^{12} - \left(\frac{\sigma}{r}\right)^{6} + \frac{1}{4} \right] & r \leq 2^{1/6}\sigma \\ 0 & r > 2^{1/6}\sigma. \end{cases} \tag{8.6}$$

Bonded beads were connected with a Finite Extensible Nonlinear Elastic (FENE) bond of the form

$$U_{FENE} = \begin{cases} -\frac{1}{2}kR_0^2 \ln \left[1 - \left(\frac{r}{R_0}\right)^2 \right] & r \leq R_0 \\ \infty & r > R_0. \end{cases} \tag{8.7}$$

As in previous studies [274], parameters were taken such that $k = 6\epsilon/\sigma^2$,$R_0 = 1.5\sigma$, and $T = \epsilon/k_B T$. The periodic boundary conditions used in literature study were not amenable to numerical study with anisotropic strain, so the edges were free to fluctuate, as would be the case in an experimental realization of systems of this size. Forces were applied to the edge beads in the longitudinal (long direction). The same force was applied to each bead along each edge, with opposite edges having opposite forces. The direction of these forces were updated every 1,000 steps based on the vector defined by the center of each edge, after projection onto a 2D surface by using the two largest components of the singular value decomposition (SVD) of the bead positions. The system was integrated using a timestep of $10^{-3}\sqrt{m/\sigma}$.

Self-avoidance in fluctuating membranes leads to an induced bending rigidity which stabilizes the flat phase of these membranes, preventing the system from crumpling. However, many practical membranes, such as 2D materials like a graphene sheet, have an explicit bending rigidity as well. To investigate the effect of the surface rigidity on measurable quantities like out-of-plane fluctuations and the Poisson ratio, three quadratic improper dihedral terms were added for each bead, as shown in Figure 8-1, of the form

$$V(r) = \kappa(\chi - \chi_0)^2, \tag{8.8}$$

where κ represented the strength of the added rigidity, χ was the dihedral angle, and $\chi_0 = \pi$ was the equilibrium angle ensuring that the equilibrium surface was flat. κ was varied from $[0\epsilon, 1000\epsilon]$ for the N=40 sheet.

Simulations were performed for systems with size N=[28, 40, 100, 150]. Forces were applied to reach longitudinal extension from approximately 0-60%. For each simulation, the first 10^7 steps were discarded for equilibration. Simulation statistics were collected every 10^5 steps thereafter, which was the minimum to provide uncorrelated samples as determined by the autocorrelation function. For larger systems, multiple replicas with random initial velocities were used to generate extra samples. For most samples, greater than 10^10 steps were achieved, resulting in approximately 10^5 independent samples. In all cases, error estimates on measurables were generated using the bootstrap method with 10^3 samples.

Simulations were performed on GPUs in HOOMD-BLUE 1.0 [9, 1], enabling several orders of magnitude more simulation capability than previous studies. This capability was

necessary to analyze surface behavior under a variety of longitudinal strains. The use of GPUs placed an upper bound on the system size that could be considered, since the volume of the simulation cell is directly proportional to the number of regional neighbor lists needed for the simulation. To maximize possible system size, the membrane was placed in a simulation cell with a large aspect ratio (e.g. a width/length proportional to the area of the membrane, and fixed cell height of 100 bead radii corresponding to relatively small out-of-plane fluctuations). To prevent the membrane from rotating out of plane and interacting with neighbors via the periodic boundary conditions, every 10^3 time steps the membrane and velocities were rotated such that the smallest basis vector from the SVD decomposition was aligned to the z-axis, keeping the membrane extent in the x- and y- directions with out-of-plane fluctuations in the z-direction. Temperature control was implemented with the default HOOMD NVT integrator with a timescale of 10^3 simulation steps. The momentum of the simulation was zeroed every 10^3 steps.

For comparison to previous studies, we also report the size scaling of the radius of gyration $R_g \propto L^{\nu}, \nu = 1.02 \pm 0.0004$, and the size-scaling roughness exponent for the out-of-plane fluctuations, $\langle z^2 \rangle \propto L^{2\zeta}, \zeta = 0.79 \pm 0.07$. The roughness scaling is slightly larger than previous studies [274, 25] due to the difference in boundary conditions.

8.5 Results:

Anisotropic straining of the membrane led to an initial flattening of the surface, as shown in Figure 8-2 for an example case of a 40x40. At approximately 10% strain for the 40x40 surface, the out-of-plane fluctuations reaches a minimum. After that point, further straining the membrane leads to an increase in the RMS height. This transition also corresponds to the point where the membrane loses its auxetic property (i.e. a transition from a negative Poisson's ratio to a positive one), as discussed later. The initial decrease can be understood using continuum elastic theory in the harmonic approximation developed for the elastic surface with the Hamiltonian in Eq. 1 [215]. That work established the RMS height fluctuation as

$$\langle h^2 \rangle = \int d\mathbf{q} G_0 \frac{2\pi|\mathbf{q}|}{(2\pi)^2}, \qquad G_0(\mathbf{q}) = \frac{k_B T}{q^2 \left(\kappa q^2 + \lambda u^{ext}_{\alpha\alpha} + 2\mu u^{ext}_{\alpha\beta} \frac{q_\alpha q_\beta}{|\mathbf{q}|^2} \right)} \tag{8.9}$$

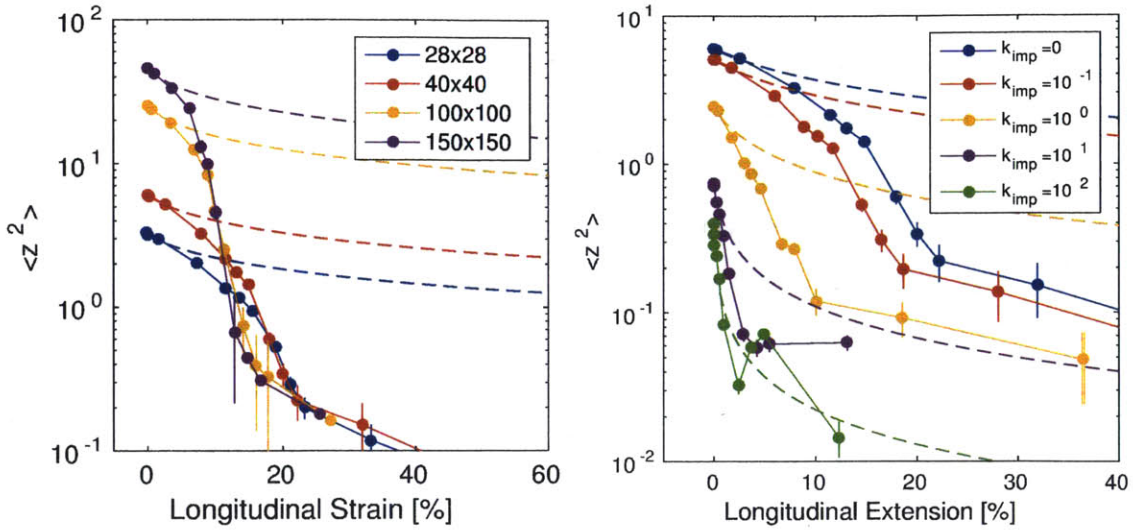

Figure 8-2: RMS out-of-plane height of the membrane under longitudinal strain. Straining the membrane initially decreases the out-of-plane fluctuations, until approximately 10% strain. Theory for each membrane size is a fit to Eq. 10. The mean-square roughness decreases faster than the theory suggests because of a reduction in the non-zero mean curvature of the unstressed membrane with free boundary conditions, which is not accounted for in the developed theory.

where G_0 is the Fourier component of the height-height correlation function and $u_{\alpha\beta}^{ext}$ is the external strain applied to the membrane. For purely longitudinal external strain ($u = yy, u_{xy} = 0$), G_0 simplifies to

$$G_0(\mathbf{q}) = \frac{k_B T}{q^2 \left(\kappa q^2 + u_{xx}^{ext}(\lambda + \mu) + \mu u_{xx}^{ext} \cos[2\theta]\right)}, \tag{8.10}$$

where θ is the angle between the Fourier mode q and the x-axis. Integrating over the magnitude of the Fourier component q in Eq 8 starting at a minimum Fourier component inversely proportional to the system size q_{min}~$2\pi/L$ yields

$$\langle h^2 \rangle = \int_0^{2\pi} d\theta \int_{q_{min}}^{\infty} dq \frac{2\pi q}{(2\pi)^2} \frac{k_B T}{q^2 \left(\kappa q^2 + u_{xx}^{ext}(\lambda + \mu) + \mu u_{xx}^{ext} \cos[2\theta]\right)} \tag{8.11}$$

$$= \int_0^{2\pi} d\theta \left[\frac{k_B T \log\left(1 + \frac{u_{xx}^{ext}(\lambda+\mu)}{q_{min}^2 \kappa} + \frac{u_{xx}^{ext} \mu \cos[2\theta]}{q_{min}^2 \kappa}\right)}{8\pi^2 u_{xx}^{ext}(\lambda + \mu + \mu \cos[2\theta])} \right]. \tag{8.12}$$

(10) This final term was integrated numerically over a range of imposed external strains for the 40x40 case as shown in Figure 8-2. This term can be evaluated in the limit of zero strain

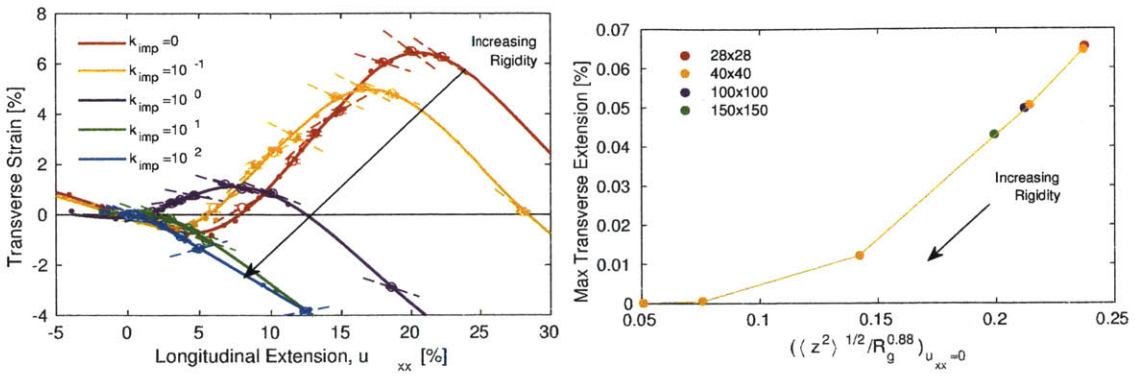

Figure 8-3: Suppression of transverse contraction with explicitly added membrane rigidity. (left) Adding an explicit bending rigidity to the surface through the application of an improper dihedral with force constant k_{imp} leads to a reduction in the maximum in the transverse extension and reduction in the maximum with respect to the applied longitudinal strain. Increasing k_{imp} above 100ε suppresses the initial contraction by reducing the mean curvature of the unstrained membrane with behavior more similar to those of previous studies (i.e. a negative Poisson ratio at zero strain). (right) As system size increases or the membrane becomes more stiff, the maximal transverse extension, a desirable property, decreases. This effect can be attributed to the RMS out-of-plane fluctuations at zero-strain, which determine far the membrane can be extended by removing these fluctuations, relative to the membrane extent represented by the radius of gyration. An empirical exponent of 0.88 for R_g collapses the results obtained by changing the membrane size or adding explicit bending rigidity to the system.

to derive two terms useful for fitting the elastic coefficients,

$$\lim_{u_{xx}^{ext}\to 0} \langle h^2 \rangle = \frac{k_B T L^2}{16\pi^3 \kappa}, \lim_{u_{xx}^{ext}\to 0} \frac{d \log \langle h^2 \rangle}{d u_{xx}^{ext}} = -\frac{L^2(\lambda+\mu)}{8\pi^2\kappa} \tag{8.13}$$

Using these two zero-strain limits allowed for the estimation of the effective bending rigidity and the combination $\lambda + \mu$. This theory appears to deviate from the simulation results at strains of just a few percent. At this point, straining the membrane is changing the effective bending rigidity and this theory, developed for constant rigidity and elastic coefficients) begins to break down. The induced bending rigidity κ from self-repulsion begins to weaken and becomes anisotropic itself and the membrane begins to collapse in the transverse direction.

8.5.1 Non-Zero Mean Curvature of Finite Membranes

âĂČ

Although finite-size self-avoiding 2D membranes are asymptotically flat (they do not

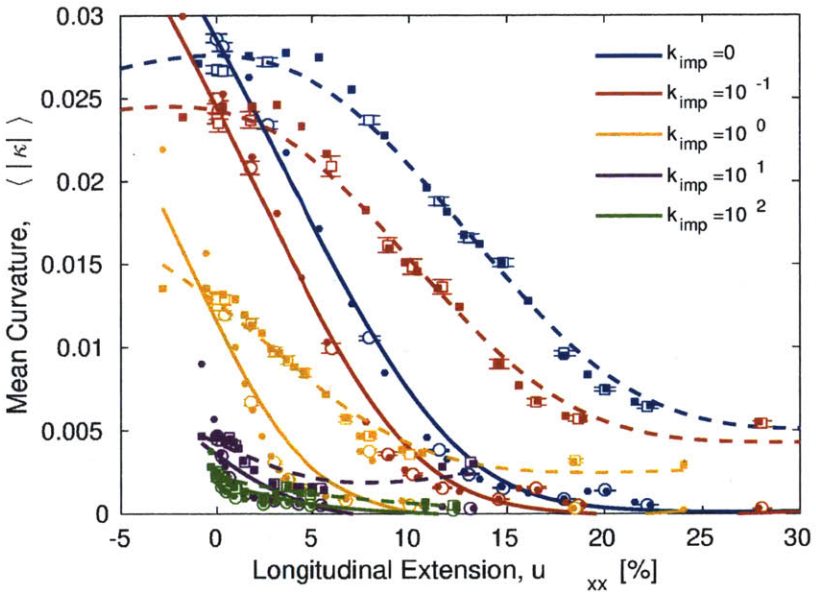

Figure 8-4: Mean curvature of surfaces during longitudinal extension. (left) Solid lines indicate the mean surface curvature in the longitudinal direction, while dashed lines indicate mean curvature in the transverse direction. Open symbols are averages for ensemble simulations (constant applied force), which filled symbols are averages taken by sub-sampling ensemble results. Lines are smoothing splines included only as visual guides. For surfaces with no added rigidity, applying a longitudinal extension causes the surface to flatten in the longitudinal direction, while becoming more curved in the transverse direction.

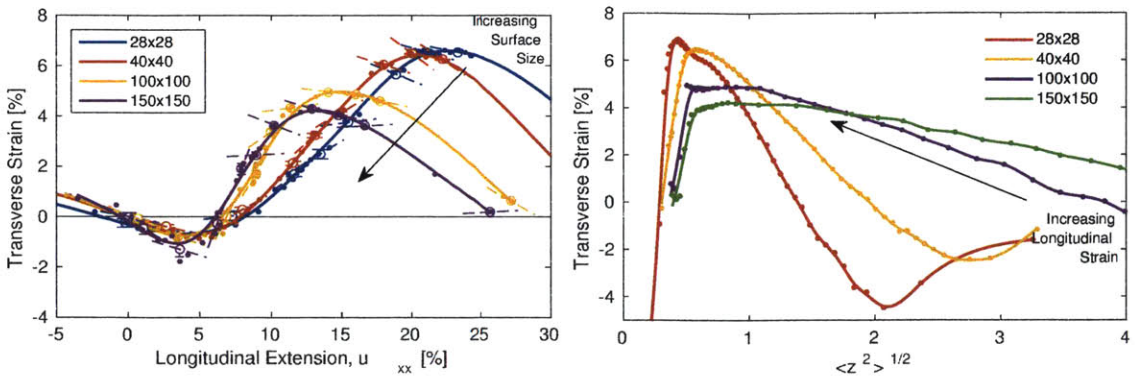

Figure 8-5: Transverse strain induced by longitudinal strain for surfaces of various sizes. (left) Circles represent ensemble averages for each simulation condition (i.e. constant end forces), with error bars generated using the bootstrap method. Small points averages of collections from each ensemble, showing variation within each condition. Solid lines are smoothing splines included for visual guides. Dotted lines are approximations of the local gradient for each set of calculations. (right) Transverse strain as a function of the out-of-plane fluctuations. As out-of-plane fluctuations are reduced the transverse strain increases, until the membrane is essentially flat at the critical value $\langle z^2 \rangle^{1/2} = 0.4$ after which the membrane beings to contract.

crumple entropically into spheres), they do contain non-zero mean curvature over the scale of the membrane, as illustrated in Figure 8-4. The extent of this curvature depends on the surface parameters (bead size, bonding, etc), the size of the sheet, and whether there is an explicit bending rigidity present. Previous simulation efforts did not observe this effect because they studied systems with periodic boundary conditions [274] or with significant bending rigidity that suppressed this curvature [25, 23, 24]. The mean curvature in the transverse and longitudinal strain directions for membranes with varying explicit bending rigidity is shown in Figure 8-4, after averaging out small-scale spatial variation using a Gaussian spatial filter. For all membranes, applying longitudinal strain to the membrane immediately leads to a reduction in curvature in that direction. However, membranes with low bending rigidity the transverse curvature actually increases slightly with initial strain application. This initial curvature reduction corresponds to the initial decrease in transverse membrane extent shown in Figure 8-3. Applying further longitudinal strain leads to a decrease in the transverse curvature, but at a rate slower than in the longitudinal direction. This process is illustrated in the cartoon in Figure 8-1.

8.5.2 Transverse Extent Under Finite Large Strain

Applying a finite longitudinal strain to these self-avoiding membranes leads to three distinct regimes of behavior, as shown in Figure 8-5. All systems initially contract in response to longitudinal strain, in contrast to previous studies due to the non-zero mean curvature of the membrane in absence of explicit bending rigidity or periodic boundary conditions. This effect lasts until approximately $u_{xx} = 5\%$ for the membranes shown and corresponds to the point at which transverse curvature begins to decrease in Figure 8-4. After an initial contraction, the surface expands in the transverse direction as entropic out-of-plane fluctuations are suppressed. In this regime (approxiately 5% to 20% for the 28x28 membrane), the Poisson ratio is negative. This continues until most out-of-plane fluctuations have been reduced $\left(\langle z^2 \rangle^{1/2} < 0.4\right)$ corresponding to approximately 10-20% applied longitudinal strain depending on system size. As applied strain increases beyond this critical level, inter-bead stretching takes over leading to a contraction. This effect can be seen more clearly in Figure 8-5b; as the out-of-plane fluctuations are reduced the transverse strain increases, until the critical point at which $\langle z^2 \rangle^{1/2} = 0.4$.

At very large applied longitudinal strains, the deformation of the triangular lattice leads to a reduction in the transverse membrane extent. This is a simple geometric effect from the surface connectivity and depends on the precise connectivity and inter-bead potential. For an infinitely stiff network (non-deformable inter-bead distances) this is a simple geometric problem, as illustrated in Figure 8-5. Under a deformation in the longitudinal direction from a longitudinal length a to a deformed longitudinal link length $a(1+x)$, the transverse distance $y(x)$ will simply be

$$y(x) = \frac{2}{\sqrt{3}} \sin\left[\arccos\left(\frac{1+x}{2}\right)\right] \tag{8.14}$$

where $y(x)$ has been scaled to the un-deformed length such that $y(0) = 1$. Necessarily $y(1) = 0$ since that is the maximum extension for this stiff model. Further, this model will under predict the transverse extent since the inter-bead links are deformable. For a system where the inter-bead potentials are Hooke-ian springs with spring constant k and equilibrium length a, the energy of the system for a configuration with transverse direction

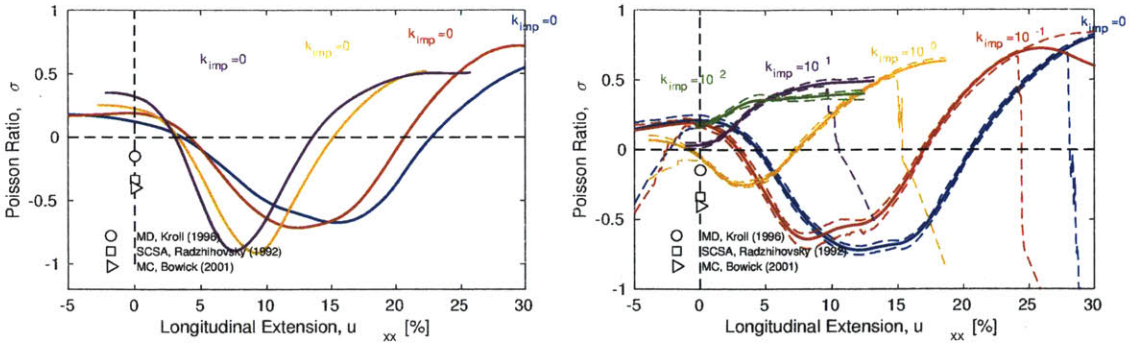

Figure 8-6: Strain-dependent Poisson ratio. (left) The macroscopic Poisson ratio, defined using the surface edge positions, for 40x40 surfaces with varying degrees of bending rigidity. Effect of surface size on the strain-dependent Poisson ratio. Larger surfaces have a lower minimum Poisson ratio, but have a larger zero-strain Poisson ratio and earlier final transition to a positive Poisson ratio. Disagreement between the results from zero-strain calculations in previous and these strain-dependent results are due to the non-zero mean curvature of the surface which must first be flattened. (right) Increasing the rigidity of the surface increases the minimum Poisson ratio and decreases longitudinal extension at which the Poisson ratio changes from negative to positive.

y and longitudinal extension x will be

$$E(y,x) = ka^2\left(1 - \sqrt{\left[\frac{a(1+x)}{2}\right]^2 + y^2}\right). \tag{8.15}$$

The average transverse direction, also scaled such that $\langle y\rangle(0) = 1$ is then

$$\langle y\rangle(x) = \frac{2}{\sqrt{3}}\frac{\int_0^\infty \exp\left[-\beta E(y,x)\right] y^2 dy}{\int_0^\infty \exp\left[-\beta E(y,x)\right] y dy}. \tag{8.16}$$

The numerator can be integrated analytically, and the denominator was integrated numerically. There is a single adjustable parameter in this model, the dimensionless elastic constant $\bar{k} = \beta k a^2$. In the limit of $\bar{k} \to \infty$, this model reduces to the inflexible limit in Eq 8.14.

8.5.3 Strain-Dependent Poisson Ratio

The strain-dependent Poisson ratio, shown in Figure 8-6, was calculated from the spline fits of the strain-strain relations in Figures 8-2&8-3. The Poisson ratio is positive at zero-strain for membranes of all sizes with no explicit bending rigidity, with larger membranes having larger zero-strain Poisson ratio. This is significantly different from previous estimates of the zero-strain Poisson ratio for the same model system due to the difference in boundary

conditions and resulting non-zero mean curvature in the membrane as discussed above. Most of the sheets transition to a negative Poisson's ratio at approximately 5% applied longitudinal strain and reach a minimum Poisson ratio significantly more negative than those reported in the zero-strain limit with larger membranes having lower minimum Poisson ratios. This continues until the membrane is essentially flat in the longitudinal direction and further strain forces neighboring beads closer together leading to a transverse contraction and a return to a positive Poisson's ratio.

The strain-dependent Poisson's ratio can be engineered by adjusting the bending rigidity of the membrane, as shown in Figure 8-3 or adjusting the membrane size. Adding rigidity by adjusting k_{imp} , the force constant for the improper dihedrals as described above, reduces the out-of-plane fluctuations and mean curvature of the membrane. Doing so reduces both the minimum Poisson ratio and the longitudinal strain at which the system transitions back to a Poisson ratio. In both situations, the change in Poisson ratio is a direct effect of adjusting the out-of-plane fluctuations at low strains that allow the system to expand when flattened. The return to a positive Poisson ratio occurs in all membranes when the mean out-of-plane fluctuations is reduced below a critical value of approximately $\langle z^2 \rangle^{1/2} \approx 0.4$, as shown in Figure 8-5b, after which there are essentially no more out-of-plane entropic fluctuations to remove.

The transition from negative to positive Poisson ratio at large strains can be correlated to the out-of-plane fluctuations and the radius of gyration of the membrane at zero-strain. A simple metric $\left[\langle z^2 \rangle^{1/2} / R_g^{0.88}\right]_{u_{xx}=0}$ predicts this maximal transverse extension under the addition of bending rigidity or varying system size, as shown in Figure 8-3b. The scaling exponents for $\langle z^2 \rangle$ and R_g given above suggest that this transition point should scale as $\langle z^2 \rangle^{1/2} / R_g^{0.88} \sim L^{-0.11}$, suggesting that even membranes sizes several orders of magnitude larger will have negative Poisson ratios over substantial strain ranges. This could be verified with further work, but simulating larger membranes takes significantly more computational resources.

8.6 Conclusion

These simulations show that exotic mechanical properties of entropic 2D surfaces are more interesting than the universal zero-strain limits proposed in previous literature and that

the properties persist over a surprisingly large range of applied strains. The most-negative Poisson ratios observed in this study are considerable more negative than the zero-strain-limit simulations suggested. Adjusting the rigidity and the size of the membrane both affect the strain range over which auxetic behavior persists, and suggests that there should be noticeable strain-dependent affects for practical surfaces. Sufficiently stiff membrane can completely suppress these regions of auxetic behavior, explaining why attempts to use graphene membranes as auxetic materials have failed. We also provide a metric for the persistence range based on a correlation the out-of-plane fluctuations and radius of gyration. These results also suggest that another path towards making materials with a specific Poisson ratio is to pre-strain the materials to the desired point. This could be achieved by embedding the membranes in a second matrix that can be adjusted.

Chapter 9

Conclusions and Future Work

In chapter 3 of this thesis, we explored how collections of stochastic SWCNT sensors respond to a chemical concentration gradient. We found an analytical solution for the probability distribution of multiple sensors responding to the same signal and used this to quantify the expected intrinsic sensor-to-sensor variation in the system. We were also able to use this analytical solution to derive estimates for the local chemical concentration given the performance of several nearby SWCNT, and we showed that this analysis gives a better estimate than a more naive method based on average the results from the analysis of individual SWCNT. In future work, we would like to extend these results to the sensing of reaction networks with multiple species (and corresponding sensors) for even more detailed chemical information. We also hope to extend these results to the sensing of spatially-distributed concentration signals and quantify the exact trade-offs between spatial and concentration accuracy in the system.

Armed with an understanding of how collections of $d(AT)_{15}$-wrapped SWCNT behaved *in vitro*, chapter 4 investigated the use of these sensors inside of melanoma cells. We found that $d(AT)_{15}$-wrapped SWCNT spontaneously uptake into A375 melanoma cells and that they retain their selectivity to nitric oxide detection through the application of a known nitric-oxide promoting drug. Unfortunately we did not observe single-molecule nitric oxide detection events as in the *in vitro* case, suggesting that multiple SWCNT were being bundled together in each location. These results demonstrated fluctuations in the nitric oxide concentration at sub-cellular length scales in contrast to previous biological literature. In the future, we hope to extend this study to the detection of multiple chemical species simul-

taneously, perhaps through the incubation of cells with collections of SWCNT with different chirality and surface wrappings.

To design new sensors, we needed a platform to quickly predict and understand interactions between SWCNT wrappings and small molecules of interest, which we achieved in chapter 5 through the development of a molecular thermodynamic model for competitive adsorption at the SWCNT/solution interface. We applied an existing surface thermodynamic model to this new interface, and developed a number of molecular simulations to quickly predict the necessary thermodynamic parameters for arbitrary small molecules. The new system was capable of quickly screening against a library of wrappings and small molecules that had been experimentally developed in our lab. The system was most effective at identifying polymers that interacted too weakly with the SWCNT surface to be useful at allowing selective recognition. In the future we hope to improve the model to more accurately model the orientation-dependent interactions between the wrappings and the small molecules of interest. The next step would be to screen against a larger number of potential small molecules to see which could be used with our existing library wrapping.

In the second part of this thesis, we improved our understanding of fluid flow and ion transport inside of SWCNTs. Chapter 6 discusses the challenges in making devices that exhibit verifiable transport through SWCNTs. Importantly, we demonstrated the challenges that our group had discovered in this process and how easy it was to make devices that actually showed transport along the outside of SWCNT or through defects in the device barriers. With this in mind, we proposed stochastic current fluctuations as a necessary indicator for whether a full seal had been achieved around the device.

Chapter 7 demonstrated the first diameter-dependent measurements of transport through 1-2 nm nanopores leading to a number of interesting insights. Interesting behavior was observed for the transport of various ions through the interior of the SWCNT, with transport rates not directly related to ion size or charge. By analyzing the transport rates of a specific ion type through devices with varying SWCNT size, we showed a maximum in transport rates at approximately 1.6 nm diameter, which is roughly related to the transition from continuum to sub-continuum flow structure. Follow-up work is investigating the phase behavior of water in these devices, and in the future we hope to construct devices that can monitor the SWCNT spectroscopically as individual blocking events occur.

Finally, chapter 8 investigated the mechanical properties of fluctuating membranes. We

showed that the expected auxetic behavior of the material did not occur in the unconstrained case for finite-size membranes due to curvature observed in the membrane. Applying strain to the sheet through edge interactions drove the Poisson ratio negative and this property persisted over a large range of strain. We showed that this effect is dependent on both the system size the and the inherent rigidity of the membrane, with more rigid membranes showing smaller windows of interesting mechanical properties. In the future, we hope to show how these effects apply to other nanoscale surfaces, such as modified graphene monolayers or perhaps chainmail structures of interlocking graphene rings. We hope that this work will accelerate the design of practical auxetic surfaces in the future.

The proliferation of nanoscale devices, including those based on SWCNT and other materials like colloidal gold and quantum dots, has led to a large number of sensors that can selectively detect various small molecules. In this thesis alone, selective recognition is shown for H_2O_2, NO, and estradiol, among many others. However, relatively few of these devices have been adopted by the biological community, and combining several sensors for multi-modal imaging is rare. Making these sensors more accessible to the biological community through commercialization, collaboration, or simplified synthesis protocols would greatly enhance the impact of this work. The availability of low-cost SWCNT bulk material and separation methods will help the availability problem for biological groups looking to use these devices. Chapter 4 was an attempt by our lab to demonstrate the usefulness of these sensors for intracellular sensing, but this is only the first step to the broader use of these sensors.

The influence of SWCNT chirality on interactions with small molecules, necessary to design multi-modal SWCNT collections, is also an exciting area of future work. Not all small molecules will cause a decrease in the SWCNT fluorescence intensity, and it is unclear how this effect depends on SWCNT chirality. This effect is roughly captured in the parameter β from Chapter 5. The current generation of devices studied in this thesis are primarily based on the quenching of SWCNTs with (6,5) chirality. A number of small molecules could be filtered out of future studies if it could be determined ahead of time that they do not interact with the SWCNT fluorescence. Furthermore, the impact of SWCNT chirality on small molecule adsorption with simulations has only been investigated through geometric effects, effectively using the same carbon force fields in different chiral arrangements. The impact of SWCNT electronic structure on interactions with small molecules or surfactants

would also be of interest, but is a significantly more expensive calculation.

Lessons learned from understanding and designing nanoscale sensors in this work can also be applied to other devices. As an example, engineering selective molecular interactions is also a key challenge in catalysis. Designing interfaces that preferentially react with certain small molecules in mixed solution would be transformative in how we approach chemical reaction engineering. Sensor design is the perfect area to develop the simulation methods and physical intuition for this application.

The majority of this thesis has been focused on understanding the mechanisms that enable selective detection in the current generation of SWCNT-based sensors, but future work should be able to design sensors for specific molecules *a priori*. The fundamental challenge for the design of selective SWCNT sensors is the prediction of how small molecules will interact with a SWCNT surface. To solve the inverse problem, designing a surface to interact with a specific small molecule of interest, advances are needed in two fundamental steps:

1. prediction of complex interfacial structures formed from adsorption of large molecules or polymers on nanoscale surfaces, and

2. screening for interactions of a selection of small molecules with a specific interfacial structure.

The first step is quickly becoming more realistic through rapidly expanding computational resources and the development of simulation techniques such as coarse-grained modeling and implicit-solvent calculations, both of which allow the simulation of longer time scales to approach steady-state adsorbed structures. These methods are being advanced by a number of groups in the polymer science, statistical mechanics, and molecular simulation communities. The second step, predicting small-molecule interactions, is similar to the challenge faced by the *in silico* drug-development community. Advances in automated force-field development for small molecules and rapid screening of small-molecule/protein interactions should directly benefit the design of SWCNT sensors. The challenge for both of these steps is how best to adapt tools from other fields to this design problem. This process requires chemical engineering groups that can understand both the challenges in nanoscale device design and these rapidly-developing molecular simulation resources.

In all of these projects, a broad understanding of available modeling and simulation tools

has been key to selecting the best approaches to give physical insight into the problems at hand and identify the most practical path forward for future modeling efforts. All of these projects contain a strong tie to experimental challenges and insight. Working directly with teams of experimentalists directly impacts the modeling approaches taken here, since their physical insights and uncertainty can be incorporated into the model selection process. Encouraging the adoption of these molecular simulation techniques in the design of new systems, as has been seen in the rapid adoption of molecular dynamics in the biological community, requires close interactions with experimental groups.

Chapter 10

Bibliography

[1] Hoomd-blue. http://codeblue.umich.edu/hoomd-blue.

[2] Ocsial tuball. http://ocsial.com/en/product/tuball/.

[3] *Towards robust fabrication of non-periodic nanoscale systems via directed self assembly*, 21st European Symposium on Computer-Aided Process Engineering, Chalkidiki, Greece, 2011.

[4] Chemistry, r. s. o. ethyl 4-[(z)-(2,4-dinitrophenoxy)-nno-azoxy]-1- piperazinecarboxylate. http://www.chemspider.com/Chemical-Structure.7847182.html. Chemspider, 2014.

[5] N. Agmon. The grotthuss mechanism. *Chemical Physics Letters*, 244(5-6):456–462, 1995.

[6] J.-H. Ahn, J.-H. Kim, N. F. Reuel, P. W. Barone, A. A. Boghossian, J. Zhang, H. Yoon, A. C. Chang, A. J. Hilmer, and M. S. Strano. Label-free, single protein detection on a near-infrared fluorescent single-walled carbon nanotube/protein microarray fabricated by cell-free synthesis. *Nano Letters*, 11(7):2743–2752, 2011.

[7] A. Aksimentiev, J. B. Heng, G. Timp, and K. Schulten. Microscopic kinetics of dna translocation through synthetic nanopores. *Biophysical Journal*, 87(3):2086–2097, 2004.

[8] A. P. Alivisatos, W. W. Gu, and C. Larabell. *Quantum dots as cellular probes*, volume 7 of *Annual Review of Biomedical Engineering*, pages 55–76. Annual Reviews, Palo Alto, 2005.

[9] J. A. Anderson, C. D. Lorenz, and A. Travesset. General purpose molecular dynamics simulations fully implemented on graphics processing units. *Journal of Computational Physics*, 227(10):5342–5359, 2008.

[10] M. J. Anderson, C. L. Hansen, and S. R. Quake. Phase knowledge enables rational screens for protein crystallization. *Proceedings of the National Academy of Sciences*, 103(45):16746–16751, 2006.

[11] P. Angelikopoulos and H. Bock. The differences in surfactant adsorption on carbon nanotubes and their bundles. *Langmuir*, 26(2):899–907, 2009.

[12] S. M. Bachilo, M. S. Strano, C. Kittrell, R. H. Hauge, R. E. Smalley, and R. B. Weisman. Structure-assigned optical spectra of single-walled carbon nanotubes. *Science*, 298(5602):2361–2366, 2002.

[13] P. W. Barone, S. Baik, D. A. Heller, and M. S. Strano. Near-infrared optical sensors based on single-walled carbon nanotubes. *Nature Materials*, 4(1):86–92, 2004.

[14] P. W. Barone, S. Baik, D. A. Heller, and M. S. Strano. Modulating single walled carbon nanotube fluorescence in response to specific molecular adsorption. *Electronic Properties of Novel Nanostructures*, 786:193–197, 2005.

[15] P. W. Barone, R. S. Parker, and M. S. Strano. In vivo fluorescence detection of glucose using a single-walled carbon nanotube optical sensor: Design, fluorophore properties, advantages, and disadvantages. *Analytical Chemistry*, 77(23):7556–7562, 2005.

[16] P. W. Barone and M. S. Strano. Reversible control of carbon nanotube aggregation for a glucose affinity sensor. *Angewandte Chemie-International Edition*, 45(48):8138–8141, 2006.

[17] C. Barta, T. Kalai, I. Vass, K. Hideg, and E. Hideg. Dansyl-and rhodamine-based fluorescent sensors for detecting singlet oxygen and superoxide production in plants in vivo. *Acta Biologica Szegediensis*, 46:149–150, 2002.

[18] J. V. Beck and K. J. Arnold. *Parameter estimation in engineering and science*. James Beck, 1977.

[19] O. Beckstein, K. Tai, and M. S. P. Sansom. Not ions alone: Barriers to ion permeation in nanopores and channels. *Journal of the American Chemical Society*, 126(45):14694–14695, 2004.

[20] E. L. Bell, T. a. Klimova, J. Eisenbart, P. T. Schumacker, and N. S. Chandel. Mitochondrial reactive oxygen species trigger hypoxia-inducible factor-dependent extension of the replicative life span during hypoxia. *Molecular and Cellular Biology*, 27:5737–45, 2007.

[21] S. Bhattacharya, D. Roxbury, X. Gong, D. Mukhopadhyay, and A. Jagota. Dna conjugated swcnts enter endothelial cells via rac1 mediated macropinocytosis. *Nano Letters*, 12:1826–30, 2012.

[22] A. A. Boghossian, J. Zhang, F. T. L. Floch-Yin, Z. W. Ulissi, P. Bojo, J.-H. Han, J.-H. Kim, J. R. Arkalgud, N. F. Reuel, R. D. Braatz, and M. S. Strano. The chemical dynamics of nanosensors capable of single-molecule detection. *The Journal of Chemical Physics*, 135(8):084124, 2011.

[23] M. Bowick, A. Cacciuto, G. Thorleifsson, and A. Travesset. Universal negative poisson ratio of self-avoiding fixed-connectivity membranes. *Physical Review Letters*, 87(14):148103, 2001.

[24] M. J. Bowick, A. Cacciuto, G. Thorleifsson, and A. Travesset. Universality classes of self-avoiding fixed-connectivity membranes. *The European Physical Journal E*, 5(2):149–160, 2001.

[25] M. J. Bowick, S. M. Catterall, M. Falcioni, G. Thorleifsson, and K. N. Anagnostopoulos. The flat phase of crystalline membranes. *Journal de Physique I*, 6(10):1321–1345, 1996.

[26] R. D. Braatz, R. Alkire, E. Seebauer, E. Rusli, R. Gunawan, T. Drews, X. Li, and Y. He. Perspectives on the design and control of multiscale systems. *Journal of Process Control*, 16(3):193–204, 2006.

[27] R. D. Braatz, R. C. Alkire, E. G. Seebauer, T. O. Drews, E. Rusli, M. Karulkar, F. Xue, Y. Qin, M. Y. Jung, and R. Gunawan. A multiscale systems approach to microelectronic processes. *Computers & Chemical Engineering*, 30(10):1643–1656, 2006.

[28] R. D. Braatz, B. Ogunnaike, J. Schwaber, and W. Rose. Autoregulation in industrial processes. In *Proceedings of the IFAC symposium on modeling and control in biomedical systems, Galveston, Texas*, pages 127–128, 1994.

[29] R. D. Braatz, E. G. Seebauer, and R. C. Alkire. Multiscale modeling and design of electrochemical systems. *Electrochemical Surface Modification: Thin Films, Functionalization and Characterization*, pages 289–334, 2008.

[30] D. Branton, D. W. Deamer, A. Marziali, H. Bayley, S. A. Benner, T. Butler, M. Di Ventra, S. Garaj, A. Hibbs, X. H. Huang, S. B. Jovanovich, P. S. Krstic, S. Lindsay, X. S. S. Ling, C. H. Mastrangelo, A. Meller, J. S. Oliver, Y. V. Pershin, J. M. Ramsey, R. Riehn, G. V. Soni, V. Tabard-Cossa, M. Wanunu, M. Wiggin, and J. A. Schloss. The potential and challenges of nanopore sequencing. *Nature Biotechnology*, 26(10):1146–1153, 2008.

[31] M. L. Brewer, U. W. Schmitt, and G. A. Voth. The formation and dynamics of proton wires in channel environments. *Biophysical Journal*, 80(4):1691–1702, 2001.

[32] M. Bucciantini, E. Giannoni, F. Chiti, F. Baroni, L. Formigli, J. Zurdo, N. Taddei, G. Ramponi, C. M. Dobson, and M. Stefani. Inherent toxicity of aggregates implies a common mechanism for protein misfolding diseases. *Nature*, 416(6880):507–511, 2002.

[33] D. Cao, P. Pang, J. He, T. Luo, J. H. Park, P. Krstic, C. Nuckolls, J. Tang, and S. Lindsay. Electronic sensitivity of carbon nanotubes to internal water wetting. *ACS Nano*, 5(4):3113–3119, 2011.

[34] Y. Cao, D. Gillespie, and L. Petzold. Multiscale stochastic simulation algorithm with stochastic partial equilibrium assumption for chemically reacting systems. *Journal of Computational Physics*, 206(2):395–411, 2005.

[35] H. Chang, F. Kosari, G. Andreadakis, M. A. Alam, G. Vasmatzis, and R. Bashir. Dna-mediated fluctuations in ionic current through silicon oxide nanopore channels. *Nano Letters*, 4(8):1551–1556, 2004.

[36] A. Chatterjee and D. G. Vlachos. An overview of spatial microscopic and accelerated kinetic monte carlo methods. *Journal of Computer-Aided Materials Design*, 14(2):253–308, 2007.

[37] G. Chen, G. Chen, and S.-H. Hsu. *Linear stochastic control systems*, volume 3. CRC press, 1995.

[38] K. Chen, L. Goh, G. He, V. Bhamidi, P. Kenis, C. Zukoski, and R. D. Braatz. Identification of bounds on nucleation rates in droplet-based microfluidic systems. In *Proceedings of the 18th International Symposium on Industrial Crystallization*, volume 264. Zürich, Switzerland, paper, 2011.

[39] K. Chen, M. Kishida, N. Nair, M. S. Strano, and R. D. Braatz. Parameter identifiability in parallel reaction networks with application to single-walled carbon nanotubes. In *American Control Conference (ACC), 2011*, pages 2873–2878. IEEE, 2011.

[40] K. Chen, N. Nair, M. S. Strano, and R. D. Braatz. Identification of chirality-dependent adsorption kinetics in single-walled carbon nanotube reaction networks. *Journal of Computational and Theoretical Nanoscience*, 7(12):2581–2585, 2010.

[41] M. P. Chin and W. M. Deen. Prediction of nitric oxide concentrations in melanomas. *Nitric Oxide*, 23(4):319–326, 2010.

[42] J. H. Choi and M. S. Strano. Solvatochromism in single-walled carbon nanotubes. *Applied Physics Letters*, 90(22):223114–223114–3, 2007.

[43] W. Choi, C. Y. Lee, M. H. Ham, S. Shimizu, and M. S. Strano. Dynamics of simultaneous, single ion transport through two single-walled carbon nanotubes: Observation of a three-state system. *Journal of the American Chemical Society*, 133(2):203–205, 2011.

[44] P. D. Christofides and A. Armaou. Control and optimization of multiscale process systems. *Computers & Chemical Engineering*, 30(10):1670–1686, 2006.

[45] L. Cognet, D. A. Tsyboulski, J. D. R. Rocha, C. D. Doyle, J. M. Tour, and R. B. Weisman. Stepwise quenching of exciton fluorescence in carbon nanotubes by single-molecule reactions. *Science*, 316(5830):1465–1468, 2007.

[46] P. Collins and P. Avouris. Multishell conduction in multiwalled carbon nanotubes. *Applied Physics A: Materials Science & Processing*, 74(3):329–332, 2002.

[47] P. Collins and P. Avouris. The electronic properties of carbon nanotubes. *Contemporary Concepts of Condensed Matter Science*, 3:49–81, 2008.

[48] P. G. Collins, M. S. Arnold, and P. Avouris. Engineering carbon nanotubes and nanotube circuits using electrical breakdown. *Science*, 292(5517):706–709, 2001.

[49] D. Colquhoun and A. Hawkes. *The Principles of the Stochastic Interpretation of Ion-Channel Mechanisms*, pages 397–482. Springer US, 2009.

[50] L. Coussens and Z. Werb. Inflammation and cancer. *Nature*, 420(6917):860–867, 2002.

[51] E. Darve, D. Rodriguez-Gomez, and A. Pohorille. Adaptive biasing force method for scalar and vector free energy calculations. *The Journal of Chemical Physics*, 128(14):144120, 2008.

[52] T. J. F. Day, A. V. Soudackov, M. Cuma, U. W. Schmitt, and G. A. Voth. A second generation multistate empirical valence bond model for proton transport in aqueous systems. *The Journal of Chemical Physics*, 117(12):5839–5849, 2002.

[53] D. De Ridder, L. Villacorte, A. Verliefde, J. Verberk, S. Heijman, G. Amy, and J. Van Dijk. Modeling equilibrium adsorption of organic micropollutants onto activated carbon. *Water Research*, 44(10):3077–3086, 2010.

[54] M. F. De Volder, S. H. Tawfick, R. H. Baughman, and A. J. Hart. Carbon nanotubes: present and future commercial applications. *Science*, 339(6119):535–539, 2013.

[55] D. W. Deamer and M. Akeson. Nanopores and nucleic acids: prospects for ultrarapid sequencing. *Trends in Biotechnology*, 18(4):147–151, 2000.

[56] T. E. Decoursey. Voltage-gated proton channels and other proton transfer pathways. *Physiological Reviews*, 83(2):475–579, 2003.

[57] P. C. Dedon and S. R. Tannenbaum. Reactive nitrogen species in the chemical biology of inflammation. *Archives of Biochemistry and Biophysics*, 423(1):12–22, 2004.

[58] C. Dekker. Solid-state nanopores. *Nature Nanotechnology*, 2(4):209–215, 2007.

[59] C. Dellago and G. Hummer. Kinetics and mechanism of proton transport across membrane nanopores. *Physical Review Letters*, 97(24), 2006.

[60] C. Dellago, M. M. Naor, and G. Hummer. Proton transport through water-filled carbon nanotubes. *Physical Review Letters*, 90(10), 2003.

[61] C. D. Doyle, J.-D. R. Rocha, R. B. Weisman, and J. M. Tour. Structure-dependent reactivity of semiconducting single-walled carbon nanotubes with benzenediazonium salts. *Journal of the American Chemical Society*, 130(21):6795–6800, 2008.

[62] B. Drawert, M. J. Lawson, L. Petzold, and M. Khammash. The diffusive finite state projection algorithm for efficient simulation of the stochastic reaction-diffusion master equation. *The Journal of Chemical Physics*, 132(7):074101, 2010.

[63] R. Drew and J. O. Miners. The effects of buthionine sulphoximine (bso) on glutathione depletion and xenobiotic biotransformation. *Biochemical Pharmacology*, 33(19):2989–2994, 1984.

[64] T. O. Drews, R. D. Braatz, and R. C. Alkire. Monte carlo simulation of kinetically limited electrodeposition on a surface with metal seed clusters. *Zeitschrift für Physikalische Chemie*, 221(9-10):1287–1305, 2007.

[65] T. O. Drews, A. Radisic, J. Erlebacher, R. D. Braatz, P. C. Searson, and R. C. Alkire. Stochastic simulation of the early stages of kinetically limited electrodeposition. *Journal of the Electrochemical Society*, 153(6):C434–C441, 2006.

[66] S. Engblom. Galerkin spectral method applied to the chemical master equation. *Communications in Computational Physics*, 5:871–896, 2009.

[67] S. Engblom, L. Ferm, A. Hellander, and P. Lötstedt. Simulation of stochastic reaction-diffusion processes on unstructured meshes. *SIAM Journal on Scientific Computing*, 31(3):1774–1797, 2009.

[68] P. D. Feigin. Maximum likelihood estimation for continuous-time stochastic-processes. *Advances in Applied Probability*, 8(4):712–736, 1976.

[69] K. A. Fichthorn and W. H. Weinberg. Theoretical foundations of dynamical monte carlo simulations. *The Journal of Chemical Physics*, 95(2):1090–1096, 1991.

[70] J. Fisher and R. Bhattacharya. Linear quadratic regulation of systems with stochastic parameter uncertainties. *Automatica*, 45(12):2831–2841, 2009.

[71] A. Fokker. Die mittlere energie rotierender elektrischer dipole im strahlungsfeld. *Annalen der Physik*, 348(5):810–820, 1914.

[72] D. Fologea, J. Uplinger, B. Thomas, D. S. McNabb, and J. L. Li. Slowing dna translocation in a solid-state nanopore. *Nano Letters*, 5(9):1734–1737, 2005.

[73] F. Fornasiero, H. G. Park, J. K. Holt, M. Stadermann, C. P. Grigoropoulos, A. Noy, and O. Bakajin. Ion exclusion by sub-2-nm carbon nanotube pores. *Proceedings of the National Academy of Sciences*, 105(45):17250–17255, 2008.

[74] D. Fukumura, S. Kashiwagi, and R. K. Jain. The role of nitric oxide in tumour progression. *Nature reviews. Cancer*, 6(7):521–34, 2006.

[75] A. Garcia-Uribe, E. B. Smith, J. Zou, M. Duvic, V. Prieto, and L. V. Wang. In-vivo characterization of optical properties of pigmented skin lesions including melanoma using oblique incidence diffuse reflectance spectrometry. *Journal of Biomedical Optics*, 16(2):020501–020501–3, 2011.

[76] P. A. Gauden, A. P. Terzyk, R. Pieńkowski, S. Furmaniak, R. P. Wesołowski, and P. Kowalczyk. Molecular dynamics of zigzag single walled carbon nanotube immersion in water. *Physical Chemistry Chemical Physics*, 13(13):5621–5629, 2011.

[77] A. K. Geim and K. S. Novoselov. The rise of graphene. *Nature Materials*, 6(3):183–191, 2007.

[78] P. Ghosh, G. Han, M. De, C. K. Kim, and V. M. Rotello. Gold nanoparticles in delivery applications. *Advanced Drug Delivery Reviews*, 60(11):1307–1315, 2008.

[79] L. Goh, K. Chen, V. Bhamidi, G. He, N. C. Kee, P. J. Kenis, C. F. Zukoski III, and R. D. Braatz. A stochastic model for nucleation kinetics determination in droplet-based microfluidic systems. *Crystal Growth & Design*, 10(6):2515–2521, 2010.

[80] X. J. Gong, J. C. Li, K. Xu, J. F. Wang, and H. Yang. A controllable molecular sieve for na(+) and k(+) ions. *Journal of the American Chemical Society*, 132(6):1873–1877, 2010.

[81] J. N. Grima, S. Winczewski, L. Mizzi, M. C. Grech, R. Cauchi, R. Gatt, D. Attard, K. W. Wojciechowski, and J. Rybicki. Tailoring graphene to achieve negative poisson's ratio properties. *Advanced Materials*, 2014.

[82] G. Gui, J. Li, and J. Zhong. Band structure engineering of graphene by strain: First-principles calculations. *Physical Review B*, 78(7):075435, 2008.

[83] I. Gurevitch and S. Srebnik. Monte carlo simulation of polymer wrapping of nanotubes. *Chemical Physics Letters*, 444(1-3):96–100, 2007.

[84] I. Gurevitch and S. Srebnik. Conformational behavior of polymers adsorbed on nanotubes. *The Journal of Chemical Physics*, 128(14):144901–8, 2008.

[85] M. Hällbrink, A. Florén, A. Elmquist, M. Pooga, T. Bartfai, and Ü. Langel. Cargo delivery kinetics of cell-penetrating peptides. *Biochimica et Biophysica Acta (BBA)-Biomembranes*, 1515(2):101–109, 2001.

[86] O. P. Hamill, A. Marty, E. Neher, B. Sakmann, and F. Sigworth. Improved patch-clamp techniques for high-resolution current recording from cells and cell-free membrane patches. *Pflügers Archiv*, 391(2):85–100, 1981.

[87] I. Hanasaki and A. Nakatani. Hydrogen bond dynamics and microscopic structure of confined water inside carbon nanotubes. *Journal of Chemical Physics*, 124(17), 2006.

[88] C. L. Hansen, E. Skordalakes, J. M. Berger, and S. R. Quake. A robust and scalable microfluidic metering method that allows protein crystal growth by free interface diffusion. *Proceedings of the National Academy of Sciences*, 99(26):16531–16536, 2002.

[89] D. M. Harrah and A. K. Swan. The role of length and defects on optical quantum efficiency and exciton decay dynamics in single-walled carbon nanotubes. *ACS Nano*, 5(1):647–655, 2010.

[90] J. He, H. Liu, P. Pang, D. Cao, and S. Lindsay. Translocation events in a single-walled carbon nanotube. *Journal of Physics: Condensed Matter*, 22(45):454112, 2010.

[91] D. A. Heller, E. S. Jeng, T.-K. Yeung, B. M. Martinez, A. E. Moll, J. B. Gastala, and M. S. Strano. Optical detection of dna conformational polymorphism on single-walled carbon nanotubes. *Science*, 311(5760):508–511, 2006.

[92] D. A. Heller, G. W. Pratt, J. Zhang, N. Nair, A. J. Hansborough, A. A. Boghossian, N. F. Reuel, P. W. Barone, and M. S. Strano. Peptide secondary structure modulates single-walled carbon nanotube fluorescence as a chaperone sensor for nitroaromatics. *Proceedings of the National Academy of Sciences*, 108(21):8544–8549, 2011.

[93] J. B. Heng, C. Ho, T. Kim, R. Timp, A. Aksimentiev, Y. V. Grinkova, S. Sligar, K. Schulten, and G. Timp. Sizing dna using a nanometer-diameter pore. *Biophysical Journal*, 87(4):2905–2911, 2004.

[94] J. Henin and C. Chipot. Overcoming free energy barriers using unconstrained molecular dynamics simulations. *The Journal of Chemical Physics*, 121(7):2904–2914, 2004.

[95] T. A. Hilder, D. Gordon, and S.-H. Chung. Computational modeling of transport in synthetic nanotubes. *Nanomedicine: Nanotechnology, Biology and Medicine*, 7(6):702–709, 2011.

[96] A. Hilmer, N. Nair, and M. S. Strano. A kinetic monte carlo analysis for the production of singularly tethered carbon nanotubes. *Nanotechnology*, 21:495703, 2010.

[97] B. J. Hinds, N. Chopra, T. Rantell, R. Andrews, V. Gavalas, and L. G. Bachas. Aligned multiwalled carbon nanotube membranes. *Science*, 303(5654):62–65, 2004.

[98] C. Ho, R. Qiao, J. B. Heng, A. Chatterjee, R. J. Timp, N. R. Aluru, and G. Timp. Electrolytic transport through a synthetic nanometer-diameter pore. *Proceedings of the National Academy of Sciences*, 102(30):10445–10450, 2005.

[99] J. K. Holt. Carbon nanotubes and nanofluidic transport. *Advanced Materials*, 21(35):3542–3550, 2009.

[100] J. K. Holt, H. G. Park, Y. M. Wang, M. Stadermann, A. B. Artyukhin, C. P. Grigoropoulos, A. Noy, and O. Bakajin. Fast mass transport through sub-2-nanometer carbon nanotubes. *Science*, 312(5776):1034–1037, 2006.

[101] S. Howorka and Z. Siwy. Nanopore analytics: sensing of single molecules. *Chemical Society Reviews*, 38(8):2360–2384, 2009.

[102] G. Hummer, J. C. Rasaiah, and J. P. Noworyta. Water conduction through the hydrophobic channel of a carbon nanotube. *Nature*, 414(6860):188–190, 2001.

[103] L. J. Ignarro. *Nitric Oxide: Biology and Pathobiology.* Academic Press, Burlington, MA, 2 edition, 2009.

[104] T. Ito, L. Sun, M. A. Bevan, and R. M. Crooks. Comparison of nanoparticle size and electrophoretic mobility measurements using a carbon-nanotube-based coulter counter, dynamic light scattering, transmission electron microscopy, and phase analysis light scattering. *Langmuir*, 20(16):6940–6945, 2004.

[105] T. Ito, L. Sun, and R. M. Crooks. Observation of dna transport through a single carbon nanotube channel using fluorescence microscopy. *Chemical Communications*, (13):1482–1483, 2003.

[106] T. Ito, L. Sun, R. R. Henriquez, and R. M. Crooks. A carbon nanotube-based coulter nanoparticle counter. *Accounts of Chemical Research*, 37(12):937–945, 2004.

[107] N. M. Iverson, P. W. Barone, M. Shandell, L. J. Trudel, S. Sen, F. Sen, V. Ivanov, E. Atolia, E. Farias, T. P. McNicholas, N. Reuel, N. M. A. Parry, G. N. Wogan, and M. S. Strano. In vivo biosensing via tissue-localizable near-infrared-fluorescent single-walled carbon nanotubes. *Nature Nanotechnology*, 8(11):873–880, 2013.

[108] Y. Iwakiri, A. Satoh, S. Chatterjee, D. K. Toomre, C. M. Chalouni, D. Fulton, R. J. Groszmann, V. H. Shah, and W. C. Sessa. Nitric oxide synthase generates nitric oxide locally to regulate compartmentalized protein s-nitrosylation and protein trafficking. *Proceedings of the National Academy of Sciences*, 103(52):19777–82, 2006.

[109] A. F. Izmailov, A. S. Myerson, and S. Arnold. A statistical understanding of nucleation. *Journal of crystal growth*, 196(2):234–242, 1999.

[110] T. Jahnke and W. Huisinga. Solving the chemical master equation for monomolecular reaction systems analytically. *Journal of Mathematical Biology*, 54(1):1–26, 2007.

[111] R. M. Jain, R. Howden, K. Tvrdy, S. Shimizu, A. J. Hilmer, T. P. McNicholas, K. K. Gleason, and M. S. Strano. Polymer-free near-infrared photovoltaics with single chirality (6,5) semiconducting carbon nanotube active layers. *Advanced Materials*, 24(32):4436–4439, 2012.

[112] R. M. Jain, K. Tvrdy, R. Han, Z. W. Ulissi, and M. S. Strano. Quantitative theory of adsorptive separation for the electronic sorting of single-walled carbon nanotubes. *ACS Nano*, 8(4):3367–3379, 2014.

[113] E. S. Jeng, P. W. Barone, J. D. Nelson, and M. S. Strano. Hybridization kinetics and thermodynamics of dna adsorbed to individually dispersed singleâĂŘwalled carbon nanotubes. *Small*, 3(9):1602–1609, 2007.

[114] E. S. Jeng, A. E. Moll, A. C. Roy, J. B. Gastala, and M. S. Strano. Detection of dna hybridization using the near-infrared band-gap fluorescence of single-walled carbon nanotubes. *Nano Letters*, 6(3):371–375, 2006.

[115] M. Jiang, X. Woo, N. Kee, L. Goh, J. Tice, L. Zhou, R. Tan, C. Zukoski III, M. Fujiwara, Z. Nagy, et al. The role of automatic process control in quality by design. *Quality by Design, John Wiley & Sons, New York*, 2011.

[116] H. Jin, D. A. Heller, M. Kalbacova, J.-H. Kim, J. Zhang, A. A. Boghossian, N. Maheshri, and M. S. Strano. Detection of single-molecule h2o2 signalling from epidermal growth factor receptor using fluorescent single-walled carbon nanotubes. *Nature Nanotechnology*, 5(4):302–309, 2010.

[117] H. Jin, D. A. Heller, J. H. Kim, and M. S. Strano. Stochastic analysis of stepwise fluorescence quenching reactions on single-walled carbon nanotubes: Single molecule sensors. *Nano Letters*, 8(12):4299–4304, 2008.

[118] H. Jin, E. S. Jeng, D. A. Heller, P. V. Jena, R. Kirmse, J. Langowski, and M. S. Strano. Divalent ion and thermally induced dna conformational polymorphism on single-walled carbon nanotubes. *Macromolecules*, 40(18):6731–6739, 2007.

[119] R. R. Johnson, A. T. C. Johnson, and M. L. Klein. The nature of dna-base-carbon-nanotube interactions. *Small*, 6(1):31–34, 2010.

[120] A. Jorio, R. Saito, J. H. Hafner, C. M. Lieber, M. Hunter, T. McClure, G. Dresselhaus, and M. S. Dresselhaus. Structural (n, m) determination of isolated single-wall carbon nanotubes by resonant raman scattering. *Physical Review Letters*, 86(6):1118–1121, 2001.

[121] A. Jorio, A. Souza Filho, G. Dresselhaus, M. Dresselhaus, A. Swan, M. ÃIJnlÃij, B. Goldberg, M. Pimenta, J. Hafner, and C. Lieber. G-band resonant raman study of 62 isolated single-wall carbon nanotubes. *Physical Review B*, 65(15):155412, 2002.

[122] A. Kalra, S. Garde, and G. Hummer. Osmotic water transport through carbon nanotube membranes. *Proceedings of the National Academy of Sciences*, 100(18):10175–10180, 2003.

[123] Y. Kasherman, S. Sturup, and D. Gibson. Is glutathione the major cellular target of cisplatin? a study of the interactions of cisplatin with cancer cell extracts. *Journal of Medicinal Chemistry*, 52(14):4319–4328, 2009.

[124] J. J. Kasianowicz, E. Brandin, D. Branton, and D. W. Deamer. Characterization of individual polynucleotide molecules using a membrane channel. *Proceedings of the National Academy of Sciences*, 93(24):13770–13773, 1996.

[125] N. Kee, X. Woo, L. Goh, E. Rusli, G. He, V. Bhamidi, R. Tan, P. Kenis, C. Zukoski, and R. D. Braatz. Design of crystallization processes from laboratory research and development to the manufacturing scale: part i. *American Pharmaceutical Review*, 11(6):110–15, 2008.

[126] N. Kee, X. Woo, L. Goh, E. Rusli, G. He, V. Bhamidi, R. Tan, P. Kenis, C. Zukoski, and R. D. Braatz. Design of crystallization processes from laboratory research and development to the manufacturing scale: part ii. *American Pharmaceutical Review*, 11(7):66–74, 2008.

[127] N. Keiding. Maximum likelihood estimation in birth-and-death process. *Annals of Statistics*, 3(2):363–372, 1975.

[128] D. G. Kendall. Stochastic processes and population growth. *Journal of the Royal Statistical Society. Series B (Methodological)*, 11(2):230–282, 1949.

[129] I. G. Kevrekidis, C. W. Gear, and G. Hummer. Equation-free: The computer-aided analysis of complex multiscale systems. *AIChE Journal*, 50(7):1346–1355, 2004.

[130] J. H. Kim, J. H. Ahn, P. W. Barone, H. Jin, J. Q. Zhang, D. A. Heller, and M. S. Strano. A luciferase/single-walled carbon nanotube conjugate for near-infrared fluorescent detection of cellular atp. *Angewandte Chemie-International Edition*, 49(8):1456–1459, 2010.

[131] J.-H. Kim, D. A. Heller, H. Jin, P. W. Barone, C. Song, J. Zhang, L. J. Trudel, G. N. Wogan, S. R. Tannenbaum, and M. S. Strano. The rational design of nitric oxide selectivity in single-walled carbon nanotube near-infrared fluorescence sensors for biological detection. *Nature Chemistry*, 1(6):473–481, 2009.

[132] J.-H. Kim, C. R. Patra, J. R. Arkalgud, A. A. Boghossian, J. Zhang, J.-H. Han, N. F. Reuel, J.-H. Ahn, D. Mukhopadhyay, and M. S. Strano. Single-molecule detection of h2o2 mediating angiogenic redox signaling on fluorescent single-walled carbon nanotube array. *ACS Nano*, 5(10):7848–7857, 2011.

[133] M. Kishida and R. D. Braatz. Optimal spatial field control of distributed parameter systems. In *American Control Conference, 2009. ACC'09.*, pages 32–37. IEEE, 2009.

[134] M. Kishida and R. D. Braatz. Rbf-based 2d optimal spatial control of the 3d reaction-convection-diffusion equation. In *Control Conference (ECC), 2009 European*, pages 1949–1954. IEEE, 2009.

[135] M. Kishida and R. D. Braatz. Structured spatial control of the reaction-diffusion equation with parametric uncertainties. In *Computer-Aided Control System Design (CACSD), 2010 IEEE International Symposium on*, pages 1097–1102. IEEE, 2010.

[136] M. Kishida and R. D. Braatz. Worst-case analysis of distributed parameter systems with application to the 2d reaction–diffusion equation. *Optimal Control Applications and Methods*, 31(5):433–449, 2010.

[137] J. Kofinger, G. Hummer, and C. Dellago. Macroscopically ordered water in nanopores. *Proceedings of the National Academy of Sciences*, 105(36):13218–13222, 2008.

[138] K. Koga, G. Gao, H. Tanaka, and X. C. Zeng. Formation of ordered ice nanotubes inside carbon nanotubes. *Nature*, 412(6849):802–805, 2001.

[139] M. V. Kothare. Dynamics and control of integrated microchemical systems with application to micro-scale fuel processing. *Computers & Chemical Engineering*, 30(10):1725–1734, 2006.

[140] J. Kroll and J. Waltenberger. Vegf-a induces expression of enos and inos in endothelial cells via vegf receptor-2 (kdr). *Biochemical and Biophysical Research Communications*, 252(3):743–746, 1998.

[141] V. Kumar, S. Y. Hong, A. E. Maciag, J. E. Saavedra, D. H. Adamson, R. K. PrudâĂŹhomme, L. K. Keefer, and H. Chakrapani. Stabilization of the nitric oxide (no) prodrugs and anticancer leads, paba/no and double js-k, through incorporation into peg-protected nanoparticles. *Molecular Pharmaceutics*, 7(1):291–298, 2009.

[142] J. Lagerqvist, M. Zwolak, and M. Di Ventra. Fast dna sequencing via transverse electronic transport. *Nano Letters*, 6(4):779–782, 2006.

[143] P. Le Doussal and L. Radzihovsky. Self-consistent theory of polymerized membranes. *Physical Review Letters*, 69(8):1209, 1992.

[144] C. Y. Lee. *Electronic detection of molecules on the exterior and molecular transport through the interior of single walled carbon nanotubes.* PhD thesis, Massachusetts Institute of Technology, 2010.

[145] C. Y. Lee, W. Choi, J. H. Han, and M. S. Strano. Coherence resonance in a single-walled carbon nanotube ion channel. *Science*, 329(5997):1320–1324, 2010.

[146] R. S. Lewis, S. Tamir, S. R. Tannenbaum, and W. M. Deen. Kinetic analysis of the fate of nitric oxide synthesized by macrophages in vitro. *Journal of Biological Chemistry*, 270(49):29350–29355, 1995.

[147] J. Li, D. Stein, C. McMullan, D. Branton, M. J. Aziz, and J. A. Golovchenko. Ion-beam sculpting at nanometre length scales. *Nature*, 412(6843):166–169, 2001.

[148] J. L. Li, M. Gershow, D. Stein, E. Brandin, and J. A. Golovchenko. Dna molecules and configurations in a solid-state nanopore microscope. *Nature Materials*, 2(9):611–615, 2003.

[149] L. Li and R. F. Ismagilov. Protein crystallization using microfluidic technologies based on valves, droplets, and slipchip. *Biophysics*, 39, 2010.

[150] D. Lide. *CRC Handbook of Chemistry and Physics, 88th Edition (CRC Handbook of Chemistry & Physics).* CRC Press, 2007.

[151] M. H. Lim, D. Xu, and S. J. Lippard. Visualization of nitric oxide in living cells by a copper-based fluorescent probe. *Nature Chemical Biology*, 2:375–80, 2006.

[152] S. Lin and D. Blankschtein. Role of the bile salt surfactant sodium cholate in enhancing the aqueous dispersion stability of single-walled carbon nanotubes: A molecular dynamics simulation study. *The Journal of Physical Chemistry B*, 114(47):15616–15625, 2010.

[153] S. Lin, J. Zhang, M. S. Strano, and D. Blankschtein. Understanding selective molecular recognition in integrated carbon nanotube-polymer sensors by simulating physical analyte binding on carbon nanotube-polymer scaffolds. *Soft Matter*, 10(32):5991–6004, 2014.

[154] M. Liong, J. Lu, M. Kovochich, T. Xia, S. G. Ruehm, A. E. Nel, F. Tamanoi, and J. I. Zink. Multifunctional inorganic nanoparticles for imaging, targeting, and drug delivery. *ACS Nano*, 2(5):889–896, 2008.

[155] C.-H. Liu and H.-L. Zhang. Chemical approaches towards single-species single-walled carbon nanotubes. *Nanoscale*, 2(10):1901–1918, 2010.

[156] F. Liu, P. Ming, and J. Li. Ab initio calculation of ideal strength and phonon instability of graphene under tension. *Physical Review B*, 76(6):064120, 2007.

[157] H. Liu, D. Nishide, T. Tanaka, and H. Kataura. Large-scale single-chirality separation of single-wall carbon nanotubes by simple gel chromatography. *Nature Communications*, 2:309, 2011.

[158] H. Liu, T. Tanaka, and H. Kataura. Industrial single-structure separation of single-wall carbon nanotubes by multicolumn gel chromatography. In *Materials Challenges and Testing for Manufacturing, Mobility, Biomedical Applications and Climate*, pages 49–56. Springer, 2014.

[159] H. T. Liu, J. He, J. Y. Tang, H. Liu, P. Pang, D. Cao, P. Krstic, S. Joseph, S. Lindsay, and C. Nuckolls. Translocation of single-stranded dna through single-walled carbon nanotubes. *Science*, 327(5961):64–67, 2010.

[160] J. Liu, C. Liu, and P. P. Conway. Kinetic monte carlo simulation of kinetically limited copper electrocrystallization on an atomically even surface. *Electrochimica Acta*, 54(27):6941–6948, 2009.

[161] J. Liu, C. Roussel, G. Lagger, P. Tacchini, and H. H. Girault. Antioxidant sensors based on dna-modified electrodes. *Analytical Chemistry*, 77:7687–94, 2005.

[162] L. Ljung. System identification: theory for the user. *PTR Prentice Hall Information and System Sciences Series*, 198, 1987.

[163] V. Lvovich and A. Scheeline. Amperometric sensors for simultaneous superoxide and hydrogen peroxide detection. *Analytical Chemistry*, 69:454–462, 1997.

[164] M. L. Macdonald, R. E. Samuel, N. J. Shah, R. F. Padera, Y. M. Beben, and P. T. Hammond. Tissue integration of growth factor-eluting layer-by-layer polyelectrolyte multilayer coated implants. *Biomaterials*, 32(5):1446–1453, 2011.

[165] R. MacKinnon. Potassium channels and the atomic basis of selective ion conduction. *Bioscience Reports*, 24(2):75–100, 2004.

[166] J. MacMicking, Q. W. Xie, and C. Nathan. Nitric oxide and macrophage function. *Annual Reviews Immunology*, 15:323–50, 1997.

[167] M. Majumder, N. Chopra, R. Andrews, and B. J. Hinds. Nanoscale hydrodynamics: Enhanced flow in carbon nanotubes. *Nature*, 438(7064):44–44, 2005.

[168] M. Manes and L. J. E. Hofer. Application of the polanyi adsorption potential theory to adsorption from solution on activated carbon. *Journal of Physical Chemistry*, 73(3):584–590, 1969.

[169] S. Manohar, T. Tang, and A. Jagota. Structure of homopolymer dna-cnt hybrids. *The Journal of Physical Chemistry C*, 111(48):17835–17845, 2007.

[170] R. A. Marcus. On the theory of oxidation-reduction reactions involving electron transfer. i. *The Journal of Chemical Physics*, 24(5):966–978, 1956.

[171] S. Marre and K. F. Jensen. Synthesis of micro and nanostructures in microfluidic systems. *Chemical Society Reviews*, 39(3):1183–1202, 2010.

[172] P. P. Mathai, A. J. Berglund, J. A. Liddle, and B. A. Shapiro. Simultaneous positioning and orientation of a single nano-object by flow control: theory and simulations. *New Journal of Physics*, 13(1):013027, 2011.

[173] K. M. Mayer and J. H. Hafner. Localized surface plasmon resonance sensors. *Chemical Reviews*, 111(6):3828–3857, 2011.

[174] B. McNally, M. Wanunu, and A. Meller. Electromechanical unzipping of individual dna molecules using synthetic sub-2 nm pores. *Nano Letters*, 8(10):3418–3422, 2008.

[175] S. Meng, P. Maragakis, C. Papaloukas, and E. Kaxiras. Dna nucleoside interaction and identification with carbon nanotubes. *Nano Letters*, 7(1):45–50, 2006.

[176] E. D. Michelakis. Diversity in mitochondrial function explains differences in vascular oxygen sensing. *Circulation Research*, 90:1307–1315, 2002.

[177] E. W. Miller, A. E. Albers, A. Pralle, E. Y. Isacoff, and C. J. Chang. Boronate-based fluorescent probes for imaging cellular hydrogen peroxide. *Journal of the American Chemical Society*, 127:16652–9, 2005.

[178] S. R. Moheimani. Invited review article: Accurate and fast nanopositioning with piezoelectric tube scanners: Emerging trends and future challenges. *Review of Scientific Instruments*, 79(7):071101, 2008.

[179] R. P. Mondescu and M. Muthukumar. Brownian motion and polymer statistics on certain curved manifolds. *Physical Review E*, 57(4):4411–4419, 1998.

[180] M. Mulqueen and D. Blankschtein. Prediction of equilibrium surface tension and surface adsorption of aqueous surfactant mixtures containing ionic surfactants. *Langmuir*, 15(26):8832–8848, 1999.

[181] R. Muniyappa and M. Quon. Insulin action and insulin resistance in vascular endothelium. *Current Opinions in Clinical Nutrition and Metabolic Care*, 10:523–530, 2007.

[182] R. Nagarajan, R. A. Bradley, and B. R. Nair. Thermodynamically stable, size selective solubilization of carbon nanotubes in aqueous solutions of amphiphilic block copolymers. *The Journal of Chemical Physics*, 131(10):104906, 2009.

[183] Z. Nagy and R. D. Braatz. Distributional uncertainty analysis using power series and polynomial chaos expansions. *Journal of Process Control*, 17(3):229–240, 2007.

[184] Z. K. Nagy and R. D. Braatz. Distributional uncertainty analysis using polynomial chaos expansions. In *Computer-Aided Control System Design (CACSD), 2010 IEEE International Symposium on*, pages 1103–1108. IEEE, 2010.

[185] N. Nair, W.-J. Kim, R. D. Braatz, and M. S. Strano. Dynamics of surfactant-suspended single-walled carbon nanotubes in a centrifugal field. *Langmuir*, 24(5):1790–1795, 2008.

[186] N. Nair, W.-J. Kim, M. L. Usrey, and M. S. Strano. A structure-reactivity relationship for single walled carbon nanotubes reacting with 4-hydroxybenzene diazonium salt. *Journal of the American Chemical Society*, 129(13):3946–3954, 2007.

[187] N. Nair, M. L. Usrey, W.-J. Kim, R. D. Braatz, and M. S. Strano. Estimation of the (n, m) concentration distribution of single-walled carbon nanotubes from photoabsorption spectra. *Analytical Chemistry*, 78(22):7689–7696, 2006.

[188] M. Naraghi, T. Filleter, A. Moravsky, M. Locascio, R. O. Loutfy, and H. D. Espinosa. A multiscale study of high performance double-walled nanotube- polymer fibers. *ACS Nano*, 4(11):6463–6476, 2010.

[189] E. Nativ-Roth, R. Shvartzman-Cohen, C. Bounioux, M. Florent, D. Zhang, I. Szleifer, and R. Yerushalmi-Rozen. Physical adsorption of block copolymers to swnt and mwnt:âĂĽ a nonwrapping mechanism. *Macromolecules*, 40(10):3676–3685, 2007.

[190] D. Nelson, T. Piran, and S. Weinberg. *Statistical Mechanics of Membranes and Surfaces*. Statistical Mechanics of Membranes and Surfaces. World Scientific Pub., 2004.

[191] Y. J. Nikas, S. Puvvada, and D. Blankschtein. Surface tensions of aqueous nonionic surfactant mixtures. *Langmuir*, 8(11):2680–2689, 1992.

[192] M. O'Connell, E. Eibergen, and S. Doorn. Chiral selectivity in the charge-transfer bleaching of single-walled carbon-nanotube spectra. *Nature Materials*, 4(5):412–418, 2005.

[193] M. J. O'Connell, S. M. Bachilo, C. B. Huffman, V. C. Moore, M. S. Strano, E. H. Haroz, K. L. Rialon, P. J. Boul, W. H. Noon, C. Kittrell, J. P. Ma, R. H. Hauge, R. B. Weisman, and R. E. Smalley. Band gap fluorescence from individual single-walled carbon nanotubes. *Science*, 297(5581):593–596, 2002.

[194] C. Oguz and M. A. Gallivan. Optimization of a thin film deposition process using a dynamic model extracted from molecular simulations. *Automatica*, 44(8):1958–1969, 2008.

[195] H. Otsuka, Y. Nagasaki, and K. Kataoka. Pegylated nanoparticles for biological and pharmaceutical applications. *Advanced Drug Delivery Reviews*, 64:246–255, 2012.

[196] G. F. Paciotti, L. Myer, D. Weinreich, D. Goia, N. Pavel, R. E. McLaughlin, and L. Tamarkin. Colloidal gold: a novel nanoparticle vector for tumor directed drug delivery. *Drug Delivery*, 11(3):169–183, 2004.

[197] W. Pan, A. B. Kolomeisky, and P. G. Vekilov. Nucleation of ordered solid phases of proteins via a disordered high-density state: Phenomenological approach. *The Journal of Chemical Physics*, 122(17):174905, 2005.

[198] P. Pang, J. He, J. H. Park, P. S. KrstiÄĞ, and S. Lindsay. Origin of giant ionic currents in carbon nanotube channels. *ACS Nano*, 5(9):7277–7283, 2011.

[199] J. H. Park, S. B. Sinnott, and N. R. Aluru. Ion separation using a y-junction carbon nanotube. *Nanotechnology*, 17(3):895–900, 2006.

[200] T. A. Pascal, W. A. Goddard, and Y. Jung. Entropy and the driving force for the filling of carbon nanotubes with water. *Proceedings of the National Academy of Sciences*, 108(29):11794–11798, 2011.

[201] S. Peleš, B. Munsky, and M. Khammash. Reduction and solution of the chemical master equation using time scale separation and finite state projection. *The Journal of Chemical Physics*, 125(20):204104, 2006.

[202] B. D. Phenix, J. L. Dinaro, M. A. Tatang, J. W. Tester, J. B. Howard, and G. J. McRae. Incorporation of parametric uncertainty into complex kinetic mechanisms: application to hydrogen oxidation in supercritical water. *Combustion and Flame*, 112(1):132–146, 1998.

[203] L. Piculell, C. Viebke, and P. Linse. Adsorption of a flexible polymer onto a rigid rod. a model study. *The Journal of Physical Chemistry*, 99(48):17423–17430, 1995.

[204] D. Pissuwan, S. M. Valenzuela, and M. B. Cortie. Therapeutic possibilities of plasmonically heated gold nanoparticles. *Trends in Biotechnology*, 24(2):62–67, 2006.

[205] M. Planck. Sitzungsber. *Preuss. Akad. Wiss. Phys. Math. Kl*, 325:3, 1917.

[206] M. Polanyi. Section iii.-theories of the adsorption of gases. a general survey and some additional remarks. introductory paper to section iii. *Transactions of the Faraday Society*, 28(0):316–333, 1932.

[207] Z. Poon, D. Chang, X. Zhao, and P. T. Hammond. Layer-by-layer nanoparticles with a ph-sheddable layer for in vivo targeting of tumor hypoxia. *ACS Nano*, 5(6):4284–4292, 2011.

[208] M. R. Powell, M. Sullivan, I. Vlassiouk, D. Constantin, O. Sudre, C. C. Martens, R. S. Eisenberg, and Z. S. Siwy. Nanoprecipitation-assisted ion current oscillations. *Nature Nanotechnology*, 3(1):51–57, 2008.

[209] X. Qian, X.-H. Peng, D. O. Ansari, Q. Yin-Goen, G. Z. Chen, D. M. Shin, L. Yang, A. N. Young, M. D. Wang, and S. Nie. In vivo tumor targeting and spectroscopic detection with surface-enhanced raman nanoparticle tags. *Nature biotechnology*, 26(1):83–90, 2008.

[210] R. Qiao and N. R. Aluru. Atypical dependence of electroosmotic transport on surface charge in a single-wall carbon nanotube. *Nano Letters*, 3(8):1013–1017, 2003.

[211] X. C. Qin, Q. Z. Yuan, Y. P. Zhao, S. B. Xie, and Z. F. Liu. Measurement of the rate of water translocation through carbon nanotubes. *Nano Letters*, 11(5):2173–2177, 2011.

[212] C. V. Rao and A. P. Arkin. Stochastic chemical kinetics and the quasi-steady-state assumption: application to the gillespie algorithm. *The Journal of Chemical Physics*, 118(11):4999–5010, 2003.

[213] A. M. Redding, F. S. Cannon, S. A. Snyder, and B. J. Vanderford. A qsar-like analysis of the adsorption of endocrine disrupting compounds, pharmaceuticals, and personal care products on modified activated carbons. *Water Research*, 43(15):3849–3861, 2009.

[214] R. Rico-Martınez, C. W. Gear, and I. G. Kevrekidis. Coarse projective kmc integration: forward/reverse initial and boundary value problems. *Journal of Computational Physics*, 196(2):474–489, 2004.

[215] R. Roldán, A. Fasolino, K. V. Zakharchenko, and M. I. Katsnelson. Suppression of anharmonicities in crystalline membranes by external strain. *Physical Review B*, 83(17):174104, 2011.

[216] D. Roxbury, S. Manohar, and A. Jagota. Molecular simulation of dna Îš-sheet and Îš-barrel structures on graphite and carbon nanotubes. *The Journal of Physical Chemistry C*, 114(31):13267–13276, 2010.

[217] D. Roxbury, J. Mittal, and A. Jagota. Molecular-basis of single-walled carbon nanotube recognition by single-stranded dna. *Nano Letters*, 12(3):1464–1469, 2012.

[218] R. Saito, M. S. Dresselhaus, and G. Dresselhaus. *Physical Properties of Carbon Nanotubes*. Imperial College Press, London, 1998.

[219] B. C. Satishkumar, L. O. Brown, Y. Gao, C. C. Wang, H. L. Wang, and S. K. Doorn. Reversible fluorescence quenching in carbon nanotubes for biomolecular sensing. *Nature Nanotechnology*, 2(9):560–564, 2007.

[220] A. M. Schrand, L. K. Braydich-Stolle, J. J. Schlager, L. Dai, and S. M. Hussain. Can silver nanoparticles be useful as potential biological labels? *Nanotechnology*, 19:235104, 2008.

[221] E. G. Seebauer, R. D. Braatz, M. Y. L. Jung, and R. Gunawan. Methods for controlling dopant concentration and activation in semiconductor structures, Dec. 7 2010. US Patent 7,846,822.

[222] E. G. Seebauer, K. Dev, M. Y. Jung, R. Vaidyanathan, C. T. Kwok, J. W. Ager, E. E. Haller, and R. D. Braatz. Control of defect concentrations within a semiconductor through adsorption. *Physical Review Letters*, 97(5):055503, 2006.

[223] V. Sgobba and D. M. Guldi. Carbon nanotubes: electronic/electrochemical properties and application for nanoelectronics and photonics. *Chemical Society Reviews*, 38(1):165–184, 2009.

[224] D. Shamah. WorldâĂŹs biggest nanotube plant coming to the negev. Technical report, Times of Israel, 2014.

[225] P. J. Shami, J. E. Saavedra, L. Y. Wang, C. L. Bonifant, B. A. Diwan, S. V. Singh, Y. Gu, S. D. Fox, G. S. Buzard, M. L. Citro, D. J. Waterhouse, K. M. Davies, X. Ji, and L. K. Keefer. Js-k, a glutathione/glutathione s-transferase-activated nitric oxide donor of the diazeniumdiolate class with potent antineoplastic activity1. *Molecular Cancer Therapeutics*, 2(4):409–417, 2003.

[226] M. M. Shulaker, G. Hills, N. Patil, H. Wei, H.-Y. Chen, H.-S. P. Wong, and S. Mitra. Carbon nanotube computer. *Nature*, 501(7468):526–530, 2013.

[227] R. Shvartzman-Cohen, M. Florent, D. Goldfarb, I. Szleifer, and R. Yerushalmi-Rozen. Aggregation and self-assembly of amphiphilic block copolymers in aqueous dispersions of carbon nanotubes. *Langmuir*, 24(9):4625–4632, 2008.

[228] C. Siettos, C. Pantelides, and I. Kevrekidis. Enabling dynamic process simulators to perform alternative tasks: A time-stepper-based toolkit for computer-aided analysis. *Industrial & engineering chemistry research*, 42(26):6795–6801, 2003.

[229] C. I. Siettos, R. Rico-Martinez, and I. G. Kevrekidis. A systems-based approach to multiscale computation: Equation-free detection of coarse-grained bifurcations. *Computers & Chemical Engineering*, 30(10):1632–1642, 2006.

[230] A. J. Siitonen, D. A. Tsyboulski, S. M. Bachilo, and R. B. Weisman. Dependence of exciton mobility on structure in single-walled carbon nanotubes. *The Journal of Physical Chemistry Letters*, 1(14):2189–2192, 2010.

[231] A. J. Siitonen, D. A. Tsyboulski, S. M. Bachilo, and R. B. Weisman. Surfactant-dependent exciton mobility in single-walled carbon nanotubes studied by single-molecule reactions. *Nano Letters*, 10(5):1595–1599, 2010.

[232] R. Smeets, U. Keyser, M. Wu, N. Dekker, and C. Dekker. Nanobubbles in solid-state nanopores. *Physical Review Letters*, 97(8):088101, 2006.

[233] E. O. Solis, P. I. Barton, and G. Stephanopoulos. Controlled formation of nanostructures with desired geometries. 1. robust static structures. *Industrial & Engineering Chemistry Research*, 49(17):7728–7745, 2010.

[234] E. O. Solis, P. I. Barton, and G. Stephanopoulos. Controlled formation of nanostructures with desired geometries. 2. robust dynamic paths. *Industrial & Engineering Chemistry Research*, 49(17):7746–7757, 2010.

[235] C. D. Spataru, S. Ismail-Beigi, R. B. Capaz, and S. G. Louie. Theory and ab initio calculation of radiative lifetime of excitons in semiconducting carbon nanotubes. *Physical Review Letters*, 95(24):247402, 2005.

[236] T. M. Squires and S. R. Quake. Microfluidics: Fluid physics at the nanoliter scale. *Reviews of Modern Physics*, 77(3):977, 2005.

[237] R. Srivastava, E. L. Haseltine, E. Mastny, and J. B. Rawlings. The stochastic quasi-steady-state assumption: reducing the model but not the noise. *The Journal of Chemical Physics*, 134(15):154109, 2011.

[238] J. J. Stickel. Data smoothing and numerical differentiation by a regularization method. *Computers & Chemical Engineering*, 34(4):467–475, 2010.

[239] A. J. Storm, C. Storm, J. H. Chen, H. Zandbergen, J. F. Joanny, and C. Dekker. Fast dna translocation through a solid-state nanopore. *Nano Letters*, 5(7):1193–1197, 2005.

[240] B. G. Sumpter, D.-E. Jiang, and V. Meunier. New insight into carbon-nanotube electronic-structure selectivity. *Small*, 4(11):2035–2042, 2008.

[241] D. Takaiwa, I. Hatano, K. Koga, and H. Tanaka. Phase diagram of water in carbon nanotubes. *Proceedings of the National Academy of Sciences*, 105(1):39–43, 2008.

[242] S. Talreja, D. Y. Kim, A. Y. Mirarefi, C. F. Zukoski, and P. J. Kenis. Screening and optimization of protein crystallization conditions through gradual evaporation using a novel crystallization platform. *Journal of Applied Crystallography*, 38(6):988–995, 2005.

[243] T. Tanaka, H. Jin, Y. Miyata, S. Fujii, H. Suga, Y. Naitoh, T. Minari, T. Miyadera, K. Tsukagoshi, and H. Kataura. Simple and scalable gel-based separation of metallic and semiconducting carbon nanotubes. *Nano Letters*, 9(4):1497–1500, 2009.

[244] T. Tanaka, H. Jin, Y. Miyata, and H. Kataura. High-yield separation of metallic and semiconducting single-wall carbon nanotubes by agarose gel electrophoresis. *Applied physics express*, 1(11):114001, 2008.

[245] M. Tang, S. Chen, R. Yuan, Y. Chai, F. Gao, and Y. Xie. Amperometric biosensor for hydrogen peroxide based on direct electrocatalysis by hemoglobin immobilized on gold nanoparticles/1,6-diaminohexane modified glassy carbon electrode. *Analytical Sciences: The International Journal of the Japan Society for Analytical Chemistry*, 24:487–91, 2008.

[246] B. A. Templeton, D. E. Cox, S. P. Kenny, M. Ahmadian, and S. C. Southward. On controlling an uncertain system with polynomial chaos and h2 control design. *Journal of Dynamic Systems, Measurement, and Control*, 132(6):061304, 2010.

[247] P. R. ten Wolde and D. Frenkel. Enhancement of protein crystal nucleation by critical density fluctuations. *Science*, 277(5334):1975–1978, 1997.

[248] J. A. Thomas and A. J. H. McGaughey. Water flow in carbon nanotubes: Transition to subcontinuum transport. *Physical Review Letters*, 102(18), 2009.

[249] K. Tvrdy, R. M. Jain, R. Han, A. J. Hilmer, T. P. McNicholas, and M. S. Strano. A kinetic model for the deterministic prediction of gel-based single-chirality single-walled carbon nanotube separation. *ACS Nano*, 7(2):1779–1789, 2013.

[250] Z. W. Ulissi, J. Zhang, A. A. Boghossian, N. F. Reuel, S. F. Shimizu, R. D. Braatz, and M. S. Strano. Applicability of birth–death markov modeling for single-molecule counting using single-walled carbon nanotube fluorescent sensor arrays. *The Journal of Physical Chemistry Letters*, 2(14):1690–1694, 2011.

[251] J. G. VanAntwerp, A. P. Featherstone, and R. D. Braatz. Robust cross-directional control of large scale sheet and film processes. *Journal of Process Control*, 11(2):149–177, 2001.

[252] K. Vanommeslaeghe, E. Hatcher, C. Acharya, S. Kundu, S. Zhong, J. Shim, E. Darian, O. Guvench, P. Lopes, I. Vorobyov, and A. D. Mackerell. Charmm general force field: A force field for drug-like molecules compatible with the charmm all-atom additive biological force fields. *Journal of Computational Chemistry*, 31(4):671–690, 2010.

[253] K. Vanommeslaeghe and A. D. MacKerell. Automation of the charmm general force field (cgenff) i: Bond perception and atom typing. *Journal of Chemical Information and Modeling*, 52(12):3144–3154, 2012.

[254] K. Vanommeslaeghe, E. P. Raman, and A. D. MacKerell. Automation of the charmm general force field (cgenff) ii: Assignment of bonded parameters and partial atomic charges. *Journal of Chemical Information and Modeling*, 52(12):3155–3168, 2012.

[255] S. Varfolomeev. Direct electron transfer effect biosensors. *Biosensors and Bioelectronics*, 11:863–871, 1996.

[256] P. G. Vekilov. Dense liquid precursor for the nucleation of ordered solid phases from solution. *Crystal Growth & Design*, 4(4):671–685, 2004.

[257] D. Vlachos, A. Mhadeshwar, and N. S. Kaisare. Hierarchical multiscale model-based design of experiments, catalysts, and reactors for fuel processing. *Computers & Chemical Engineering*, 30(10):1712–1724, 2006.

[258] E. J. Wallace and M. S. P. Sansom. Carbon nanotube/detergent interactions via coarse-grained molecular dynamics. *Nano Letters*, 7(7):1923–1928, 2007.

[259] Y. Wang, Z. Li, J. Wang, J. Li, and Y. Lin. Graphene and graphene oxide: biofunctionalization and applications in biotechnology. *Trends in Biotechnology*, 29(5):205–212, 2011.

[260] M. Wanunu, J. Sutin, B. McNally, A. Chow, and A. Meller. Dna translocation governed by interactions with solid-state nanopores. *Biophysical Journal*, 95(10):4716–4725, 2008.

[261] Z. Wei, A. B. Al-mehdi, A. B. Fisher, P. J. Bernal, K. Leelavanichkul, E. Bauer, R. Cao, A. Wilson, K. J, S. C. Watkins, B. R. Pitt, C. M. S. Croix, T. Milovanova, S. Chatterjee, Y. Manevich, I. Kotelnikova, and K. Debolt. Signaling pathway for nitric oxide generation with simulated ischemia in flow-adapted endothelial cells signaling pathway for nitric oxide generation with simulated ischemia in flow-adapted endothelial cells. *Assessment*, 2011.

[262] T. Werder, J. H. Walther, R. L. Jaffe, T. Halicioglu, and P. Koumoutsakos. On the water-carbon interaction for use in molecular dynamics simulations of graphite and carbon nanotubes. *The Journal of Physical Chemistry B*, 107(6):1345–1352, 2003.

[263] N. Wiener. The homogeneous chaos. *American Journal of Mathematics*, pages 897–936, 1938.

[264] R. C. Wilson, D. T. Phuong, E. Chainani, and A. Scheeline. Flexible, micron-scaled superoxide sensor for in vivo applications. *Journal of ElectroAnalytical Chemistry*, 662:2–6, 2011.

[265] J. Wu, J. P. Ferrance, J. P. Landers, and S. G. Weber. Integration of a precolumn fluorogenic reaction, separation, and detection of reduced glutathione. *Analytical Chemistry*, 82(17):7267–7273, 2010.

[266] Z. Xiao, X. Wang, X. Xu, H. Zhang, Y. Li, and Y. Wang. Base- and structure-dependent dna dinucleotide-carbon nanotube interactions: Molecular dynamics simulations and thermodynamic analysis. *The Journal of Physical Chemistry C*, 115(44):21546–21558, 2011.

[267] W. Yang, Z.-M. Li, W. Shi, B.-H. Xie, and M.-B. Yang. Review on auxetic materials. *Journal of Materials Science*, 39(10):3269–3279, 2004.

[268] H. Zhang, H. Ye, Y. Zheng, and Z. Zhang. Prediction of the viscosity of water confined in carbon nanotubes. *Microfluidics and Nanofluidics*, 10(2):403–414, 2011.

[269] J. Zhang, A. A. Boghossian, P. W. Barone, A. Rwei, J.-H. Kim, D. Lin, D. A. Heller, A. J. Hilmer, N. Nair, N. F. Reuel, and M. S. Strano. Single molecule detection of nitric oxide enabled by d(at)15 dna adsorbed to near infrared fluorescent single-walled carbon nanotubes. *Journal of the American Chemical Society*, 133(3):567–581, 2010.

[270] J. Zhang and R. Hofmann. Modeling the adsorption of emerging contaminants on activated carbon: classical and quantum qsar approaches. *Water Science & Technology: Water Supply*, 13(6):1543–1552, 2013.

[271] J. Zhang, M. P. Landry, P. W. Barone, J.-H. Kim, S. Lin, Z. W. Ulissi, D. Lin, B. Mu, A. A. Boghossian, A. J. Hilmer, A. Rwei, A. C. Hinckley, S. Kruss, M. A. Shandell, N. Nair, S. Blake, F. Sen, S. Sen, R. G. Croy, D. Li, K. Yum, J.-H. Ahn, H. Jin, D. A. Heller, J. M. Essigmann, D. Blankschtein, and M. S. Strano. Molecular recognition using corona phase complexes made of synthetic polymers adsorbed on carbon nanotubes. *Nature Nanotechnology*, 8(12):959–968, 2013.

[272] R. Zhang, Q. Wen, W. Qian, D. S. Su, Q. Zhang, and F. Wei. Superstrong ultralong carbon nanotubes for mechanical energy storage. *Advanced Materials*, 23(30):3387–3391, 2011.

[273] X. Zhang, W.-S. Kim, N. Hatcher, K. Potgieter, L. L. Moroz, R. Gillette, and J. V. Sweedler. Interfering with nitric oxide measurements: 4,5-diaminofluorescein reacts with dehydroascorbic acid and ascorbic acid. *Journal of Biological Chemistry*, 277(50):48472–48478, 2002.

[274] Z. Zhang, H. Davis, and D. Kroll. Molecular dynamics simulations of tethered membranes with periodic boundary conditions. *Physical Review E*, 53(2):1422, 1996.

[275] B. Zheng, L. S. Roach, and R. F. Ismagilov. Screening of protein crystallization conditions on a microfluidic chip using nanoliter-size droplets. *Journal of the American Chemical Society*, 125(37):11170–11171, 2003.

[276] M. Zheng, A. Jagota, E. Semke, B. Diner, R. McLean, S. Lustig, R. Richardson, and N. Tassi. Dna-assisted dispersion and separation of carbon nanotubes. *Nature Materials*, 2(5):338–342, 2003.

[277] Z. Zheng, R. M. Stephens, R. D. Braatz, R. C. Alkire, and L. R. Petzold. A hybrid multiscale kinetic monte carlo method for simulation of copper electrodeposition. *Journal of Computational Physics*, 227(10):5184–5199, 2008.

[278] Y. F. Zhou, J. H. Morais-Cabral, A. Kaufman, and R. MacKinnon. Chemistry of ion coordination and hydration revealed by a k+ channel-fab complex at 2.0 angstrom resolution. *Nature*, 414(6859):43–48, 2001.

Appendix A

Experimental Analysis of Sensors from Chapter 4

Chapter 4 describes the analysis method used to analyze the near-IR movies for the response of individual cells to various stimuli (for example, the introduction of JS-K to cells with or without cisplatin incubation). The analysis and corresponding data is presented for each condition in Figure A-1. Each condition contains (subfigures A-E): The NIR fluorescent intensity of the cell at the start of the experiment, marked with the identified SWCNT locations. The total integrated intensity of the NIR signal over the course of the experiment. A histogram of the distribution of concentration gradients over the entire experiment. When only a single point is identified in the image, gradient information is not available. The fitted intensity of each point, and the de-noised intensity over the course of the experiment. The calculated nitric oxide concentration at each point over the course of the experiment.

Analysis is provided for the following sets of experiments, all mentioned and discussed in the main text

- A375 melanoma cells, after exposure to 16, 20, 25, 28 μM JS-K solution.
- A375 melanoma cells, after incubation with cisplatin and then exposed to 16, 20, 25 μM JS-K solution.
- A375 melanoma cells, after incubation with BSO and then exposed to 16, 20, 25 μM JS-K solution.
- A375 melanoma cells, after exposure to 16, 20, 25 μM NO solution.

- A375 melanoma cells, after incubation with sodium azide and after exposure to 28 μM JS-K solution.
- A375 melanoma cells, after exposure to 28 μM JS-K solution.
- HUVEC cells after exposure to 1, 2, 5, 10, 25, 50, 100 ng/ml VEGF solution.

Figure A-1: Full analysis data for all of the experiments and controls discussed in chapter 4. For each experiment, the organization of the figures is the following: (A) Total cumulative photoluminescence intensity for each cell is displayed along with endosomal centers used for calculations. (B) Whole cell photoluminescence intensity as a function of time for each experimental condition. (C) Display of gradient distribution between all endosomal centers detected. (D) Photoluminescence intensity and curve fitting for each endosomal center. (E) Calculation of NO concentration at each endosomal center.

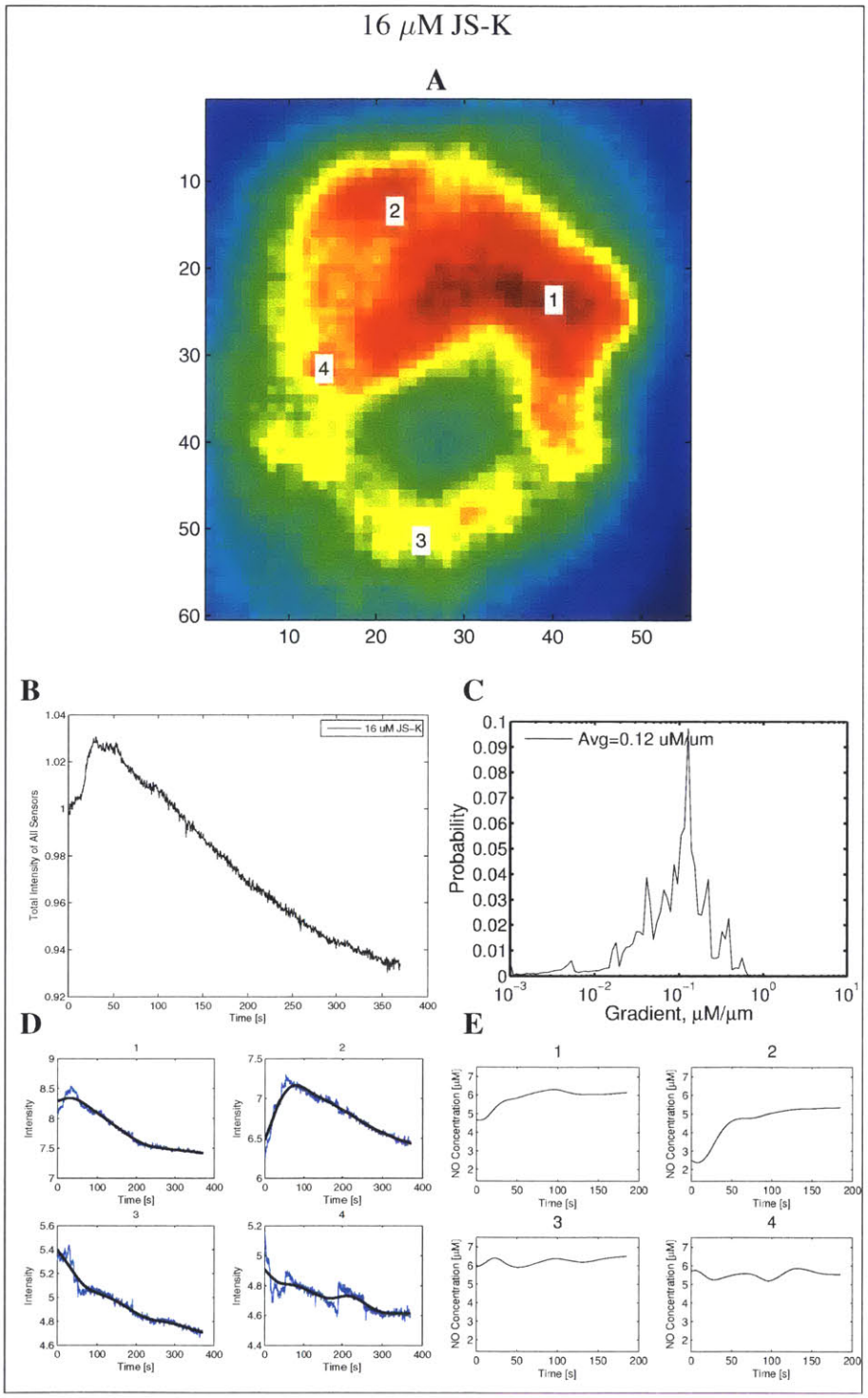
16 μM JS-K
A
B
C
D
E
16 uM JS-K
Total Intensity of All Sensors
Time [s]
Avg=0.12 uM/um
Probability
Gradient, μM/μm
Intensity
NO Concentration [μM]

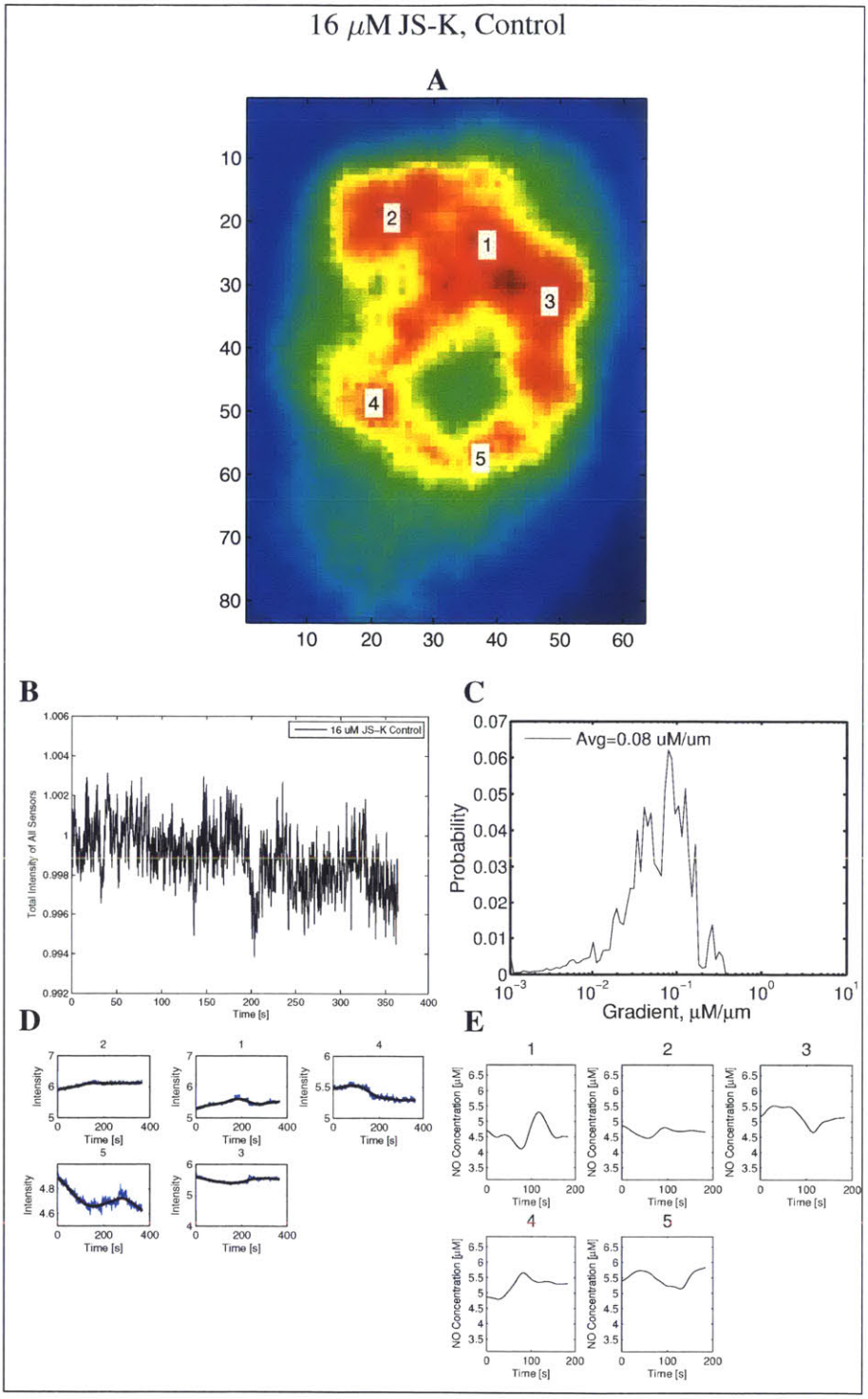
16 μM JS-K, Control
A
B
C
D
E
16 uM JS-K Control
Total Intensity of All Sensors
Time [s]
Avg=0.08 uM/um
Probability
Gradient, μM/μm
Intensity
NO Concentration [μM]

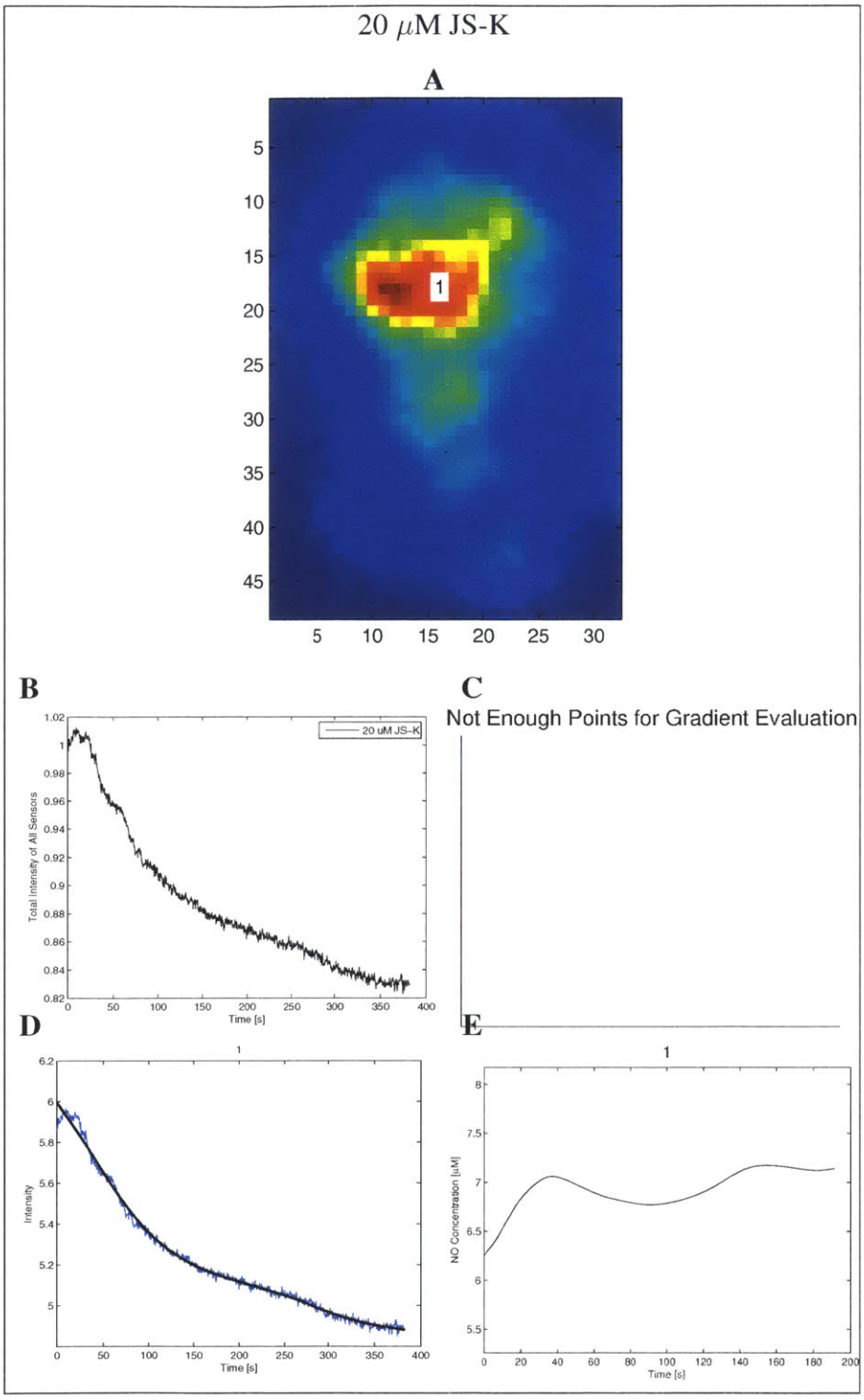
20 μM JS-K
A
1
B
20 uM JS-K
Total Intensity of All Sensors
Time [s]
C
Not Enough Points for Gradient Evaluation
D
1
Intensity
Time [s]
E
1
NO Concentration [uM]
Time [s]

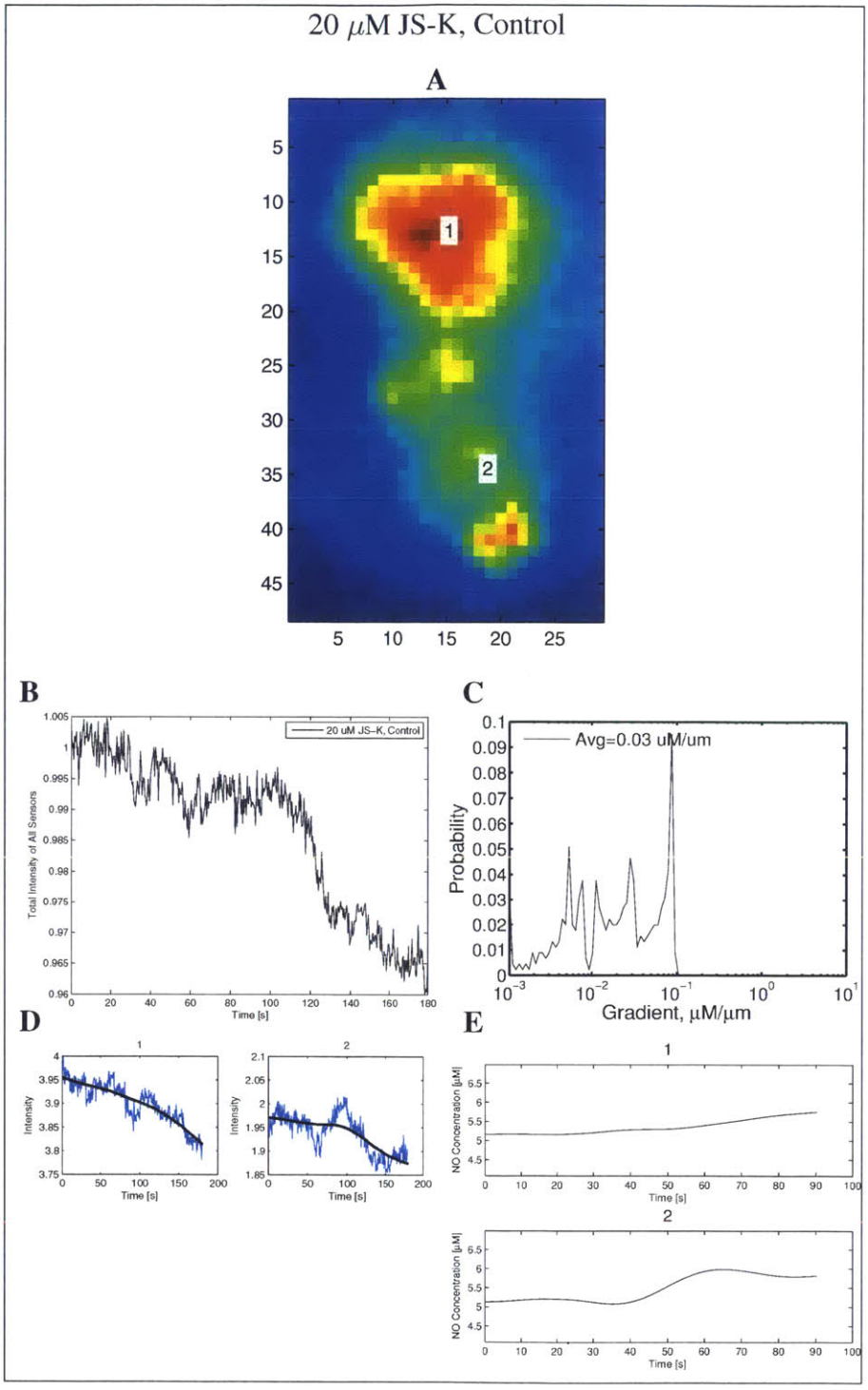
20 μM JS-K, Control
A
1
2
B
20 uM JS-K, Control
Total Intensity of All Sensors
Time [s]
C
Avg=0.03 uM/um
Probability
Gradient, μM/μm
D
1
2
Intensity
Time [s]
E
1
2
NO Concentration [μM]
Time [s]

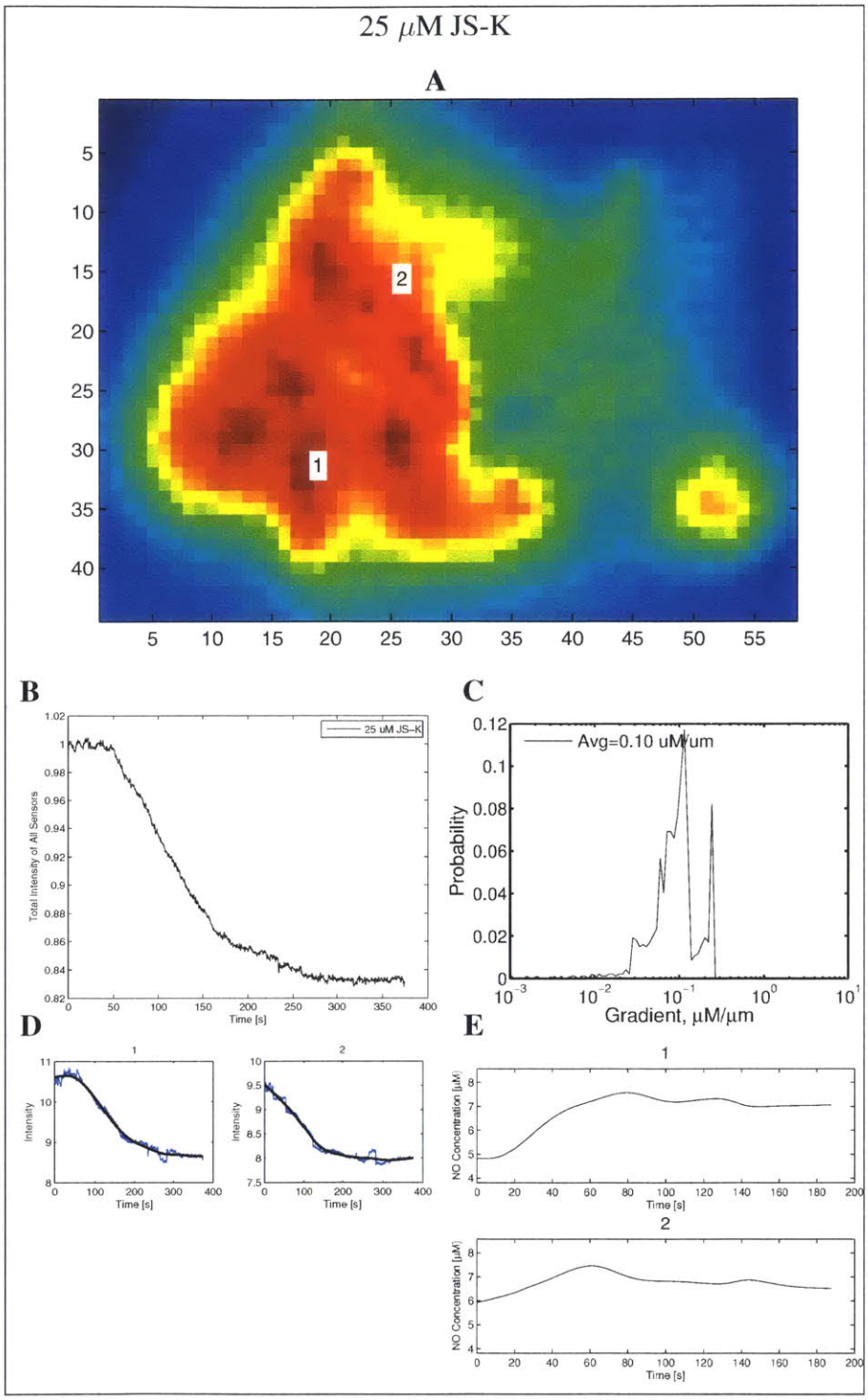
25 μM JS-K
A
B
C
D
E
25 uM JS-K
Total Intensity of All Sensors
Time [s]
Avg=0.10 uM/um
Probability
Gradient, μM/μm
Intensity
NO Concentration [μM]

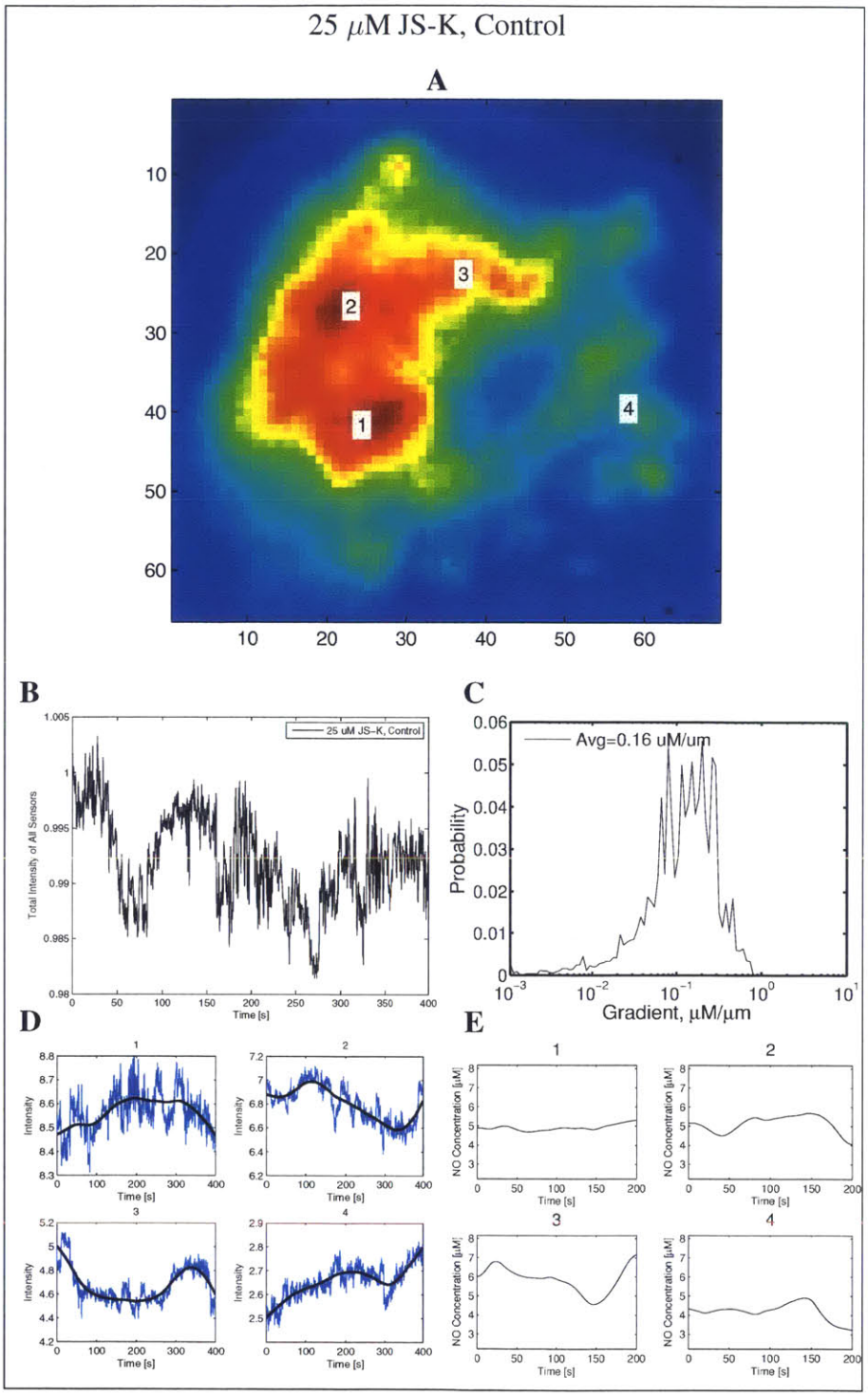
25 μM JS-K, Control
A
1
2
3
4
B
25 uM JS-K, Control
Total Intensity of All Sensors
Time [s]
C
Avg=0.16 uM/um
Probability
Gradient, μM/μm
D
Intensity
Time [s]
E
NO Concentration [μM]
Time [s]

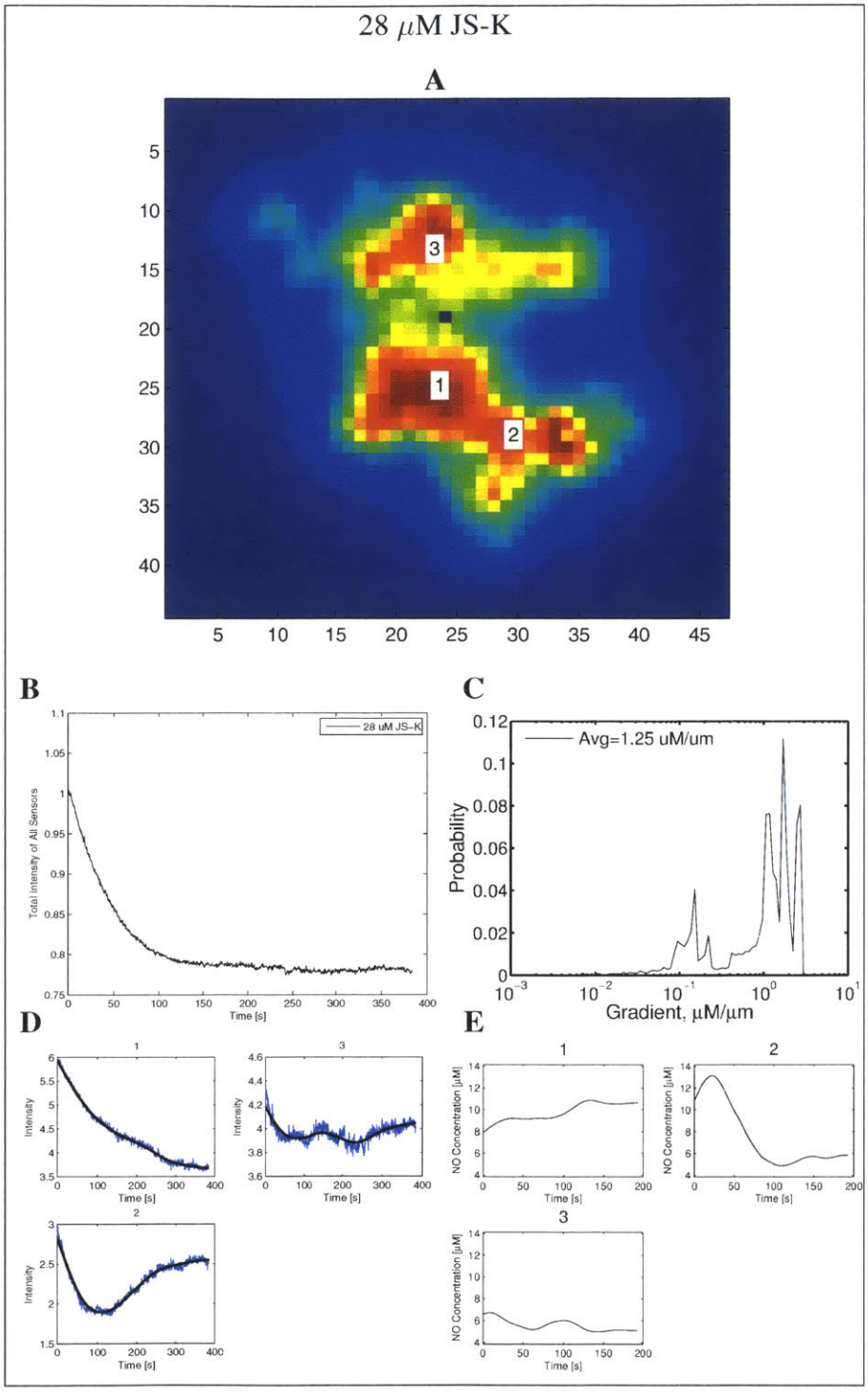
28 μM JS-K
A
B
C
D
E
28 uM JS-K
Total Intensity of All Sensors
Time [s]
Avg=1.25 uM/um
Probability
Gradient, μM/μm
Intensity
NO Concentration [μM]

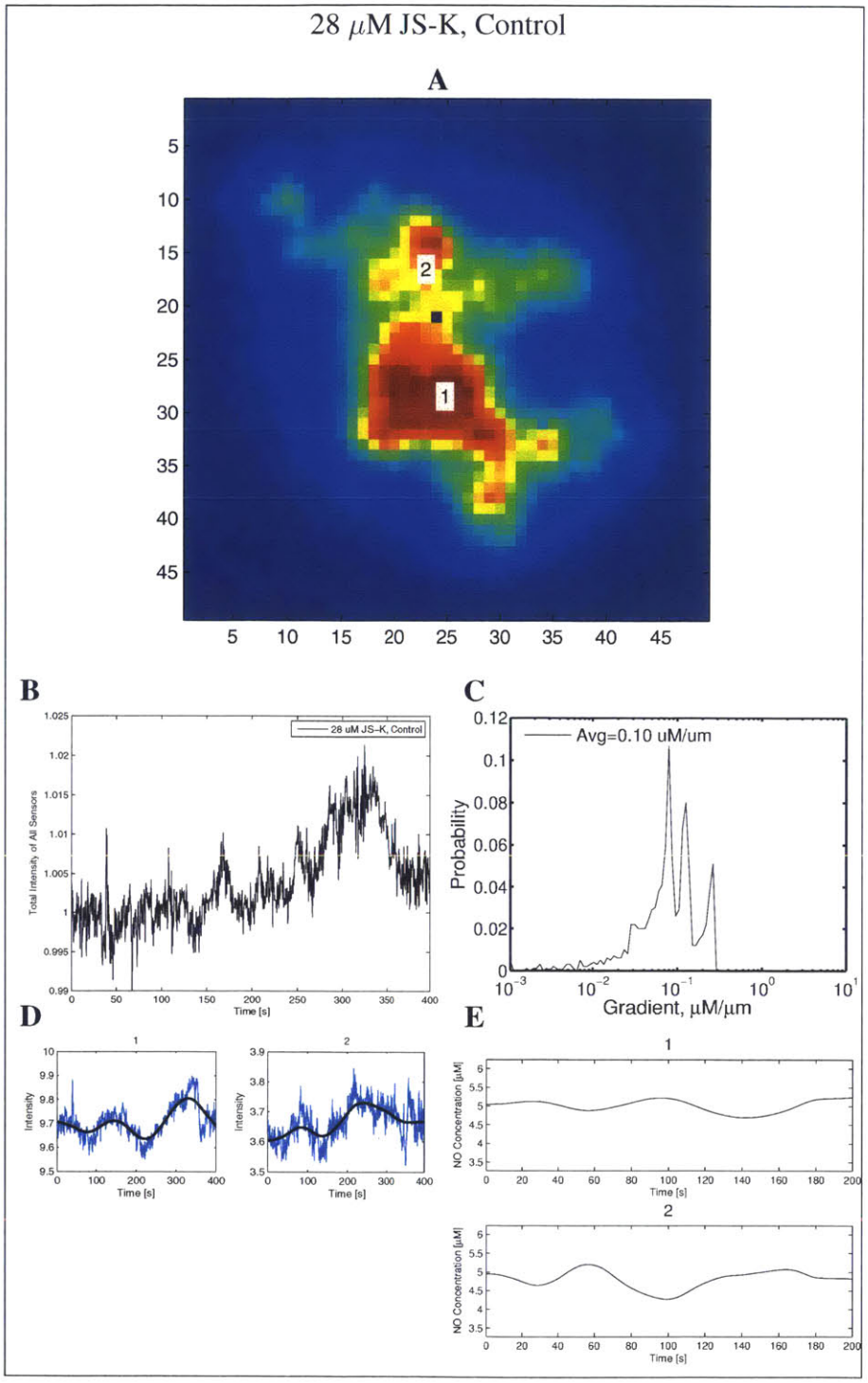
28 μM JS-K, Control
A
B
C
D
E
28 uM JS-K, Control
Total Intensity of All Sensors
Time [s]
Avg=0.10 uM/um
Probability
Gradient, μM/μm
Intensity
NO Concentration [μM]

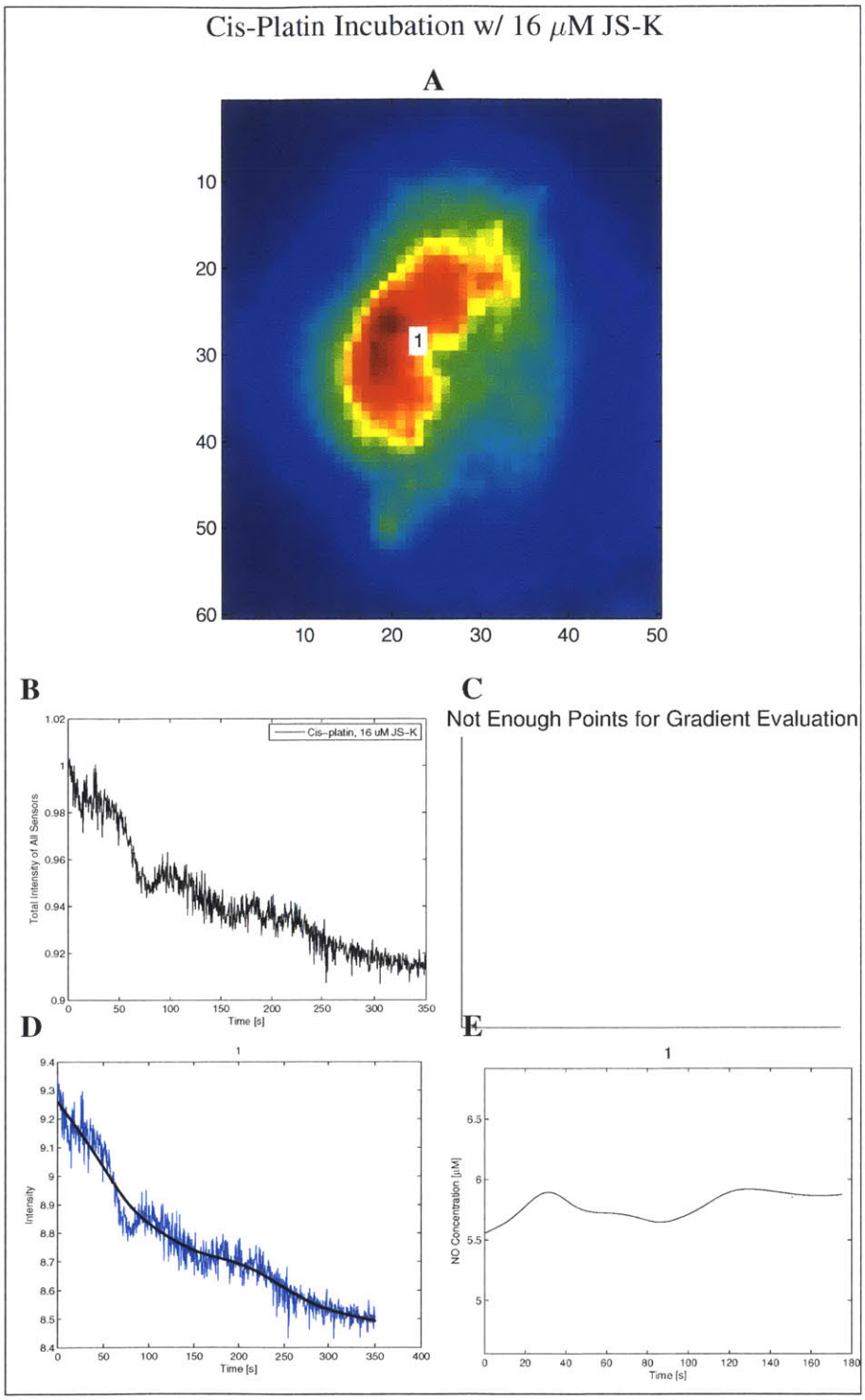
Cis-Platin Incubation w/ 16 μM JS-K
A
1
B
Cis–platin, 16 uM JS–K
Total Intensity of All Sensors
Time [s]
C
Not Enough Points for Gradient Evaluation
D
1
Intensity
Time [s]
E
1
NO Concentration [μM]
Time [s]

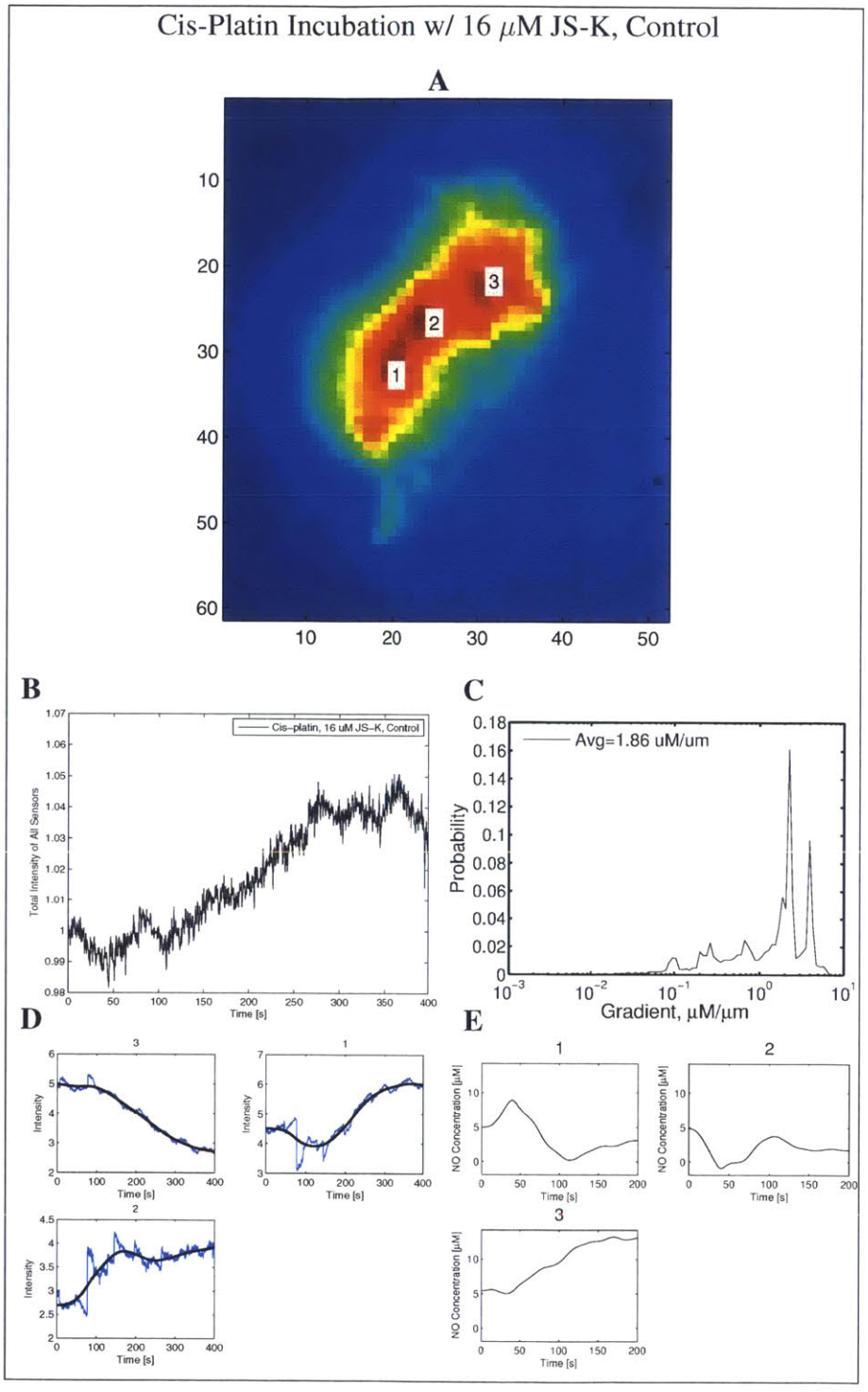
Cis-Platin Incubation w/ 16 μM JS-K, Control
A
B
C
D
E
Cis−platin, 16 uM JS−K, Control
Total Intensity of All Sensors
Time [s]
Avg=1.86 uM/um
Probability
Gradient, μM/μm
Intensity
NO Concentration [μM]

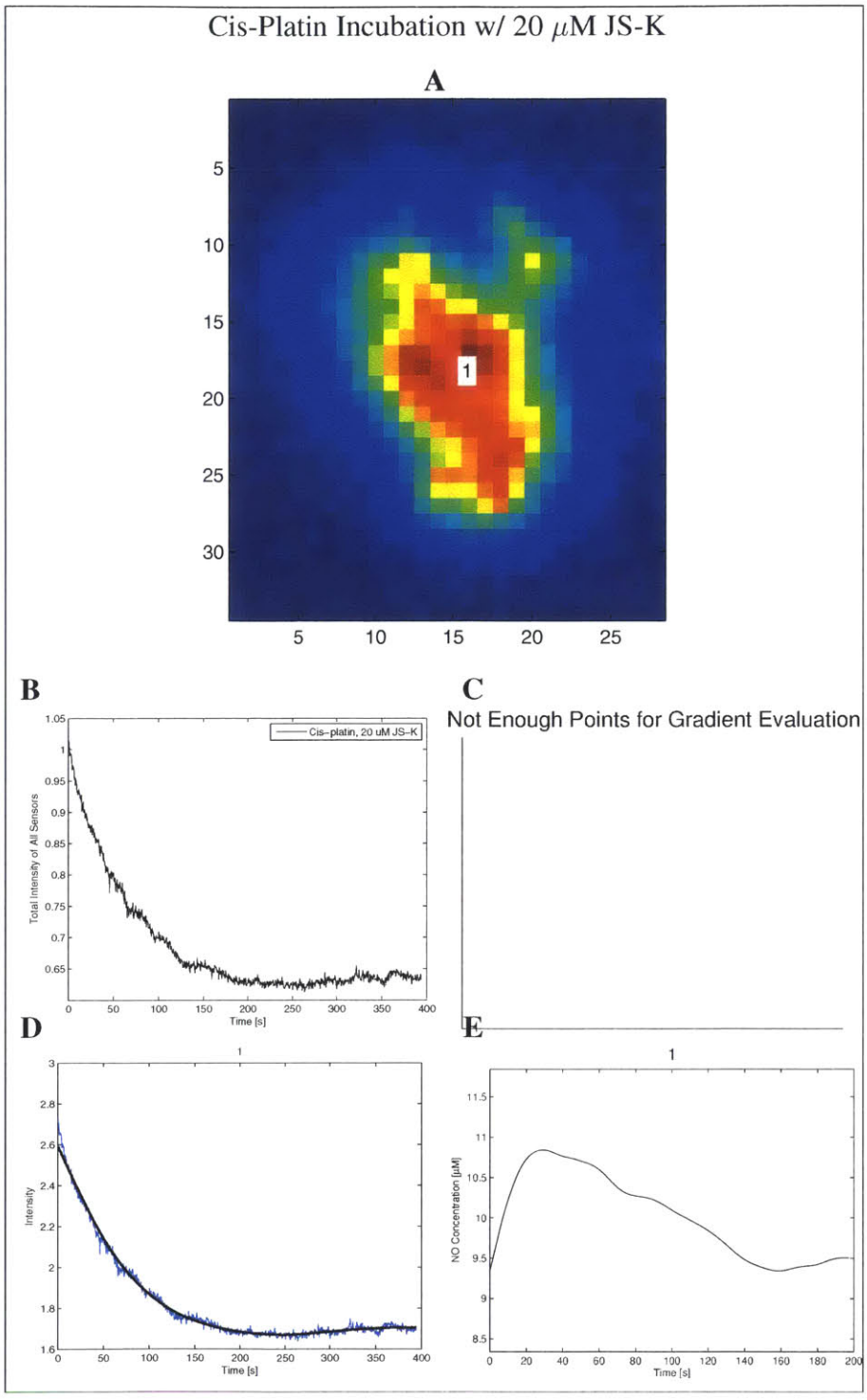
Cis-Platin Incubation w/ 20 μM JS-K
A
1
B
Cis−platin, 20 uM JS−K
Total Intensity of All Sensors
Time [s]
C
Not Enough Points for Gradient Evaluation
D
1
Intensity
Time [s]
E
1
NO Concentration [μM]
Time [s]

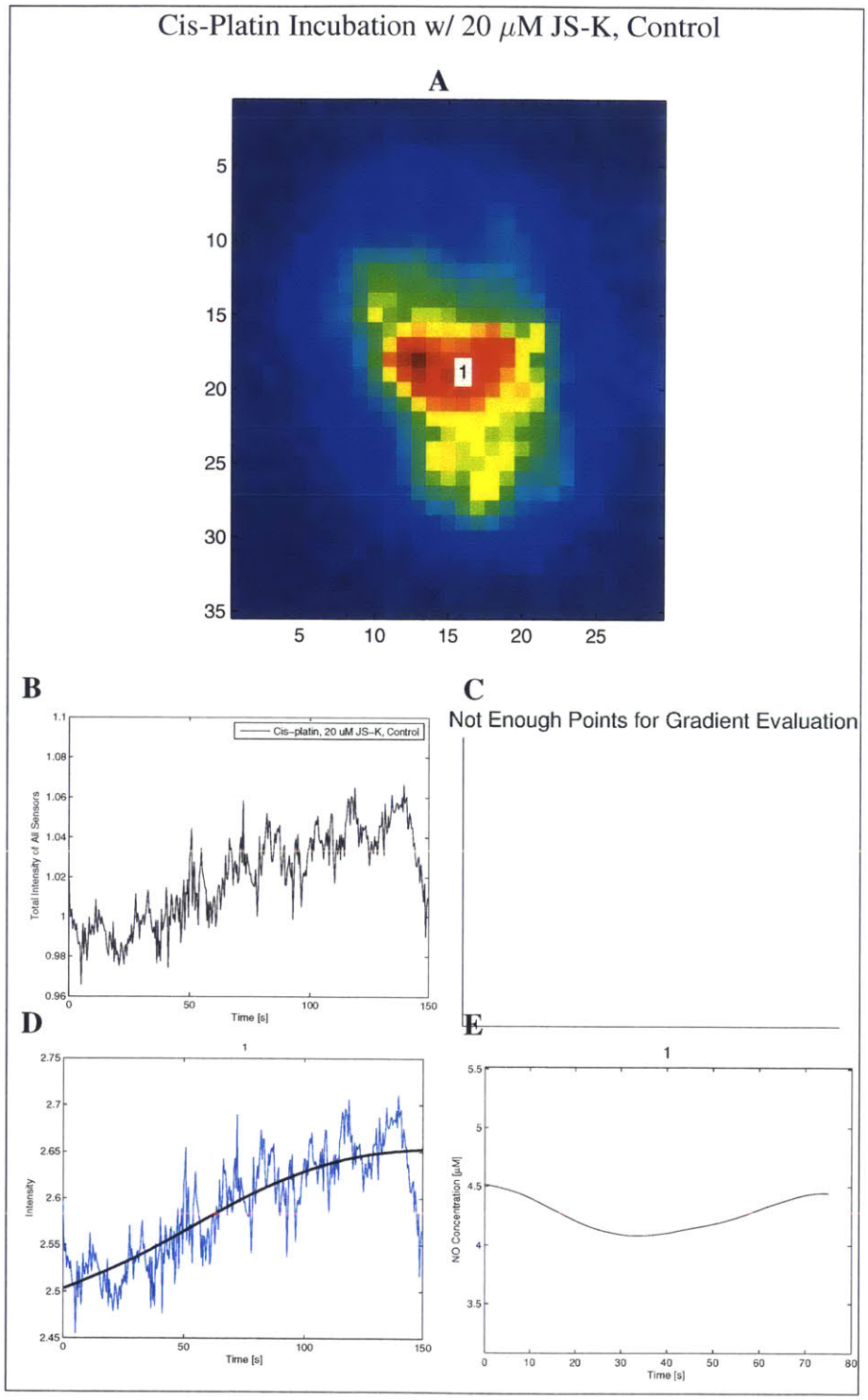
Cis-Platin Incubation w/ 20 μM JS-K, Control
A
1
B
Cis--platin, 20 uM JS--K, Control
Total Intensity of All Sensors
Time [s]
C
Not Enough Points for Gradient Evaluation
D
1
Intensity
Time [s]
E
1
NO Concentration [uM]
Time [s]

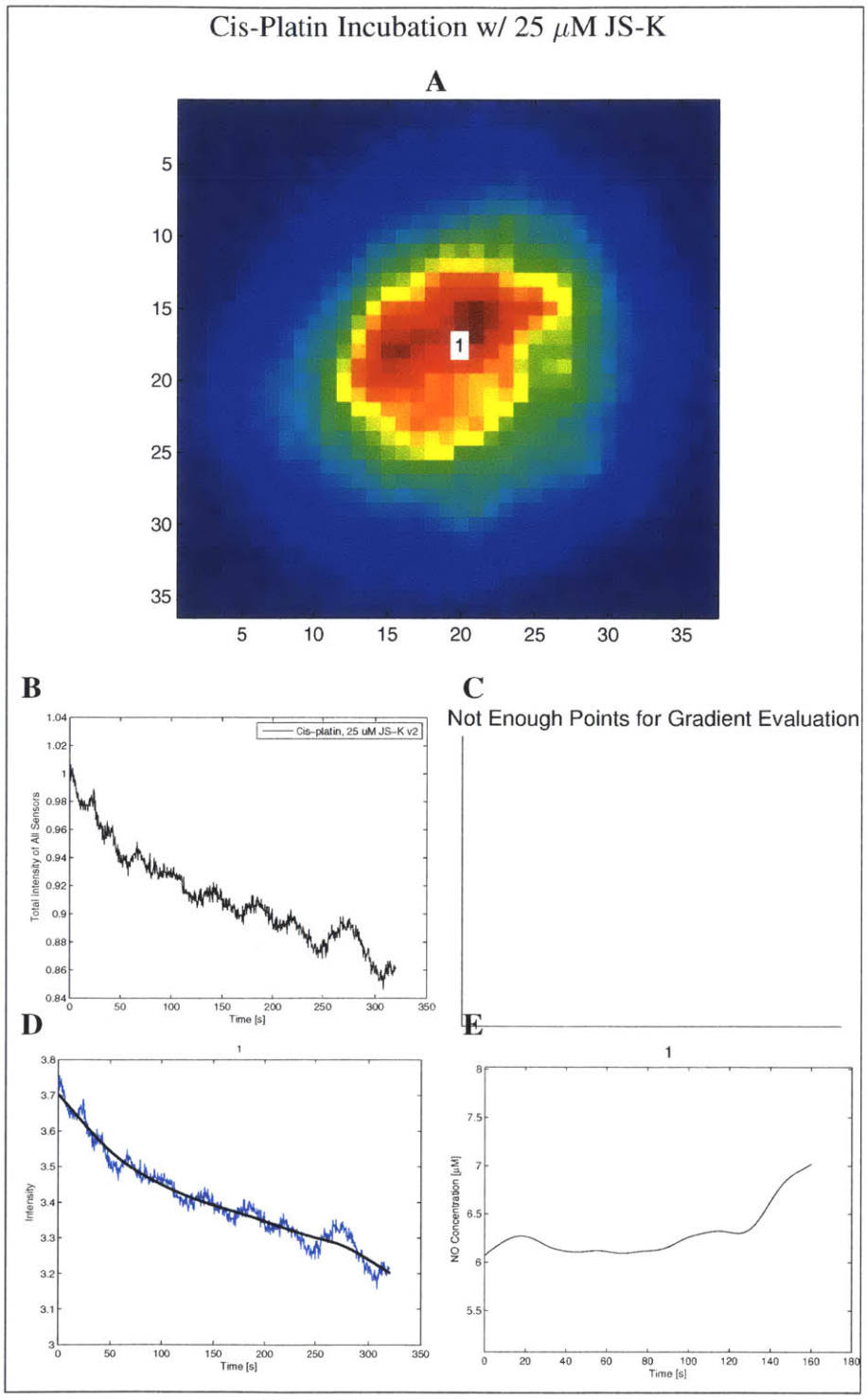
Cis-Platin Incubation w/ 25 μM JS-K
A
1
B
Cis-platin, 25 uM JS-K v2
Total Intensity of All Sensors
Time [s]
C
Not Enough Points for Gradient Evaluation
D
1
Intensity
Time [s]
E
1
NO Concentration [μM]
Time [s]

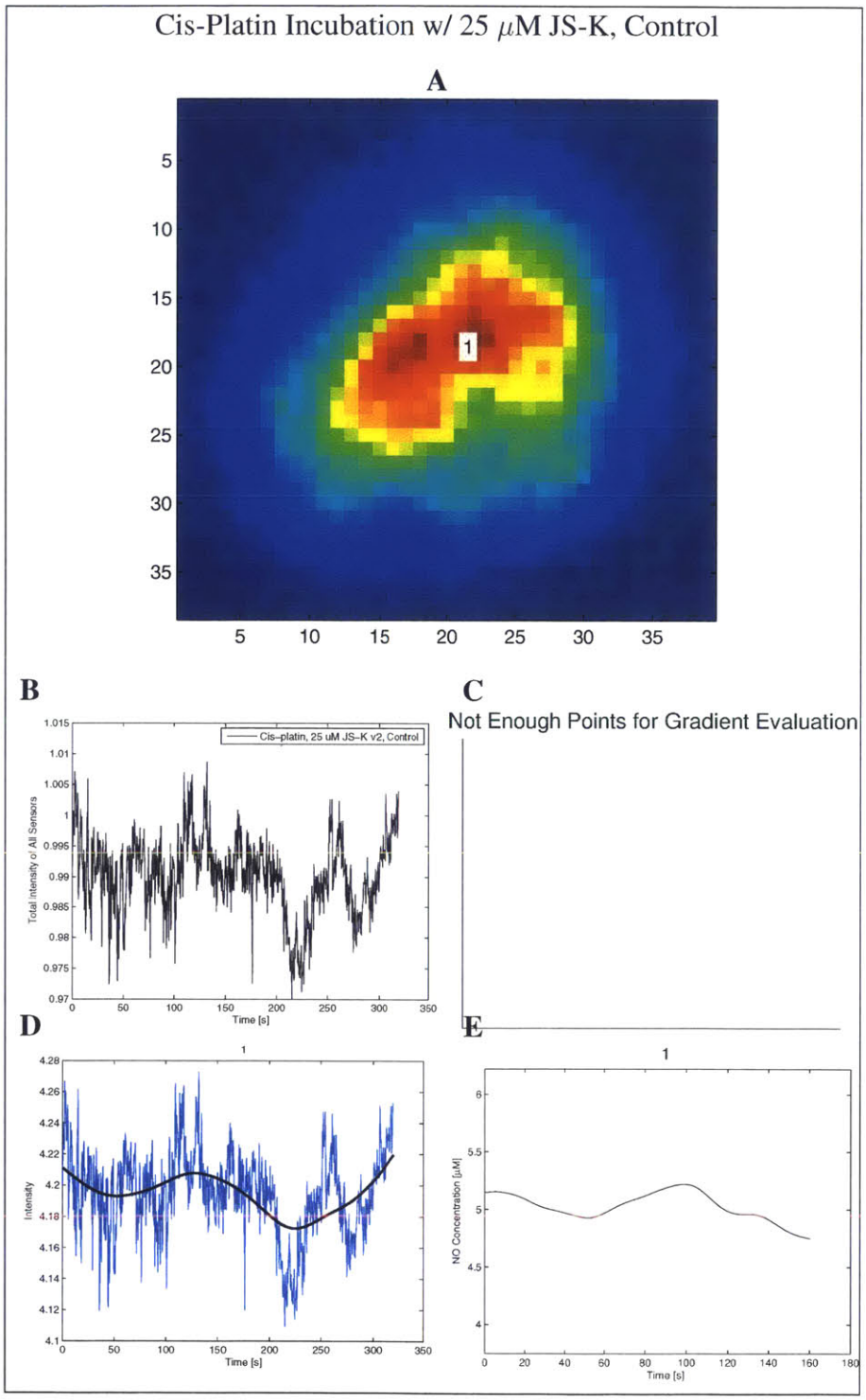
Cis-Platin Incubation w/ 25 μM JS-K, Control
A
1
B
Cis–platin, 25 uM JS–K v2, Control
Total Intensity o/ All Sensors
Time [s]
C
Not Enough Points for Gradient Evaluation
D
1
Intensity
Time [s]
E
1
NO Concentration [μM]
Time [s]

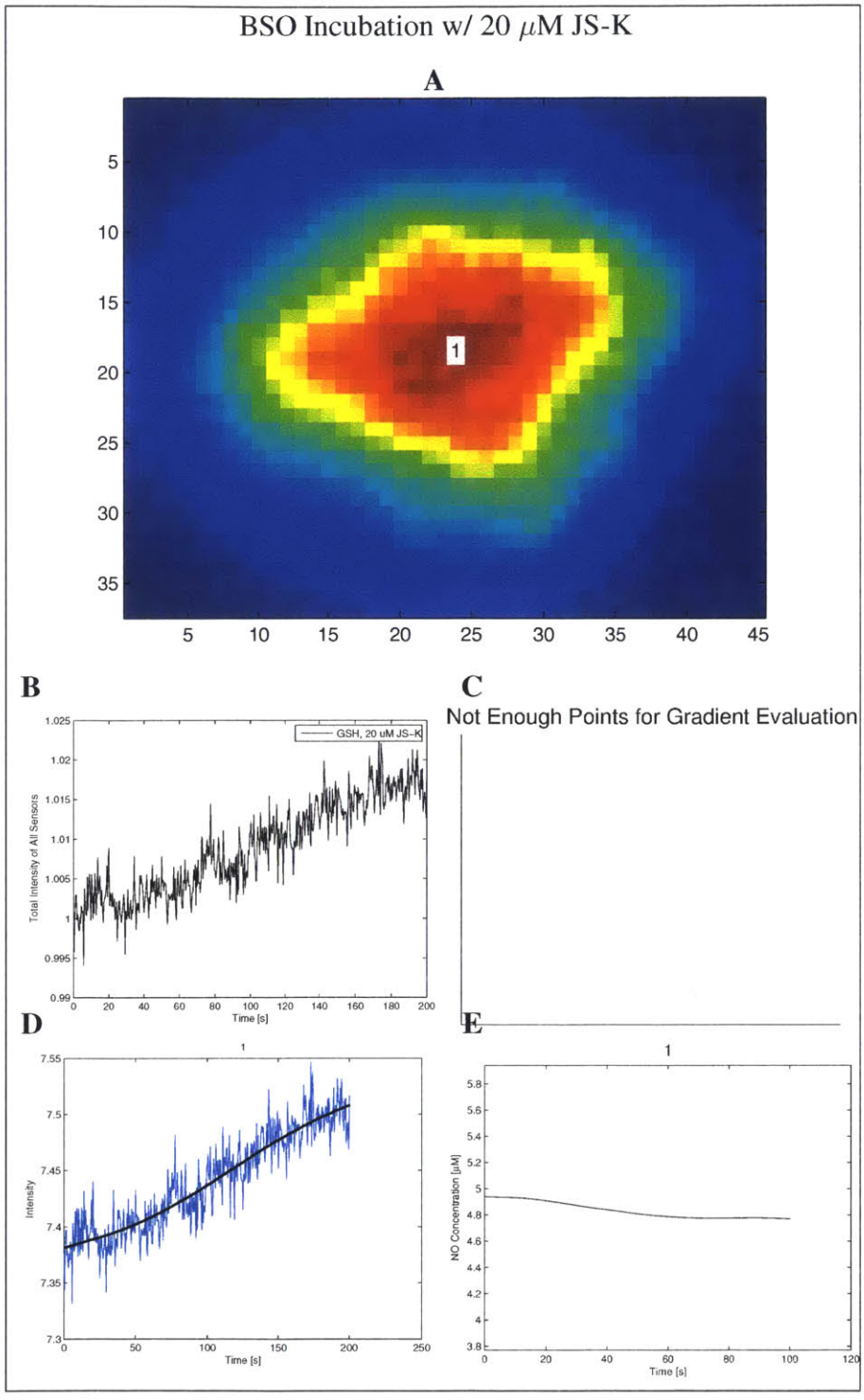
BSO Incubation w/ 20 μM JS-K
A
1
B
GSH, 20 uM JS-K
Total Intensity of All Sensors
Time [s]
C
Not Enough Points for Gradient Evaluation
D
1
Intensity
Time [s]
E
1
NO Concentration [μM]
Time [s]

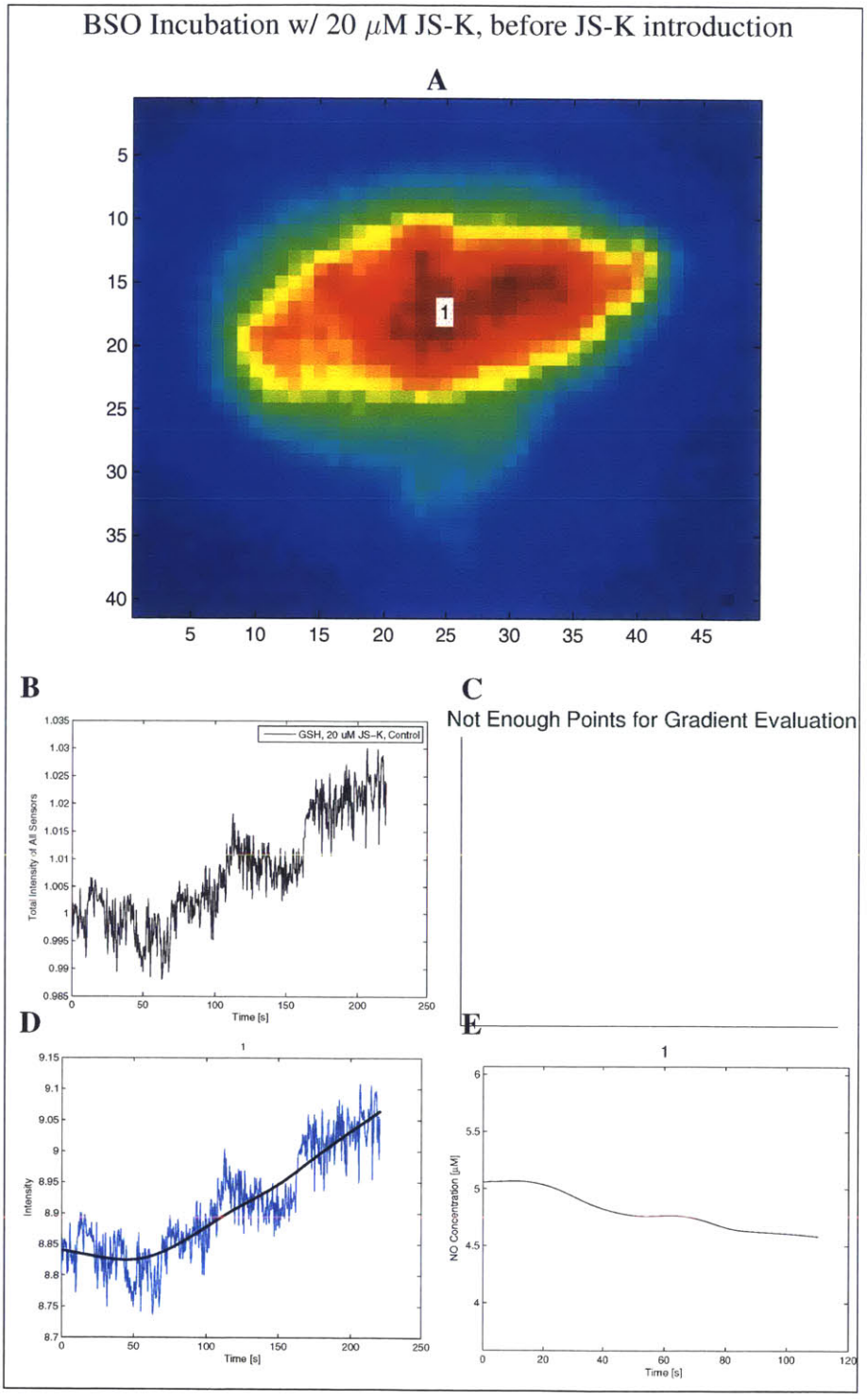
BSO Incubation w/ 20 μM JS-K, before JS-K introduction
A
1
B
GSH, 20 uM JS-K, Control
Total Intensity of All Sensors
Time [s]
C
Not Enough Points for Gradient Evaluation
D
1
Intensity
Time [s]
E
1
NO Concentration [μM]
Time [s]

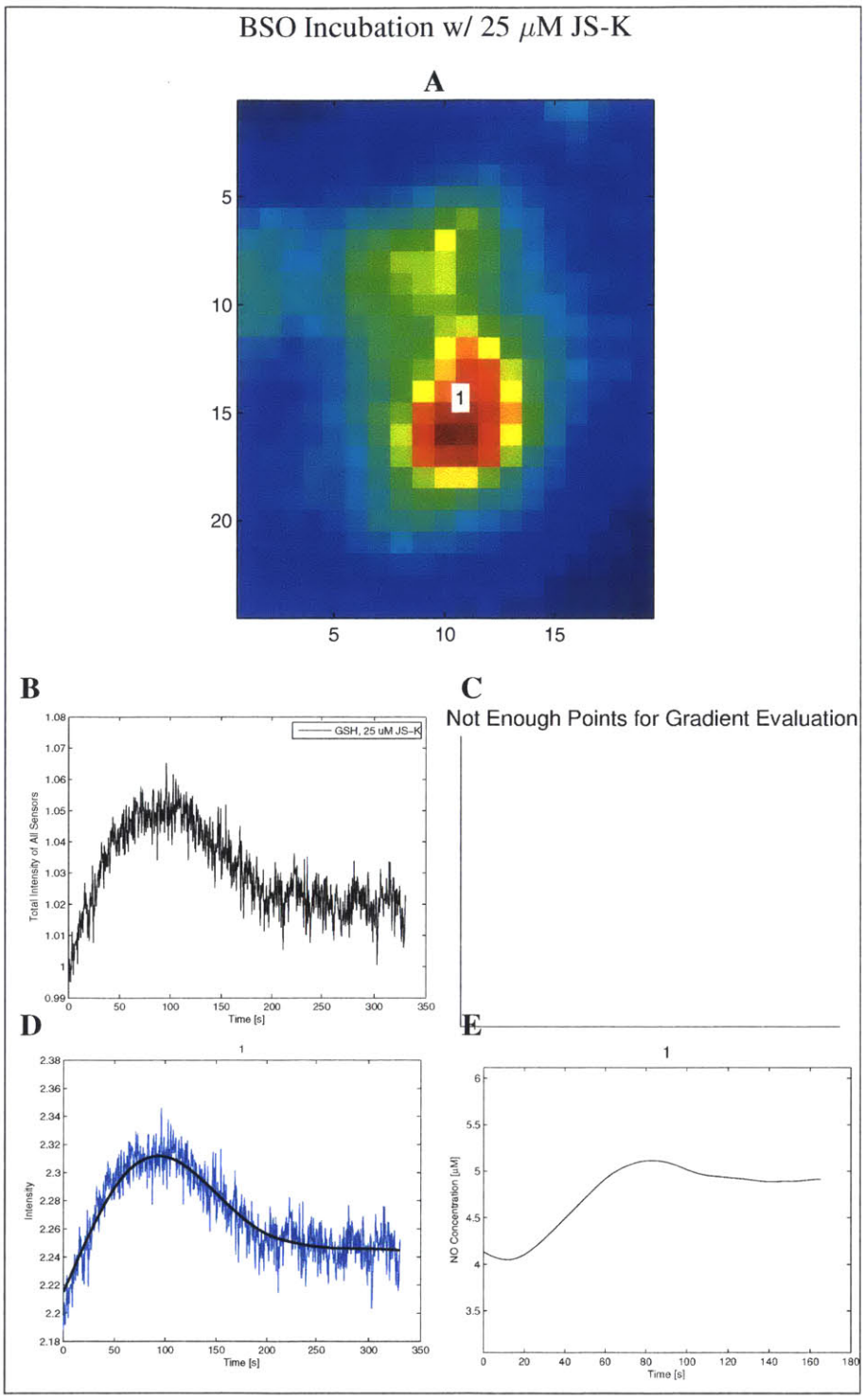
BSO Incubation w/ 25 μM JS-K
A
1
B
GSH, 25 uM JS-K
Total Intensity of All Sensors
Time [s]
C
Not Enough Points for Gradient Evaluation
D
Intensity
Time [s]
E
NO Concentration [μM]
Time [s]

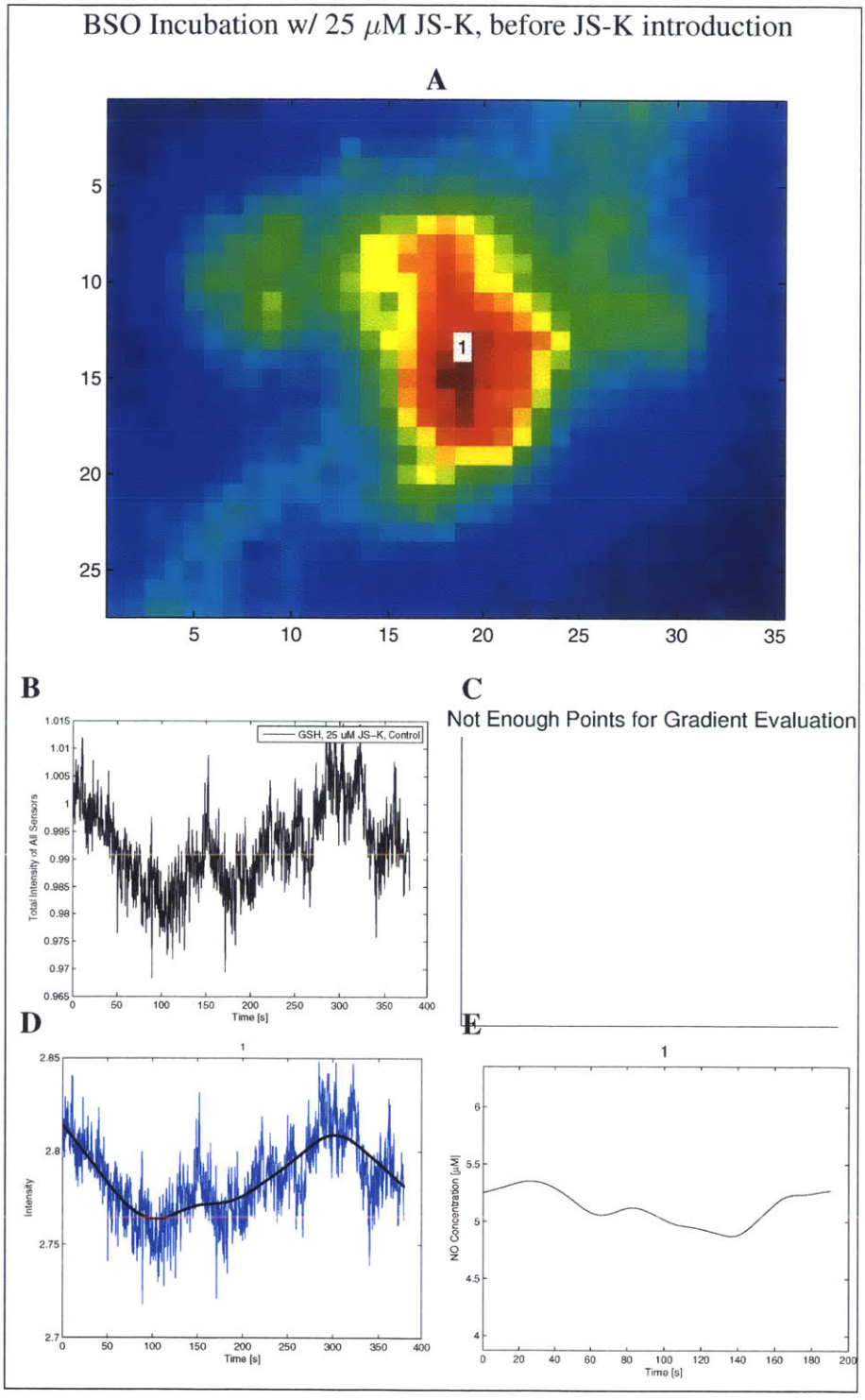
BSO Incubation w/ 25 μM JS-K, before JS-K introduction
A
1
B
GSH, 25 uM JS-K, Control
Total Intensity of All Sensors
Time [s]
C
Not Enough Points for Gradient Evaluation
D
1
Intensity
Time [s]
E
1
NO Concentration [μM]
Time [s]

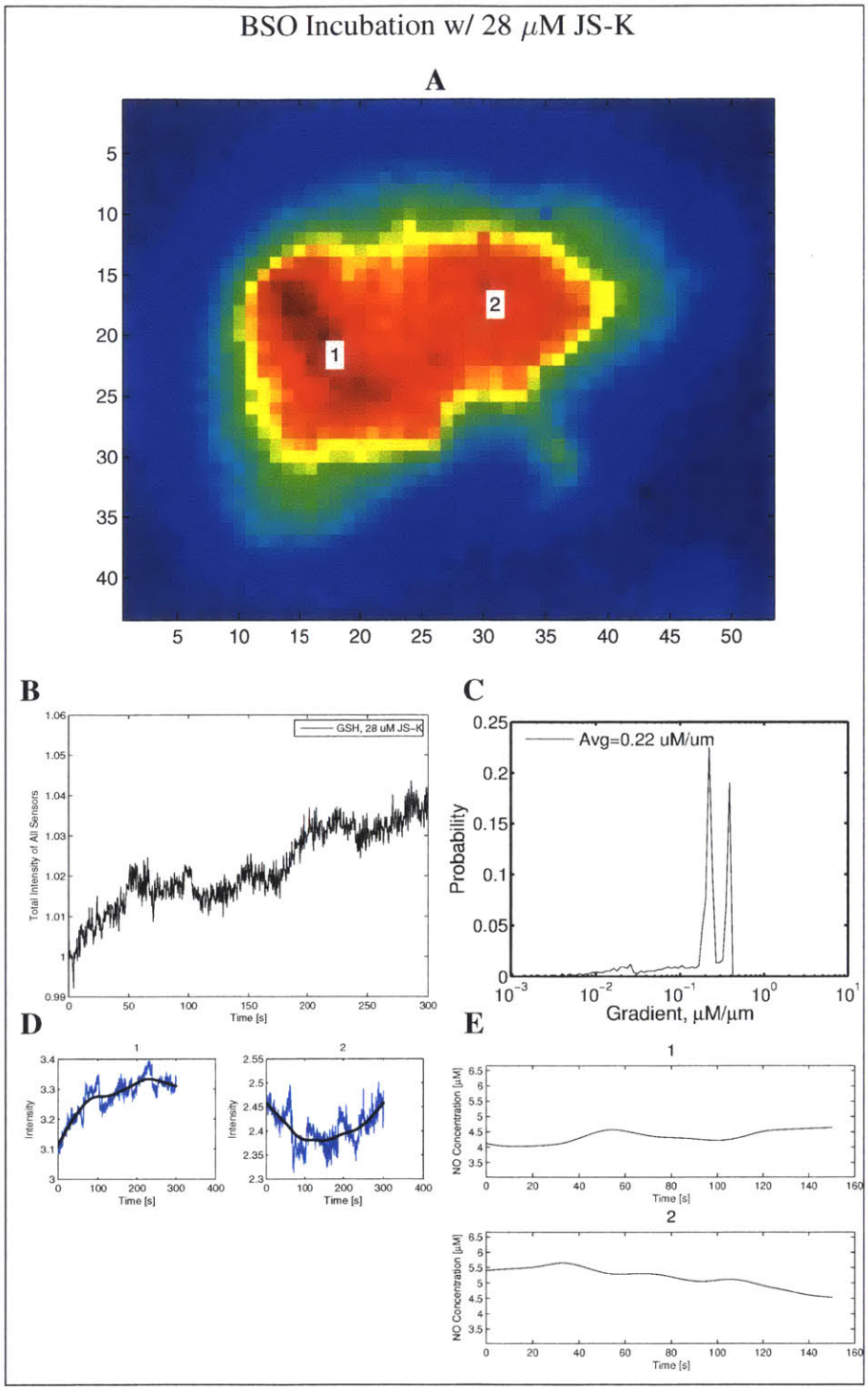
BSO Incubation w/ 28 μM JS-K
A
1
2
B
GSH, 28 uM JS-K
Total Intensity of All Sensors
Time [s]
C
Avg=0.22 uM/um
Probability
Gradient, μM/μm
D
1
2
Intensity
Time [s]
E
1
2
NO Concentration [μM]
Time [s]

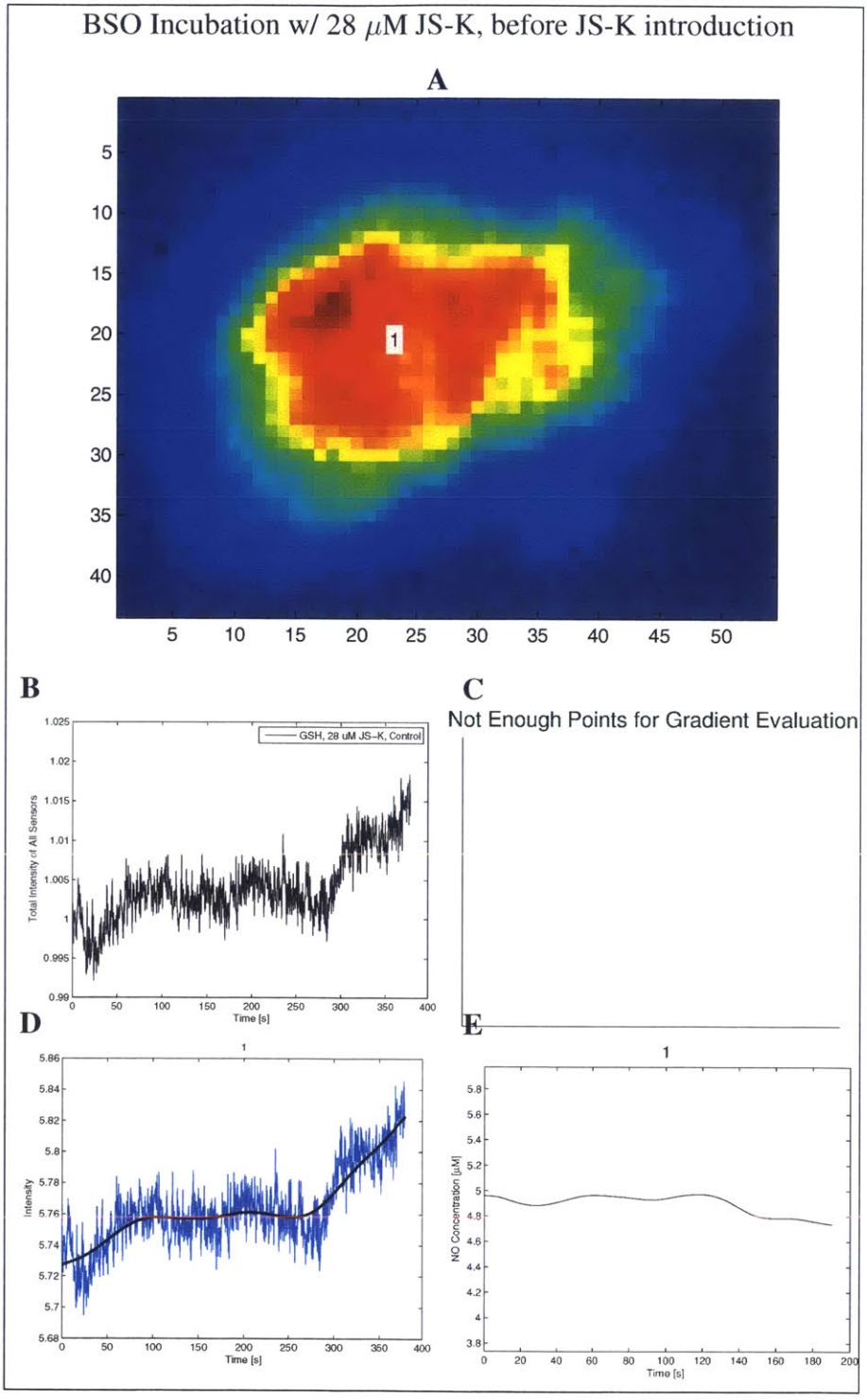
BSO Incubation w/ 28 μM JS-K, before JS-K introduction
A
1
B
GSH, 28 uM JS-K, Control
Total Intensity of All Sensors
Time [s]
C
Not Enough Points for Gradient Evaluation
D
1
Intensity
Time [s]
E
1
NO Concentration [μM]
Time [s]

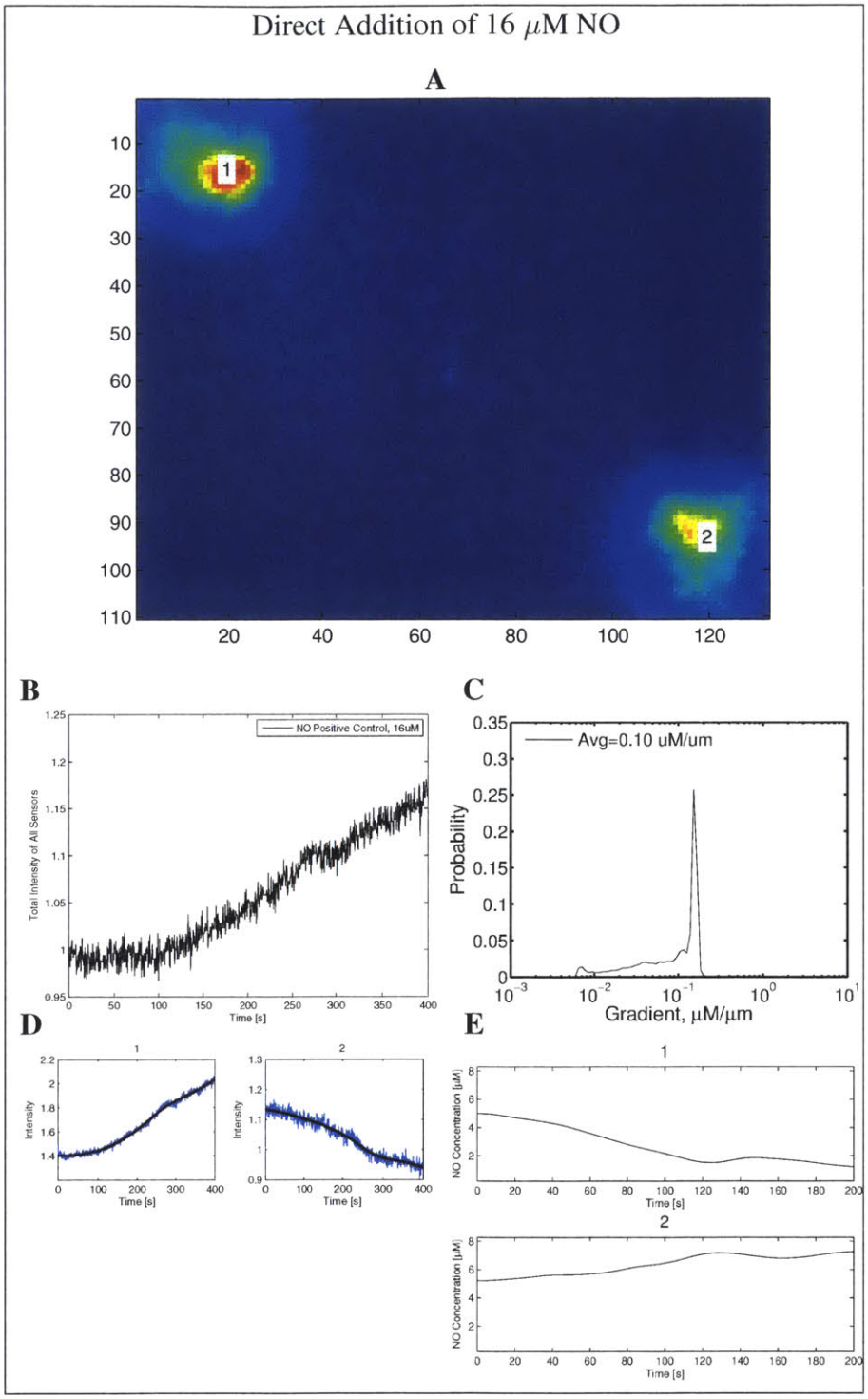
Direct Addition of 16 μM NO
A
B
C
D
E
NO Positive Control, 16uM
Total Intensity of All Sensors
Time [s]
Avg=0.10 uM/um
Probability
Gradient, μM/μm
Intensity
NO Concentration [μM]

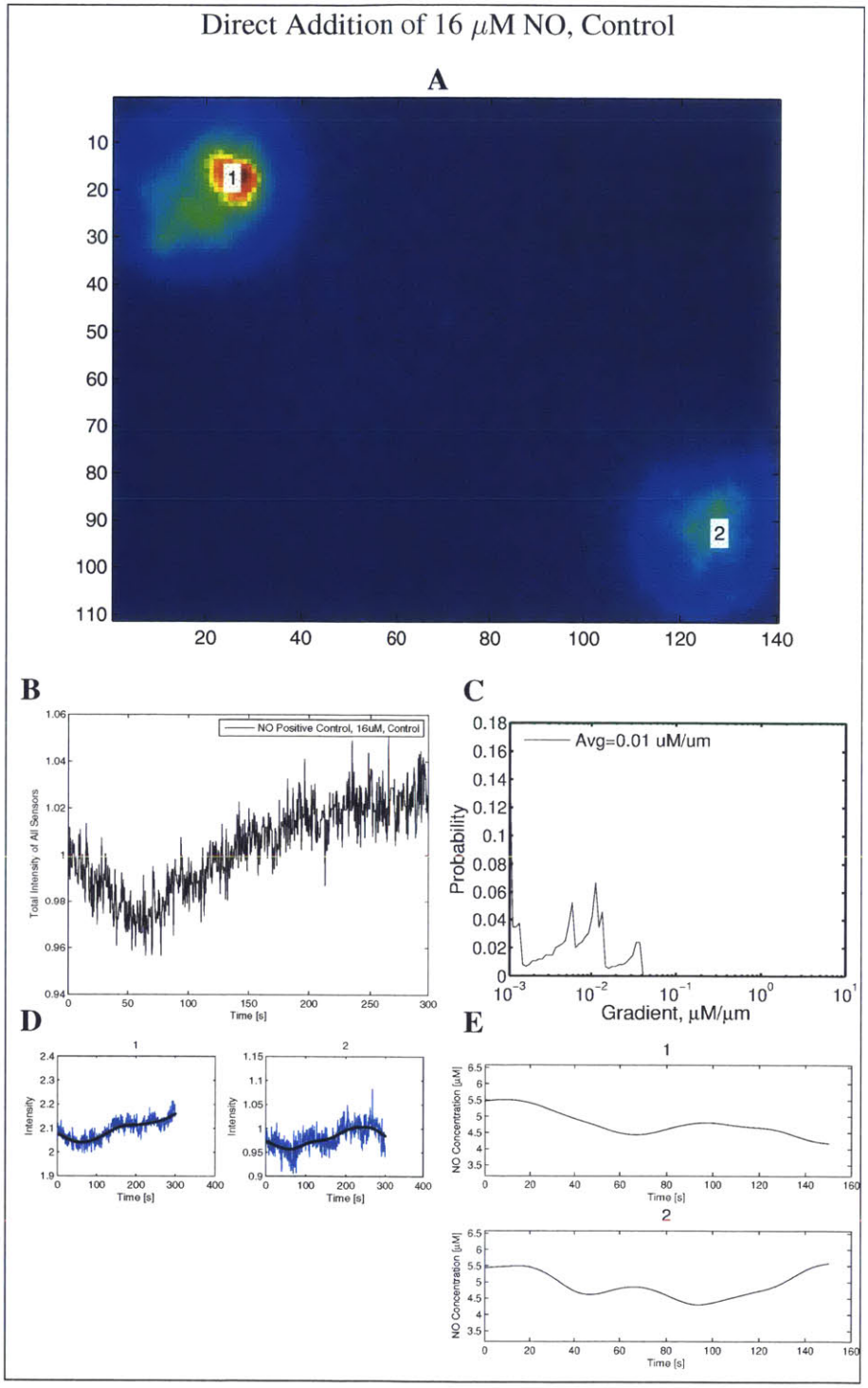
Direct Addition of 16 μM NO, Control
A
1
2
B
NO Positive Control, 16uM, Control
Total Intensity of All Sensors
Time [s]
C
Avg=0.01 uM/um
Probability
Gradient, μM/μm
D
1
2
Intensity
Time [s]
E
1
2
NO Concentration [μM]
Time [s]

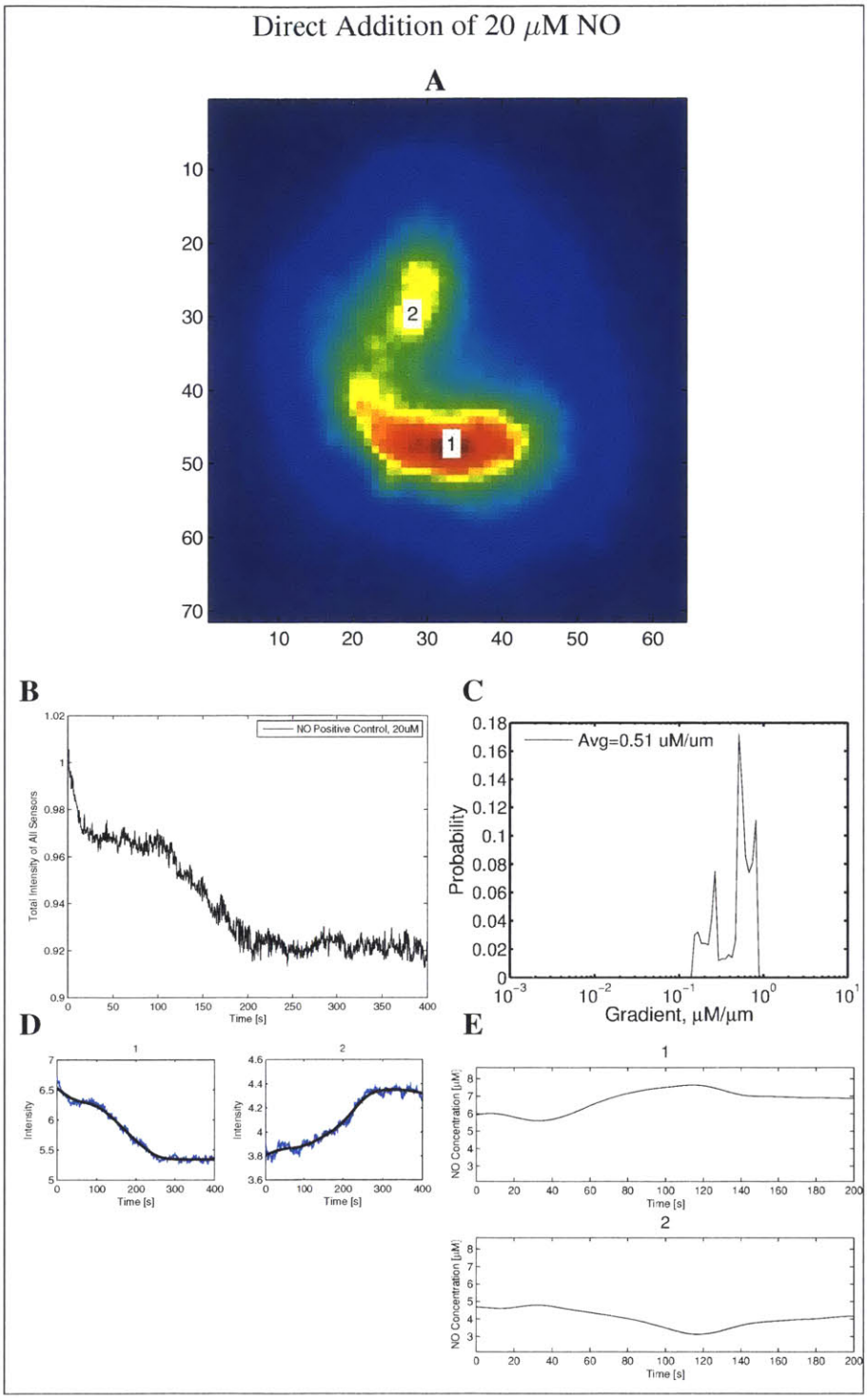
Direct Addition of 20 μM NO
A
B
C
D
E
NO Positive Control, 20uM
Total Intensity of All Sensors
Time [s]
Avg=0.51 uM/um
Probability
Gradient, μM/μm
Intensity
NO Concentration [μM]

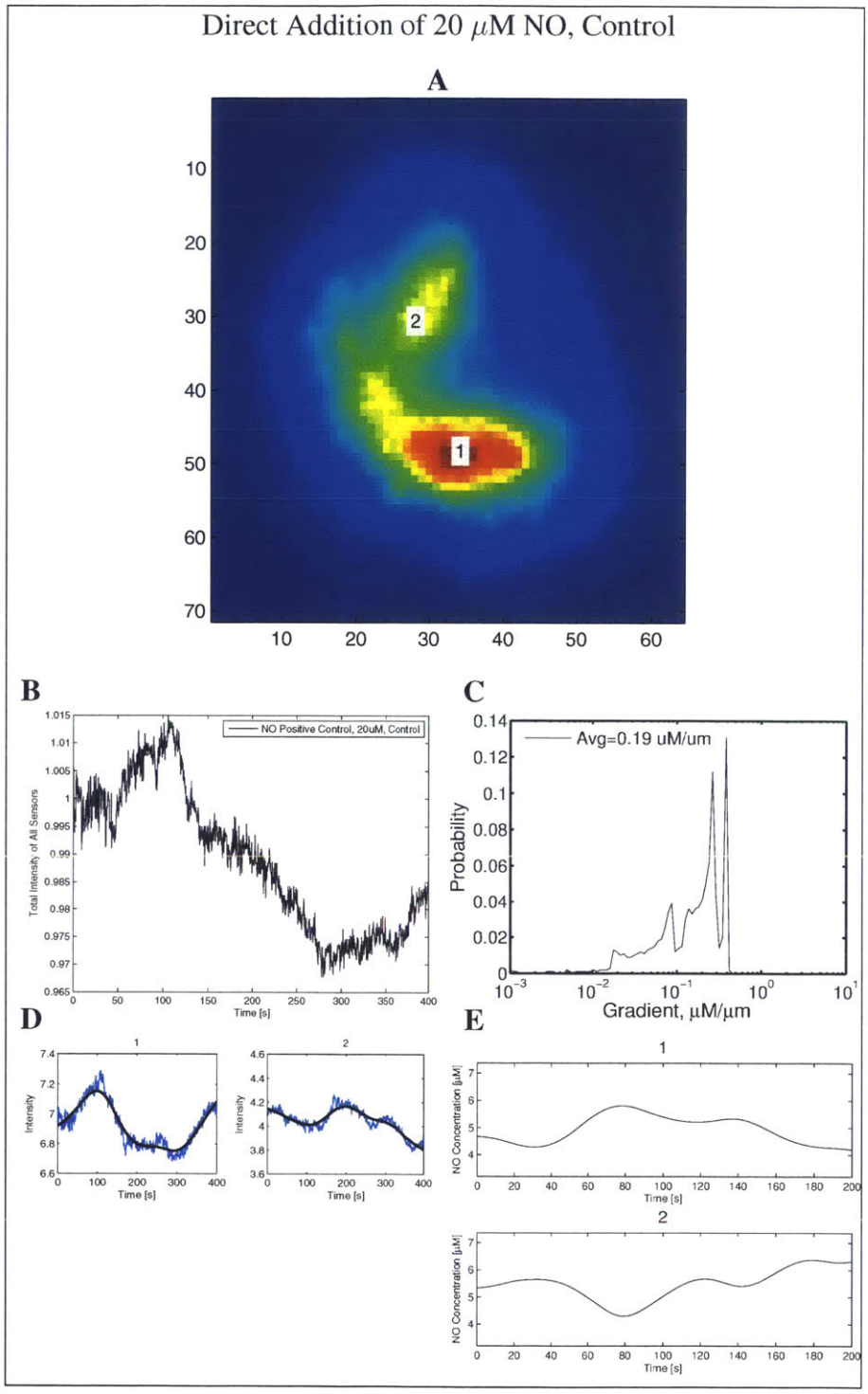
Direct Addition of 20 μM NO, Control
A
B
C
D
E
NO Positive Control, 20uM, Control
Total Intensity of All Sensors
Time [s]
Avg=0.19 uM/um
Probability
Gradient, μM/μm
Intensity
NO Concentration [μM]

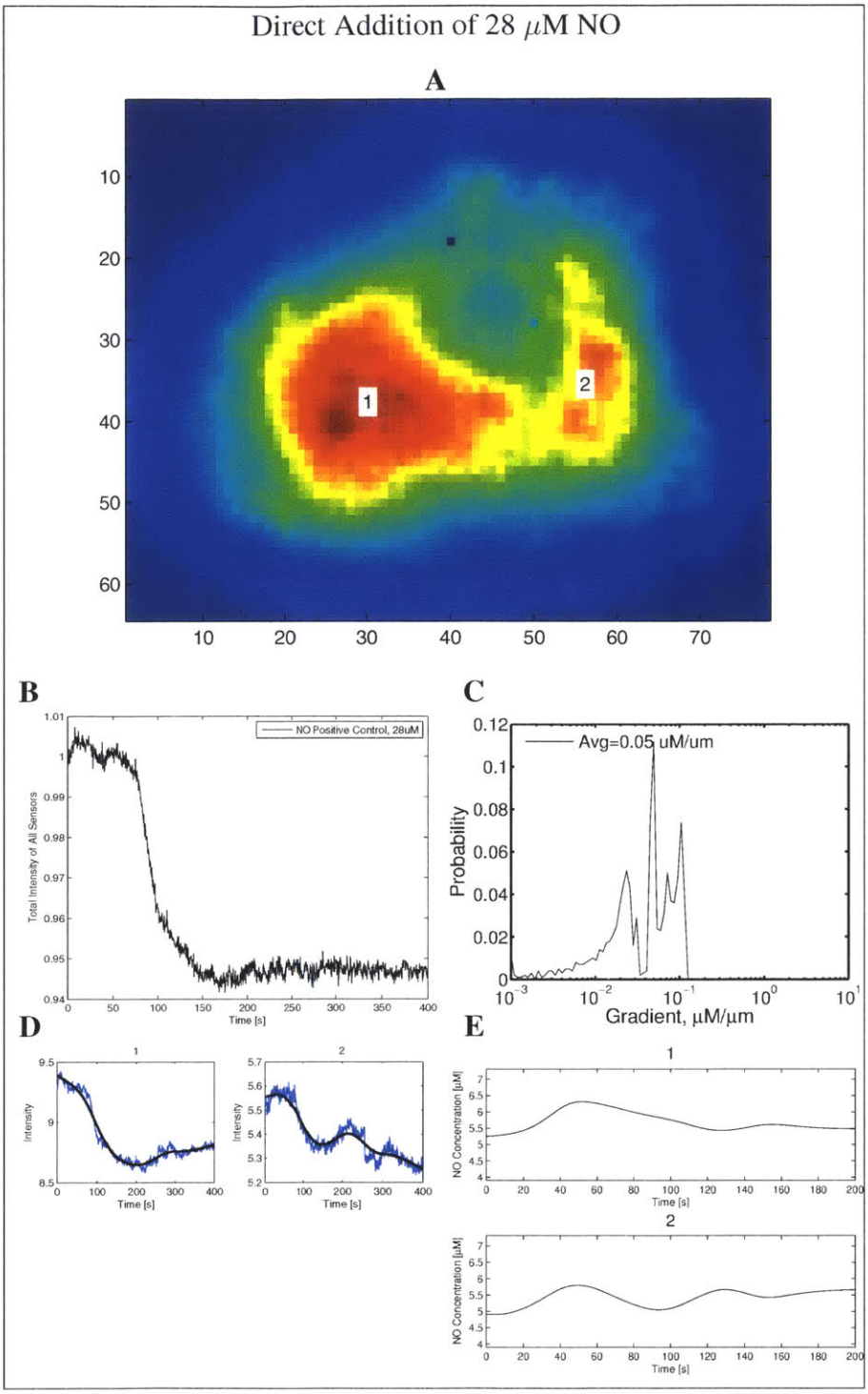
Direct Addition of 28 μM NO
A
1
2
B
NO Positive Control, 28uM
Total Intensity of All Sensors
Time [s]
C
Avg=0.05 uM/um
Probability
Gradient, μM/μm
D
1
2
Intensity
Time [s]
E
1
2
NO Concentration [μM]
Time [s]

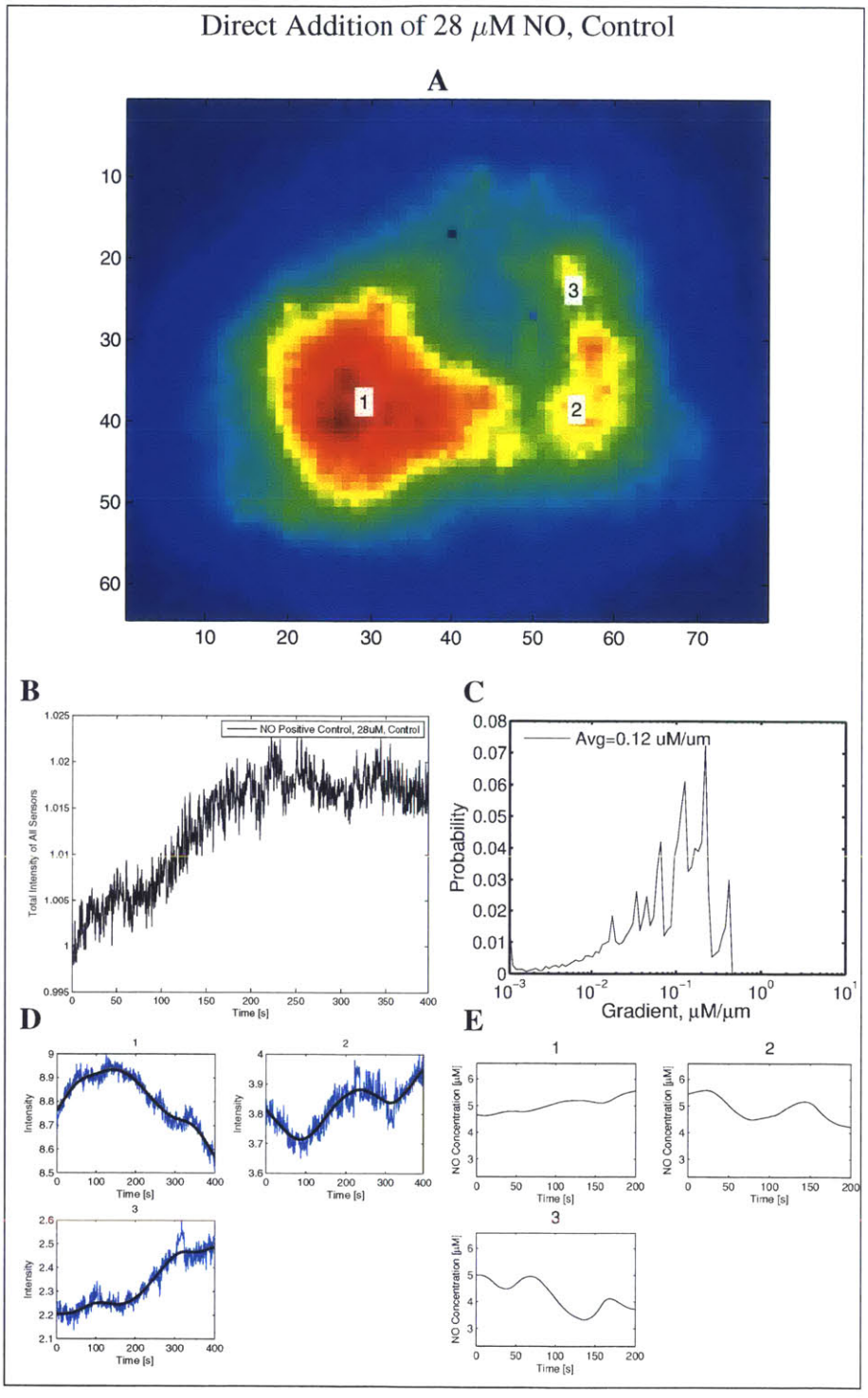
Direct Addition of 28 μM NO, Control
A
B
C
D
E
NO Positive Control, 28uM, Control
Total Intensity of All Sensors
Time [s]
Avg=0.12 uM/um
Probability
Gradient, μM/μm
Intensity
NO Concentration [μM]
1
2
3

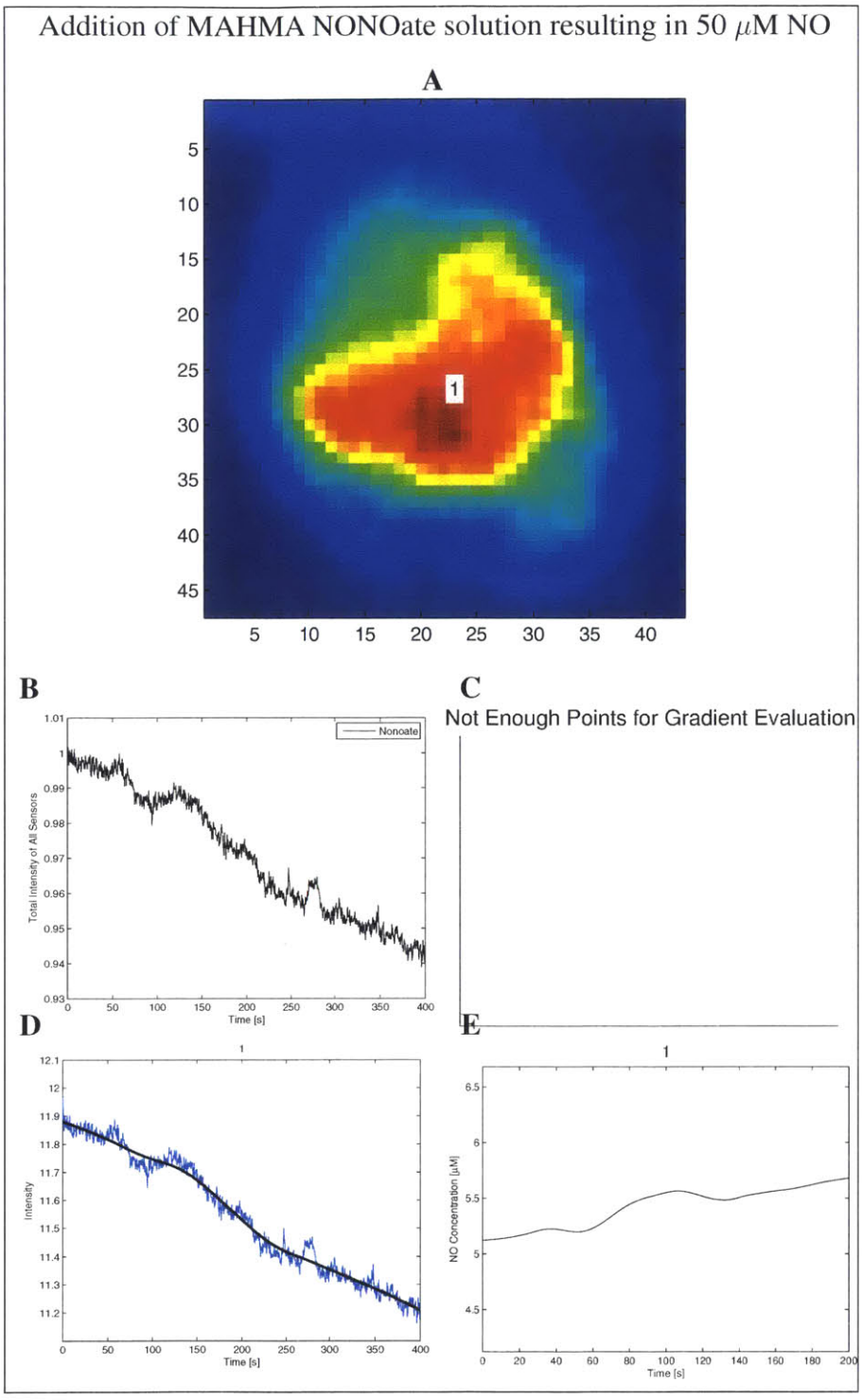
Addition of MAHMA NONOate solution resulting in 50 μM NO
A
1
B
Nonoate
Total Intensity of All Sensors
Time [s]
C
Not Enough Points for Gradient Evaluation
D
1
Intensity
Time [s]
E
1
NO Concentration [μM]
Time [s]

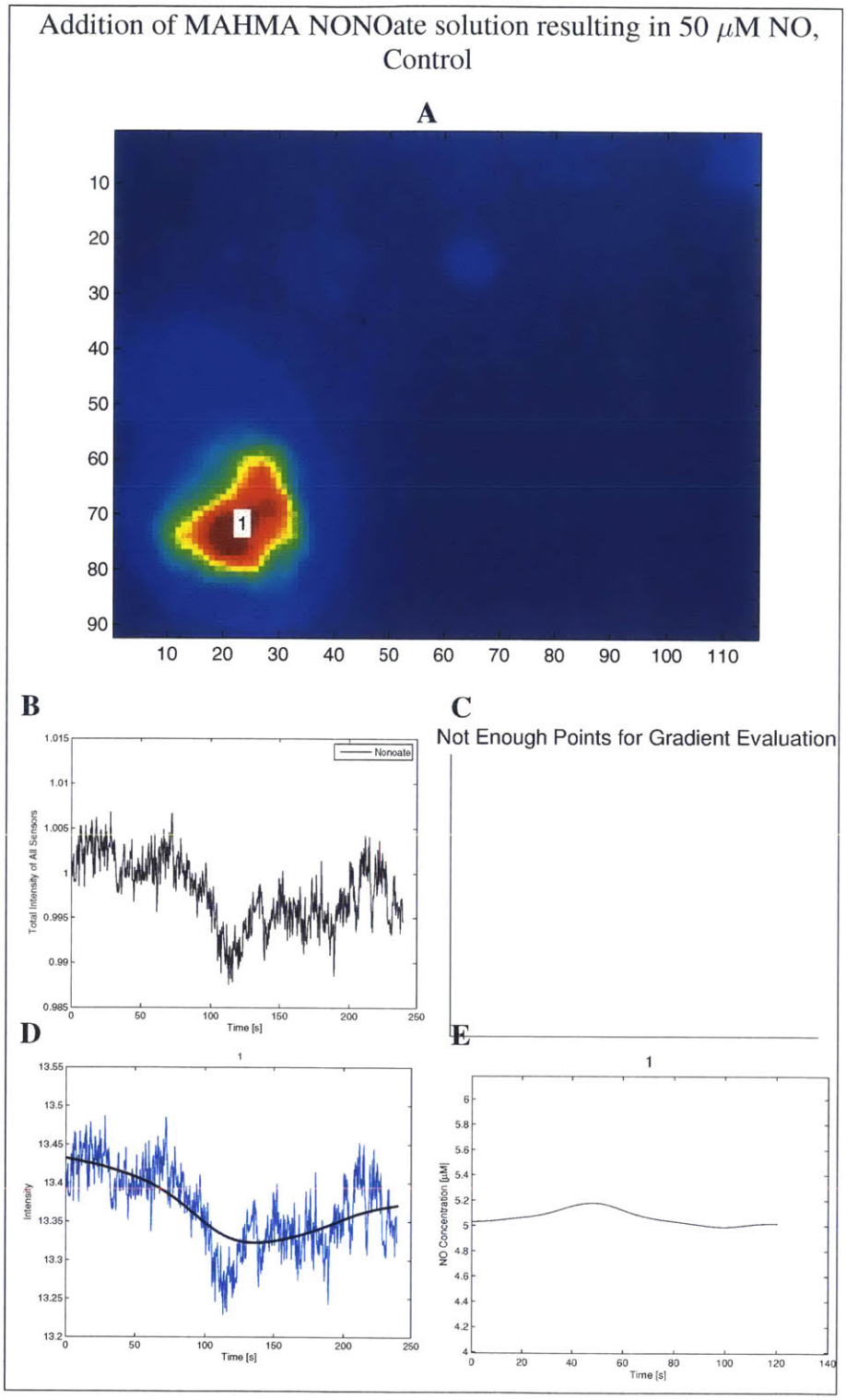
Addition of MAHMA NONOate solution resulting in 50 μM NO, Control
A
B
C
Not Enough Points for Gradient Evaluation
Nonoate
Total Intensity of All Sensors
Time [s]
D
E
Intensity
NO Concentration [μM]

Addition of 28 μM JS-K after incubation with sodium azide (#1)

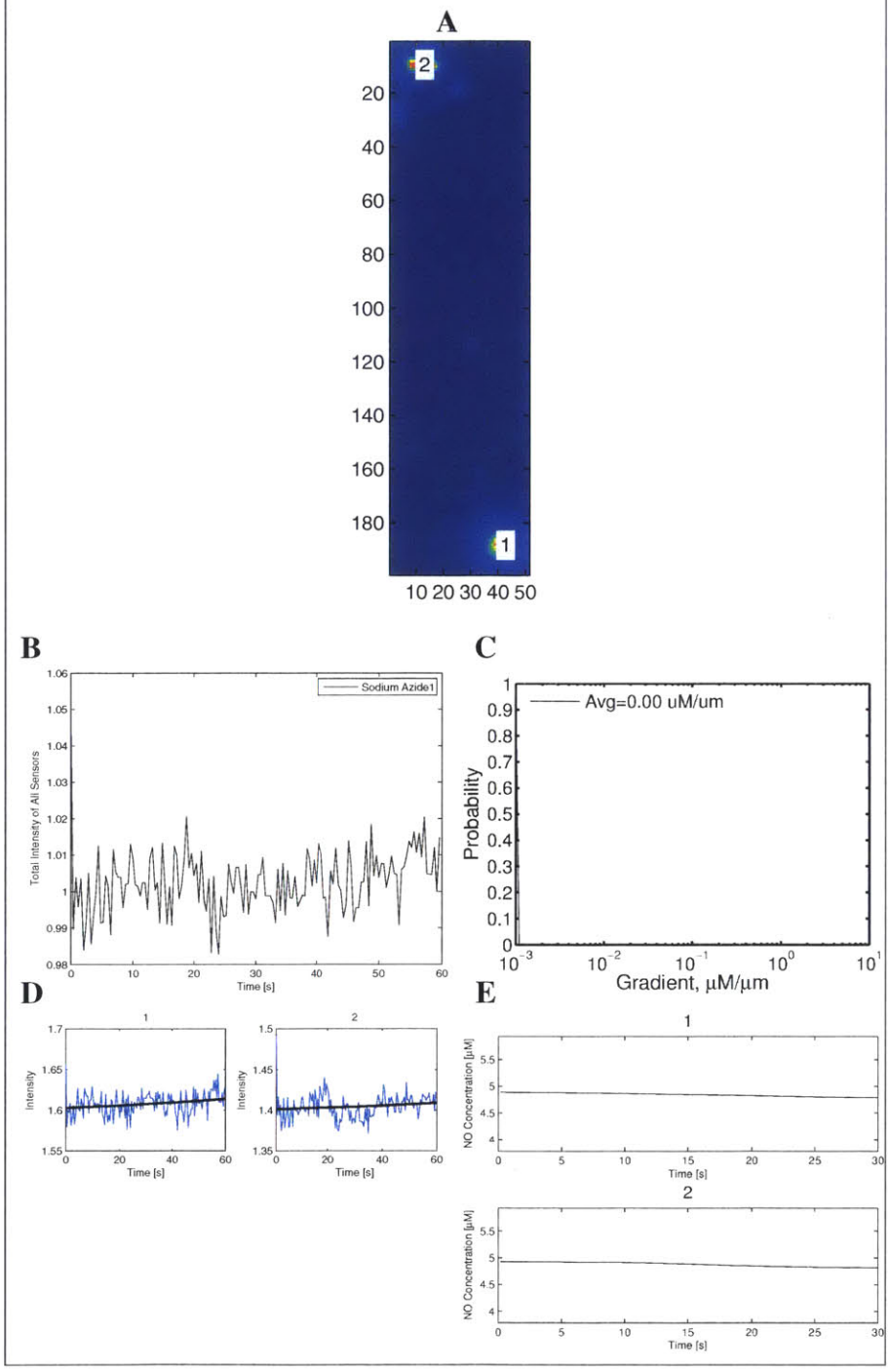

Addition of 28 μM JS-K after incubation with Sodium Azide (#2)

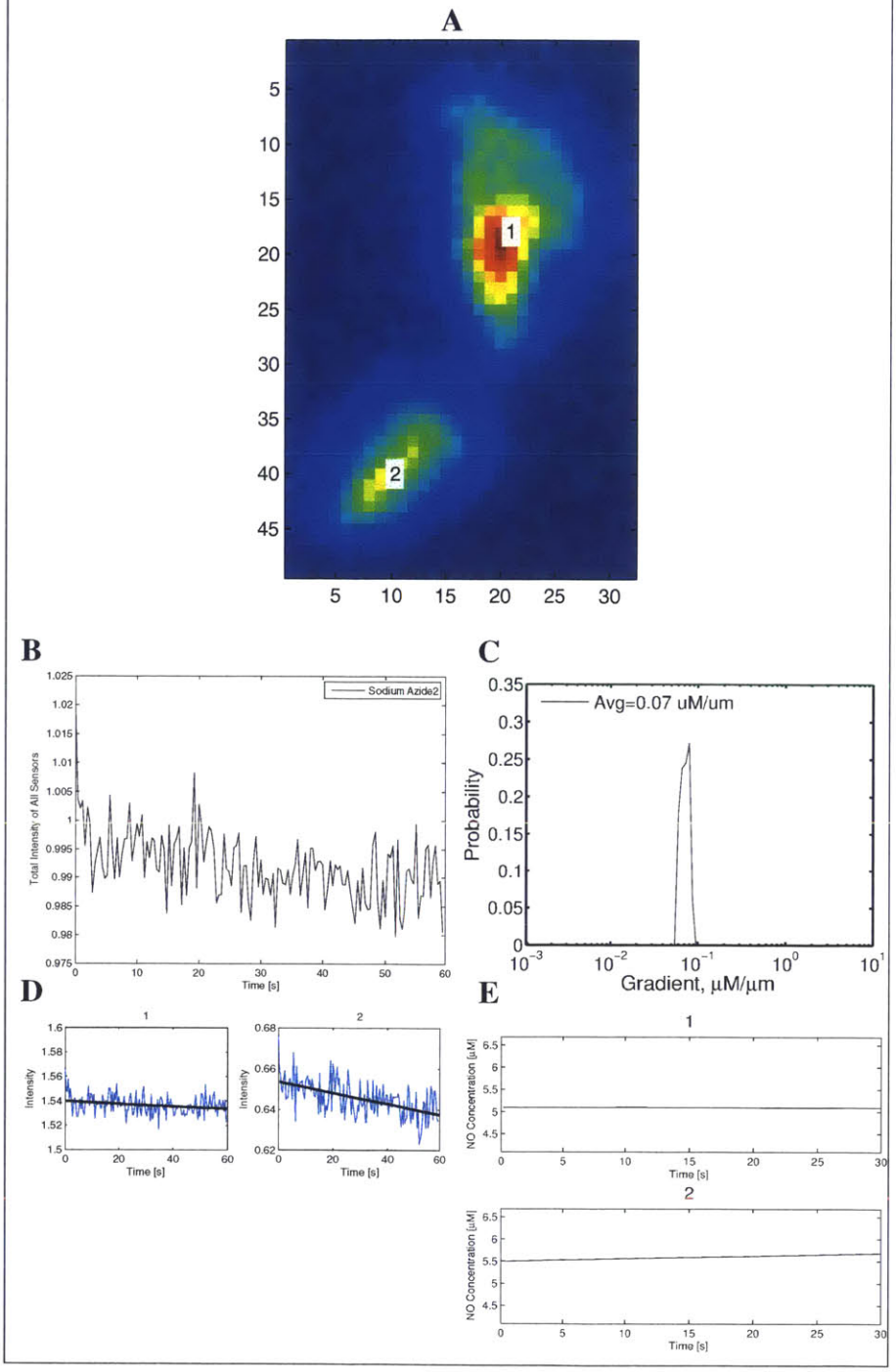

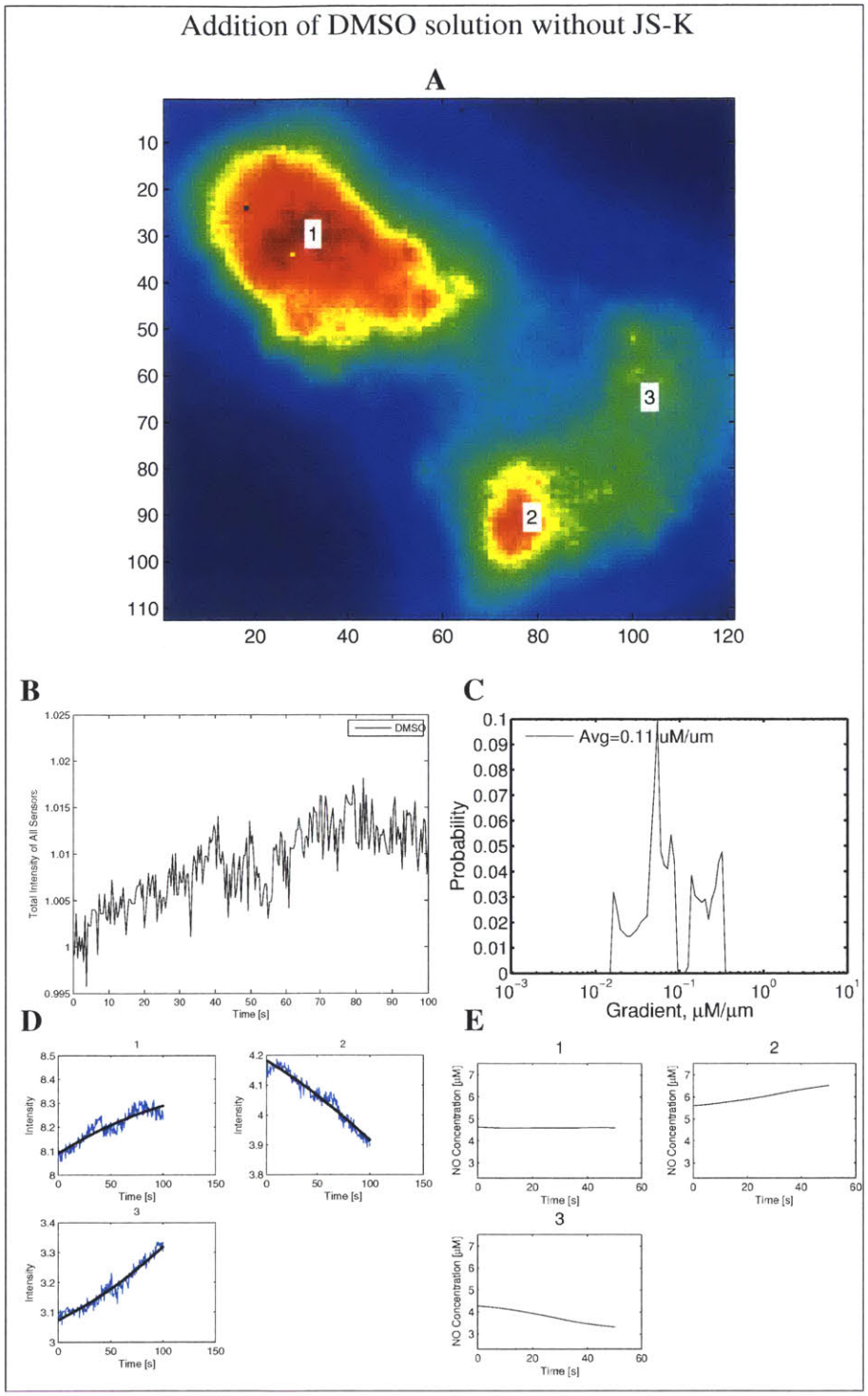
Addition of DMSO solution without JS-K
A
1
2
3
B
DMSO
Total Intensity of All Sensors
Time [s]
C
Avg=0.11 uM/um
Probability
Gradient, µM/µm
D
1
2
3
Intensity
Time [s]
E
1
2
3
NO Concentration [µM]
Time [s]

Addition of DMSO solution without JS-K, before solution addition

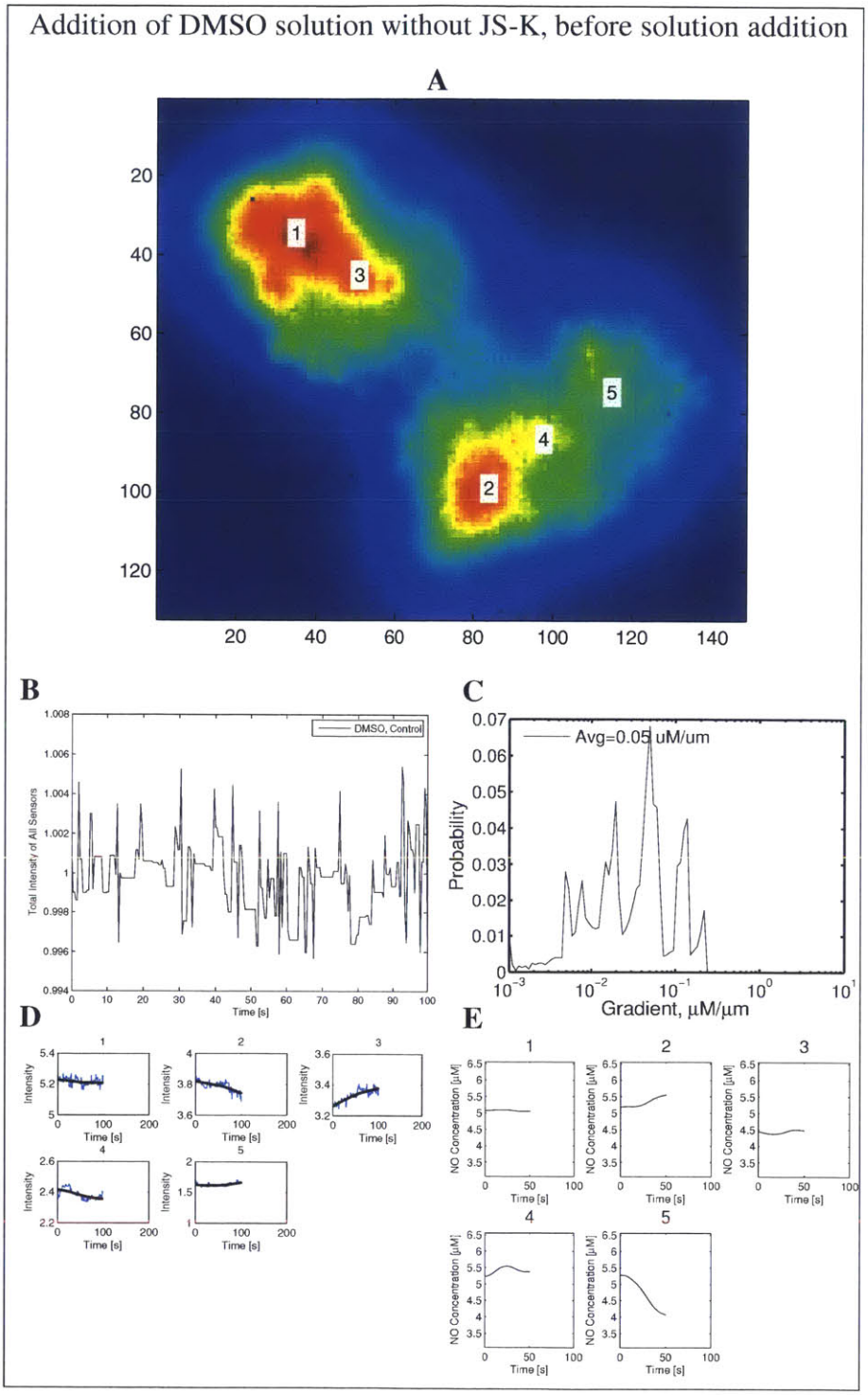

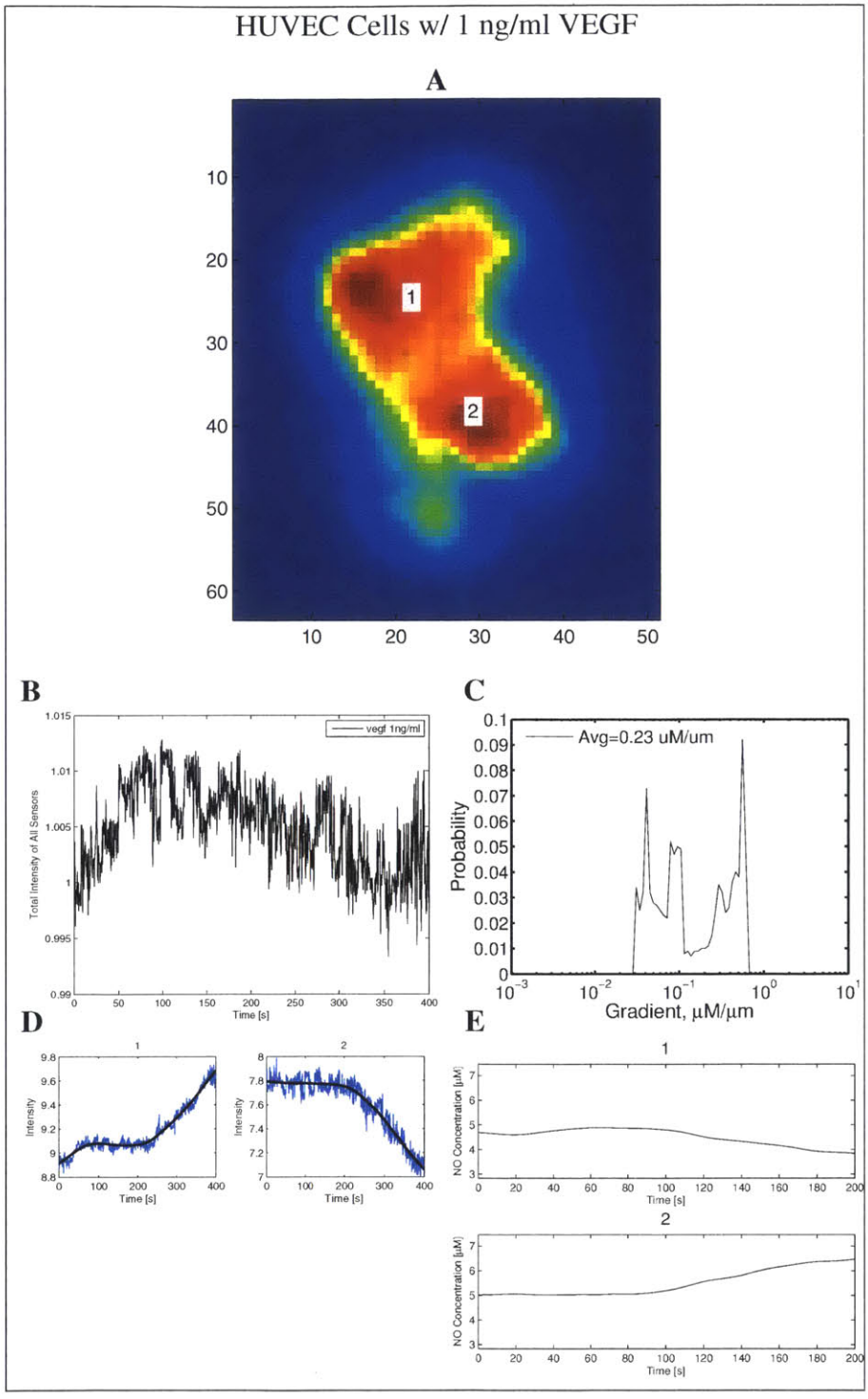
HUVEC Cells w/ 1 ng/ml VEGF
A
B
C
D
E
vegf 1ng/ml
Total Intensity of All Sensors
Time [s]
Avg=0.23 uM/um
Probability
Gradient, µM/µm
Intensity
NO Concentration [µM]

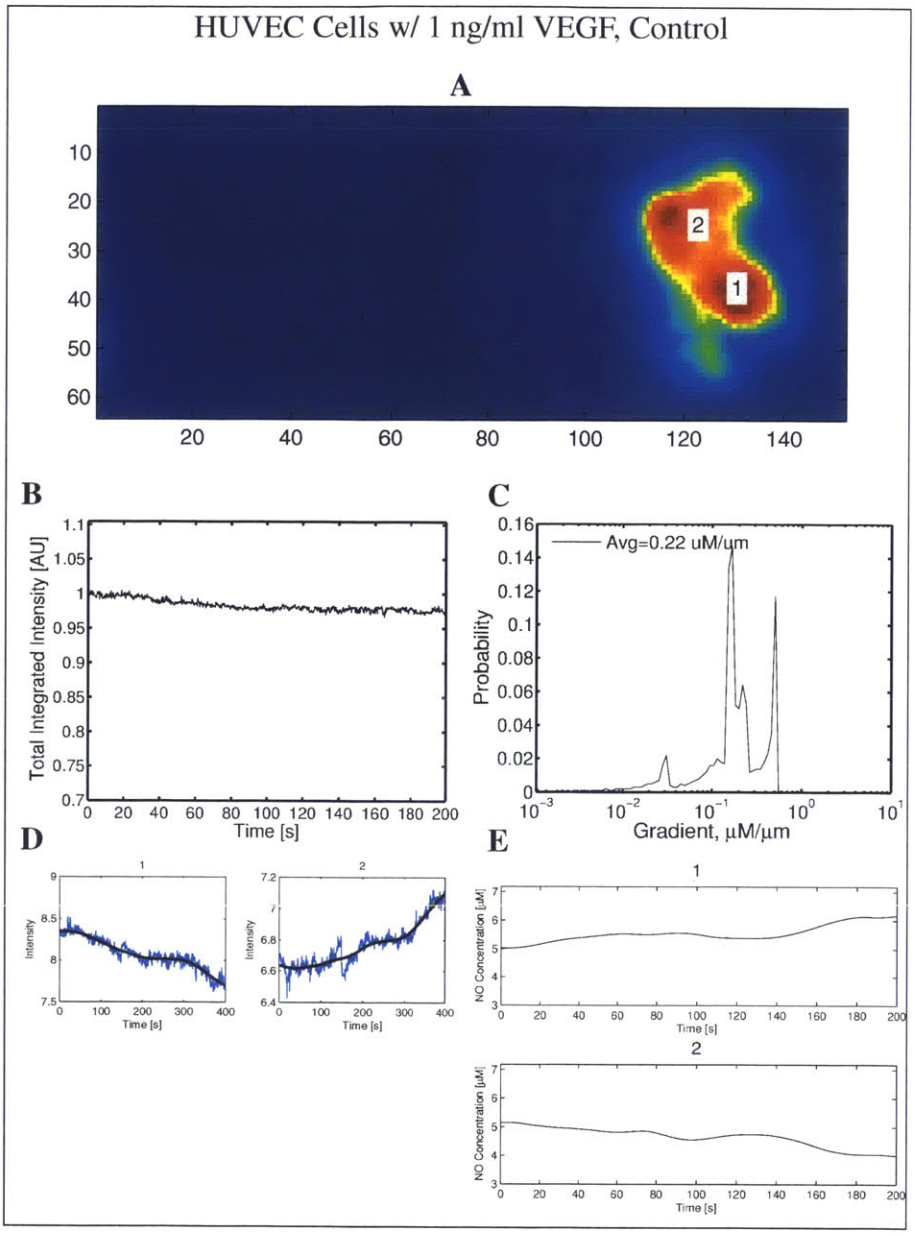
HUVEC Cells w/ 1 ng/ml VEGF, Control
A
B
C
D
E
Total Integrated Intensity [AU]
Time [s]
Avg=0.22 uM/um
Probability
Gradient, µM/µm
Intensity
NO Concentration [µM]
1
2

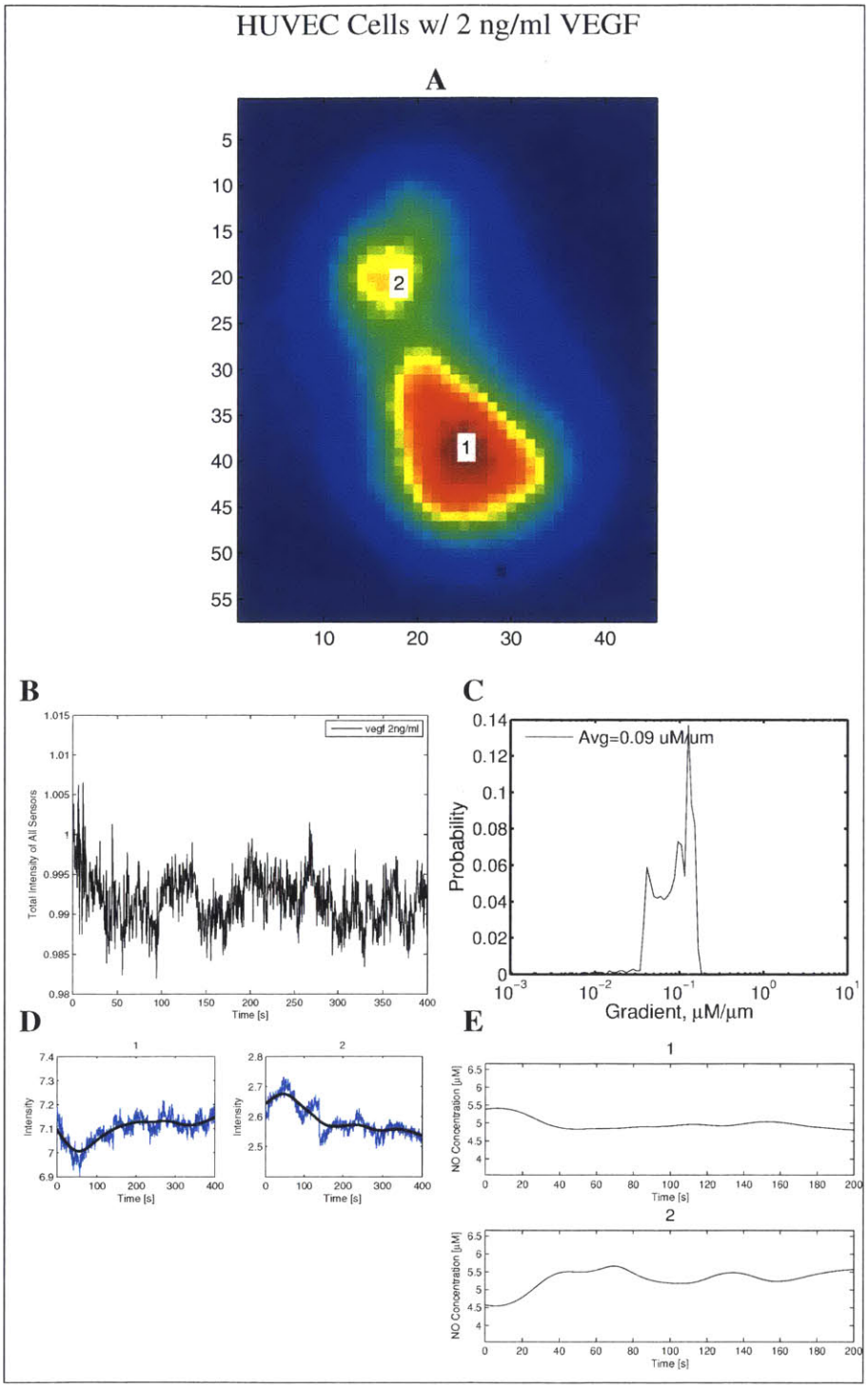
HUVEC Cells w/ 2 ng/ml VEGF
A
B
C
D
E
vegf 2ng/ml
Total Intensity of All Sensors
Time [s]
Avg=0.09 uM/um
Probability
Gradient, µM/µm
Intensity
NO Concentration [uM]

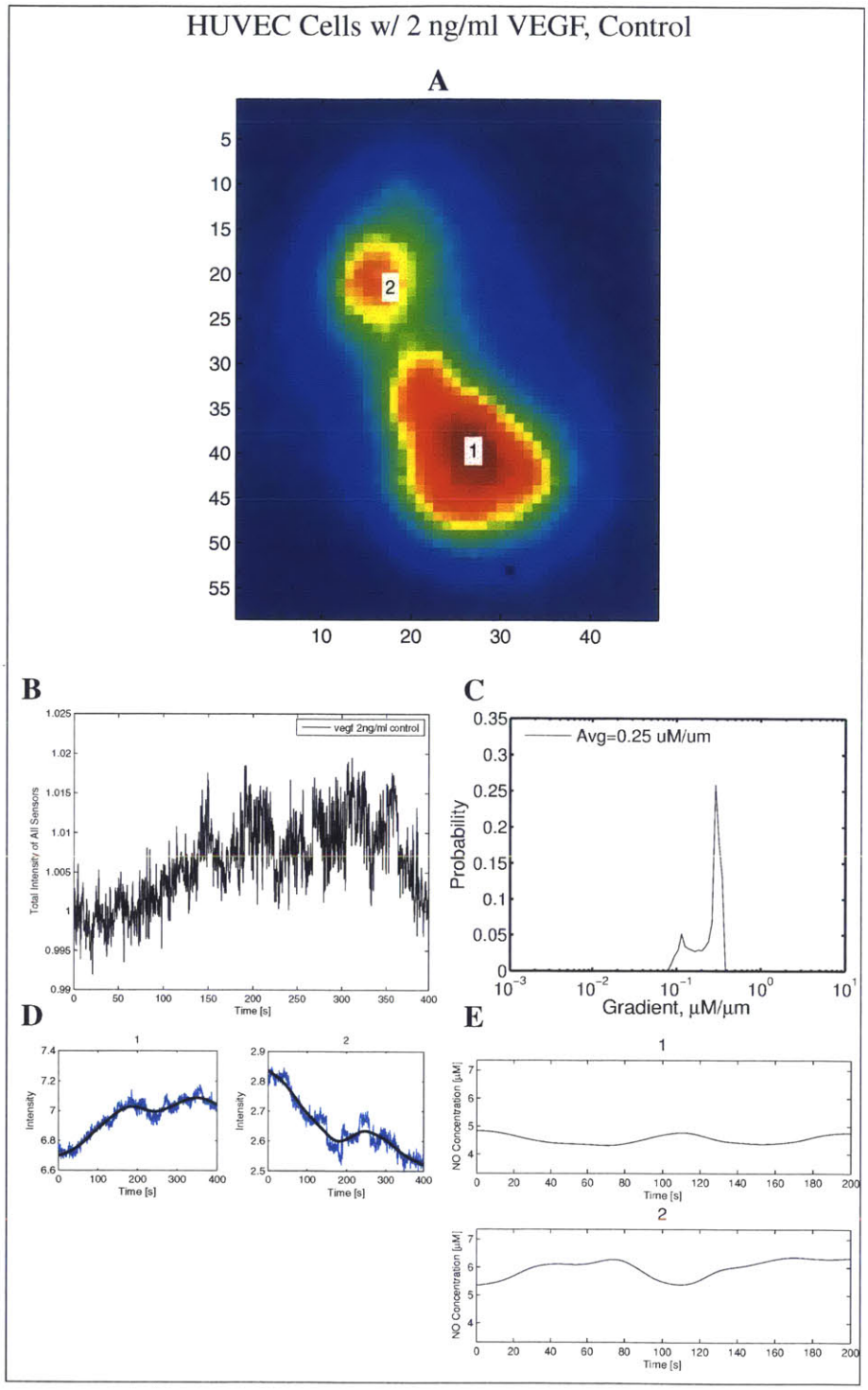
HUVEC Cells w/ 2 ng/ml VEGF, Control
A
B
C
D
E
vegf 2ng/ml control
Total Intensity of All Sensors
Time [s]
Avg=0.25 uM/um
Probability
Gradient, µM/µm
Intensity
NO Concentration [µM]

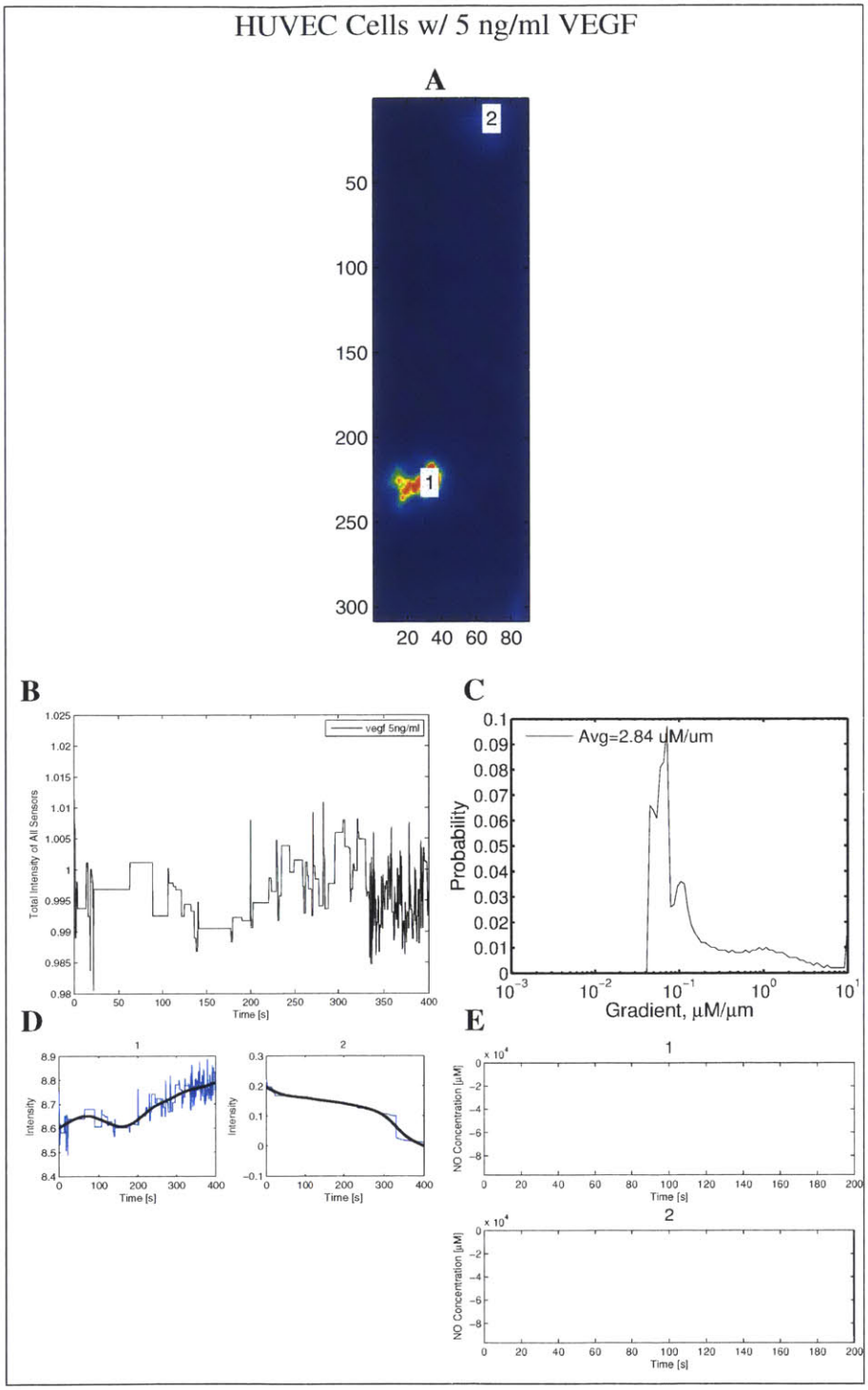
HUVEC Cells w/ 5 ng/ml VEGF
A
2
1
50
100
150
200
250
300
20 40 60 80
B
vegf 5ng/ml
Total Intensity of All Sensors
Time [s]
C
Avg=2.84 uM/um
Probability
Gradient, µM/µm
D
1
2
Intensity
Time [s]
E
1
2
x 10^4
NO Concentration [µM]
Time [s]

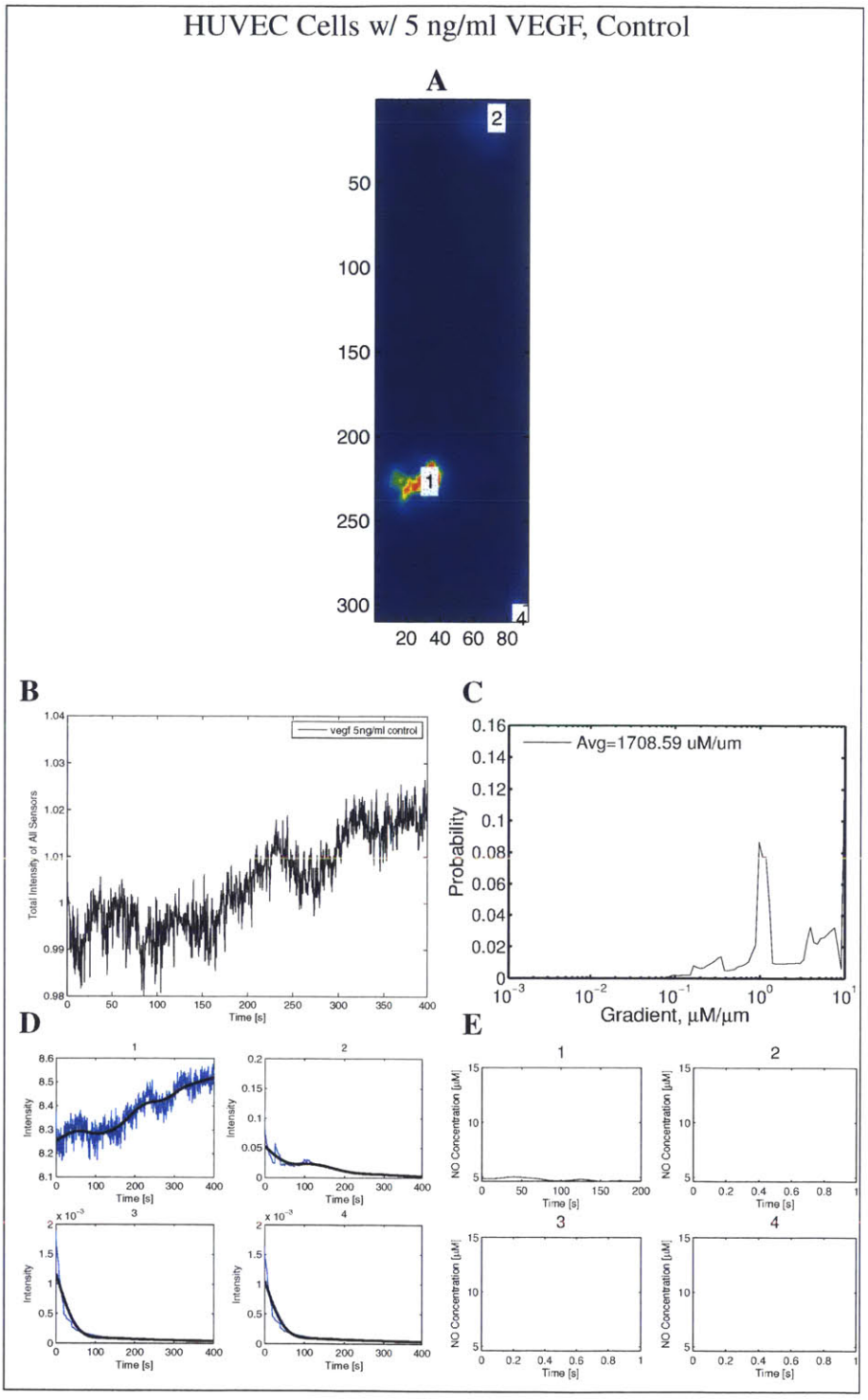
HUVEC Cells w/ 5 ng/ml VEGF, Control
A
B
C
D
E
vegf 5ng/ml control
Total Intensity of All Sensors
Time [s]
Avg=1708.59 uM/um
Probability
Gradient, µM/µm
Intensity
NO Concentration [µM]

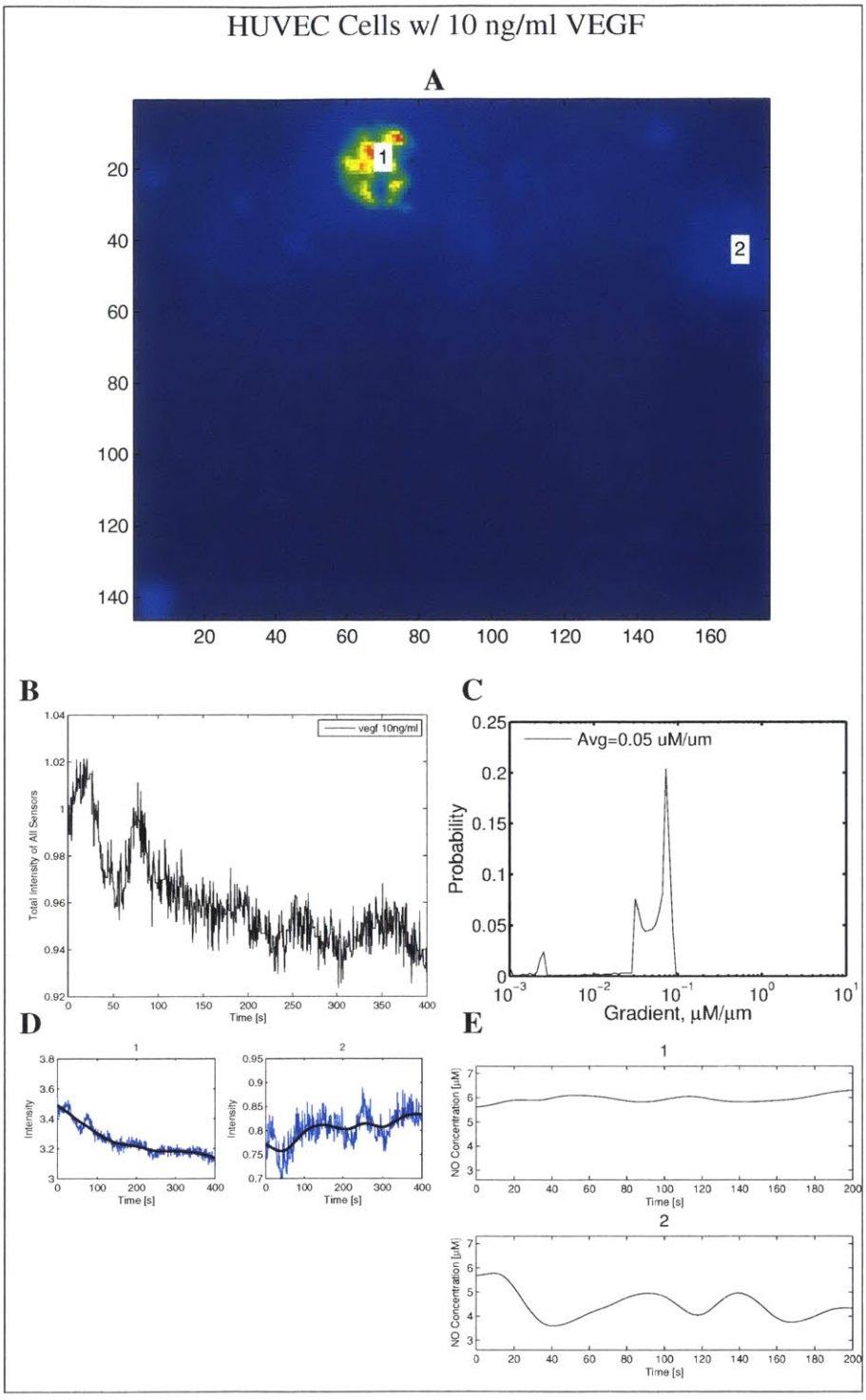
HUVEC Cells w/ 10 ng/ml VEGF
A
1
2
B
vegf 10ng/ml
Total Intensity of All Sensors
Time [s]
C
Avg=0.05 uM/um
Probability
Gradient, µM/µm
D
1
2
Intensity
Time [s]
E
1
2
NO Concentration [uM]
Time [s]

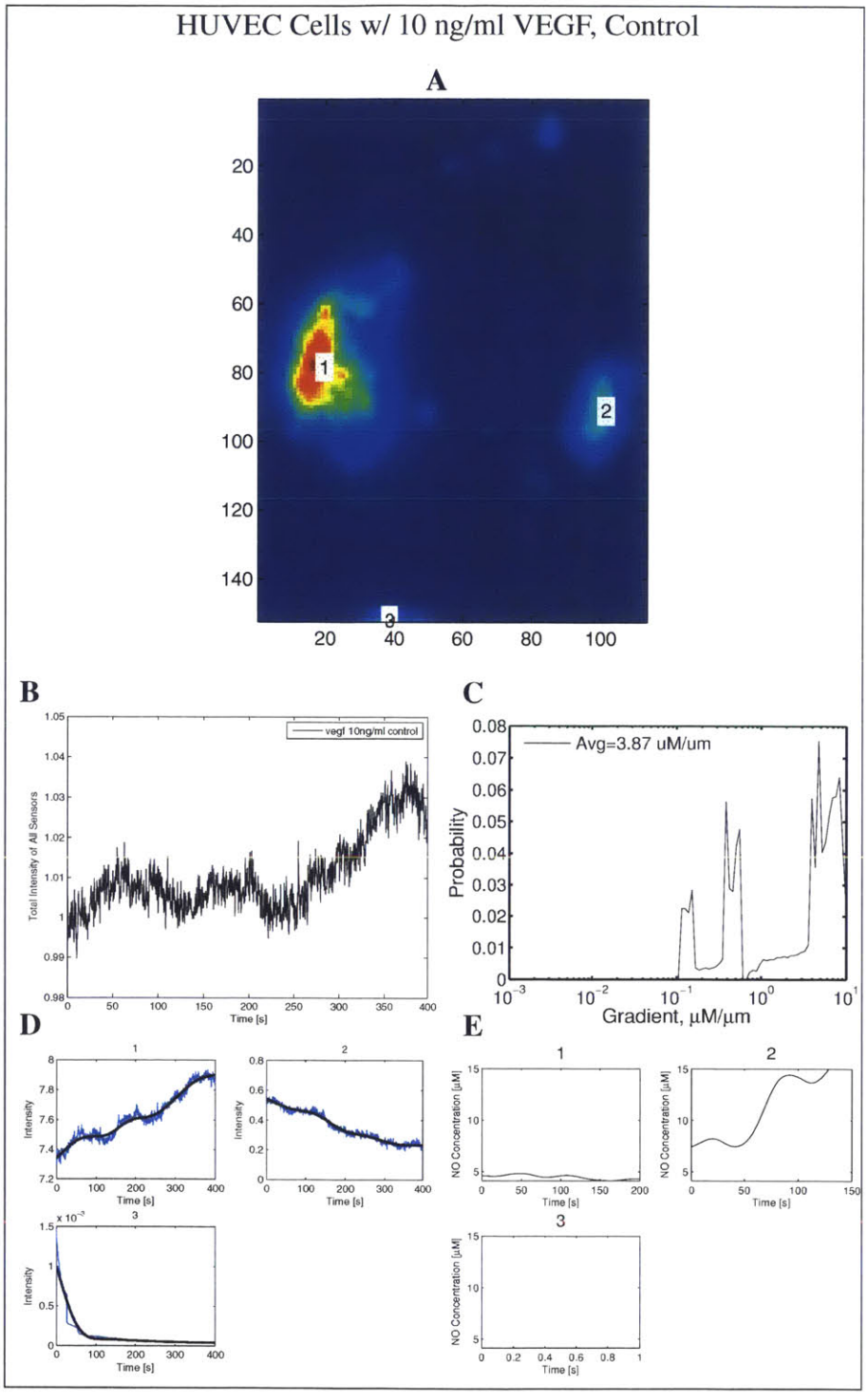
HUVEC Cells w/ 10 ng/ml VEGF, Control
A
B
C
D
E
vegf 10ng/ml control
Total Intensity of All Sensors
Time [s]
Avg=3.87 uM/um
Probability
Gradient, µM/µm
Intensity
NO Concentration [µM]

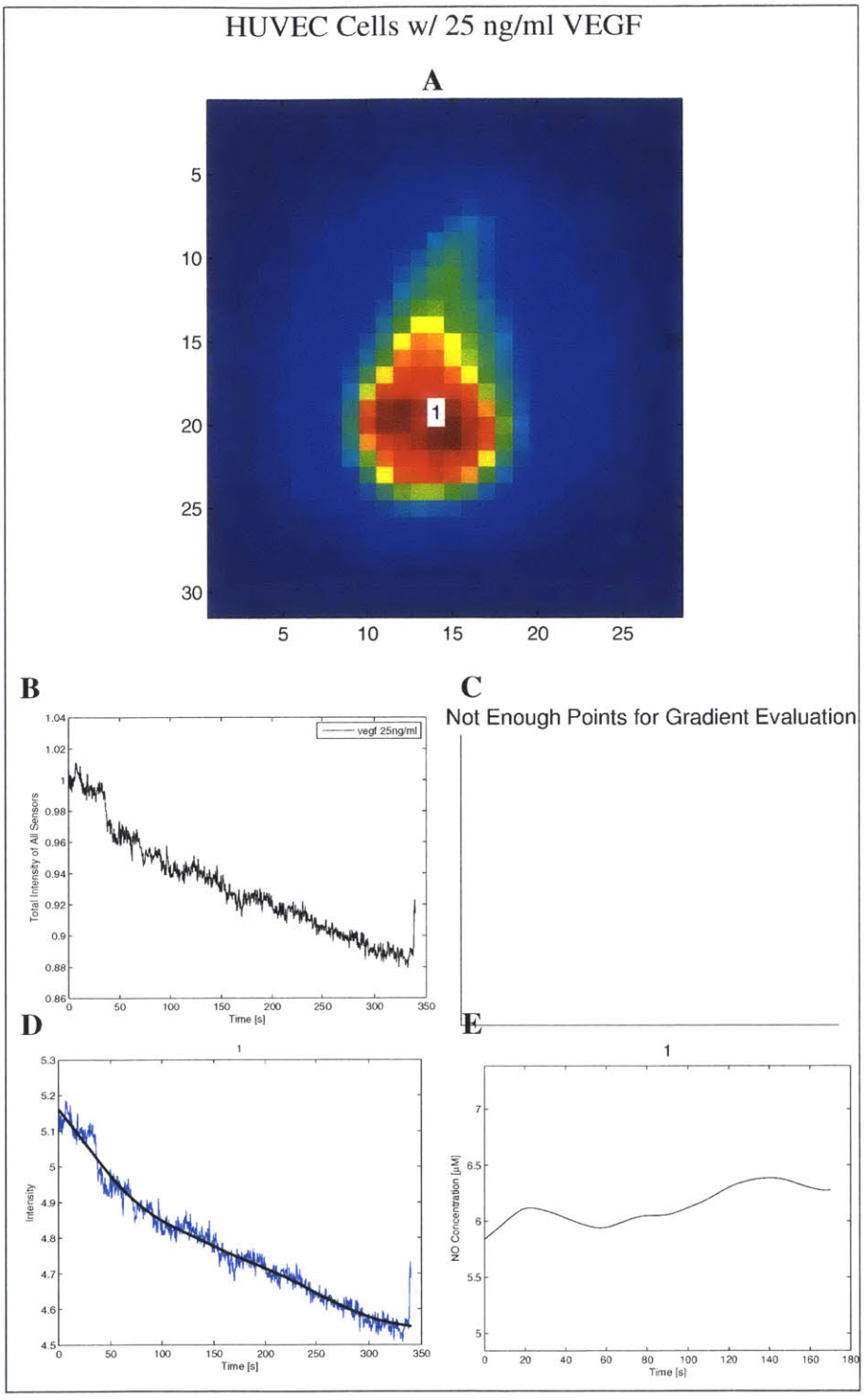
HUVEC Cells w/ 25 ng/ml VEGF
A
1
B
vegf 25ng/ml
Total Intensity of All Sensors
Time [s]
C
Not Enough Points for Gradient Evaluation
D
1
Intensity
Time [s]
E
1
NO Concentration [μM]
Time [s]

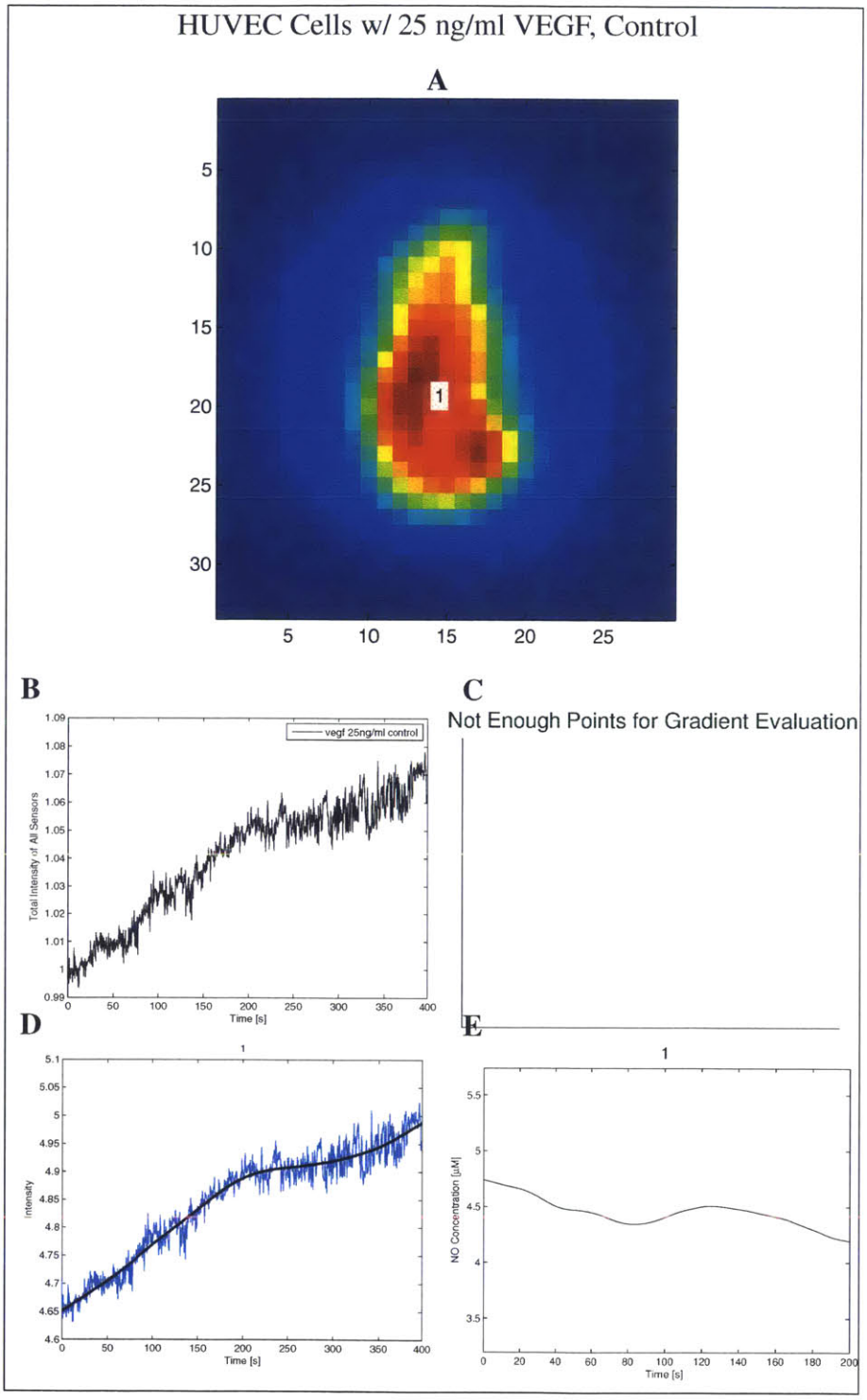
HUVEC Cells w/ 25 ng/ml VEGF, Control
A
1
B
vegf 25ng/ml control
Total Intensity of All Sensors
Time [s]
C
Not Enough Points for Gradient Evaluation
D
1
Intensity
Time [s]
E
1
NO Concentration [μM]
Time [s]

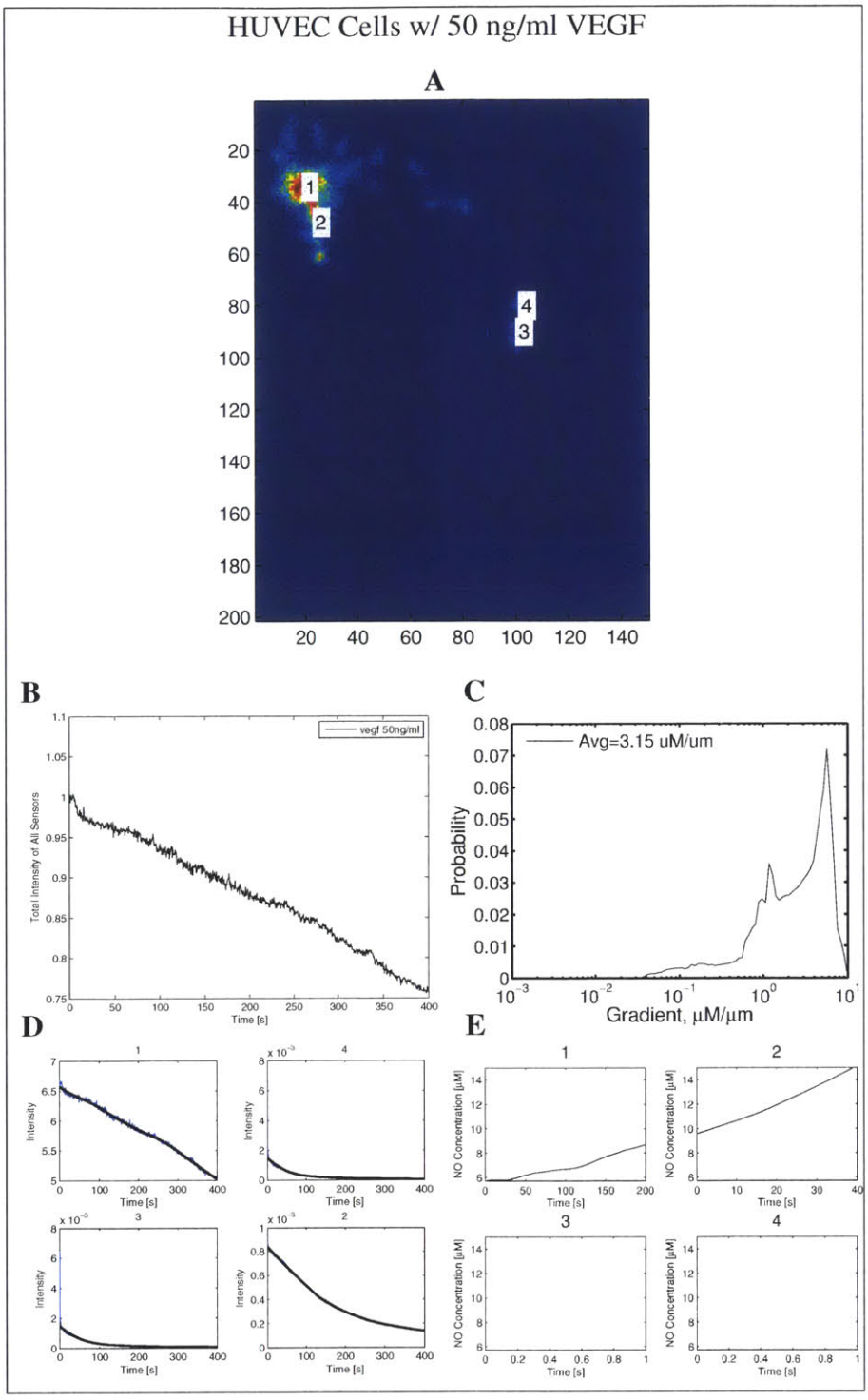
HUVEC Cells w/ 50 ng/ml VEGF
A
B
C
D
E
vegf 50ng/ml
Total Intensity of All Sensors
Time [s]
Avg=3.15 uM/um
Probability
Gradient, µM/µm
Intensity
NO Concentration [µM]

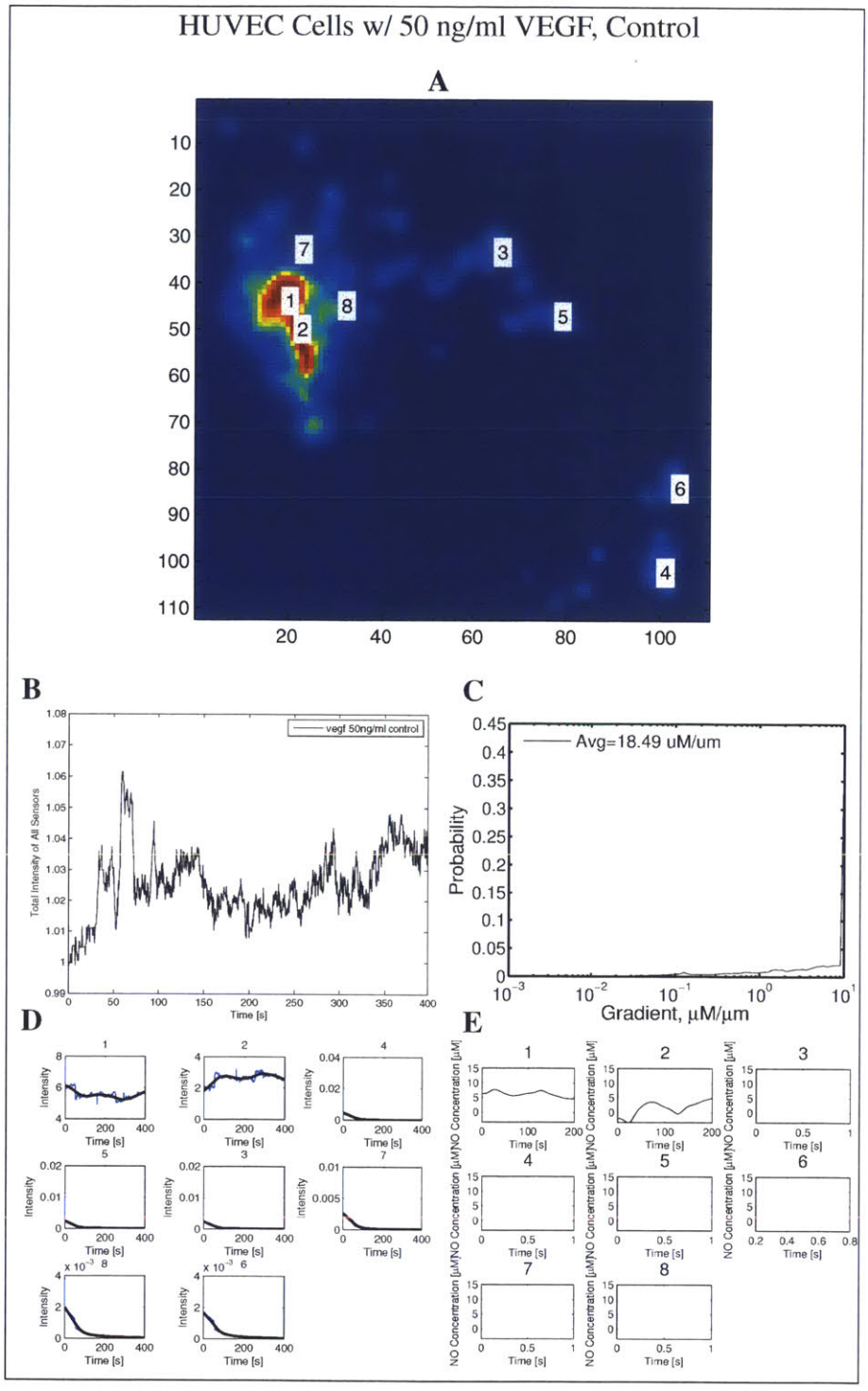
HUVEC Cells w/ 50 ng/ml VEGF, Control
A
B
C
D
E
vegf 50ng/ml control
Total Intensity of All Sensors
Time [s]
Avg=18.49 uM/um
Probability
Gradient, µM/µm
Intensity
NO Concentration [µM]

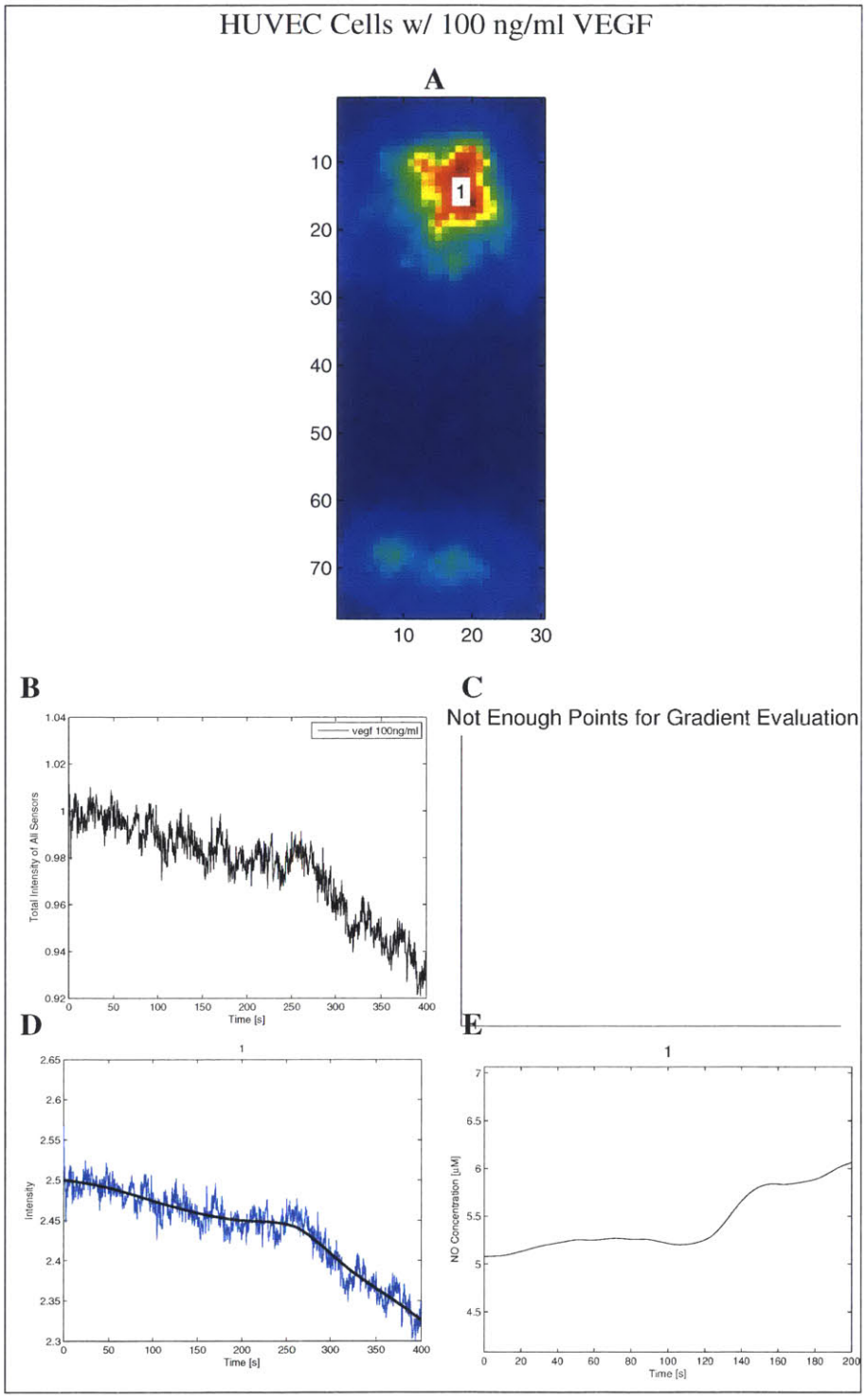
HUVEC Cells w/ 100 ng/ml VEGF
A
1
10
20
30
40
50
60
70
10
20
30
B
vegf 100ng/ml
Total Intensity of All Sensors
Time [s]
C
Not Enough Points for Gradient Evaluation
D
1
Intensity
Time [s]
E
1
NO Concentration [uM]
Time [s]

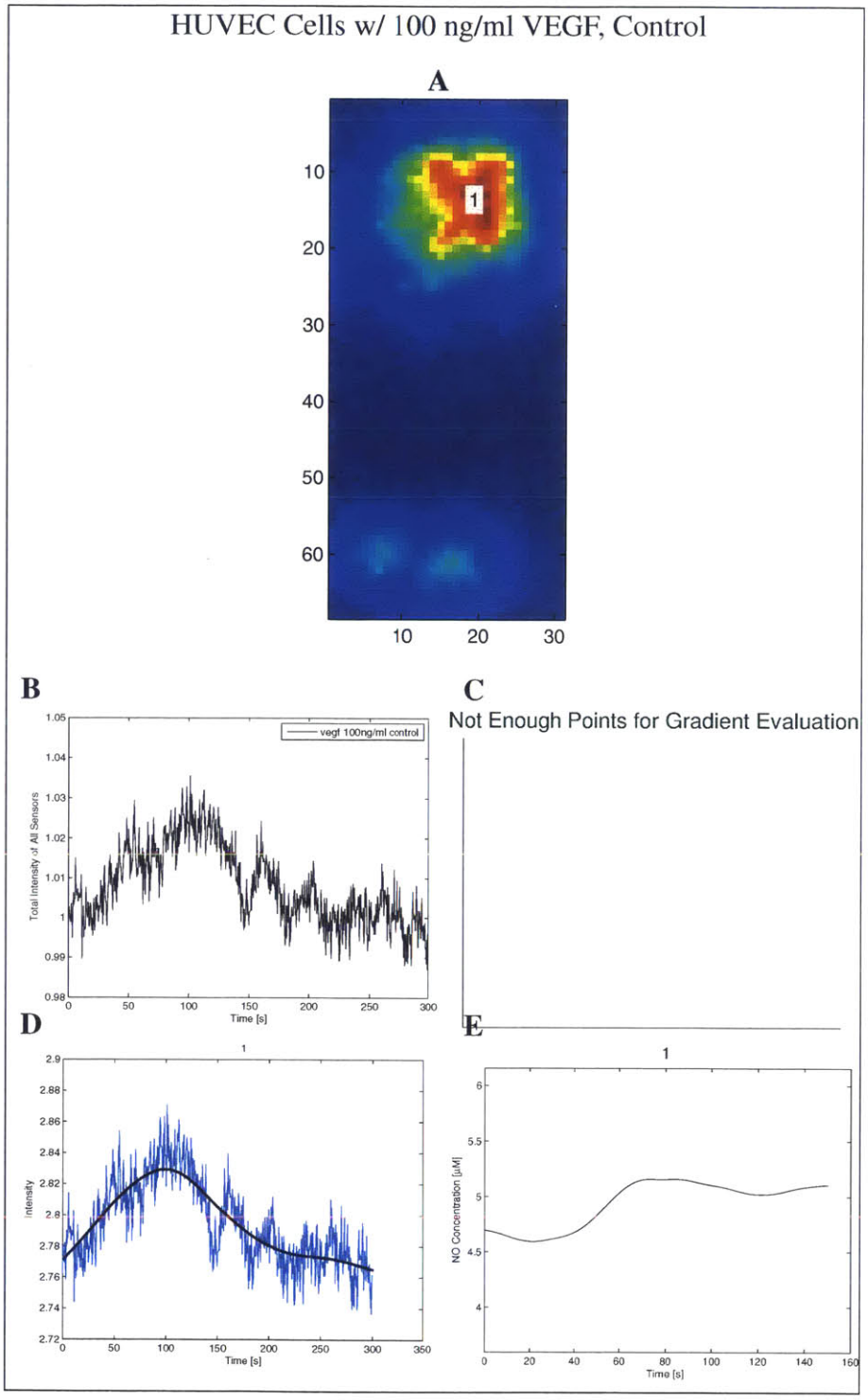
HUVEC Cells w/ 100 ng/ml VEGF, Control
A
1
10
20
30
40
50
60
10
20
30
B
vegf 100ng/ml control
Total Intensity of All Sensors
Time [s]
C
Not Enough Points for Gradient Evaluation
D
1
Intensity
Time [s]
E
1
NO Concentration [uM]
Time [s]